Technische Universität München
Institut für Energietechnik

Lehrstuhl für Thermodynamik

Numerically Efficient Hybrid RANS/LES of Supersonic Combustion

Konrad Makowka

Vollständiger Abdruck der von der Fakultät für Maschinenwesen der Technischen Universität München zur Erlangung des akademischen Grades eines

DOKTOR – INGENIEURS

genehmigten Dissertation.

Vorsitzender:
Univ.-Prof. Dr.-Ing. Horst Baier
Prüfer der Dissertation:
1. Univ.-Prof. Dr.-Ing. Thomas Sattelmayer
2. Univ.-Prof. Dr.-Ing. Jens von Wolfersdorf, Universität Stuttgart

Die Dissertation wurde am 12.06.2015 bei der Technischen Universität München eingereicht und durch die Fakultät für Maschinenwesen am 28.09.2015 angenommen.

Vorwort

Die vorliegende Dissertation ist das Ergebnis meiner Forschungstätigkeit am Lehrstuhl für Thermodynamik der Technischen Universität München und Teil des Graduiertenkollegs 1095/2 der Deutschen Forschungsgemeinschaft zum Thema "Aero-/thermodynamische Auslegung eines Scramjet-Antriebssystems für zukünftige Raumtransportsysteme".

Mein besonderer Dank gilt meinem Doktorvater Herrn Professor Dr.-Ing. Thomas Sattelmayer für die wissenschaftliche Betreuung meiner Arbeit. Ebenso danke ich Herrn Professor Dr.-Ing. Jens von Wolfersdorf für die Unterstützung innerhalb des Graduiertenkollegs und freundliche Übernahme des Koreferates, sowie Herrn Professor Dr.-Ing. Horst Baier für die Übernahme des Prüfungsvorsitzes.

Ich danke allen aktuellen und ehemaligen Mitarbeitern des Lehrstuhls für Thermodynamik herzlich für die freundschaftliche Zusammenarbeit. Einen großen Dank möchte ich auch meinen zahlreichen Partnern innerhalb des Graduiertenkollegs aussprechen, insbesondere meinen Kollegen an den Lehrstühlen für Flugantriebe, Aerodynamik und Strömungsmechanik der Technischen Universität München, sowie dem Institut für Thermodynamik der Luft- und Raumfahrt der Universität Stuttgart. Unsere Zusammenarbeit war stets von großer Kollegialität geprägt und sowohl auf fachlicher als auch persönlicher Ebene eine Bereicherung. Insbesondere folgenden Kollegen möchte ich für ihre Anregungen danken: Michael Gurtner, Daniel Paukner, Sebastian Eberhardt, Nils Dröske, Felix Förster, Johannes Weinzierl, Florian Ettner und Josef Haßlberger.

Abschließend möchte ich aus ganzem Herzen meiner Familie danken, ohne deren langjährige Unterstützung diese Arbeit nie entstanden wäre.

München, im Dezember 2015 Konrad Makowka

Kurzfassung

Überschallverbrennungsantriebe haben das Potential den Raumtransport zu revolutionieren, da sie zu einer deutlichen Effizienzsteigerung bestehender Raketensysteme führen könnten. Das Resultat wäre eine erhebliche Nutzlasterhöhung bei gleicher Startmasse. Jedoch hat das heutige Verständnis der Prozesse in einem Überschallverbrennungsantrieb noch lange nicht den Wissensstand erreicht, den man mittlerweile für konventionelle Raketen- und Fluggasturbinen aufbauen konnte. Diese Arbeit steuert einen Beitrag zur Erweiterung dieses Verständnisses bei, indem zunächst ein Strömungslöser für Überschallverbrennung entwickelt wird. Aufbauend auf diesem Löser werden Methoden vorgeschlagen, um die rechenintensive Large Eddy Simulation (LES) mit einer numerisch günstigen Reynolds-averaged Navier-Stokes (RANS) Methode zu hybridisieren. Das Ziel ist die Vorhersage transienter, turbulenter Verbrennungsprozesse basierend auf LES und eine gleichzeitige Reduktion der Laufzeiten und Kosten von Simulationen durch den stellenweisen Einsatz von RANS. Darüber hinaus wird ein Modell zur Beschreibung von verbrennungsinduzierter Turbulenz vorgeschlagen. Der Strömungslöser und die vorgestellten Methoden werden auf drei verschiedene, für Überschallverbrennung relevante Testfälle angewendet und unterschiedliche Aspekte beleuchtet. Der erste Testfall ist ein verbrennungsloses Überschallinjektionsexperiment am Lehrstuhl für Flugantriebe der TUM. Danach wird eine vielzitierte Überschalldiffusionsflamme der NASA für eine numerische Untersuchung herangezogen. Schließlich mündet die Arbeit in der hybriden RANS/LES Simulation der Überschallbrennkammer am Institut für Thermodynamik der Luft- und Raumfahrt der Universität Stuttgart.

Abstract

Supersonic combustion engines offer the potential to enhance today's space transportation by improving the efficiency of a space launcher system result-

ing in a payload increase. However, present-day understanding of the processes governing engines of this type is not on the same level as the knowledge of conventional rockets or turbojet propulsion systems, yet. In a first step, this work contributes a computational fluid dynamics flow solver developed for the simulation of supersonic combustion. Based on this solver, methods are proposed that shall combine the computationally expensive large eddy simulation (LES) with the efficient Reynolds-averaged Navier Stokes (RANS) methodology in a hybrid model. The goal is the prediction of transient, turbulent combustion processes based on LES, while maintaining an affordable computational cost by means of a boundary layer treatment with RANS. Furthermore, a model for combustion induced turbulence is proposed. The developed solver and models are applied to three different test cases relevant for supersonic combustion. The first test case is a supersonic injection experiment without combustion conducted at the Institute for Flight Propulsion at TUM. Subsequently, an often-cited supersonic diffusion flame experiment by NASA is investigated. Finally, this work results in the hybrid RANS/LES simulation of the supersonic combustion chamber at the Institute of Aerospace Thermodynamics at the University of Stuttgart.

Contents

List of Figures

List of Tables

Nomenclature

Latin Symbols

A	Cross sectional area	[m^2]
A_j	Reaction rate pre-exponential factor for reaction j	-
a	Speed of sound	[m/s]
C_{ij}	Cross stress term	[m^2/s^2]
$C_{A,d}$	Method A dynamic turbulence indicator threshold	-
$C_{A,t}$	Method A turbulence sensor threshold	-
$C_{A,z,min}$	Method A minimum RANS zone thickness	[m]
$C_{A,z,max}$	Method A maximum RANS zone thickness	[m]
$C_{B,z,max}$	Method B maximum RANS zone thickness	[m]
$C_{B,tr}$	Method B Mach number threshold	-
C_{kk}	Combustion induced turbulence model source term	[kg/(m s^3)]
C_{pz}	Method A/B pure zonal RANS zone thickness	[m]
C_{tc}	Combustion induced turbulence model constant	-
c_i	Concentration of species i	[mol/m^3]
c_k	Concentration of species k	[mol/m^3]
c_p	Isobaric specific heat capacity	[J/(kg K)]
c_v	Isochoric specific heat capacity	[J/(kg K)]
D	Diameter	[m]
D	Diffusion coefficient	[m^2/s]
D_{kk}	Turbulent kinetic energy viscous diffusion	[kg/(m s^3)]
d_k	Turbulent kinetic energy diffusion coefficient	[kg/(m s)]
E	Total specific internal energy	[J/kg]
E_j^a	Activation energy for reaction j	[J/mol]
e	Specific internal energy	[J/kg]

e_k	Specific kinetic energy	[J/kg]
e_s	Specific sensible energy	[J/kg]
f_c	Combustion induced turbulence model function	-
f_k	Combustion induced turbulence model function	-
f_w	Method A scaling function	-
G	Filter function	-
h	Specific enthalpy	[J/kg]
h_c	Specific chemical enthalpy	[J/kg]
J	Jet momentum ratio	-
i	Index	-
j	Index	-
j	Species diffusion flux	[kg/(m^2 s)]
k	Index	-
k	Specific turbulent kinetic energy	[J/kg]
k_j^f	Forward reaction rate	[mol, m^3, s]
k_j^b	Backward reaction rate	[mol, m^3, s]
L_{ij}	Leonard stress term	[m^2/s^2]
l	Length scale	[m]
M	Molar mass of species mixture	[g/mol]
M_i	Molar mass of species i	[g/mol]
$\dot{m}$	Mass flow rate	[kg/s]
N_r	Amount of chemical reactions	-
N_{sp}	Amount of chemical species	-
n_j	Reaction rate temperature coefficient for reaction j	-
P_{kk}	Production of turbulent kinetic energy	[kg/(m s^3)]
p	Pressure	[Pa]
R	Specific gas constant	[J/(kg K)]
R_g	Universal gas constant	[J/(mol K)]
R_{ij}	Reynolds stress term	[m^2/s^2]
r	Turbulence mode indicator	-
r_A	Method A turbulence mode indicator	-
$r_{A,d}$	Method A dynamic turbulence mode indicator	-
$r_{A,t}$	Method A turbulence sensor	-
$r_{A,z,min}$	Method A minimum RANS zone thickness indicator	-

$r_{A,z,max}$	Method A maximum RANS zone thickness indicator	-
r_B	Method B turbulence mode indicator	-
$r_{B,d}$	Method B dynamic turbulence mode indicator	-
$r_{B,z,max}$	Method B maximum RANS zone thickness indicator	-
r_C	Method C turbulence mode indicator	-
T	Temperature	[K]
T_{kk}	Turbulent kinetic energy triple correlation	[kg/(m s^3)]
$T_{L,E}$	LES unclosed turbulent energy transport term	[J/(m^3 s)]
$T_{L,U}$	LES unclosed turbulent momentum transport term	[kg/(m^2 s^2)]
$T_{L,Y}$	LES unclosed turbulent species transport term	[kg/(m^3 s)]
$T_{R,E}$	RANS unclosed turbulent energy transport term	[J/(m^3 s)]
$T_{R,U}$	RANS unclosed turbulent momentum transport term	[kg/(m^2 s^2)]
$T_{R,Y}$	RANS unclosed turbulent species transport term	[kg/(m^3 s)]
t	Time	[s]
t_c	Chemical time scale	[s]
U	Velocity	[m/s]
u_η	Kolmogorov velocity	[m/s]
$u'_{j,c}$	Combustion induced velocity fluctuation	[m/s]
X_k	Name of chemical compound k	-
x	Coordinate	[m]
Y	Species mass fraction	-
y	Coordinate, wall distance	[m]
y^+	Dimensionless wall distance	-
Z	State vector	-
z	Coordinate	[m]

Greek Symbols

Δ	Spatial filter width	[m]
δ	Boundary layer thickness	[m]
δ_{ij}	Kronecker delta	-
ϵ	Rate of turbulent energy dissipation	[J /(kg s)]
η	Kolmogorov length scale	[m]

κ	Isentropic exponent	-
λ	Thermal conductivity	[W/(m K)]
μ	Dynamic viscosity	[kg/(m s)]
ν	Kinematic viscosity	[m^2/s]
$\nu^{'}$	Stoichiometric coefficient for forward reaction	-
$\nu^{''}$	Stoichiometric coefficient for backward reaction	-
Φ_{kk}	Pressure dilatation	[kg/(m s^3)]
ϕ	Fuel equivalence ratio	-
ϕ	Generic field	-
Ψ_{kk}	Pressure-velocity correlation	[kg/(m s^3)]
ψ	Generic field	-
ρ	Density	[kg/m^3]
τ_{ij}	Stress tensor	[N/m^2]
τ_η	Kolmogorov time scale	[s]
Ω	Generic field	-
$\dot{\omega}$	Species source term	[kg/(m^3 s)]
ξ	Generic distance variable	[m]

Subscripts

c	Chemical
d	Dynamic
E	Energy
i	Internal
k	Kinetic
kk	Turbulent kinetic energy (Luo)
L	LES
m	Molecular
pz	Pure zonal
R	RANS
SGS	Subgrid scale
s	Sensible
stoich	Stoichiometric

t	Turbulent
tot	Total
U	Momentum
Y	Species
z	Zonal

Superscripts

$()^{'}$	Fluctuating component
$()^{''}$	Fluctuating component w.r.t. Favre averaging/filtering
$\overline{()}$	Ensemble averaged
$\widetilde{()}$	Favre averaged/filtered
$\widehat{()}$	Filtered field
$\check{()}$	Computable field
$\vec{()}$	Vector
$()^{\tau}$	Stress
$()^{E}$	Total internal energy
$()^{e_k}$	Kinetic energy
$()^{e_s}$	Sensible energy
$()^{h_c}$	Chemical enthalpy
$()^{p}$	Pressure
$()^{U}$	Momentum
$()^{Y}$	Species

Non-Dimensional Parameters

CFL	Courant-Friedrichs-Lewy number
Ma	Mach number
Re	Reynolds number
Pr	Prandtl number
Pr_t	Turbulent Prandtl number

Sc	Schmidt number
Sc_t	Turbulent Schmidt number

Abbreviations

CFD	Computational fluid dynamics
DFG	Deutsche Forschungsgemeinschaft
GRK	Graduiertenkolleg
ISA	International standard atmosphere
LES	Large eddy simulation
RANS	Reynolds-averaged Navier Stokes
SFB	Sonderforschungsbereich
SST	Shear stress transport
URANS	Unsteady Reynolds-averaged Navier Stokes

1 Introduction

1.1 Motivation

The fundament of current space transportation systems are conventional rockets based on the recoil principle. Fuel and oxidizer, both carried by the rocket, are burned in the engine and ejected leading to an acceleration. Considerable improvements regarding payload mass and reliability have been made since the first rocket-powered orbital space flights in the late 1950s, leading to efficient launcher systems like the European Ariane 5 [106]. Despite this development, all state-of-the-art rocket systems underlie the constraint of the Ziolkowski-equation, effectively limiting all optimization efforts [142]. The result is that even a highly sophisticated rocket like the Ariane 5 ES requires a launch mass of 760 t to bring a payload of 20 t to a low-earth orbit, which corresponds to less than 3% of the launch mass.

In order to improve the ratio of payload to launch mass one might think of a conventional rocket enhanced with an additional air-breathing propulsion system that takes advantage of the oxygen still available in the lower parts of the atmosphere in the first ascent phase. The reduction of necessary oxidizer carried on board would lead to an increase in payload mass. A well-known air-breathing propulsion system is the jet engine being composed of the four basic elements compressor, combustor, turbine and nozzle [29]. The energy brought into the system within the combustion chamber is partly used to propel the turbine. The turbine in turn drives the compressor necessary to achieve a higher pressure level, such that the system can profit from the divergence of the isobars in the underlying Joule-Brayton-Cycle [81].

However, in order to be applicable for space transportation, a propulsion system making use of atmospheric oxygen must be able to operate at hypersonic

speeds, which are reached soon after launch [106]. This requirement cannot be met by conventional jet engines, due to the high stagnation temperatures occurring at hypersonic velocities. The sensitive turbo-machinery components would not be able to withstand these extreme operating conditions. Fortunately, gas dynamic shock waves can lead to a sufficient compression of the inflowing air at speeds relevant for space transportation rendering the classical compressor concept obsolete at hypersonic speeds. An engine utilizing this concept is termed ramjet. The underlying engine concept has been investigated since the 1920s and was applied especially in missile systems. The basic thermodynamic cycle of a ramjet remains identical to the conventional turbojet engine, but the turbo compressor is replaced by an aerodynamic inlet generating oblique shocks, which also renders the turbine obsolete. Therefore, as a convenient side-effect, a ramjet does not need any rotating parts decreasing system complexity.

Nevertheless, an efficient and realistic ramjet operational envelope is limited to speeds smaller than approximately Mach five to seven, due to the following two reasons: Firstly, the deceleration of inflowing air to subsonic speeds before entering the combustion chamber leads to enormous static temperatures. Secondly, a deceleration to subsonic speeds involves a large loss of total pressure, decreasing the effective pressure rise within the engine, which in turn reduces the cycle efficiency and thrust [118]. For this reason, researchers began to investigate the possibility of adding heat to a supersonic flow starting in the late 1940s [30]. If the main portion of the engine duct flow remains supersonic, considerably smaller stagnation pressure losses and manageable heat loads are achieved. Such a version of a ramjet engine is termed a supersonic combustion ramjet, or in short: scramjet. Further engine concepts have been investigated that build upon the scramjet engine, like the rocket-scramjet combination proposed by Billig et al. [15].

Obviously, the concept of the scramjet engine introduces new challenges, like flame stabilization due to the extremely small fuel and air residence times or fuel injection into the high-impulse crossflow with sufficient penetration depth. In order to address these challenges, the German Research Foundation DFG (Deutsche Forschungsgemeinschaft) funds the Germany-wide research

program GRK 1095 dedicated to the aero-/thermodynamic design of a scramjet propulsion system for future space transportation systems. This work constitutes a part of this research program.

1.2 Investigation of Supersonic Combustion

The beginnings of ramjet research are the experimental and theoretical investigations of Leduc in the 1920s [121]. The idea of utilizing gas dynamic shocks to compress the inflowing air at supersonic velocities appeared to be a promising approach for high-speed air-breathing missile propulsion. The development of weapon systems of this kind remained the driving motivation for the pursuit of ramjet and scramjet research until today. A foundation for the understanding of the potential benefits of supersonic in comparison to subsonic combustion was the system analysis conducted by Weber and MacKay in 1958 [143]. Their work addressed the differences between ramjet and scramjet efficiency with respect to velocity and outlined the advantages of supersonic combustion when exceeding velocities of Mach five. At the same time as Weber and MacKay published their work, supersonic combustion began to attract researchers and military on both sides of the Iron Curtain due to the option for air-breathing propulsion exceeding velocities of Mach seven. Since then, both computational and experimental work has been conducted, while the latter incorporates both ground and flight experiments. Generally, the requirement for high-speed and simultaneously high-enthalpy flows renders the experimental testing of scramjet engines technically demanding and expensive.

Designing and building an experimental vehicle for supersonic combustion research constitutes a challenging task, since hypersonic velocities must be achieved as a prerequisite for the functionality of a scramjet engine. A noteworthy example for a successful development and implementation of such an experiment was the U.S. American Hypersonic Research Engine (HRE) program initiated by NASA and the U.S. Navy in 1964. Its goal was the flight-testing of a scramjet engine attached to a X-15 aircraft reaching Mach five. However, the X-15 experimental aircraft program was canceled in 1968, such

that the necessary test bed was not available anymore. Hence, the HRE flight testing plans were terminated. Despite the canceling of the X-15 program, ground experiments continued until the mid 1970s successfully validating the developed engine concept. Simultaneously to the first U.S. American efforts, Russian interest in hypersonic scramjet-based propulsion came to life in the late 1950s and resulted in the first flight test of a dual-mode combustion ramjet vehicle termed Kholod in 1991 [115]. The engine was designed to operate both in the subsonic and supersonic regime. Subsequent flight tests in cooperation with the French ONERA and U.S. American NASA resulted in further successful verifications of the subsonic and supersonic combustion modes [19]. Temporary international cooperation projects of this kind continued to be an important facet of scramjet research after the cold war, see for example the HyShot program involving the U.S., Australia, Germany and other countries [63].

Ground experiments require facilities that can establish supersonic and hypersonic flows at high enthalpies within the scramjet flight envelope [121], whereas especially the latter requirement constitutes the cost driver. Supersonic combustion ground test facilities either feature high-enthalpy shock tunnels or continuously operating, preheated supersonic wind tunnels. In the latter case, the continuous operation allows long test times of several minutes, while shock tubes generally deliver higher enthalpies and velocities. Concerning the U.S. American research, the General Applied Science Laboratories (GASL) executed two pioneering scramjet engine research programs in the 1960s. Although it seemed obvious to finally flight test the technologies successfully ground tested within this and following programs until the mid 1970s, it was not until the early 2000s that U.S. American NASA flew a hydrogen-fueled hypersonic scramjet demonstrator termed X-43A within the Hyper-X scramjet program [93].

Numerous other scramjet research projects have been carried out by the U.S., Russia, France, Germany, Japan and Australia and other countries, see the comprehensive overview given by Curran [30]. The design of a hypersonic cruise missile remains the main motivation for the majority of these projects. One of the few programs explicitly dedicated to the utilization of scram-

jet technology for space access propulsion system is the Research Training Group GRK 1095 funded by the German Research Foundation DFG (Deutsche Forschungsgemeinschaft) since 2005. It is a successor of the three German Special Research Centres SFB 253, SFB 255 and SFB 259 [66]. In contrast to other projects, its focus is rather the investigation of particular aspects of scramjet technology. The goal is to provide methods and data supporting the understanding and design of scramjets.

The high demands of scramjet experiments motivate the development and application of computational methods that shall substitute or at least enrich the experimental work. This involves not only the simulation of the combustion process. To name a few, also flight path and attitude control, heat management and uncertainty quantification require attention. However, the computational prediction of combustion remains a challenge until today. Nevertheless, the experience gained within numerous research projects to date provides a substantial basis for a choice of reasonable computational methods for supersonic combustion. To name a few, Gerlinger et al. provide a computational study of a small-scale supersonic flame by means of Reynolds-averaged Navier-Stokes (RANS) methods [54]. Boivin et al. and Moule et al. investigate the same case based on large eddy simulation (LES) [16, 100]. Karl [69] contributes a comprehensive RANS investigation of the HyShot II combustor [63]. Berglund et al. provide valuable investigations of scramjet combustors based on LES [12, 13, 50]. In recent years, even attempts towards the hybridization of RANS and LES in the context of supersonic combustion have been made, see Edwards et al. [36–38] and Potturi [111].

Also, the chair for thermodynamics at the Technische Universität München has a tradition in supersonic combustion research: Grünig experimentally investigated the mixing of fuel and air and subsequent supersonic combustion based on flame holders perpendicularly protruding into the flow [60]. Sander further deepened the understanding of the utilized injector and proposed improved concepts. Lyubar complemented the work of Sander with numerical investigations based on detailed reaction kinetics [88]. Lyubar further introduced a reaction mapping concept that increased the computational efficiency of the combustion simulation. Förster utilized the framework provided

by Lyubar and investigated the effects of a turbulence chemistry interaction model [47]. All aforementioned computational investigations were based on Reynolds-averaged Navier-Stokes methods (RANS).

1.3 Problem Statement

Supersonic combustor ducts feature per definition exceptionally large mean flow velocities. Moreover, a short combustor length is an important requirement in order to meet weight and pressure loss constraints [121]. As a result, fuel and air residence times within the combustor are extremely small. The time for fuel mixing, ignition and combustion is consequently very limited. A typical combustor residence time is of the order of approximately one millisecond, which is close to the order of species mixing and the slower portions of the chemical processes [121]. Reliable combustor design methods must be able to answer the question whether a given engine provides stable combustion. The goal of this thesis is to support the development of such methods through the improvement of techniques for the computational prediction of scramjet combustion in the form of coupled flow and combustion simulations. The strong coupling of highly compressible flows involving gas dynamic effects and chemical reactions represents the biggest difference to classical subsonic combustion problems. An adequate computational simulation system accounting for this interaction is developed within this work.

A further aspect of supersonic combustion is turbulence. Since large eddy simulation (LES) resolves large and mid-scale turbulent structures, it offers the potential of improving the prediction of fuel mixing and subsequent combustion. However, the resolution of turbulent structures requires very fine computational meshes especially in the boundary layers, rendering properly resolved LES of application-oriented wall-confined geometries almost impossible at this point in time. Reynolds-averaged Navier Stokes (RANS) methods model the complete spectrum of turbulent motions and hence require significantly less computational cells. Yet, their predictive power usually does not achieve the same level as LES. Combining LES with a RANS method such that the RANS model takes over the modeling of near-wall flows can enable the uti-

lization of LES for the simulation of supersonic combustor ducts, while benefiting from the computational efficiency of a near-wall RANS. Based on the developed computational solver for supersonic combustion, a hybrid RANS and LES turbulence modeling method is proposed, which shall enable the utilization of LES for realistic scramjet combustor geometries.

In addition, a new combustion to turbulence action model is proposed that accounts for the influence of combustion on the generation of turbulence. Previous modeling efforts concerning turbulence chemistry interaction, e.g. the valuable work by Sabelnikov and Fureby [116], focused on the impact of turbulence on combustion but usually neglected the influence in the other direction.

1.4 Thesis Outline

The fundamentals for the comprehension and description of supersonic combustion are given in chapter 2 covering the following major aspects: Compressible fluid flow involving gas dynamic effects, turbulence and combustion. In particular, the ensemble averaged and spatially filtered governing equations for compressible fluid flow are derived as a fundament for the hybrid RANS/LES turbulence model formulation. Chapter 3 describes the methods utilized within the developed computational fluid dynamics solver. In particular, the chosen turbulence closure approximations are discussed. Furthermore, the applied turbulence models for RANS and LES are explained, which are utilized to compute model quantities in the closure terms. Chapter 4 presents the developed methods for the hybridization of RANS and LES. The novel approach to the modeling of turbulence chemistry interaction is presented in chapter 5.

In order to validate the functionality of the solver for the simulation of wall-confined supersonic flows, a supersonic injection experiment is simulated, see chapter 6. The test case involves the perpendicular injection of a sonic carbon dioxide jet into a supersonic crossflow. In particular, the test case features shock boundary layer and shock jet interaction. The developed hybrid

RANS/LES method is applied and compared to pure RANS results.

Subsequently, the well-known fundamental supersonic combustion experiment by Cheng et al. [24] is utilized to demonstrate and validate the capability of the developed solver to account for supersonic combustion in its pure RANS mode, see chapter 7. Furthermore, the novel model for combustion induced turbulence is applied.

Finally, the model scramjet combustor at the Institute of Aerospace Thermodynamics (ITLR) at the University of Stuttgart is simulated by means of pure RANS and hybrid RANS/LES. The combustor operates in the supersonic portion of the challenging ramjet to scramjet transition regime, which covers the crucial Mach number range from approximately Mach four to eight. Non-reacting and reacting cases are examined and compared, see chapter 8. In particular, the differences between a hybrid RANS/LES and pure RANS approach are outlined. Furthermore, the investigated operational points are related to appropriate definitions of common classifications of the scramjet/ramjet operational regime. At the end, chapter 9 provides a summary and suggestions for further work.

2 Fundamentals

This chapter contains the following necessary fundamentals: Firstly, the governing equations of compressible fluid flow utilized within this work are presented [26, 52, 53, 109, 117]. Despite their differences, subsonic and supersonic flows and all phenomena related to them are described by the same set of equations, the Navier-Stokes equations. Secondly, the governing equations are expressed in the context of turbulence modeling identifying the unclosed turbulent correlations requiring further modeling, both for RANS and LES [53, 144]. Subsequently, the characteristics of turbulent combustion at transonic velocities are discussed [53, 109]. Finally, phenomenological descriptions of shock boundary layer interactions and jet in supersonic crossflow configurations are provided [2, 3].

2.1 Governing Equations of Multi-Species Compressible Fluid Flow

The relevant fundamental equations describing the physics of a compressible flow including a mixture of different species are given below in their Eulerian form [26, 53]. The set of equations is comprised of the continuity equation, the three momentum transport equations for each direction in space and the energy transport equation. Additionally, the inclusion of reacting species yields further scalar transport equations for each reacting species mass fraction. The multitude of gas dynamic phenomena like shock waves, expansion fans or shock trains [2, 128] is contained within this set of equations.

The mass transport equation, also called continuity equation, describes the conservation of mass within a moving fluid through the transport of density ρ, cf. eq. 2.1. All transported chemical species are contained in this mass. The

exchange of mass takes place due to the convection of the fluid with the bulk velocity vector field U. Diffusive processes can change the local species composition but do not lead to a change in the total mass flow described by eq. 2.1.

$$\frac{\partial \rho}{\partial t} + \frac{\partial (\rho U_j)}{\partial x_j} = 0 \tag{2.1}$$

The conservation of momentum $\rho \mathrm{U}_i$ is represented by the momentum transport equation given in eq. 2.2. Actually, eq. 2.2 is comprised of three equations, each for one direction. Momentum exchange can occur due to convective and diffusive transport processes and the presence of a pressure gradient. The equations do not contain any source terms, since volume forces are not considered within this work.

$$\frac{\partial (\rho U_i)}{\partial t} + \frac{\partial (\rho U_i U_j)}{\partial x_j} + \frac{\partial p}{\partial x_i} - \frac{\partial \tau_{ij}}{\partial x_j} = 0 \tag{2.2}$$

Stokes's hypothesis is the basis for the formulation of the viscous stress tensor τ_{ij}, see eq. 2.3, which links the viscous stress to the viscosity and the strain rate tensor [8, 119]. In contrast to the mechanics of solids, stress is caused by the rate of change of the deformation within a fluid instead of the magnitude of the displacement of fluid elements. Therefore, solely derivatives of the velocity vector appear in the constituting equation of the stress tensor. Stokes' stress tensor is composed of an isotropic part being the average of the three normal stresses and a non-isotropic part [8]. The isotropic part would vanish in an incompressible flow, since the divergence of the velocity vector would be zero. The proportionality constant μ is termed viscosity and relates the velocity gradient to the resulting shear stress. Generally, μ is a fluid property and a function of the temperature [71].

$$\tau_{ij} = 2\mu \left(\frac{1}{2} \left(\frac{\partial U_i}{\partial x_j} + \frac{\partial U_j}{\partial x_i} \right) - \frac{1}{3} \frac{\partial U_k}{\partial x_k} \right) = \mu \left(\frac{\partial U_i}{\partial x_j} + \frac{\partial U_j}{\partial x_i} - \frac{2}{3} \frac{\partial U_k}{\partial x_k} \right) \tag{2.3}$$

Inserting Stokes's hypothesis for the viscous stress tensor into the momentum

equation yields the Navier-Stokes equations, see. eq. 2.4.

$$\frac{\partial(\rho U_i)}{\partial t} + \frac{\partial(\rho U_i U_j)}{\partial x_j} + \frac{\partial p}{\partial x_i} - \frac{\partial}{\partial x_j}\left(\mu\left(\frac{\partial U_i}{\partial x_j} + \frac{\partial U_j}{\partial x_i} - \frac{2}{3}\frac{\partial U_k}{\partial x_k}\right)\right) = 0 \tag{2.4}$$

Furthermore, the chemical compounds taking part in the combustion process are represented by mass fractions of the transported density field in eq. 2.1. A transport equation transporting the respective mass fraction Y_i is solved for each involved chemical species, cf. eq. 2.5. The equations are comprised of a convective term, a diffusive term and a source term representing the production and consumption of species in the course of chemical reactions.

$$\frac{\partial(\rho Y_i)}{\partial t} + \frac{\partial(\rho Y_i U_j)}{\partial x_j} - \frac{\partial j_i}{\partial x_j} - \dot{\omega}_i = 0 \tag{2.5}$$

The diffusion flux of species i, j_i, can be written in terms of Fick's law, such that the diffusion process becomes proportional to the species mass fraction gradient scaled with a species-dependent diffusion coefficient D_i [53], cf. eq. 2.6.

$$j_i = \rho D_i \frac{\partial Y_i}{\partial x_j} \tag{2.6}$$

Moreover, the kinetic energy of the flow cannot be neglected with increasing flow velocity. At transonic and supersonic speeds, the kinetic energy given in eq. 2.7 constitutes a substantial percentage of the total energy. Hence, the transformation of kinetic energy into internal energy and vice versa must be taken into account by including the kinetic energy in the energy transport equation given in eq. 2.8. In summary, the total energy E is comprised of the following energy forms, cf. eq. 2.9: the internal (or sensible) energy e_s, kinetic energy e_k and mixture heat of formation h_c.

$$e_k = \frac{1}{2} U_i U_i \tag{2.7}$$

$$\frac{\partial(\rho E)}{\partial t} + \frac{\partial\left(\left[\rho E + p\right] U_j\right)}{\partial x_j} - \frac{\partial(\tau_{ij} U_i)}{\partial x_j} - \frac{\partial q_j}{\partial x_j} = 0 \tag{2.8}$$

$$E = h_c + e_s + e_k \tag{2.9}$$

It is assumed that the fluid components are thermically perfect, hence, the specific heat capacities of the involved species $c_{v,k}$ are solely a function of the temperature. The sensible internal energy e_s of the mixture can therefore be computed as the mass fraction weighted sum of the temperature integrals of the specific isochoric heat capacities for all species N_{sp}, see eq. 2.10. The local temperature is computed on the basis of the internal energy being the difference between the total energy and the remaining energy forms. This calculation must occur iteratively due to the fact the isochoric specific heat capacity c_v of the mixture, being the link between the temperature and the internal energy, is a function of the temperature.

$$e_s = \sum_{k=1}^{N_{sp}} \left(Y_k \int_{T_{ref}}^{T} c_{v,k}(T)\, dT \right) \tag{2.10}$$

Furthermore, the test cases considered within this work admit to treat the fluid as an ideal gas. Hence the pressure can be computed based on the ideal gas law, see eq. 2.11. The ideal gas equation provides a link between the temperature, pressure and density and links the energy and enthalpy as described by eq. 2.13. The specific gas constant R for the species mixture is defined by the universal gas constant R_g and the molar mass of the mixture M, see eq. 2.12

$$p = \rho R T \tag{2.11}$$

$$R = \frac{R_g}{M} \tag{2.12}$$

$$h = e + \frac{p}{\rho} \tag{2.13}$$

The inclusion of the mixture heat of formation h_c, see eq. 2.14, takes into account the effect of chemical reactions. Due to this approach, no combustion induced energy source term is required, since the interchange of species composition and their respective heats of formation due to chemical reactions reduces or increases the portion of the total energy remaining for the internal energy. Hence, the effect of combustion is included through the source term in the species transport equation.

$$h_c = \sum_{k=1}^{N_{sp}} \left(Y_k h_{c,k} \right) \tag{2.14}$$

At this point, the concept of turbulent kinetic energy shall be introduced, although it already implies the temporal averaging or spatial filtering of the governing equations by means of RANS or LES. The turbulent kinetic energy k participates in the exchange between different energy forms and reduces the portion of energy remaining for the internal energy within the governing equations of RANS and LES. Its definition is given by the product of turbulent fluctuating velocities, see eq. 2.15.

$$k = \frac{1}{2} U_i^{'} U_i^{'} \tag{2.15}$$

The viscous stress tensor τ_{ij} in the energy transport equation, see eq. 2.8 corresponds to the stress tensor in the momentum transport equations in eq. 2.4. Hence, τ_{ij} is described with Stokes' hypothesis given in formula 2.3 as specified previously.

Furthermore, diffusive heat flux based on two processes is considered: Firstly, heat conduction due to Fourier's law, secondly, the exchange of enthalpy due to the diffusion of species. The inclusion of the latter flux is necessary, since the diffused species may have varying temperatures and heats of formation.

It is noteworthy that the enthalpy is necessary at this point instead of the energy used above, because the diffusion of species is tied to work [71]. Applying Fourier's law of heat diffusion and Fick's law of species diffusion yields the expression for the heat flux presented in eq. 2.16.

$$\begin{aligned} q_j &= \lambda \frac{\partial T}{\partial x_j} + \sum_{k=1}^{N_{sp}} \left(h_k j_k \right) \\ &= \lambda \frac{\partial T}{\partial x_j} + \sum_{k=1}^{N_{sp}} \left((h_{c,k} + h_{s,k}) \rho D_k \frac{\partial Y_k}{\partial x_j} \right) \end{aligned} \tag{2.16}$$

Inserting all relations explained above in the energy transport equation yields eq. 2.17. This formula is subject to temporal averaging or spatial filtering respectively in the context of turbulence modeling based on RANS and LES as discussed in chapter 3.

$$\begin{aligned} &\frac{\partial}{\partial t} \left(\rho (h_c + e_s + \frac{1}{2} U_i U_i) \right) \\ &+ \frac{\partial}{\partial x_j} \left(\left[\rho (h_c + e_s + \frac{1}{2} U_i U_i) + p \right] U_j \right) \\ &- \frac{\partial}{\partial x_j} \left(\mu \left(\frac{\partial U_i}{\partial x_j} + \frac{\partial U_j}{\partial x_i} - \frac{2}{3} \frac{\partial U_k}{\partial x_k} \right) U_i \right) \\ &- \frac{\partial}{\partial x_j} \left(\lambda \frac{\partial T}{\partial x_j} + \sum_{k=1}^{N_{sp}} \left((h_{c,k} + h_{s,k}) \rho D_k \frac{\partial Y_k}{\partial x_j} \right) \right) \\ &= 0 \end{aligned} \tag{2.17}$$

2.2 Governing Equations of Compressible Fluid Flow in the Context of Turbulence

The governing equations of compressible flow considered as the basis for this work were given in the previous section. Modeling efforts were reduced to

the description of viscous stresses and diffusion processes so far. This set of equations theoretically accounts for all effects of compressible fluid flow. The shear force between fluid elements described by the Stokes stress tensor in eq. 2.3 allows the flow to induce chaotic rotational motions known as turbulence. The result is an unsteady flow field with a high degree of transiently convective transport. Although the unsteady turbulent motions give the impression that they are purely chaotic, turbulence exhibits a certain structure. The theory introduced by Kolmogorov [74, 75] describes turbulence as a spectrum of vortices with well-definable upper and lower sizes determined by the macroscopic geometry on the one hand and viscous dissipation of microscale vortices on the other hand. According to this theory, energy is transfered from larger scale to smaller scale vortical structures through vortex breakup until the smallest length scales are reached. At the length scales of the smallest possible vortices, the rate of energy transfer termed ϵ is in equilibrium with the viscous dissipation of turbulent structures being defined by the kinematic viscosity ν. Kolmogorov derived expressions for these smallest time, length and velocity scales of turbulence based on a dimension analysis assuming that they solely depend on ϵ and ν [82, 110]. The corresponding relations for the Kolmogorov length scale η, time scale τ_η and velocity u_η are given in eqs. 2.18 to 2.20.

$$\eta = \left(\frac{\nu^3}{\epsilon}\right)^{\frac{1}{4}} \tag{2.18}$$

$$\tau_\eta = \left(\frac{\nu}{\epsilon}\right)^{\frac{1}{2}} \tag{2.19}$$

$$u_\eta = (\nu\epsilon)^{\frac{1}{4}} \tag{2.20}$$

In theory, numerical simulations are possible that resolve the complete spectrum of turbulent structures, since a comprehensive mathematical description exists and the length and time scales are limited to a specific range

defined by Kolmogorov's theory. For this purpose, very fine computational meshes and small time integration steps are necessary in order to provide a spatial and temporal resolution of all structures down to the smallest turbulent scales described by eqs. 2.18 to 2.20. Such an approach is called direct numerical simulation (DNS). In practice, however, this procedure comes at the cost of enormous computational demands, because of the tiny dimensions of small scale turbulent vortices. In particular, the resulting computational meshes for technically interesting simulations would require several orders of magnitude more finite elements than currently realizable on present supercomputing cluster. Hence, DNS are limited to fundamental investigations of academic examples at the present moment.

In order to account for the important effects of turbulence but maintain a reasonable level of computational costs, it is possible to look at the statistic consequences of turbulence. Instead of resolving every vortex at every length scale, the influence of turbulent motions on the temporally averaged flow field is predicted. The resulting time or ensemble averaged governing equations underlying this approach are termed the Reynolds-averaged Navier-Stokes (RANS) equations. The mathematical averaging operation yields additional terms in the governing equations, which are referred to as the Reynolds stresses. Since those terms include quantities that are outside the scope of the governing equations, those terms are unclosed. Models are required to compute these values in order to obtain a closed system of equations. The models utilized for the computation of the Reynolds stresses respectively the unknown quantities are the RANS turbulence models. The application of RANS is computationally very efficient concerning the description of turbulence, yet, it requires models that can describe the statistic effects of the whole turbulent spectrum. Without elaborating hereupon, it appears obvious that meeting this requirement with a universal model is a difficult task.

A third, intermediate concept exists in addition to the comprehensive resolution of all turbulent scales with a DNS and the entire modeling of turbulence through RANS. This third concept is based on the separation of small and large turbulent scales. While the small turbulent scales exhibit universality to some extent [74, 75, 110], the larger scales depend on the geometry and specifica-

tions of the treated problem. The latter aspect implies difficulties formulating a generally valid model covering all possible problems being the bottleneck of RANS. Hence, it is expected that the resolution of large scale vortices and modeling of solely the smaller scales yields a higher degree of universality while reasonable computational runtimes are maintained. This concept is called large eddy simulation (LES). The aforementioned scale separation is performed through the application of a spatial filter. So, in contrast to the transport equations underlying the RANS approach, which are the result of an ensemble averaging operation, LES rests upon a spatial filtering of the governing equations. The application of a spatial filter introduces additional unclosed terms compared to the RANS approach, such that the necessary model complexity appears to increase in comparison to a RANS. However, the influence of the modeled small scale turbulence is generally far smaller than the influence of the resolved scales [40]. Moreover, following Kolmogorov's theory, the medium and small scale vortices depend less on the geometry than the resolved eddies. Therefore, LES should at least in theory require less complex models than RANS.

The governing equations utilized in this thesis are formulated and utilized in their Favre averaged respectively filtered form. This can be thought of as a variable transformation from the original field to the density weighted field. This approach reduces the number of unclosed terms in a variable density flow for both RANS and LES and therefore simplifies both averaging and filtering [109], as shown in the following.

2.2.1 Ensemble Averaged Governing Equations

The foundation for RANS turbulence modeling are the time or more generally ensemble averaged governing equations [26, 53, 144]. The ensemble averaging operator, called Reynolds operator [26, 53, 117, 144], is denoted by an overline in the following. Within this context, a generic transported field ϕ can be decomposed into a mean $\overline{\phi}$ and a fluctuating part $\phi^{'}$, see eq. 2.21. Per definition, the ensemble average of the fluctuating part is zero, see eq. 2.22, being the purpose of the averaging. Furthermore, the latter aspect implies that also the

averaged product of an arbitrary mean field $\overline{\psi}$ with the fluctuation ϕ' is zero, see eq. 2.23, since the average of a scaled fluctuation remains zero. Eq. 2.23 further implies that there is no correlation between the mean and fluctuating field parts with respect to the averaging procedure. Additionally, the average of a sum is equal to the sum of the averages, see eq. 2.24. Moreover, the average of the product of two averages is obviously equal to solely the product of the averages, see eq. 2.25. Furthermore, it is usually assumed that the Reynolds operator commutes with the differential operators. Finally, the previously defined properties of the Reynolds operator result in eq. 2.26 effectively meaning that the average of the product of two fields is the sum of the respective average products and the average correlation between the fluctuations.

$$\phi = \overline{\phi} + \phi' \tag{2.21}$$

$$\overline{\phi'} = 0 \tag{2.22}$$

$$\overline{\overline{\psi}\phi'} = 0 \tag{2.23}$$

$$\overline{\psi + \phi} = \overline{\psi} + \overline{\phi} \tag{2.24}$$

$$\overline{\overline{\psi}\overline{\phi}} = \overline{\psi}\overline{\phi} \tag{2.25}$$

$$\overline{\psi\phi} = \overline{\psi}\overline{\phi} + \overline{\psi'\phi'} \tag{2.26}$$

The application of the Reynolds operator to the mass transport equation 2.1 initially yields in the most general sense eq. 2.27a. Inserting the decompositions of velocity and density according to eq. 2.21 yields eq. 2.27b, resp. eq. 2.27c. Utilizing the relation given in eq. 2.23 allows to discard the cross terms of the type $\overline{\overline{\psi}\phi'}$ and finally leads to the simplified expression given in eq. 2.27d.

$$\frac{\partial \overline{\rho}}{\partial t} + \overline{\frac{\partial (\rho U_j)}{\partial x_j}} = 0 \tag{2.27a}$$

$$\frac{\partial \overline{\overline{\rho} + \rho'}}{\partial t} + \frac{\partial \overline{\left((\overline{\rho} + \rho')(\overline{U_j} + U_j') \right)}}{\partial x_j} = 0 \tag{2.27b}$$

$$\frac{\partial \overline{\rho}}{\partial t} + \frac{\partial (\overline{\rho}\,\overline{U_j})}{\partial x_j} + \frac{\partial \overline{\rho'}}{\partial t} + \frac{\partial \overline{(\rho'\overline{U_j})} + \overline{(\overline{\rho} U_j')} + \overline{(\rho' U_j')}}{\partial x_j} = 0 \tag{2.27c}$$

$$\frac{\partial \overline{\rho}}{\partial t} + \frac{\partial (\overline{\rho}\,\overline{U_j})}{\partial x_j} + \frac{\overline{(\rho' U_j')}}{\partial x_j} = 0 \tag{2.27d}$$

As a consequence of the Reynolds operator application eq. 2.27d contains an additional term compared to the original mass transport equation. This term is comprised of the concealed correlation between the unknown velocity and density fluctuations. Unclosed density correlations of this type also appear in the remaining equations in addition to further fluctuation correlation terms, if the Reynolds operator is applied. In order to avoid these density fluctuation correlations, the averaging procedure can be extended to a mass-weighted averaging of the transported fields, called Favre averaging [109, 144]. Eq. 2.28a provides the definition of the Favre average in terms of a generic field ϕ. This leads to a decomposition of the field ϕ into a density averaged value $\tilde{\phi}$ and a fluctuating part ϕ'', see eq. 2.29.

$$\widetilde{\phi} = \frac{\overline{\rho\phi}}{\overline{\rho}} \tag{2.28a}$$

$$\overline{\rho}\widetilde{\phi} = \overline{\rho\phi} \tag{2.28b}$$

$$\overline{\rho}\widetilde{\phi} = \overline{\rho}\,\overline{\phi} + \overline{\rho'\phi'} \tag{2.28c}$$

$$\phi = \tilde{\phi} + \phi'' \tag{2.29}$$

While the Reynolds operator constitutes a physical simplification of the problem through ensemble averaging, Favre averaging further simplifies the problem on a purely mathematical basis [144]. It can be regarded as a variable transformation of the Reynolds averaged fields. Finally, it should be noted that the Reynolds (time) average of the Favre fluctuation is not equal to zero as can be inferred from eq. 2.30.

$$\begin{aligned} \overline{\phi''} &= \overline{\phi - \tilde{\phi}} \\ &= \overline{\phi} - \overline{\tilde{\phi}} \\ &= \overline{\phi} - \tilde{\phi} \\ &\neq 0 \end{aligned} \tag{2.30}$$

The definition of the Favre average given in 2.28a can be trivially transformed to eq. 2.28b. Due to this relation, the average of the product of the density with a generic field ϕ can generally be decomposed into the product of the Reynolds averaged density and the Favre averaged field. In particular, Favre averaging is applied by transforming the respective Reynolds averages within the transport equations into the Favre averages based on 2.28b. Inserting the Favre decomposition into the continuity equation as previously done for the Reynolds operator directly results in the equivalent but simpler expression in eq. 2.31. It is furthermore assumed that the relations given in eqs. 2.22 and 2.23 are also valid for the Favre averaged quantities. Now, the usefulness of the Favre averaging becomes obvious, since no additional terms appear and the continuity equation formally appears like the original equation given in eq. 2.1.

$$\frac{\partial \overline{\rho}}{\partial t} + \frac{\partial (\overline{\rho} \widetilde{U_j})}{\partial x_j} = 0 \tag{2.31}$$

Although the Favre decomposition expressed in eq. 2.29 resembles the Reynolds decomposition previously given in eq. 2.21, the resulting average and fluctuating fields are not the same. In fact, no straightforward correlation exists that would allow to transform one type of formulation to the other, which is the reason for the relation in eq. 2.30. Furthermore, the density correlations of the type $\overline{(\rho' \phi')}$ remain unexplored within the Favre averaged governing equations, see eq. 2.28c. After all, Favre averaging is chosen as the basis for the statistical turbulence description within this work due to the reduction of the number of unclosed terms. In the following, the remaining Favre averaged governing equations are derived.

Recalling the Favre average definition expressed in eq. 2.28, the density products in the momentum transport equation eq. 2.32a can be decoupled from the remaining terms yielding eq. 2.32b. Inserting the Favre decomposition of the velocity vector in the convective term yields eq. 2.32c. The application of the relations from eqs. 2.23 and 2.25 and utilizing the fact that the density Favre average corresponds to its Reynolds average, the ensemble density averaged momentum transport equation can be simplified to eq. 2.32d. The Favre average is especially convenient regarding the convective transport term. Instead of a complicated correlation between the density and the dyadic product of the velocity vectors, solely the product of the mean density with the averaged velocity product remains. The stress tensor τ_{ij} is given through the ansatz of Stokes in eq. 2.3. The Stokes stress tensor is solely a superposition of velocity derivatives and therefore does not require the splitting of averaged products as it the case with the convective term.

$$\frac{\partial(\overline{\rho U_i})}{\partial t} + \frac{\partial(\overline{\rho U_i U_j})}{\partial x_j} + \frac{\partial \overline{p}}{\partial x_i} - \frac{\partial \overline{\tau_{ij}}}{\partial x_j} = 0 \tag{2.32a}$$

$$\frac{\partial(\overline{\rho}\widetilde{U_i})}{\partial t} + \frac{\partial(\overline{\rho}\widetilde{U_i U_j})}{\partial x_j} + \frac{\partial \overline{p}}{\partial x_i} - \frac{\partial \overline{\tau_{ij}}}{\partial x_j} = 0 \tag{2.32b}$$

$$\frac{\partial(\overline{\rho}\widetilde{U_i})}{\partial t} + \frac{\partial}{\partial x_j}\left(\overline{\rho}(\widetilde{\widetilde{U_i}\widetilde{U_j}} + \widetilde{\widetilde{U_i}U_j''} + \widetilde{U_i''\widetilde{U_j}} + \widetilde{U_i''U_j''})\right) + \frac{\partial \overline{p}}{\partial x_i} - \frac{\partial \overline{\tau_{ij}}}{\partial x_j} = 0 \tag{2.32c}$$

$$\frac{\partial(\overline{\rho}\widetilde{U_i})}{\partial t} + \frac{\partial(\overline{\rho}\widetilde{U_i}\widetilde{U_j})}{\partial x_j} + \frac{\partial \overline{p}}{\partial x_i} - \frac{\partial \overline{\tau_{ij}}}{\partial x_j} = -\frac{\partial(\overline{\rho}\widetilde{U_i''U_j''})}{\partial x_j} \tag{2.32d}$$

$$\equiv T_{R,U} \tag{2.32e}$$

The right hand side of eq. 2.32d contains the unclosed correlation of velocity fluctuations termed the Reynolds stress in the context of Favre averaging and is abbreviated by $T_{R,U}$ within this work. It represents the effect of convective transport induced by turbulent motions on the ensemble averaged flow momentum. The goal of the RANS turbulence model is to provide a closure for this term.

The Favre average of the species transport equation previously given in eq. 2.5 is derived in the same manner resulting in eq. 2.33. Again, an unresolved correlation appears. Here, it is the average of the species and velocity fluctuations. The physical interpretation of this term is the transient convective transport of each chemical compound due to the effects of turbulence. The variable $\check{D}_i$ denotes the computable species diffusion coefficient evaluated at the conditions given by the Favre averaged fields. The latter aspect implies a simplification that goes beyond the pure mathematical application of the averaging operators. It constitutes a necessary step, since the thermodynamic species properties need to be evaluated at a given thermodynamic state. Since only the averaged fields are known, it seems natural to utilize them as a basis for this evaluation.

$$\frac{\partial(\overline{\rho}\widetilde{Y_i})}{\partial t} + \frac{\partial(\overline{\rho}\widetilde{Y_i}\widetilde{U_j})}{\partial x_j} - \frac{\partial}{\partial x_j}\left(\overline{\rho}\check{D}_i\frac{\partial\widetilde{Y_i}}{\partial x_j}\right) - \overline{\dot{\omega}_i} = -\frac{\partial\left(\overline{\rho}\widetilde{Y_i''U_j''}\right)}{\partial x_j} \equiv T_{R,Y} \tag{2.33}$$

The ensemble averaging of the energy equation eq. 2.17 is more complex than for the previous equations, since more terms are involved, see eq. 2.34. Applying the Favre average definition from eq. 2.28 again allows to separate the averages of the products of the density and the remaining terms.

$$\begin{aligned}
&\frac{\partial}{\partial t}\left(\overline{\rho E}\right) \\
&+\frac{\partial}{\partial x_j}\left(\overbrace{\overline{\rho h_c U_j}}^{IIa} + \overbrace{\overline{\rho e_s U_j}}^{IIb} + \overbrace{\overline{\frac{1}{2}\rho U_i U_i U_j}}^{IIc}\right) \\
&+\frac{\partial}{\partial x_j}\left(\overbrace{\overline{pU_j}}^{III}\right) - \frac{\partial}{\partial x_j}\left(\overbrace{\overline{\tau_{ij}U_i}}^{IV}\right) \\
&-\frac{\partial}{\partial x_j}\left(\overbrace{\overline{\lambda\frac{\partial T}{\partial x_j}}}^{V} + \sum_{k=1}^{N_{sp}}\overbrace{\overline{\left((h_{c,k}+h_{s,k})\rho D_k\frac{\partial Y_k}{\partial x_j}\right)}}^{VI}\right) \\
&=0
\end{aligned} \tag{2.34}$$

At first, the total energy E is expanded in eq. 2.35 based on its definition in eq. 2.9 and the definition of the kinetic energy in eq. 2.7. The Favre averages of the fluctuating portions of each field actually vanish. However, the velocity vector product originating in the definition of the kinetic energy leaves the cross-correlation of Favre averaged velocity fluctuations. The latter can be identified as the turbulent kinetic energy previously defined in eq. 2.15.

$$\begin{aligned}
\overline{\rho E} &= \overline{\rho}\widetilde{E} \\
&= \overline{\rho}\left(\widetilde{h_c + e_s + e_k}\right) \\
&= \overline{\rho}\left(\widetilde{(\widetilde{h_c} + h_c'')} + \widetilde{(\widetilde{e_s} + e_s'')} + \frac{1}{2}\widetilde{(\widetilde{U_i}\widetilde{U_i} + 2U_i''\widetilde{U_i} + U_i''U_i'')}\right) \\
&= \overline{\rho}\left(\widetilde{h_c} + \widetilde{e_s} + \frac{1}{2}\widetilde{U_i}\widetilde{U_i} + \frac{1}{2}\widetilde{U_i''U_i''}\right)
\end{aligned} \tag{2.35}$$

Now, the Favre filtered total energy $\widetilde{E}$ can be split into a computable part $\check{E}$ and the turbulent kinetic energy k, see eq. 2.36. Due to eq. 2.36, the turbulent kinetic energy needs to be subtracted from the amount of transported energy resulting from the ensemble averaged transport equation in order to obtain the amount of energy remaining for the chemical, internal and kinetic energy. This is in accordance with the conservation of total energy, which the turbulent kinetic energy is a part of.

$$\begin{aligned}
\widetilde{E} &= \overbrace{\widetilde{h_c} + \widetilde{e_s} + \frac{1}{2}\widetilde{U_i}\widetilde{U_i}}^{\check{E}} + \overbrace{\frac{1}{2}\widetilde{U_i''U_i''}}^{k} \\
&= \check{E} + k
\end{aligned} \tag{2.36}$$

The expression IIa in eq. 2.34 can be reformulated through the Favre decomposition in eq. 2.29 and by applying the rules of averaging yielding the decomposition provided in eq. 2.37.

$$
\begin{aligned}
\overline{\rho h_c U_j} &= \overline{\rho}\widetilde{h_c U_j} \\
&= \overline{\rho}\left(\widetilde{\widetilde{h_c}\widetilde{U_j}} + \widetilde{\widetilde{h_c}U_j''} + \widetilde{h_c''\widetilde{U_j}} + \widetilde{h_c''U_j''}\right) \\
&= \overline{\rho}\left(\widetilde{\widetilde{h_c}\widetilde{U_j}} + \widetilde{h_c''U_j''}\right) \\
&= \overline{\rho}\left(\widetilde{h_c}\widetilde{U_j} + \widetilde{h_c''U_j''}\right)
\end{aligned}
\tag{2.37}
$$

The term IIb exhibits the same structure as the previous expression. Hence, the result of the Favre averaging of IIb is given in eq. 2.38 without further derivation. Both fluctuation correlation terms in eqs. 2.37 and 2.38 represent the effect of transient convective transport of chemical and internal energy on the mean energy field.

$$
\overline{\rho e_s U_j} = \overline{\rho}\left(\widetilde{e_s}\widetilde{U_j} + \widetilde{e_s''U_j''}\right) \tag{2.38}
$$

The decomposition of the kinetic energy convection term IIc is more complex, since it involves the triple product of velocity vectors. Similar to the preceding terms, the application of the Favre average definition decouples the density from the velocity vector product average. Inserting the Favre decomposition of the velocity field into the mean and fluctuating parts and a subsequent expansion of the resulting products leads to six separate terms. Two of the resulting terms are zero after averaging, since only terms containing solely the products of averages or cross-correlations between turbulent fluctuations remain, ultimately yielding the last expression in eq. 2.39.

$$
\begin{aligned}
&\overline{\frac{1}{2}\rho U_i U_i U_j} \\
&= \frac{1}{2}\overline{\rho}\widetilde{U_i U_i U_j} \\
&= \frac{1}{2}\overline{\rho}\left(\widetilde{(\widetilde{U_i} + U_i'')(\widetilde{U_i} + U_i'')(\widetilde{U_j} + U_j'')}\right) \\
&= \frac{1}{2}\overline{\rho}\left(\widetilde{\widetilde{U_i}\widetilde{U_i}\widetilde{U_j}} + 2\widetilde{\widetilde{U_i}U_i''\widetilde{U_j}} + \widetilde{U_i''U_i''\widetilde{U_j}} + \widetilde{\widetilde{U_i}\widetilde{U_i}U_j''} + 2\widetilde{\widetilde{U_i}U_i''U_j''} + \widetilde{U_i''U_i''U_j''}\right) \\
&= \frac{1}{2}\overline{\rho}(\widetilde{U_i}\widetilde{U_i}\widetilde{U_j}) + \frac{1}{2}\overline{\rho}\widetilde{U_j}\widetilde{U_i''U_i''} + \overline{\rho}\widetilde{U_i}\widetilde{U_i''U_j''} + \frac{1}{2}\overline{\rho}\widetilde{U_i''U_i''U_j''}
\end{aligned}
\tag{2.39}
$$

$$
\begin{aligned}
\overline{pU_j} &= \overline{(\overline{p} + p')(\widetilde{U_j} + U_j'')} \\
&= \overline{\overline{p}\widetilde{U_j}} + \overline{\overline{p}U_j''} + \overline{p'\widetilde{U_j}} + \overline{p'U_j''} \\
&= \overline{\overline{p}\widetilde{U_j}} + \overline{\overline{p}U_j''} + \overline{p'U_j''} \\
&= \overline{p}\widetilde{U_j} + \overline{pU_j''}
\end{aligned}
\tag{2.40}
$$

The decomposition of term III leads to the expression in eq. 2.40. Structurally, term IV is equivalent, see eq. 2.41, hence, the following explanations hold for both terms. Since the density does not appear within the product, the Reynolds average is not reformulated in terms of the Favre average. However, the Favre decomposition is applied to the velocity field consistently with the previous derivations. Hence, the Reynolds average of the product $\overline{p}U_i''$ respectively $\overline{\tau_{ij}}U_i''$ remains, although the product contains solely one fluctuation. This is due to the fact that the Reynolds average of a Favre fluctuation is generally not zero, see eq. 2.30.

$$\begin{aligned}\overline{\tau_{ij}U_i} &= \overline{(\overline{\tau_{ij}}+\tau_{ij}{}')(\widetilde{U_i}+U_i{}'')} \\ &= \overline{\overline{\tau_{ij}}\widetilde{U_i}} + \overline{\overline{\tau_{ij}}U_i{}''} + \overline{\tau_{ij}{}'\widetilde{U_i}} + \overline{\tau_{ij}{}'U_i{}''} \\ &= \overline{\overline{\tau_{ij}}\widetilde{U_i}} + \overline{\overline{\tau_{ij}}U_i{}''} + \overline{\tau_{ij}{}'U_i{}''} \\ &= \overline{\tau_{ij}}\widetilde{U_i} + \overline{\tau_{ij}U_i{}''}\end{aligned} \tag{2.41}$$

Furthermore, also the last terms denoted with V and VI can be expanded yielding the separate contributions of the mean fields and the cross-correlation of turbulent fluctuations, see eq. 2.42. Here, the same simplification is made as for the derivation for the ensemble averaged species transport equation, cf. eq. 2.33: The diffusion coefficients D_k for species k and the heat conductivity λ are decoupled from the averaging procedure and evaluated at the mean conditions yielding the computable diffusion coefficients $\check{D}_k$ and $\check{\lambda}$. It should be noted that the Reynolds average of the temperature Favre fluctuation does not vanish due to eq. 2.30.

$$\begin{aligned}&\overline{\lambda\frac{\partial T}{\partial x_j} + \sum_{k=1}^{N_{sp}}\left((h_{c,k}+h_{s,k})\rho D_k\frac{\partial Y_k}{\partial x_j}\right)} \\ &= \check{\lambda}\frac{\partial\widetilde{T}}{\partial x_j} + \sum_{k=1}^{N_{sp}}\left((\widetilde{h_{c,k}}+\widetilde{h_{s,k}})\overline{\rho}\check{D}_k\frac{\partial\widetilde{Y_k}}{\partial x_j}\right) \\ &+ \check{\lambda}\frac{\partial\overline{T''}}{\partial x_j} + \sum_{k=1}^{N_{sp}}(\overline{\rho}\check{D}_k\overline{(h_{c,k}{}''+h_{s,k}{}'')\frac{\partial Y_k{}''}{\partial x_j}})\end{aligned} \tag{2.42}$$

Finally, the ensemble Favre averaged energy transport equation from eq. 2.34 can be reformulated in terms of computable mean quantities and unexplored turbulent cross-correlation terms based on the previous derivations, see eq. 2.43.

Now, the set of ensemble averaged governing equations given by the mass transport equation eq. 2.31, the momentum transport equation eq. 2.32, the

species transport equation eq. 2.33 and the energy transport equation 2.43 is complete. While the left hand side of each equation contains solely known and computable quantities, the right hand sides denote the apriori unexplored influence of turbulent transport processes on the mean field. The terms on the right hand side are subject to turbulence modeling, which is specific to the utilized solver and are thus discussed in the following chapter.

$$
\begin{aligned}
&\frac{\partial}{\partial t}\left(\overline{\rho}(\check{E}+k)\right)\\
&+\frac{\partial}{\partial x_j}\left(\overline{\rho}\widetilde{h_c}\widetilde{U_j}+\overline{\rho}\widetilde{e_s}\widetilde{U_j}+\frac{1}{2}\overline{\rho}\widetilde{U_i}\widetilde{U_i}\widetilde{U_j}\right)\\
&+\frac{\partial}{\partial x_j}\left(\overline{p}\widetilde{U_j}\right)-\frac{\partial}{\partial x_j}\left(\overline{\tau_{ij}}\widetilde{U_i}\right)\\
&-\frac{\partial}{\partial x_j}\left(\check{\lambda}\frac{\partial\widetilde{T}}{\partial x_j}+\sum_{k=1}^{N_{sp}}\left((\widetilde{h_{c,k}}+\widetilde{h_{s,k}})\overline{\rho}\check{D}_k\frac{\partial\widetilde{Y_k}}{\partial x_j}\right)\right)\\
=&-\frac{\partial}{\partial x_j}\left(\overline{\rho}\widetilde{h_c{}''U_j{}''}+\overline{\rho}\widetilde{e_s{}''U_j{}''}+\overline{\rho}\widetilde{U_i}\widetilde{U_i{}''U_j{}''}+\frac{1}{2}\overline{\rho}\widetilde{U_i{}''U_i{}''U_j{}''}+\frac{1}{2}\overline{\rho}\widetilde{U_j}\widetilde{U_i{}''U_i{}''}\right)\\
&+\frac{\partial}{\partial x_j}\left(\overline{\tau_{ij}U_i{}''}\right)-\frac{\partial}{\partial x_j}\left(\overline{pU_j{}''}\right)\\
&+\frac{\partial}{\partial x_j}\left(\check{\lambda}\frac{\partial\overline{T''}}{\partial x_j}+\sum_{k=1}^{N_{sp}}(\overline{\rho}\check{D}_k\overline{(h_{c,k}{}''+h_{s,k}{}'')\frac{\partial Y_k{}''}{\partial x_j}})\right)\\
&\equiv T_{R,E}
\end{aligned}
\tag{2.43}
$$

2.2.2 Spatially Filtered Governing Equations

The concept of large eddy simulation rests upon the separation of large and small scale turbulent structures through the application of a spatial filter. This is in contrast to RANS, which is based on the ensemble or time average of the governing equations. Although both approaches are based on mathematically different concepts, the resulting governing equations, filtered and ensemble

averaged, can be formulated in a similar way. Here, the Favre filtered governing equations are derived equivalently to the previous derivation of the RANS equations. Subsequently, the similarities are outlined, which are the basis for the hybrid RANS/LES modeling framework presented later within this thesis.

In general, the application of a spatial filter function $G(\vec{x}-\vec{\xi})$ to a generic field ϕ is provided by eq. 2.44, see Sagaut et al. [117] and Chung [26] for details. The filter function $G(\vec{x}-\vec{\xi})$ is large, if $\vec{x}$ and $\vec{\xi}$ are close. Figuratively speaking, the filter combines local values of the field ϕ and yields a smoothed field $\widehat{\phi}$. Additionally, the spatial integral of the filter kernel $G(\vec{x}-\vec{\xi})$ must satisfy the relation in eq. 2.45.

$$\widehat{\phi}(\vec{x}) = \int G(\vec{x}-\vec{\xi})\phi(\vec{\xi})d^3\vec{\xi} \tag{2.44}$$

$$\int G(\vec{x}-\vec{\xi})d^3\vec{\xi} = 1 \tag{2.45}$$

The spatial LES filter leaves solely the large scale part of the turbulent flow field. Therefore, turbulent fluctuations on the subgrid scale are canceled out by the filter and can be written as the difference between the complete and the filtered field, see eq. 2.46a. Hence, the LES scale separation is formulated in terms of the sum of large and small scale structures of a given field, see eq. 2.46b. The tophat symbol denotes the application of a generic spatial filter in terms of eq. 2.44.

$$\phi' = \phi - \widehat{\phi} \tag{2.46a}$$

$$\phi = \widehat{\phi} + \phi' \tag{2.46b}$$

A generic spatial filtering operation exhibits properties that partially match and partially deviate from the characteristics of the Reynolds operator given in section 2.2.1 [52, 117]. Firstly, the scale separation represented by eq. 2.46 is tied to the particular filter leading to the decomposition. The application of

another filter would lead to a different scale separation and therefore different decomposition in eq. 2.46. Furthermore, the filter is commutative with respect to addition, see eq. 2.47. Moreover, it is assumed that the filtering operator commutes with the differential operator also in the later introduced density-weighted case, which is not exactly true. Moreover, multiple applications of the same filter lead to different results represented by eq. 2.48. This feature of spatial filtering is in contrast to the concept of a time average, which remains the same if it is time averaged again.

The latter aspect implies that the fluctuating portion of the field does not vanish if it is filtered, see eq. 2.49: The application of the filter to eq. 2.46a leads to eq. 2.49a. Due to eq. 2.48, this expression is not equal to the original difference between the complete field and the large scale part, see eq. 2.49b. Hence, $\widehat{\phi'}$ is also not equal to ϕ'. There is also no reason why eq. 2.49a should be zero, such that the filtered fluctuation does not vanish, cf. eq. 2.49c.

$$\widehat{\phi+\psi} = \widehat{\phi} + \widehat{\psi} \tag{2.47}$$

$$\widehat{\widehat{\phi}} \neq \widehat{\phi} \tag{2.48}$$

$$\widehat{\phi'} = \widehat{\phi} - \widehat{\widehat{\phi}} \tag{2.49a}$$

$$\neq \phi - \widehat{\phi} = \phi' \tag{2.49b}$$

$$\neq 0 \tag{2.49c}$$

As a consequence, the cross term products between large scale and small-scale contributions do not disappear in general, cf. eq. 2.50. This stands in contrast to the application of the Reynolds operator, which leads to the disappearance of cross terms with respect to ensemble averaging, cf. eq. 2.23. Consequently, the spatially filtered governing equations contain additional terms compared to the equations underlying RANS.

$$\widehat{\overline{\psi}\phi'} \neq 0 \tag{2.50}$$

In order to decouple density fluctuations from the remaining fields, the filtering is extended to mass-weighted Favre filtering. The motivation is similar to the justification of Favre averaging for the RANS case as discussed previously. The generic definition of a Favre filtered quantity is given in eq. 2.51a in terms of the generic filter denoted by the overhat symbol. Here, the tilde denotes the Favre filtered field in the context of LES, whereas it denoted the Favre averaged field in the RANS case, see section 2.2.1. Consequently, the filtered product of the density and any field can be rewritten in terms of the product of the filtered density and the Favre filtered field, see eq. 2.51b. This variable transformation leads to a considerable simplification of the following derivations. Nevertheless, it should be noted that this simplification is of pure mathematical nature.

$$\widetilde{\phi} = \frac{\widehat{\rho\phi}}{\widehat{\rho}} \tag{2.51a}$$

$$\widehat{\rho\phi} = \widehat{\rho}\widetilde{\phi} \tag{2.51b}$$

Due to the introduction of the Favre filter, the spatially filtered mass transport equation eq. 2.1 can be written in the form of eq. 2.52. Hence, it formally corresponds to the Favre averaged continuity equation, cf. eq. 2.31.

$$\frac{\partial\widehat{\rho}}{\partial t} + \frac{\partial(\widehat{\rho}\widetilde{\phi})}{\partial x_j} = 0 \tag{2.52}$$

Spatial filtering leads to the momentum equation eq. 2.53. The application of the Favre filter leads to the decoupling of cross-correlations that include the density in the spirit of eq. 2.51b.

$$\frac{\partial(\widehat{\rho}\widetilde{U_i})}{\partial t} + \frac{\partial(\widehat{\rho}\widetilde{U_iU_j})}{\partial x_j} + \frac{\partial\widehat{p}}{\partial x_i} - \frac{\partial\widehat{\tau_{ij}}}{\partial x_j} = 0 \tag{2.53}$$

Similarly to the RANS case the dyadic product of the velocity vector $\mathrm{U}_i\mathrm{U}_j$ needs to be decomposed into a product of computable variables. Such

a generic formulation is given by the triple decomposition introduced by Leonard [117]. This decomposition in terms of the Favre filter is derived in eq. 2.54 and leads to four components: Firstly, the desired computable product of the filtered fields. Secondly, a term appears depending only on the resolved scales, which is named Leonard stress L_{ij}. Furthermore, the cross term denoted with C_{ij} represents the interaction of resolved large scale and unresolved subgrid turbulent scales. Finally, the Reynolds stress term R_{ij} is comprised of cross-correlations between spatially unresolved turbulent fluctuations. The latter is formally identical to RANS. Yet, it represents a different concept, since the RANS Reynolds stress represents the statistic influence of the whole turbulent spectrum on the ensemble averaged fields. The large scale and cross scale terms within the triple decomposition would vanish if the filter operator was a Reynolds operator, see eqs. 2.25 and 2.23. The triple decomposition provides the basis for a class of turbulence models that make use of the Leonard and cross term correlations as discussed in the following chapter.

$$\begin{aligned}
\widetilde{\phi\psi} &= \widetilde{\phi}\widetilde{\psi} + \left(\widetilde{\phi\psi} - \widetilde{\phi}\widetilde{\psi}\right) \\
&= \widetilde{\phi}\widetilde{\psi} + \left(\widetilde{(\widetilde{\phi} + \phi'')(\widetilde{\psi} + \psi'')} - \widetilde{\phi}\widetilde{\psi}\right) \\
&= \widetilde{\phi}\widetilde{\psi} + \left(\overbrace{\widetilde{\widetilde{\phi}\widetilde{\psi} - \widetilde{\phi}\widetilde{\psi}}}^{L_{ij}} + \overbrace{\widetilde{\widetilde{\phi}\psi'' + \phi''\widetilde{\psi}}}^{C_{ij}} + \overbrace{\widetilde{\phi''\psi''}}^{R_{ij}}\right)
\end{aligned} \tag{2.54}$$

The Favre filtered momentum transport equation eq. 2.53 can be reformulated on the basis of the triple decomposition yielding eq. 2.55a and finally 2.55b.

$$\frac{\partial(\widehat{\rho}\widetilde{U_i})}{\partial t}+\frac{\partial(\widehat{\rho}\widetilde{U_i}\widetilde{U_j})}{\partial x_j}+\frac{\partial \widehat{p}}{\partial x_i}-\frac{\partial \widehat{\tau_{ij}}}{\partial x_j}=-\frac{\partial(\widehat{\rho}(\widetilde{U_iU_j}-\widetilde{U_i}\widetilde{U_j}))}{\partial x_j} \tag{2.55a}$$

$$\frac{\partial(\widehat{\rho}\widetilde{U_i})}{\partial t}+\frac{\partial(\widehat{\rho}\widetilde{U_i}\widetilde{U_j})}{\partial x_j}+\frac{\partial \widehat{p}}{\partial x_i}-\frac{\partial \widehat{\tau_{ij}}}{\partial x_j} \tag{2.55b}$$

$$=-\frac{\partial}{\partial x_j}\left(\widehat{\rho}\left(\overbrace{\widetilde{U_i}\widetilde{U_j}-\widetilde{U_i}\widetilde{U_j}}^{L_{ij}^U}+\overbrace{\widetilde{U_i}{U_j}''+{U_i}''\widetilde{U_j}}^{C_{ij}^U}+\overbrace{{U_i}''{U_j}''}^{R_{ij}^U}\right)\right)$$

$$\equiv T_{L,U} \tag{2.55c}$$

The derivation of the spatially Favre filtered species transport equations follows a similar procedure and finally yields the equation given in eq. 2.56. The right hand side again contains the additional terms that arise due to the filter operation. The Leonard stress term L_{ij}^{Y} represents species mixing on the resolved scales close to the filter cut-off wavelength still unaffected by the spatial low-pass LES filter. The term R_{ij}^{Y} contains the turbulent transport of chemical compounds on the subgrid level, thus at the small scales removed by the filter. Finally, the cross term C_{ij}^{Y} represents the species mixing due to the interaction of spatially resolved and subgrid vortical structures at length scales close to the filter cut-off length.

$$
\begin{aligned}
&\frac{\partial(\widehat{\rho}\widetilde{Y_i})}{\partial t} + \frac{\partial(\widehat{\rho}\widetilde{Y_i}\widetilde{U_j})}{\partial x_j} - \frac{\partial}{\partial x_j}\left(\widehat{\rho}\check{D}_i\frac{\partial\widetilde{Y_i}}{\partial x_j}\right) - \widehat{\dot{\omega}_i} \\
&= -\frac{\partial}{\partial x_j}\left(\widehat{\rho}\left(\underbrace{\widetilde{Y_i}\widetilde{U_j} - \widetilde{Y_i}\widetilde{U_j}}_{L_{ij}^Y} + \underbrace{\widetilde{Y_i U_j}'' + Y_i''\widetilde{U_j}}_{C_{ij}^Y} + \underbrace{Y_i'' U_j''}_{R_{ij}^Y}\right)\right) \\
&\equiv T_{L,Y}
\end{aligned}
\tag{2.56}
$$

Filtering the energy transport equation introduces more terms, similarly to the RANS case. The inclusion of kinetic energy leads to an unresolved cross-correlation of velocity fluctuations due to the dyadic velocity product. Instead of expanding the term as done for the ensemble averaged equation in eq. 2.36, the filtered total energy $\widetilde{E}$ is simplified as the product of computable filtered velocities and enhanced with the turbulent kinetic energy k [52] according to the procedure by Ragab and Sreedhar [113] in order to avoid the unknown correlations in eq. 2.57b. Hence, the energy definition is formally equivalent to the previously derived RANS formulation. The computable part is denoted with $\check{E}$, see eq. 2.57c. Within the given context, k represents the subgrid portion of the turbulent kinetic energy that remains spatially unresolved due to the application of the spatial filter. Whereas eq. 2.36 constitutes a mathematically comprehensive expression, eq. 2.57c represents a simplification, which is necessary in order to formulate the filtered energy in terms of known variables.

$$\widetilde{E} = \widetilde{h_c} + \widetilde{e_s} + \frac{1}{2}\widetilde{U_i U_i} \tag{2.57a}$$

$$= \widetilde{h_c} + \widetilde{e_s} + \frac{1}{2}\left(\widetilde{\widetilde{U_i}\widetilde{U_i}} + 2\widetilde{\widetilde{U_i}U_i''} + \widetilde{U_i''U_i''}\right) \tag{2.57b}$$

$$\approx \overbrace{\widetilde{h_c} + \widetilde{e_s} + \frac{1}{2}\widetilde{U_i}\widetilde{U_i}}^{\check{E}} + \overbrace{\frac{1}{2}\widetilde{U_i''U_i''}}^{k_{SGS}} \tag{2.57c}$$

Structurally, the computable left hand side of the resulting filtered energy transport equation eq. 2.58 resembles the RANS counterpart, cf. eq. 2.43. The terms on the right hand side contain the inter-length scale correlations and can be expanded based on the triple decomposition in eq. 2.54 similarly to the preceding momentum and species transport equations. The Leonard decomposition of the kinetic energy and velocity product leads to the Leonard, cross- and Reynolds stress terms denoted with $L_{ij}^{e_k}$, $C_{ij}^{e_k}$ and $R_{ij}^{e_k}$. However, the cross term involves further correlations due to the triple product, see eq. 2.59, as can be trivially reproduced by inserting the Favre decomposition of the velocity vectors and expanding the resulting terms.

A comprehensive formulation of the Favre filtered energy transport equation including the triple decomposition of the turbulent terms is provided in eq. 2.60. Now, with eqs. 2.52, 2.55, 2.56 and 2.60 the set of spatially filtered governing equations of reacting, compressible fluid flow is complete. The triple decomposed turbulent transport contributions on the respective right hand sides $\mathrm{T}_{L,U}$, $\mathrm{T}_{L,Y}$, $\mathrm{T}_{L,E}$ are utilized for the formulation of the turbulence model closure for LES in the next chapter.

$$
\begin{aligned}
&\frac{\partial}{\partial t}\left(\widehat{\rho}(\check{E}+k)\right)\\
&+\frac{\partial}{\partial x_j}\left(\widehat{\rho}\widetilde{h_c}\widetilde{U_j}+\widehat{\rho}\widetilde{e_s}\widetilde{U_j}+\frac{1}{2}\widehat{\rho}\widetilde{U_i}\widetilde{U_i}\widetilde{U_j}\right)\\
&+\frac{\partial}{\partial x_j}\left(\widehat{p}\widetilde{U_j}\right)-\frac{\partial}{\partial x_j}\left(\widehat{\tau_{ij}}\widetilde{U_i}\right)-\frac{\partial\widehat{q_j}}{\partial x_j}\\
=&-\frac{\partial}{\partial x_j}\left(\widehat{\rho}\left(\widetilde{h_cU_j}-\widetilde{h_c}\widetilde{U_j}\right)\right)\\
&-\frac{\partial}{\partial x_j}\left(\widehat{\rho}\left(\widetilde{e_sU_j}-\widetilde{e_s}\widetilde{U_j}\right)\right)\\
&-\frac{\partial}{\partial x_j}\left(\widehat{\rho}\left(\widetilde{U_iU_jU_j}-\widetilde{U_i}\widetilde{U_j}\widetilde{U_j}\right)\right)\\
&-\frac{\partial}{\partial x_j}\left(\widehat{pU_j}-\widehat{p}\widetilde{U_j}\right)+\frac{\partial}{\partial x_j}\left(\widehat{\tau_{ij}U_i}-\widehat{\tau_{ij}}\widetilde{U_i}\right)
\end{aligned}
\tag{2.58}
$$

$$
\begin{aligned}
&\widetilde{U_iU_iU_j}-\widetilde{U_i}\widetilde{U_i}\widetilde{U_j}\\
&\overbrace{\phantom{=\widetilde{U_i}\widetilde{U_i}\widetilde{U_j}-\widetilde{U_i}\widetilde{U_i}\widetilde{U_j}}}^{L_{ij}^{e_k}}\\
&=\widetilde{U_i}\widetilde{U_i}\widetilde{U_j}-\widetilde{U_i}\widetilde{U_i}\widetilde{U_j}\\
&\overbrace{\phantom{+\widetilde{U_i}\widetilde{U_i}U_j''+2\widetilde{U_i}U_i''\widetilde{U_j}+2\widetilde{U_i}U_i''U_j''+U_i''U_i''\widetilde{U_j}}}^{C_{ij}^{e_k}}\\
&+\widetilde{U_i}\widetilde{U_i}U_j''+2\widetilde{U_i}U_i''\widetilde{U_j}+2\widetilde{U_i}U_i''U_j''+U_i''U_i''\widetilde{U_j}\\
&\overbrace{}^{R_{ij}^{e_k}}\\
&+U_i''U_i''U_j''
\end{aligned}
\tag{2.59}
$$

$$
\begin{aligned}
&\frac{\partial}{\partial t}\left(\widehat{\rho}(\check{E}+k)\right)\\
&+\frac{\partial}{\partial x_j}\left(\widehat{\rho}\widetilde{h_c}\widetilde{U_j}+\widehat{\rho}\widetilde{e_s}\widetilde{U_j}+\frac{1}{2}\widehat{\rho}\widetilde{U_i}\widetilde{U_i}\widetilde{U_j}\right)\\
&+\frac{\partial}{\partial x_j}\left(\widehat{p}\widetilde{U_j}\right)-\frac{\partial}{\partial x_j}\left(\widehat{\tau_{ij}}\widetilde{U_i}\right)-\frac{\partial\widehat{q_j}}{\partial x_j}\\
&=-\frac{\partial}{\partial x_j}(\widehat{\rho}(\overbrace{\widetilde{h_c}\widetilde{U_j}-\widetilde{h_c}\widetilde{U_j}}^{L_{ij}^{h_c}}+\overbrace{\widetilde{h_c U_j}''+\widetilde{h_c}''\widetilde{U_j}}^{C_{ij}^{h_c}}+\overbrace{\widetilde{h_c}''\widetilde{U_j}''}^{R_{ij}^{h_c}}))\\
&-\frac{\partial}{\partial x_j}(\widehat{\rho}(\overbrace{\widetilde{e_s}\widetilde{U_j}-\widetilde{e_s}\widetilde{U_j}}^{L_{ij}^{e_s}}+\overbrace{\widetilde{e_s U_j}''+\widetilde{e_s}''\widetilde{U_j}}^{C_{ij}^{e_s}}+\overbrace{\widetilde{e_s}''\widetilde{U_j}''}^{R_{ij}^{e_s}}))\\
&-\frac{\partial}{\partial x_j}(\widehat{\rho}(L_{ij}^{e_k}+C_{ij}^{e_k}+R_{ij}^{e_k}))\\
&-\frac{\partial}{\partial x_j}(\overbrace{\widehat{\rho}\widetilde{U_j}-\widehat{\rho}\widetilde{U_j}}^{L_{ij}^{p}}+\overbrace{\widehat{\rho U_j}''+\widehat{p'}\widetilde{U_j}}^{C_{ij}^{p}}+\overbrace{\widehat{p'U_j}''}^{R_{ij}^{p}})\\
&+\frac{\partial}{\partial x_j}(\overbrace{\widehat{\tau_{ij}}\widetilde{U_i}-\widehat{\tau_{ij}}\widetilde{U_i}}^{L_{ij}^{\tau}}+\overbrace{\widehat{\tau_{ij}U_i}''+\widehat{\tau_{ij}'}\widetilde{U_i}}^{C_{ij}^{\tau}}+\overbrace{\widehat{\tau_{ij}'U_i}''}^{R_{ij}^{\tau}})\\
&\equiv T_{L,E}
\end{aligned}
\tag{2.60}
$$

2.2.3 Summary

The governing equations of compressible fluid flow in the context of RANS and LES turbulence modeling are derived in the previous two sections 2.2.1 and 2.2.2. The right-hand sides of the resulting equations provide the mathematical formulation of unclosed turbulent terms that require modeling either based on RANS or LES. Table 2.1 provides a summary of the derived unclosed terms within the momentum, species and energy transport equations. The

Table 2.1: Summary of unclosed turbulent terms derived in sections 2.2.1 and 2.2.2 for RANS and LES

Transport equation	**RANS**	**LES**
Momentum	$\mathrm{T}_{R,U}$ (eq. 2.32)	$\mathrm{T}_{L,U}$ (eq. 2.55)
Species	$\mathrm{T}_{R,Y}$ (eq. 2.33)	$\mathrm{T}_{L,Y}$ (eq. 2.56)
Energy	$\mathrm{T}_{R,E}$ (eq. 2.43)	$\mathrm{T}_{L,E}$ (eq. 2.60)

formulation of appropriate closures for these terms is discussed in sections 3.3 and 3.4 of the subsequent chapter describing the developed fluid dynamics solver for supersonic combustion. Finally, chapter 4 provides a method to combine both RANS and LES to a hybrid turbulence modeling approach.

2.3 Turbulent Deflagration in Transonic and Supersonic Flows

Supersonic combustion does not imply that the physics of combustion fundamentally change. Combustion remains the result of chemical reactions proceeding within a fluid moving at supersonic speeds, where the local static temperatures and pressures are sufficient to provide conditions for ignition and combustion of the fuel before it leaves the observed volume. Shock waves caused by injector elements or the flow itself locally increase the temperature and lead to the conversion of kinetic to thermal energy. More specifically, shock waves decrease both the flow velocity and ignition delay time, therefore generating favorable conditions for combustion. Furthermore, flame holders may locally reduce the flow velocity to subsonic Mach numbers and increase fuel residence times, thus also promoting combustion.

Furthermore, the combustion processes investigated within this thesis occur at flow speeds close or above the speed of sound. Depending on the combustor Mach number, total temperature and pressure as well as the injected fuel

mass, local subsonic regions form. Therefore, the term supersonic combustion is regarded in a wider sense within this work by extending it to the formulation transonic and supersonic combustion. Both supersonic and subsonic flow regions locally coexist next to each other and their formation underlies fluctuations in time and space. This is especially true for the investigated combustor configuration at the ITLR at the University of Stuttgart. The ITLR combustor features conditions that correspond to the transition regime between ramjet and scramjet operation located at the lower boundary of the scramjet flight regime.

The strong flow variations caused by shocks paired with intense turbulent fluctuations induced by fuel injection and shear layers result in a locally very inhomogeneous structure of supersonic flames. Burned and unburned fuel coexists with air in partially mixed conditions dominated by convective processes induced by the main flow and superimposed turbulent vortices. In addition, combustion induced heat release locally decreases the Mach number such that subsonic regions affecting the flow further upstream might form. Hence, supersonic combustion involves a complex mixture of partly premixed diffusion flame regions at subsonic and supersonic speeds. The significant spatial and temporal variations in temperature, pressure and species composition encountered in supersonic flames thus impede an obvious flame regime classification, e.g. in terms of the Borghi diagram [17]. Potturi [111,112] provides a valuable computational investigation of the distribution of fuel and air within a supersonic combustor and reveals the aforementioned complex structure of the mixture. Nonetheless, a discussion of supersonic combustion in the context of flame regimes can be found in the work of Gabler [51] and Förster [47]. Essentially, Förster states that the flame regime within the Borghi diagram relevant for supersonic combustion is outside the flamelet region, such that flamelet models do not appear to be applicable. The subsequent chapter provides information about the mathematical and physical modeling of the combustion process.

2.4 Relevant Compressible Flow Phenomena in Supersonic Combustors

In the following, the phenomenological description of two aspects of compressible fluid flow shall be given, which constitute major elements of the flow within supersonic combustor ducts. Both appear as components of the test cases investigated in chapters 6 and 8. The first aspect is related to the interaction of shock waves impinging on the combustor wall boundary layers. The subsequent section provides a brief description of a fuel injection configuration known as jet in supersonic crossflow, since this is the most widely utilized fuel injection setup.

2.4.1 Shock Boundary Layer Interaction

A crucial facet of supersonic combustor ducts is the interaction of shocks with the boundary layer. Shock waves induce several effects relevant to supersonic combustion: First of all, shocks serve as reaction accelerators due to the accompanying temperature rise. Secondly, shocks can promote turbulent mixing of fuel and air through baroclinic vorticity production. Furthermore, shock impingement can cause local boundary layer separation and subsequent boundary layer growth with crucial consequences for the surrounding supersonic flow field within a supersonic combustor duct.

In an idealized inviscid flow no boundary layer is present. The interaction between a shock wave and the wall reduces to the requirement that the reflected shock wave adjusts the streamlines to be parallel to the wall. However, the viscosity and no-slip condition of a real fluid flow enforce a reduced velocity in the vicinity of the wall resulting in the formation of the boundary layer. In consequence, the flow can be divided in two regions: The supersonic far-field and the near-wall flow. The near-wall region is dominated by viscous effects, whereas inertia effects determine the supersonic far-field [3]. Hence, the problem of a shock impinging on a wall is actually an interaction between the shock and the boundary layer. In particular, a phenomenon potentially accompanying the interaction is the shock induced separation of the boundary

layer, which is mainly driven by the magnitude of the adverse, shock induced pressure gradient. Depending on the strength of the shock the induced pressure rise might be sufficient to promote boundary layer separation and the formation of a separation bubble with local flow recirculation.

Here, a short summary of important boundary layer features shall be provided together with a qualitative description of shock boundary layer interactions relevant for supersonic combustor ducts. These interactions constitute dominant elements of the ducted supersonic flows investigated in chapters 6 and 8. A comprehensive work on the interaction of shocks and boundary layers is provided by Babinsky and Harvey [3]. In fact, all aforementioned phenomena are described by the governing equations of compressible fluid flow explained at the beginning of this chapter.

2.4.1.1 Boundary Layer Fundamentals

The boundary layer thickness is an important factor influencing the effective geometry of the combustor duct. A thicker boundary layer decreases the supersonic portion of the flow and blocks a portion of the channel. Generally, the boundary layer thickness grows with the distance traversed along the combustor duct and is a function of the density, viscosity and velocity of the fluid [59]. This relationship is embodied by the Reynolds number Re, see eq. 2.61.

$$Re(x) = \frac{\rho U x}{\mu} \tag{2.61}$$

Fundamental boundary layer theory as described by Schlichting and Gersten [119] provides the mathematical relationship between the boundary layer thickness and the Reynolds number given in eq. 2.62 for a flat plate laminar boundary layer. The test cases investigated within this thesis exhibit turbulent boundary layers, yet, the universal essence of the relation in eq. 2.62 is the monotonical boundary layer growth as a function of the distance x [101, 114], whereas the Reynolds number Re serves as a scaling factor. The smaller the Reynolds number, the thicker is the resulting boundary layer.

$$\delta \propto \frac{x}{\sqrt{Re(x)}} \tag{2.62}$$

These fundamental relations can be used to derive qualitative statements about the boundary layer thickness within a given combustor: Evidently, a long isolator duct preceding the combustor will induce a thick boundary layer. Furthermore, large Mach numbers or low flight altitudes will result in high total pressures and a large density, such that the Reynolds number will increase reducing the boundary layer thickness. On the other hand, large Mach numbers result in high static temperatures increasing the viscosity. This will in turn reduce the Reynolds number, see eq. 2.61 and therefore have an increasing effect on the boundary layer thickness.

It is evident from these considerations, that generally valid statements about the boundary layer thickness within a scramjet combustor duct are rather difficult. Nonetheless, it is an important insight that the flight conditions have a considerable influence on the boundary layer thickness, which might in turn amount to considerable portions of the combustor cross-section. The ITLR combustor investigated in chapter 8 features a considerable boundary layer thickness, which leads to a specific combustion mode specific to the transition between ramjet and scramjet operation, see section 8.4.

In addition, any supersonic boundary layer features a subsonic layer close to the wall, which allows information to travel upstream. A sonic line separates the subsonic and supersonic boundary layer parts. A relevant feature of the sonic line is its property to follow local boundary layer deflections, e.g. due to the impingement of shocks. This can be utilized for the formulation of a criterion switching between RANS and LES as shown in chapter 4. A further consequence is that every wall-confined supersonic flow exhibits subsonic regions potentially allowing for an upstream propagation of information close to the wall [3]. The ability of a partly subsonic/supersonic flow to transmit information upstream can have crucial consequences for the operation of a combustor as shown in section 8.5.2 describing the hybrid RANS/LES of the ITLR combustor.

2.4.1.2 Oblique Shock Reflection

A typical situation is the reflection of an oblique shock impinging on a wall. The case of a rather weak shock is sketched on the left hand side of figure 2.1. The reflection mechanism is as follows: The oblique shock (A) causes a pressure rise in the boundary layer (D) resulting in a local bump in the sonic line (C). A system of shocks forms ahead of the bump due to the continuously increasing ramp angle. In the far-field, these shocks fuse into the shock that is perceived as the reflected oblique shock (B). The original shock bends due to the locally decreasing Mach number and almost vanishes the closer it comes to the sonic line. An important insight is that the effect of the shock impingement is spread over an area upstream and downstream of the actual location of impingement. For this reason, the effect of the pressure jump induced by the initial shock is spread over a broad region in the viscous zone. Hence, the boundary layer effectively perceives a smaller pressure gradient than the pressure jump across the shock would suggest.

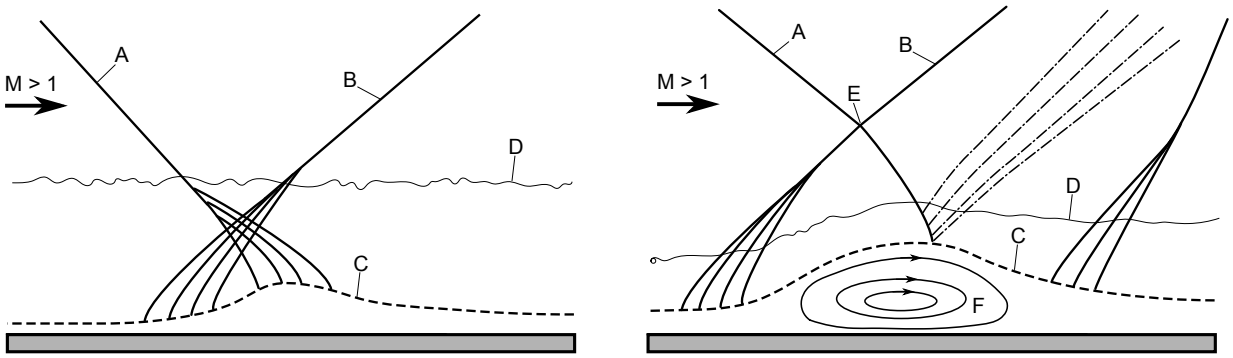

Figure 2.1: Oblique shock reflection without (left) and with boundary layer separation (right)

If the oblique shock (A) induces a large enough pressure rise, boundary layer separation occurs as sketched on the right hand side of figure 2.1. A recirculation bubble (F) forms in the separation region within the subsonic region below the sonic line (C). The upstream influence of the interaction is increased due to the recirculating flow within the bubble in comparison to the non-separated interaction case. The separation point upstream of the bubble induces a relatively sharp kink in the boundary layer, which acts as a ramp and

induces a system of weaker shocks that merge into the reflected shock (B) in the far-field, which is further deflected at the shock intersection point (E). The incoming shock (A) is reflected as a series of expansions waves at the sonic line, enforcing a reattachment shock behind the separation region. The recirculation zone considerably increases the boundary layer thickness (D) around the interaction location. This separation induced increase in local boundary layer thickness can amount to a considerable percentage of cross-section of a combustor duct.

2.4.1.3 Normal Shock Wave Boundary Layer Interaction

A further type of interaction is given by a normal shock wave impinging on a wall. As in the previous case, the effect of the sharp pressure gradient induced by the shock is spread over an interaction region within the viscosity-dominated near-wall region. Depending on the shock strength, the boundary layer either remains attached to the wall or separation occurs.

The left part of figure 2.2 shows the situation without separation. The normal shock (A) penetrates the boundary layer up to the sonic line (C) and induces a pressure increase within the boundary layer (D) leading in turn to an increase in its thickness. This continuous increase in boundary layer thickness serves as a smooth ramp causing a series of compression waves (B) ahead of the shock (A), such that the terminating compression wave degenerates to a sonic line.

In the case of boundary layer separation, sketched on the right hand side of figure 2.2, a separation region (F) forms within the boundary layer considerably increasing the boundary layer thickness. A system of weak shocks (B) forms close to the kink in the boundary layer caused by the separation. Since the system of weak shocks is not able to reproduce the pressure rise enforced by the strong shock, a rear shock (C) forms, which adjusts the pressure level according to the strong normal shock (A). However, this near-wall shock system induces a smaller entropy rise than the original shock. As a result, a mixing layer (E) forms in order to adapt both entropy levels behind the triple point (D), where the normal shock, the system of oblique shocks and the rear shock

meet.

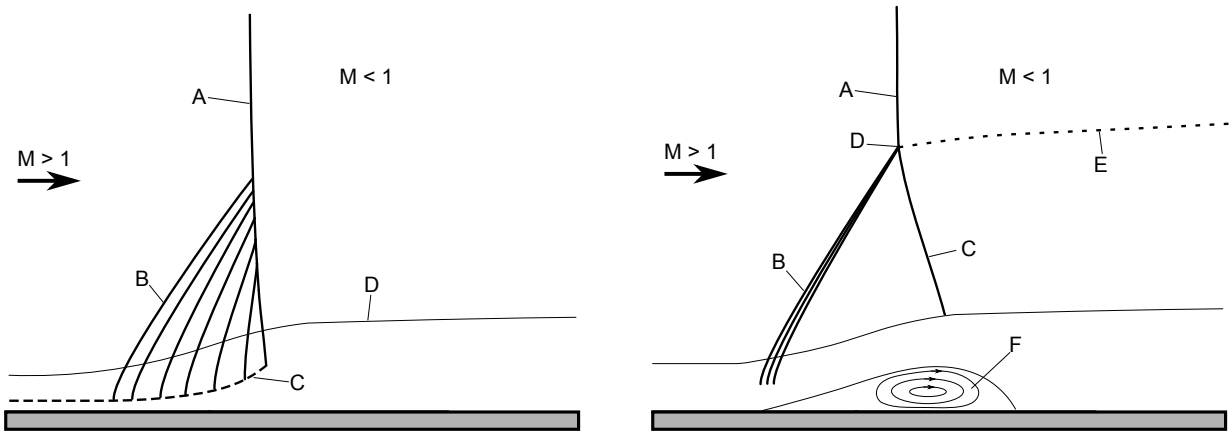

Figure 2.2: Normal shock boundary layer interaction without (left) and with boundary layer separation (right)

2.4.1.4 Shock Train

The combination of a thick boundary layer and a small height within a wall-confined duct can result in a particular transonic shock system called shock train, see figure 2.3. A shock train is a succession of subsonic and supersonic regions that produces considerable total pressure losses and leads to an extensive boundary layer growth.

Shock trains develop through the following mechanism: A strong shock interacts with the boundary layer, therefore increases the boundary layer thickness and reduces the Mach number to subsonic speeds behind the shock. However, the boundary layer growth continuously narrows the effective duct height and locally acts as a convergent nozzle re-accelerating the flow to supersonic speeds. This can cause a further normal shock in close distance downstream of the previous one. This second shock causes further growth of the boundary layer and again induces the nozzle effect. The succession of these subsonic and supersonic regions results in the structure sketched in figure 2.3. An important consequence is the obstruction of the channel due to the considerable increase of the boundary layer thickness.

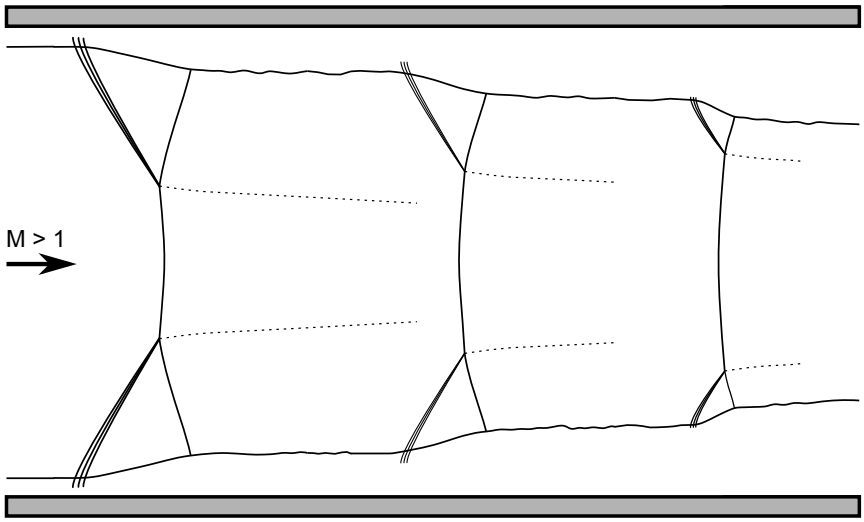

Figure 2.3: Shock train

2.4.2 Jet in Supersonic Crossflow

Several fuel injection strategies exist for supersonic combustion. An often encountered concept is the injection of fuel perpendicular to the main crossflow through circular injection holes. This basic setup can be further extended to cases with non-orthogonal injection [31]. Chapter 6 describes the simulation of an experimental jet in supersonic crossflow configuration of this type by means of RANS and hybrid RANS/LES. The fundamental phenomena related to the jet in supersonic crossflow setup are depicted in the schematic illustration given in figure 2.4.

Usually, the fuel injection pressure is high enough to establish sonic flow through the injector exit giving rise to a further acceleration to supersonic velocities after the exit. Obviously, this would not be the case, if the injection pressure was insufficient. Yet, this case does not have significant technological relevance, since this would result in very low fuel mass flow rates. For this reason, this case is omitted here and the fuel jet is assumed to be at underexpanded sonic conditions at the injection port exit.

The injected fuel jet constitutes an obstacle for the crossflow enforcing a highly three-dimensional bow shock (A) covering the injection region. As a consequence, a barrel shock (B) forms terminated by a Mach disk (C) [61].

The distribution of jet fluid follows the shape of the barrel shock and Mach disk in the vicinity of the injection port and extends slightly beyond the shock boundaries [70], see figure 2.4. Recirculation regions develop close to the wall upstream and downstream of the bow shock as well as behind the barrel shock. A counter-rotating vortex pair (E) forms in the wake of the shock barrel that dominates the fuel transport and mixing with the surrounding air further downstream [70]. The major portion of the injected fluid is entrained within this vortex pair after leaving the shock barrel [61, 70].

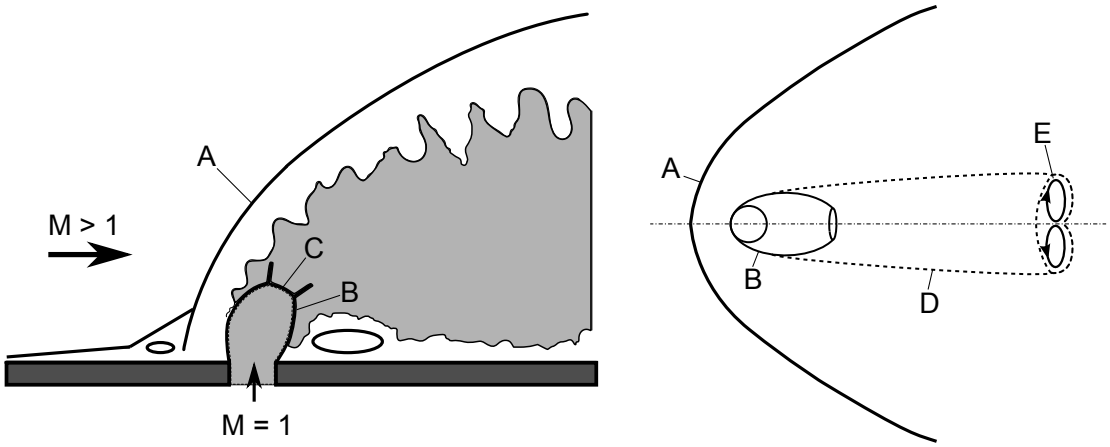

Figure 2.4: Simplified jet in supersonic crossflow configuration: A: bow shock induced by injection of fuel (light gray), B: barrel shock with Mach disk C, D: mean fuel jet width, E: counter-rotating vortex pair; side-view (left) and top view (right)

A characteristic parameter describing the jet in crossflow configuration is the ratio of the mass specific jet momentum and the mass specific momentum of the crossflow. This momentum ratio J is given in eq. 2.63. The larger the momentum ratio, the deeper is the anticipated jet penetration depth and impact on the crossflow.

$$J = \frac{\rho_{jet} U_{jet}^2}{\rho_{cross} U_{cross}^2} \tag{2.63}$$

3 Unsteady, Compressible Flow Solver for Transonic and Supersonic Combustion

A computational fluid dynamics solver was developed for the numerical research within this thesis. The solver is able to account for supersonic combustion processes and accompanying phenomena encountered in highly compressible flows [34, 90–92]. This chapter provides information about the following aspects of the implemented flow solver that rest upon the fundamentals given in chapter 2: Firstly, the discretization of the governing equations and related terms based on the finite volume method. Secondly, the description of the thermodynamic state of the involved chemical compounds. Thirdly, the formulation of appropriate closures for the unexplored turbulent terms derived for RANS and LES in terms of the mathematical representation and the chosen turbulence models. Finally, the utilized combustion model is explained and the influence of turbulence chemistry interaction modeling discussed.

As a basis, the implementation of a compressible, density-based solver for high-speed flows of Greenshields et al. [58] within the open-source CFD software package OpenFOAM [1] was taken and enhanced with finite-rate chemistry and multi-species transport. OpenFOAM constitutes a convenient framework for own implementations, due to its modular structure in the context of the programming language C++. The code published by Greenshields et al. implements the efficient yet accurate central-upwind spatial discretization scheme for convective fluxes by Kurganov et al. [76] based on the central scheme by Kurganov and Tadmor [77]. The spatial discretization is discussed in section 3.1.1 providing the justification for utilizing the implementation of Greenshields et al. as a basic framework. The explanation for the application of explicit time integration is provided in the subsequent section 3.1.2.

The reasons for choosing a density-based in contrast to a pressure-based solver are the following, see Ettner [39] for a comprehensible discussion: Pressure-based solvers coupled with implicit time integration provide an efficient simulation framework employing large time steps. However, they are highly dissipative especially at discontinuities, since second order pressure derivatives are included within the involved pressure-correction equation [39, 40]. Yet, the supersonic flows investigated within this work require the preferably exact resolution of compressible flow phenomena, essentially shock waves and expansion fans. In contrast to a pressure-based solver, a density-based approach does not include the highly diffusive spatial second order pressure derivatives and thus represents the more appropriate choice here [39].

Based on the aforementioned solver fundament by Greenshields et al., numerous additional features were implemented. The most important changes shall be summarized here: The transport equations for mass, momentum, species and total energy were implemented in the form provided in chapter 2 with appropriate closures for turbulent terms for RANS or LES, see table 2.1. The implementation of the species transport equations was accompanied by the incorporation of species diffusion, see section 3.2, and finite-rate chemistry, see section 3.5. The utilized turbulent closures for RANS and LES are discussed in sections 3.3 and 3.4 of this chapter. Within this context, especially the scale similarity LES model constitutes a relevant part of the implementation.

Moreover, a novel hybrid RANS/LES method was integrated in the form of an extended turbulence software library, which combines both turbulence modeling strategies as explained in chapter 4. In summary, the solver can be utilized in pure RANS, pure LES or in its hybrid RANS/LES mode. Furthermore, optional Runge-Kutta time integration was integrated, consistently including the turbulence model transport equations discussed in sections 3.3 and 3.4. All equations are implemented such that time integration is purely explicit, including the turbulence model equations. Finally, a novel model for combustion induced turbulence, see chapter 5 was developed and implemented. The user can thus choose between different turbulence modeling and time integration modes and can enable the novel model for combustion induced

turbulence based on input files defined prior to the simulation.

3.1 Discretization of Time and Space

3.1.1 Spatial Discretization

The governing equations derived for RANS and LES in chapter 2 are formulated in the context of the finite volume method allowing for a flexible spatial discretization also on unstructured computational grids [26,108]. For this purpose, the computational domain is split into a multitude of finite control volumes, which hold a discrete, local value for every variable defining the state of the flow represented by the state vector Z, see eq. 3.1. The governing equations are thereupon integrated over these finite volumes. Subsequently, the volume integrals are replaced by surface integrals on the basis of Gauss's divergence theorem. The actual discretization step is conducted through the replacement of the exact surface integrals by a summation over the discrete cell faces of each finite volume [26]. Yet, the cell face fluxes are not know and need to be computed based on the known field values at the cell centers. The approximation of cell face fluxes constitutes the centerpiece of the spatial discretization.

$$Z = \left(\rho, \rho U_i, \rho Y_k, \rho E\right)^T \tag{3.1}$$

Two major requirements for the convective cell face flux scheme can be identified: On the one hand, the scheme must be as little dissipative as possible in order to ensure that shock discontinuities are reproduced [39] and that the numerical viscosity does not dampen turbulent structures resolved in the LES mode of the solver [40]. On the other hand, the scheme must maintain a sufficient numerical stability at the same time. An established method fulfilling these requirements is given by the Riemann solver concept [39, 136]. Every cell face is treated as a discontinuity with different left and right states that are used to compute the actual cell face value based on the solution of the Riemann problem. Essentially, the Riemann problem constitutes an initial value problem given by a differential equation with discontinuous initial

conditions [136]. Yet, the flux computation in Riemann solvers is computationally expensive [77]. Initial investigations conducted for this thesis showed a considerable runtime increase by an order of magnitude based on the HLLC (Harten-Lax-van Leer-Contact) approximate Riemann solver [39, 135] in comparison to a simple, conventional central scheme.

Another type of discretization for the cell face fluxes was introduced by Kurganov et al. [76, 77], which does not require the expensive evaluation of the Riemann fluxes, but nevertheless meets the two requirements stated further above [77]. The initial idea of the upstream-centered discretization scheme by Kurganov et al. is similar to the Riemann solver, since every cell face is assigned a left and a right state, e.g. representing a shock wave discontinuity. The essence of the scheme is that it takes into account that information does not only travel in the direction of the flow velocity, but also in the direction of sound wave propagation [58, 76, 77]. The complexity of the flux computation is decisively reduced in comparison to a Riemann solver [77], since the only additional aspect in comparison to e.g. a conventional central scheme is the evaluation of the local speed of sound, see section 3.1.2.

The procedure exhibits nearly the same behavior as an actual Riemann solver for a one-dimensional shock tube problem [91] but requires less resources for the flux computation. For the stated reasons, the scheme by Kurganov et al. represents a reasonable choice for this work. The OpenFOAM solver developed by Greenshields et al. [58] implements this flux scheme, providing the motivation for the selection of this solver as a basic framework for the developments within this thesis as discussed at the beginning of this chapter. Additionally, the gamma flux limiter introduced by Jasak et al. [68] is imposed on the resulting convective fluxes. The limiter effectively switches from second to first order upwind accuracy in cells with high gradients, particularly if a shock wave is present and leads to a stabilization of the computations. Diffusive fluxes are computed based on linear interpolation [39].

In summary, the accuracy of the spatial discretization is of second order, locally of first order due to the flux limiters [68]. In the context of LES, second order spatial schemes paired with flux limiters have proven to perform well for LES of combustion problems [12, 50, 72]. Hence, it also appears adequate

to utilize this approach for the LES simulations within this work.

3.1.2 Temporal Discretization

The implemented solver is capable of explicit time integration utilizing either the Euler forward scheme or the classical fourth order Runge-Kutta scheme [32]. The computational time step is limited by the acoustic Courant-Friedrichs-Lewy (CFL) condition, cf. eq. 3.2, which provides an upper threshold value for the ratio of local convection of information and grid size.

$$CFL = \frac{(|u| + a)\,\Delta t}{\Delta x} < CFL_{max} \tag{3.2}$$

A limitation of the computational time step through the acoustic CFL number is necessary for two reasons: Firstly, the applied spatial discretization scheme by Kurganov et al. [76], see section 3.1.1, requires that information may not travel across more than one cell within one numerical time step for reasons of numerical stability [39]. Secondly, turbulent time scales must be resolved by the simulation requiring a time step in the range of the Kolmogorov time scale at least in the LES mode of the solver. Whereas the spatial resolution required for LES has been investigated by many researchers, the influence of the time resolution has not received as much attention. However, Choi and Moin report that low CFL numbers are required to provide a sufficient temporal resolution of turbulent structures [25, 117]. Their computational LES investigation required a time step smaller than the Kolmogorov time scale in order to maintain turbulent structures yielding a CFL number of less than one. For the given reasons, CFL condition limited explicit time integration is performed limiting the CFL number to values less or equal to 0.3 for the explicit Euler and 0.5 for the fourth order Runge-Kutta scheme.

The main benefit of implicit time integration is the possibility to employ large numerical time steps providing fast and thus efficient numerical simulations. Yet, the aforementioned need to maintain a small CFL number enforces time steps in the range between 1e-8 and 1e-9 s for the treated test cases in chapters

6, 7 and 8. This renders implicit time integration obsolete, since the time step could not be further increased.

3.2 Fluid Properties

Species enthalpies and specific heat capacities $c_{p,i}$ are computed with temperature dependent polynomials developed by Chase et al. [22], which are referred to as the joint army-navy-air force (JANAF) polynomials. The mixture viscosity is evaluated on the basis of Sutherland's law [26, 71], see eq. 3.3. The constants A_S and T_S are set to 1.458e-6 kg/(msK$^{1/2}$) and 110.4 K respectively.

$$\mu = A_S \frac{T^{3/2}}{T + T_S} \tag{3.3}$$

Individual species viscosities are taken into account by different Schmidt numbers [12, 16]. The Schmidt number settings are summarized in table 3.1 and applied to all simulations presented in this thesis. Realistically, the turbulent viscosities induced by turbulence models exceed and dominate the viscosity, such that the inaccuracy caused by this simplified approach is of marginal importance. Nevertheless, the diffusion of reactants obviously constitutes an existing effect, which can be easily incorporated into the flow solver at a barely noticeable increase in computational runtime. Moreover, species diffusion gains in importance with decreasing cell size in the case of LES, since the modeled subgrid turbulence scales with the grid spacing, see section 3.4.3. Both aspects provide the motivation for including the species diffusion in the flow solver. The species diffusion coefficients correspond to the viscosity divided by the individual Schmidt numbers as explained above, see eq. 3.4. Heat conductivity is computed on the basis of the viscosity scaled with the inverse of the Prandtl number, see eq. 3.5 [71].

$$D_i = \frac{\mu}{\rho Sc_i} \tag{3.4}$$

Table 3.1: List of species Schmidt numbers

	O_2	H	OH	O	H_2	H_2O	N_2	HO_2	H_2O_2
Sc_i	0.99	0.17	0.65	0.64	0.28	0.77	0.87	0.65	0.65

$$\lambda = \frac{\mu c_p}{Pr} \tag{3.5}$$

3.3 RANS Turbulence Modeling

3.3.1 Discussion of the Model Approach

The ensemble averaged governing equations underlying the RANS approach have been derived in section 2.2.1. The result of the density weighted averaging procedure is the appearance of unclosed correlations between fluctuations of the transported fields. These correlations represent the influence of transient turbulent transport on the mean fields. The continuity equation does not contain any unclosed terms due to the introduction of the Favre average, see eq. 2.31. On the contrary, the momentum, species and energy transport equations eqs. 2.32, 2.33 and 2.43 require the closure of the unknown turbulent correlation terms $T_{R,U}$, $T_{R,Y}$ and $T_{R,E}$ given in eqs. 3.6a, 3.8a and 3.9.

Different classes of RANS turbulence models have been developed over the years, which can be roughly put in two categories: Eddy viscosity type turbulence models and second order closure Reynolds stress models [26]. Eddy viscosity type models replace the unknown turbulent correlation terms with model expressions that incorporate an artificial viscosity. This additional, turbulent viscosity is supposed to induce the effects of turbulent transport through a considerable increase of diffusivity within the respective transport equations, which usually notably exceeds the molecular diffusion. Models developed for the purpose of computing the turbulent viscosity are based either on a purely algebraic approach or on additional equations transporting quantities that shall represent the statistic effects of turbulence. Most established

turbulence models for RANS rest upon the solution of usually two additional transport equations, since they provide information about the history and local development of turbulent motions. Two transport equations are favorable over only one, since they provide the possibility to predict the local turbulent kinetic energy on the one hand and its rate of decay on the other hand [144].

As opposed to eddy viscosity models, Reynolds stress type closures directly compute the components of the unresolved stresses based on the Reynolds stress transport equations, which can be derived from the Navier-Stokes equations [40, 67]. Considering the momentum transport equations, six additional model transport equations are solved for the six unknown Reynolds stress components plus at least one transport equation representing the decay of turbulence. However, those equations introduce additional unclosed terms, which in turn need further models for their computation. If Reynolds stress models are to be utilized also for the remaining transported fields, additional transport equations are necessary. Although their higher level of complexity and therefore higher computational cost, Reynolds stress models not always considerably exceed results obtained with two-equation eddy viscosity models [40, 99]. Furthermore, numerous computational investigations of supersonic combustion have shown that nominally simpler eddy viscosity type RANS models yield a very satisfactory prediction of experimental data [47, 54, 140]. For the stated reasons, an eddy viscosity type RANS model is chosen for the work presented in this thesis. The mathematical closure formulations for the unresolved turbulent terms are provided and justified in the following before the actual model utilized to compute the turbulent viscosity is discussed.

3.3.2 Formulation of RANS Turbulence Closure Terms

The turbulent momentum transport term $T_{R,U}$ in eq. 3.6a was previously derived as the right hand side of the Favre averaged momentum transport equation eq. 2.32. Essentially, the product of uncorrelated velocity fluctuations can be regarded as an additional, turbulent stress $\tau_{ij,t}$ acting on the fluid, see eq. 3.6b. The conventional way to model the turbulent stress $\tau_{ij,t}$ by means of

an eddy viscosity closure is to utilize Stokes' hypothesis for the shear stress, see eq. 2.3 and apply an additional viscosity μ_t [26, 71, 144]. The approach is called the Boussinesq approximation and the resulting formula is given in eq. 3.7a. Hence, the structure of the turbulent stress is supposed to be the same as for the shear stress. Now, the aspect of turbulence modeling is transfered to the modeling of the turbulent viscosity μ_t, being the outcome of the eddy viscosity turbulence model. A common approximation is made by neglecting the last term of eq. 3.7a yielding eq. 3.7b [111, 144].

$$T_{R,U} = -\frac{\partial(\overbrace{\overline{\rho} U_i'' U_j''}^{\sim})}{\partial x_j} \tag{3.6a}$$

$$\approx \frac{\partial \tau_{ij,t}}{\partial x_j} \tag{3.6b}$$

$$\tau_{ij,t} = \mu_t \left(\left(\frac{\partial \widetilde{U_i}}{\partial x_j} + \frac{\partial \widetilde{U_j}}{\partial x_i} \right) - \frac{2}{3} \frac{\partial \widetilde{U_k}}{\partial x_k} \right) - \frac{2}{3} \overline{\rho} k \delta_{ij} \tag{3.7a}$$

$$\approx \mu_t \left(\left(\frac{\partial \widetilde{U_i}}{\partial x_j} + \frac{\partial \widetilde{U_j}}{\partial x_i} \right) - \frac{2}{3} \frac{\partial \widetilde{U_k}}{\partial x_k} \right) \tag{3.7b}$$

The unclosed term $T_{R,Y}$ on the right hand side of the species transport equation eq. 2.33 contains the correlation between turbulent fluctuations of velocity and chemical compound mass fractions. In order to derive a closure approximation for this term, an analogous conceptual transfer can be established as previously done for the turbulent stress tensor $\tau_{ij,t}$: The gradient approach to species diffusion embodied by Fick's law is utilized and enhanced with a turbulent species diffusivity D_t, see eq. 3.8b. Now, D_t requires a closure formulation, which is provided by the turbulent viscosity μ_t previously utilized for the turbulent stress tensor computation, scaled with the turbulent Schmidt number Sc_t, cf. eq. 3.8c.

$$T_{R,Y} = -\frac{\partial\left(\overline{\rho}\widetilde{Y_i''U_j''}\right)}{\partial x_j} \tag{3.8a}$$

$$\approx \frac{\partial}{\partial x_j}\left(D_t\frac{\partial\widetilde{Y_i}}{\partial x_j}\right) \tag{3.8b}$$

$$= \frac{\partial}{\partial x_j}\left(\frac{\mu_t}{Sc_t}\frac{\partial\widetilde{Y_i}}{\partial x_j}\right) \tag{3.8c}$$

In contrast to the momentum and species transport equations, the Favre averaging of the energy transport equation generates a multitude of unclosed terms, see eq. 3.9. The term $T^I_{R,E}$ embodies the turbulent transport of chemical energy due to the turbulent convection of chemical compounds. Essentially, the formulation for this term is already provided by the closure for the turbulent species transport in eq. 3.8c. Therefore, the closure for $T^I_{R,E}$ is given by eq. 3.10 being the product of the turbulent species flux and the respective species enthalpy of formation.

$$\begin{aligned}
T_{R,E} = &-\frac{\partial}{\partial x_j}\left(\overbrace{\overline{\rho}h_c''U_j''}^{T^I_{R,E}} + \overbrace{\overline{\rho}e_s''U_j''}^{T^{II}_{R,E}} + \overbrace{\overline{\rho}\widetilde{U_i}U_i''U_j''}^{T^{III}_{R,E}} + \overbrace{\overline{\rho}\frac{1}{2}U_i''U_i''U_j''}^{T^{IV}_{R,E}} + \overbrace{\overline{\rho}\frac{1}{2}\widetilde{U_j}U_i''U_i''}^{T^{V}_{R,E}}\right) \\
&+ \frac{\partial}{\partial x_j}(\overbrace{\tau_{ij}U_i''}^{T^{VI}_{R,E}}) - \frac{\partial}{\partial x_j}(\overbrace{\overline{p}U_j''}^{T^{VIIa}_{R,E}}) - \frac{\partial}{\partial x_j}(\overbrace{p'U_j''}^{T^{VIIb}_{R,E}}) \\
&+ \frac{\partial}{\partial x_j}\left(\overbrace{\check{\lambda}\frac{\partial\overline{T''}}{\partial x_j}}^{T^{VIII}_{R,E}} + \overbrace{\sum_{k=1}^{N_{sp}}(\overline{\rho}\check{D}_k(h_{c,k}'' + h_{s,k}'')\frac{\partial Y_k''}{\partial x_j})}^{T^{IX}_{R,E}}\right)
\end{aligned} \tag{3.9}$$

$$T^{I}_{R,E} \approx -\sum_{k=1}^{N_{sp}} \left(h_{c,k} \frac{\mu_t}{Sc_t} \frac{\partial \widetilde{Y_k}}{\partial x_j} \right) \tag{3.10}$$

The turbulent transport of sensible energy denoted by $\mathrm{T}^{II}_{R,E}$ is modeled on the basis of two contributions. Firstly, a conventional gradient closure is applied linking the spatial derivative of the temperature field to the turbulent heat flux [26, 53, 71, 144], cf. eq. 3.11. Thus, similarly to the previous cases, the turbulence closure model is motivated by the laminar counterpart, here it is Fourier's law of heat transport. The turbulent viscosity μ_t initially utilized for the Boussinesq approximation again appears as a part of the turbulent diffusion coefficient. Furthermore, μ_t is multiplied with the isobaric specific heat capacity c_p and scaled with the turbulent Prandtl number. Moreover, $\check{T}$ denotes the computable temperature evaluated at the conditions provided by the Favre averaged mean field. The application of the isobaric specific heat capacity c_p instead of solely the isochoric specific heat capacity c_v incorporates an approximation for the work conducted by the turbulent velocity fluctuations against the averaged pressure $\mathrm{T}^{VIIa}_{R,E}$. The second contribution is due to the enthalpy change induced by the turbulent transport of chemical compounds featuring varying internal energies. This second closure term for the sum of $\mathrm{T}^{II}_{R,E}$ and $\mathrm{T}^{VIIa}_{R,E}$ is essentially given by the turbulent species transport multiplied by the respective computable species internal enthalpy $\check{h}_{s,k}$. The enthalpy needs to be considered here instead of the energy, since the transport of species across control volume boundaries is tied to work [71]. The complete closure for the sum of $\mathrm{T}^{II}_{R,E}$ and $\mathrm{T}^{VIIa}_{R,E}$ is provided by eq. 3.11.

$$T^{II}_{R,E} + T^{VIIa}_{R,E} \approx -\mu_t \frac{c_p}{Pr_t} \frac{\partial \check{T}}{\partial x_j} - \sum_{k=1}^{N_{sp}} \left(\check{h}_{s,k} \frac{\mu_t}{Sc_t} \frac{\partial \widetilde{Y_k}}{\partial x_j} \right) \tag{3.11}$$

The terms $\mathrm{T}^{III}_{R,E}$, $\mathrm{T}^{IV}_{R,E}$ and $\mathrm{T}^{V}_{R,E}$ arise due to the Favre averaging of the kinetic energy convection term, see eqs. 2.34 and 2.39. $\mathrm{T}^{IV}_{R,E}$ and $\mathrm{T}^{V}_{R,E}$ represent the turbulent and convective transport of turbulent kinetic energy respectively. Term $\mathrm{T}^{III}_{R,E}$ can be identified as the work contributed by the turbulent stress $\tau_{ij,t}$, hence its closure is straightforward and given in eq. 3.12.

$$T_{R,E}^{III} \approx -\tau_{ij,t}\widetilde{U_i} \tag{3.12}$$

Moreover, the turbulent transport of turbulent kinetic energy represented by term $\mathrm{T}_{R,E}^{IV}$ and the turbulent molecular diffusion $\mathrm{T}_{R,E}^{VI}$ are neglected according to Wilcox [144]. Furthermore, a separate transport equation for the turbulent kinetic energy is solved and the result subtracted from the energy available for the remaining forms of energy corresponding to eq. 2.36, hence, also the convective term $\mathrm{T}_{R,E}^{V}$ is neglected. Also the correlation between the pressure and velocity fluctuations $\mathrm{T}_{R,E}^{VIIb}$ is neglected. Finally, the turbulent contributions to the molecular heat fluxes $\mathrm{T}_{R,E}^{VIII}$ and $\mathrm{T}_{R,E}^{IX}$ are also ignored. Effectively, this means that the filtered laminar heat flux $\widetilde{q}$ is approximated by the computable heat flux $\check{q}$.

3.3.3 RANS Turbulence Model Choice

The most prominent eddy viscosity RANS model is the k-ϵ model [26, 109, 110] including a transport equation for the turbulent kinetic energy k and an equation for its dissipation rate ϵ. Another successful and thus often encountered model is the k-ω model by Wilcox et al. [144], which utilizes a transport equation for the kinetic energy specific dissipation rate ω instead of the dissipation rate ϵ. On the one hand, the k-ϵ model has proven to be reliable in a variety of applications. On the other hand, the k-ω model is superior concerning the prediction of near wall regions [110] and boundary layers. In particular, Wilcox showed that the k-ω model features good predictions of shock wave/boundary layer interactions, being a necessary prerequisite for the solution of the problems discussed in this thesis [144]. Furthermore, Menter [95, 96] proposed a model known as the shear stress transport (SST) model, which is intended to combine the advantages of the k-ϵ and k-ω models. Basically, the SST model blends between the k-ϵ and k-ω models such that the near wall regions are treated with the k-ω part. Due to its promising capabilities to reliably predict the statistical effects of turbulence in both the near wall regions and mixing regions in the core of the flow, the SST model is utilized to compute the RANS

eddy viscosity μ_t within this thesis.

The SST model transport equations for the turbulent kinetic energy k and the energy specific dissipation rate of turbulent kinetic energy ω are given in eqs. 3.13 and 3.14. Note that $\tau_{ij,t}$ is utilized in its exact form based on eq. 3.7a. The function F_1 blends between the k-ϵ and k-ω model constants yielding the SST specific model constants β, β^*, σ_ω, σ_k and γ on the basis of eq. 3.15. The utilized model constants being the basis for this blending are listed in table 3.2.

$$\frac{\partial(\overline{\rho}k)}{\partial t} + \frac{\partial(\overline{\rho}k\widetilde{U_j})}{\partial x_j} = \tau_{ij,t}\frac{\partial\widetilde{U_i}}{\partial x_j} - \beta^*\overline{\rho}\omega k + \frac{\partial}{\partial x_j}\left((\mu + \sigma_k\mu_t)\frac{\partial k}{\partial x_j}\right) \tag{3.13}$$

$$\begin{aligned}\frac{\partial(\overline{\rho}\omega)}{\partial t} + \frac{\partial(\overline{\rho}\omega\widetilde{U_j})}{\partial x_j} = \gamma\frac{\overline{\rho}}{\mu_t}\tau_{ij,t}\frac{\partial\widetilde{U_i}}{\partial x_j} - \beta\overline{\rho}\omega^2 + \frac{\partial}{\partial x_j}\left((\mu + \sigma_\omega\mu_t)\frac{\partial\omega}{\partial x_j}\right) \\ + 2\overline{\rho}(1-F_1)\sigma_{\omega 2}\frac{1}{\omega}\frac{\partial k}{\partial x_j}\frac{\partial\omega}{\partial x_j}\end{aligned} \tag{3.14}$$

$$\Phi = F_1\Phi_1 + (1-F_1)\Phi_2 \tag{3.15}$$

Finally, the SST model formulation of the searched-for turbulent viscosity μ_t is provided by eq. 3.16. Within this context, F_2 denotes a second blending function and Ω represents the magnitude of the vorticity field $\nabla x\vec{U}$. The equations

Table 3.2: SST model constants

	Φ_1	Φ_2
β^*	0.09	0.09
β	0.075	0.0828
σ_ω	0.5	0.85616
σ_k	0.85034	1.0
γ	0.5532	0.4403

determining the blending functions F_1 and F_2 can be found in the work by Menter [96].

$$\mu_t = \min\left(\frac{\overline{\rho}k}{\omega}, \frac{a_1\overline{\rho}k}{\Omega F_2}\right) \tag{3.16}$$

Now, based on the mathematical formulation of the closure terms in the previous section and the formulation of the turbulent viscosity μ_t provided here, the turbulent correlation terms within the Favre ensemble averaged governing equations are closed.

3.4 LES Turbulence Modeling

3.4.1 Discussion of the Model Approach

The spatially filtered governing equations being the fundament for LES were derived in section 2.2.2. As a result of the spatial scale separation, a multitude of unclosed terms appears requiring adequate closure approximations. Yet, the subject of the filtering itself needs to be discussed, before the topic of an adequate turbulence model describing the subgrid scales is addressed.

The computational mesh utilized as a basis for the spatial discretization of the simulated domain, automatically serves as a spatial filter in the context of eq. 2.44. This is intuitively evident, since structures being smaller than the grid size cannot be resolved. The filter function $G(\vec{x}-\vec{\xi})$ originating in the computational mesh effectively represents a box or tophat filter defined by eq. 3.17.

$$G(\vec{x}-\vec{\xi}) = \begin{cases} \frac{1}{\Delta} & \text{, if } \left|\vec{x}-\vec{\xi}\right| \leq \frac{\Delta}{2} \\ 0 & \text{, else} \end{cases} \tag{3.17}$$

Hence, a large eddy simulation can be performed by refining the mesh to an adequate level, such that relevant turbulent structures are resolved while subgrid structures are truncated. Such an approach based on the mesh filter is termed implicit filtering. However, realistic computational grids usually vary significantly across the simulated domain. Hence, the filter width is not constant resulting in an uncertainty about the wave length at which the scale separation occurs. In order to remedy this issue, an explicit filter might be applied providing a homogeneous and more definite scale separation [85]. Yet, this comes at the cost of a reduction of the effective filter width meaning that the ability of the computational mesh to resolve turbulent structures is not fully exploited [62]. For this reason, implicit filtering is utilized within this work in order to maintain a reasonable level of computational cost. Explicit filtering is solely applied in the context of subgrid scale modeling, as discussed in the following.

LES requires the modeling of turbulence solely at the subgrid scales truncated by the LES filter. The unresolved subgrid turbulence draws energy from the larger, resolved structures and therefore accounts for the decay of turbulence. The latter aspect provides the pragmatic purpose of the LES turbulence model. Several possibilities exist in order to provide the necessary level and structure of the turbulent subgrid dissipation, which can be roughly put in two categories: functional and structural LES models. The fundament of functional LES models is the assumption, that the influence of subgrid turbulence is mainly due to the energy transfer finally resulting in the just mentioned dissipation of turbulence. On the other hand, structural models try to reproduce the anisotropy and spatial orientation of turbulence, which go beyond the integral treatment of turbulence as an energy sink, see section 3.4.3 and Sagaut [117] for a discussion.

Apart from the inherent property of LES to resolve large scale turbulence, LES features an additional advantage over RANS with respect to the modeling of unclosed turbulent terms. This advantage is given by the triple decomposition introduced in section 2.2.2 and given by eq. 2.54. The decomposition into additional terms might appear valueless at the first place. However, it provides a separation into three different types of turbulent contributions: Firstly, the

Leonard term L_{ij} being composed of computable values. Secondly, the cross-term C_{ij} represents the interaction of resolved eddy scales and unresolved scales. Finally, the last component R_{ij} embodies the effect of unresolved turbulence on the subgrid scale.

Now, this separation can be utilized to create a structural turbulence model for LES assuming that the largest non-resolved scales have a similar structure to the smallest resolved scales as introduced by Bardina et al. [6,7,46,109,117]. The essence of this model is the second application of the LES filter such that the cross term and Reynolds stress term are modeled as the difference between the product of filtered fields minus the product of twice-filtered fields. This finally results in a model expression for the cross and Reynolds stress terms C_{ij} and R_{ij} as shown in eq. 3.18 in terms of the generic fields ϕ and ψ, see Sagaut et al. [117] for a derivation.

$$R_{ij} + C_{ij} \approx \widetilde{\phi}\widetilde{\psi} - \widetilde{\widetilde{\phi}}\widetilde{\widetilde{\psi}} \tag{3.18}$$

Based on the model expression for the sum of C_{ij} and R_{ij}, the triple decomposition from eq. 2.54 can be reformulated in terms of known quantities, see eq. 3.19a. This can be further simplified to eq. 3.19b, such that the complete subgrid stress tensor being the sum of Leonard, cross and Reynolds stresses is modeled as the difference between the filtered product of filtered (and therefore computable) fields and the product of twice-filtered fields.

The scale similarity procedure can be generalized to a generic second filter and therefore second cutoff scale as proposed by Liu et al. [84, 117]. This generalization results in eq. 3.19c, where the second model filter is denoted by the arc symbol. Moreover, eqs. 3.18 and 3.19 describe rather a general procedure than a specific model in a similar way as the eddy viscosity constitutes a concept for the modeling of turbulence, not a specific model.

$$\widetilde{\phi\psi} \approx \widetilde{\phi}\widetilde{\psi} + \left(\overbrace{\widetilde{\widetilde{\phi}\widetilde{\psi}} - \widetilde{\phi}\widetilde{\psi}}^{L_{ij}} + \widetilde{\phi}\widetilde{\psi} - \widetilde{\widetilde{\phi}}\widetilde{\widetilde{\psi}} \right) \tag{3.19a}$$

$$= \widetilde{\phi}\widetilde{\psi} + \left(\widetilde{\widetilde{\phi}\widetilde{\psi}} - \widetilde{\widetilde{\phi}}\widetilde{\widetilde{\psi}} \right) \tag{3.19b}$$

$$\approx \widetilde{\phi}\widetilde{\psi} + \left(\widehat{\widetilde{\phi}\widetilde{\psi}} - \widehat{\widetilde{\phi}}\widehat{\widetilde{\psi}} \right) \tag{3.19c}$$

Despite the compelling feature of the scale similarity procedure to deduce information about subgrid scales from the resolved scales, the problem with this model type is the general underestimation of subgrid viscosity as reported by various authors [40, 82, 109, 117]. An option to remedy this issue is to combine the structural scale similarity model with a functional eddy viscosity type model resulting in a so-called mixed model [46, 109, 117]. Essentially, the mixed model closure for a Favre filtered product of two generic fields is given by eq. 3.20. Here, μ_{SGS} denotes the eddy viscosity of unresolved turbulence at the subgrid level, which is subject to the eddy viscosity turbulence model part.

$$\widetilde{\phi\psi} - \widetilde{\phi}\widetilde{\psi} \approx \left(\widehat{\widetilde{\phi}\widetilde{\psi}} - \widehat{\widetilde{\phi}}\widehat{\widetilde{\psi}} \right) + \mu_{SGS} f(\phi, \psi) \tag{3.20}$$

Bensow and Fureby [11] provide further detailed information about the application of mixed models. In particular, Berglund et al. showed that mixed models have the capability of successfully predicting scramjet combustion in the context of LES [12]. Therefore, this model type constitutes a reasonable choice for the simulation of supersonic combustion and is utilized as a basis for the LES turbulence model within this thesis.

3.4.2 Formulation of LES Turbulence Closure Terms

Based on the generic mixed model formulation given in eq. 3.20, the closures for the turbulent terms $T_{L,U}$, $T_{L,Y}$ and $T_{L,E}$ within the Favre filtered momentum, species and energy transport equations eq. 2.55, 2.56 and 2.60 can be formulated. Beginning with the momentum transport equation, the model expression for the subgrid stress given in eq. 3.21b is comprised of the scale similarity closure part and the Boussinesq stress tensor approximation previously introduced in the context of RANS modeling and represented by the subgrid scale stress tensor $\tau_{ij,SGS}$, see eq. 3.7. The latter incorporates the eddy viscosity μ_{SGS} of the unresolved subgrid scales, which requires further modeling.

$$T_{L,U} = -\frac{\partial}{\partial x_j}\left(\widehat{\rho}\left(\overbrace{\widetilde{\widetilde{U_i}\widetilde{U_j}-\widetilde{U_i}\widetilde{U_j}}}^{L_{ij}^U}+\overbrace{\widetilde{\widetilde{U_i}U_j''+U_i''\widetilde{U_j}}}^{C_{ij}^U}+\overbrace{\widetilde{U_i''U_j''}}^{R_{ij}^U}\right)\right) \tag{3.21a}$$

$$\approx -\frac{\partial}{\partial x_j}\left(\widehat{\rho}\left(\widetilde{\widetilde{U_i}\widetilde{U_j}}-\widetilde{\widetilde{U_i}}\widetilde{\widetilde{U_j}}\right)\right)+\frac{\partial}{\partial x_j}\left(\overbrace{\mu_{SGS}\left(\left(\frac{\partial\widetilde{U_i}}{\partial x_j}+\frac{\partial\widetilde{U_j}}{\partial x_i}\right)-\frac{2}{3}\frac{\partial\widetilde{U_k}}{\partial x_k}\right)}^{\tau_{ij,SGS}}\right) \tag{3.21b}$$

An equivalent closure approximation can be formulated for the unresolved turbulence term $T_{L,Y}$ within the species transport equation, see eq. 3.22. The eddy viscosity type closure part features the same structure as the RANS closure for this term previously introduced in eq. 3.8. The difference is the eddy viscosity, which needs to be evaluated only for the subgrid scales in terms of a LES subgrid scale model.

$$T_{L,Y} = -\frac{\partial}{\partial x_j}\left(\widehat{\rho}\left(\overbrace{\widetilde{Y_i}\widetilde{U_j} - \widetilde{Y_i}\widetilde{U_j}}^{L_{ij}^Y} + \overbrace{\widetilde{Y_i U_j}'' + \widetilde{Y_i}'' \widetilde{U_j}}^{C_{ij}^Y} + \overbrace{\widetilde{Y_i}'' U_j''}^{R_{ij}^Y}\right)\right) \tag{3.22a}$$

$$\approx -\frac{\partial}{\partial x_j}\left(\widehat{\rho}\left(\widetilde{\widetilde{Y_i}\widetilde{U_j}} - \widetilde{\widetilde{Y_i}}\widetilde{\widetilde{U_j}}\right)\right) + \frac{\partial}{\partial x_j}\left(\frac{\mu_{SGS}}{Sc_t}\frac{\partial \widetilde{Y_i}}{\partial x_j}\right) \tag{3.22b}$$

Concerning the energy transport equation, a multitude of unclosed terms appears requiring model approximations, see eq. 3.23. Instead of writing out the unclosed contributions in terms of all their components as done for the Favre averaged energy transport equation turbulent terms, see. eq. 3.9, $T_{L,E}$ is written in the triple decomposition form. This directly provides the justification for the previously introduced closure approximation based on the scale similarity ansatz.

$$\begin{aligned} T_{L,E} = &-\frac{\partial}{\partial x_j}(\overbrace{\widehat{\rho}(L_{ij}^{h_c} + C_{ij}^{h_c} + R_{ij}^{h_c})}^{T_{L,E}^I}) - \frac{\partial}{\partial x_j}(\overbrace{\widehat{\rho}(L_{ij}^{e_s} + C_{ij}^{e_s} + R_{ij}^{e_s})}^{T_{L,E}^{II}}) \\ &- \frac{\partial}{\partial x_j}(\overbrace{\widehat{\rho}(L_{ij}^{e_k} + C_{ij}^{e_k} + R_{ij}^{e_k})}^{T_{L,E}^{III}}) \\ &- \frac{\partial}{\partial x_j}(\overbrace{L_{ij}^{p} + C_{ij}^{p} + R_{ij}^{p}}^{T_{L,E}^{IV}}) + \frac{\partial}{\partial x_j}(\overbrace{L_{ij}^{\tau} + C_{ij}^{\tau} + R_{ij}^{\tau}}^{T_{L,E}^{V}}) \end{aligned} \tag{3.23}$$

The subgrid contribution to the transport of chemical energy h_c denoted by $T_{L,E}^I$ is given by the closure for the turbulent species transport in eq. 3.22b, since it is the turbulent interchange of chemical compounds that leads to $T_{L,E}^I$. Hence, the closure formulation is straightforward and obtained by multiplying the turbulent species flux from eq. 3.22b with the chemical enthalpy of the respective species, see eq. 3.24.

$$T_{L,E}^{I} \approx \sum_{k=1}^{N_{sp}} \left(h_{c,k} \widehat{\rho} \left(\widetilde{\widetilde{Y_i} \widetilde{U_j}} - \widetilde{\widetilde{Y_i}} \widetilde{\widetilde{U_j}} \right) \right) - \sum_{k=1}^{N_{sp}} \left(h_{c,k} \frac{\mu_{SGS}}{Sc_t} \frac{\partial \widetilde{Y_i}}{\partial x_j} \right) \tag{3.24}$$

Furthermore, the turbulent transport of internal energy $\mathrm{T}_{L,E}^{II}$ is likewise modeled based on the scale similarity and eddy viscosity contributions. The scale similarity closure is composed of two elements: Firstly, the turbulent energy transport due to the turbulent mixing of the entirety of the fluid, secondly, the turbulent sensible energy mixing caused by the local change of species composition due to turbulent species mixing. The latter happens on top of the bulk transport and therefore needs to be considered separately. The bulk eddy viscosity closure part is based on the local temperature gradient and scaled with the subgrid scale eddy viscosity μ_{SGS}. Furthermore, the enthalpy flux due to species mixing originating in the eddy viscosity closure part for the turbulent species transport from eq. 3.22b is added to the eddy viscosity closure. The pressure contribution $\mathrm{T}_{L,E}^{IV}$ is approximated by formulating the closure for $\mathrm{T}_{L,E}^{II}$ in terms of the enthalpy. Finally, the closure approximation for $\mathrm{T}_{L,E}^{II}$ and $\mathrm{T}_{L,E}^{IV}$ is given in eq. 3.25.

$$\begin{aligned} T_{L,E}^{II} + T_{L,E}^{IV} \approx & \sum_{k=1}^{N_{sp}} \left(\check{e}_{s,k} \widehat{\rho} \left(\widetilde{\widetilde{Y_i} \widetilde{U_j}} - \widetilde{\widetilde{Y_i}} \widetilde{\widetilde{U_j}} \right) \right) + \widehat{\rho} \left(\widetilde{\widetilde{e_s} \widetilde{U_j}} - \widetilde{\widetilde{e_s}} \widetilde{\widetilde{U_j}} \right) \\ & - \mu_{SGS} \frac{c_p}{Pr_t} \frac{\partial \check{T}}{\partial x_j} - \sum_{k=1}^{N_{sp}} \left(\check{e}_{s,k} \frac{\mu_{SGS}}{Sc_t} \frac{\partial \widetilde{Y_i}}{\partial x_j} \right) \end{aligned} \tag{3.25}$$

Next, the unclosed correlations for the turbulent transport of kinetic energy $\mathrm{T}_{L,E}^{III}$ need to be approximated, see also eq. 2.59. Here, a triple product of the velocity field appears leading to additional cross-terms compared to the triple decomposition from eq. 2.54. In order to remedy this issue, the filtered kinetic energy is approximated by the product of filtered velocities, see eq. 3.26. The latter simplification can be regarded as a consequent application of the assumption underlying the scale similarity procedure, see eq. 3.18. Eq. 3.26 allows to reduce the complex triple product from eq. 2.59 to the already introduced decomposition of two filtered fields. Hence, the scale similarity closure

part of $T_{L,E}^{III}$ can be finally expressed by the first term in eq. 3.27. The second term in eq. 3.27 is the product of the subgrid shear stress with the velocity representing the eddy viscosity closure part of $T_{L,E}^{III}$. Finally, term $T_{L,E}^{V}$ is disregarded, since it is assumed that the contribution of work originating in the interaction between turbulent fluctuations and the molecular stress τ_{ij} is negligible [111, 144].

$$\widetilde{U_i U_i} \approx \widetilde{U_i}\widetilde{U_i} \tag{3.26}$$

$$\begin{aligned} T_{L,E}^{III} \approx \widehat{\rho}\left(\widetilde{\widetilde{U_i}\widetilde{U_i}\widetilde{U_j}} - \widetilde{\widetilde{U_i}\widetilde{U_i}}\widetilde{\widetilde{U_j}}\right) \\ - \mu_{SGS}\left(\left(\frac{\partial\widetilde{U_i}}{\partial x_j} + \frac{\partial\widetilde{U_j}}{\partial x_i}\right) - \frac{2}{3}\frac{\partial\widetilde{U_k}}{\partial x_k}\right)\widetilde{U_i} \end{aligned} \tag{3.27}$$

3.4.3 LES Turbulence Model Choice

Finally, the mathematical formulation of the closure approximation terms for the Favre filtered governing equations is complete. Two aspects remain: Firstly, an appropriate model formulation for the turbulent eddy viscosity of the subgrid scales μ_{SGS} must be chosen. Secondly, a test filter for the scale similarity model needs to be specified.

Historically, the most famous LES model is the Smagorinsky model developed in the earliest stages of LES [122]. Essentially, algebraic models of the Smagorinsky type assume equilibrium between the production and dissipation of subgrid turbulent kinetic energy. However, this is not always a good approximation [94]. Generally, it is desirable to incorporate the non-local development of subgrid turbulence. For the same reason, namely the prediction of the non-local evolution of turbulence, a two-equation model was chosen for the computation of the turbulent viscosity in the RANS case. Hence, it appears favorable to choose a model incorporating at least one transport equation also for LES. A foundation for LES models of this type can be e.g. found in

the one-equation turbulent eddy viscosity model by Schumann [120], which utilizes a transport equation for the subgrid kinetic energy. Several variants of this model equation exist utilizing varying constants, whereas the differences in the results appear to be rather marginal [102]. The utilized model equation for the subgrid kinetic energy adapted for compressible flows is given in eq. 3.28 and is based on the model by Yoshizawa and Horiuti [146] and the work of Menon et al. [94]. The searched-for subgrid turbulent viscosity μ_{SGS} is given by eq. 3.29. The model constants C_ϵ and C_k are set to 1.048 and 0.094. Generally, the grid size measure Δ is represented by the cube root of the local cell volume.

$$\frac{\partial(\overline{\rho}k_{SGS})}{\partial t} + \frac{\partial(\overline{\rho}k_{SGS}\widetilde{U_j})}{\partial x_j} = \frac{\partial}{\partial x_j}\left((\mu+\mu_{SGS})\frac{\partial k_{SGS}}{\partial x_j}\right) + \tau_{ij,SGS}\frac{\partial \widetilde{U_i}}{\partial x_j} - C_\epsilon\overline{\rho}\frac{{k_{SGS}}^{\frac{3}{2}}}{\Delta} \tag{3.28}$$

$$\mu_{SGS} = C_k\overline{\rho}\sqrt{k_{SGS}}\Delta \tag{3.29}$$

Furthermore, the additional filter necessary for the similarity model part of the mixed model is based on an averaging of the cell face values for every computational cell. This effectively reduces the mesh resolution and corresponds to the application of a spatial filter. The cell face values are obtained through linear interpolation of the respective cell values. Figuratively speaking, the effective coarsening of the mesh flattens local minima and maxima canceling out small scale turbulent fluctuations. Finally, the difference of the additionally filtered and the unfiltered field provides the required information about the smallest resolved scales being the fundament of the scale similarity model.

Obviously, further LES models exist beyond the implemented mixed model based on the one-equation model for the subgrid turbulent kinetic energy and the scale similarity model. A relevant representative of eddy viscosity LES models is the dynamic Smagorinsky model [117], which applies an additional test filter to the computed fields. The purpose is to obtain a dynamic estimate

of the local scaling parameter of the Smagorinsky model, which is fixed prior to the simulation in the classical model version. Chemnitz [23] conducts hybrid RANS/LES simulations of a supersonic combustor based on the solver described in this chapter and the hybrid RANS/LES model discussed in chapter 4. Furthermore, Chemnitz compares the wall pressure results obtained with the mixed model discussed above and the mixed model based on the dynamic Smagorinsky model. Two further simulations are conducted solely with the eddy viscosity part of the mixed model, based on either the one equation or the dynamic Smagorinsky model. The resulting wall pressures and the four flow fields feature solely insignificant differences. Hence, the influence of the turbulence model choice appears to have a surprisingly small influence on the global results, at least in the context of the particular choice of methods for the mixed model.

Moreover, a relevant representative of structural LES models is the approximate deconvolution model (ADM) developed by Stolz et al. [131, 132]. The basic idea of this approach is to provide an approximate operator inverting the filtering conducted by the LES filter. Provided that this inversion to the filtering operator G, see eq. 2.44, is known, one can approximately retrieve the unfiltered, comprehensive fields from the available filtered fields. Although the ADM model represents a sophisticated state-of-the-art approach to the LES modeling of turbulence, its application to realistic supersonic combustor ducts appears to be unrealistic at this point in time due to the enormous spatial resolution requirements, especially in the boundary layers [35]. Furthermore, it is not clear whether the theoretical improvement of predictive capability of LES simulations based on the ADM method could justify the increased computational cost.

3.5 Modeling of Turbulent Deflagration

3.5.1 Combustion Model

The turbulent combustion present in ramjet and scramjet combustors is subject to strong spatial and temporal variations in pressure, temperature and velocity due to the compressible nature of the high-speed flow. As a consequence, also the distribution of fuel, air and intermediate reactants underlies significant fluctuations. Due to the spatially and temporally inhomogeneous species composition, pressure and temperature, also chemical time scales vary significantly across the combustor. Altogether, this increases the uncertainty about ignition and flame stabilization. Taking these considerations into account, it appears reasonable to utilize a comprehensive combustion model being able to capture these variations necessary for a trustworthy prediction of flame stabilization. Therefore, the combustion modeling is based on a finite-rate chemistry approach coupled with multi-species transport. The system of chemical reaction equations including the reacting species is solved in every computational cell at each time step, see eq. 3.31. Although this approach constitutes a major increase in runtime, it appears feasible due to the limited number of hydrogen-air reactions. Support for this choice can be found in the multitude of results obtained with simulations of supersonic combustion based on finite-rate hydrogen-air chemistry [12, 27, 47, 54, 98, 111, 112]. Implicitly, the aforementioned results agree that reducing the dimensionality of the combustion model, e.g. by means of flamelet models, leads to unsatisfactory results in the case of supersonic combustion.

The evolution of a generic chemical reaction j can be described by the expression in eq. 3.30 [53, 71, 109] implying that a chemical reaction is comprised of a forward and a backward reaction step. The respective chemical compounds are denoted by X_k, the amount of species by N_{sp}. The variable $\nu'_{k,j}$ stands for the stoichiometric coefficient for species k for the forward reaction, and $\nu''_{k,j}$ for the backward reaction step in reaction j. The stoichiometric coefficients are determined by the applied reaction mechanism. The total amount of re-

actions j is denoted by N_r.

$$\sum_{k=1}^{N_{sp}} \nu'_{k,j} X_k \rightleftharpoons \sum_{k=1}^{N_{sp}} \nu''_{k,j} X_k \tag{3.30}$$

The sum of all chemical reactions results in an effective rate of progress of the production and destruction for every chemical compound. Finally, the system of reaction rate equations given in eq. 3.31 yields a mass fraction source term for every chemical species involved in the combustion process [53, 71]. The concentration of species i is denoted by c_i, see eq. 3.32, where M_i denotes the molar mass of species i.

$$\dot{\omega}_i = M_i \sum_{j=1}^{N_r} \left(\nu''_{i,j} - \nu'_{i,j}\right) \left(k_j^f \prod_{k=1}^{N_{sp}} c_k^{\nu'_{k,j}} - k_j^b \prod_{k=1}^{N_{sp}} c_k^{\nu''_{k,j}} \right) \tag{3.31}$$

$$c_i = \frac{\rho Y_i}{M_i} \tag{3.32}$$

In addition, each reaction is determined by the forward and backward reaction rates k_j^f and k_j^b that define the progress of each respective reaction. Since the reaction rates are generally highly temperature dependent, they are evaluated with the Arrhenius equation, cf. eq. 3.33 [71]. The activation energy is denoted by E_j^a and is specific to each chemical reaction j just as the temperature coefficient n_j and the pre-exponential factor A_j. All three parameters are specified by the applied reaction mechanism. The dimensionality of the reaction rate equation system in eq. 3.31 corresponds to the number of involved species times the amount of reactions. The reaction mechanism primarily utilized within the following simulations is the comprehensive 21-step scheme by O'Conaire et al. [104], which constitutes a detailed reaction mechanism from a technical point of view. There exist other, more specialized chemical mechanism employing less reactions, yet, the O'Conaire scheme is widely validated and thus represents a reliable choice [54, 148].

$$k_j = A_j T^{n_j} exp\left(\frac{-E_j^a}{R_g T}\right) \tag{3.33}$$

Furthermore, a convenient parameter used to identify the amount of fuel is the equivalence ratio ϕ [138], see eq. 3.34. It is the quotient of the global fuel to air mass ratio and the stoichiometric fuel to air mass ratio. Hence, equivalence ratios of less than one indicate a globally lean mixture, and values larger than one a fuel rich mixture.

$$\phi = \frac{\frac{\dot{m}_{fuel}}{\dot{m}_{air}}}{\left(\frac{\dot{m}_{fuel}}{\dot{m}_{air}}\right)_{stoich}} \tag{3.34}$$

3.5.2 Turbulence Chemistry Interaction

The term turbulence chemistry interaction refers to the influence of combustion on the surrounding turbulent structures and vice versa. Turbulent motions lead to the mixing of fuel, intermediate reactants and air and thus change the local species compositions and temperature. On the other hand, combustion alters the pressure and density and features the potential to induce turbulence, e.g. through baroclinic vorticity production [9, 55]. Furthermore, chemical reaction rates are highly non-linear, see eq. 3.33. Hence, local temperature variations may strongly affect the progress of chemical reactions [53, 109]. Altogether, the potential influence of the interplay between turbulence and combustion provides enough motivation for considering this process in the computational model, at least in the first place.

Various model approaches for this process have been developed over the years. Poinsot and Veynante classify them into three categories [109], although also other classifications exist [116]: Firstly, models based on a geometrical analysis of the flame front including flamelet models [107]. Secondly, models assuming that chemical time scales are smaller than the turbulent mixing time scales, such that chemical reactions are dominated and controlled

by turbulence. An example for this model type is the eddy-break-up model by Spalding [127]. Thirdly, models incorporating the statistic influence of turbulent fluctuations on the chemical source terms. The most common model of this type is the presumed probability density function (PDF) model [53].

Generally, turbulence chemistry interaction models influence the chemical species source term $\dot{\omega}_i$, see eqs. 2.33 and 2.56, if a finite-rate combustion model is applied. The application of comprehensive models of this type usually requires a second evaluation of the system of chemical reactions at the perturbed temperatures and species compositions provided by the turbulence chemistry interaction model. This comes at a great cost, since the numerical solution of the reaction rate systems consumes the largest portion of the simulation time [47].

Some of the mentioned model types have been applied to the simulation of supersonic combustion by various researchers. A prominent example is the partially stirred reactor (PaSR) turbulence chemistry interaction model applied to LES of supersonic combustion by Berglund et al. [12], and further extend by Sabelnikov and Fureby [116]. Concerning the classification of turbulence chemistry interaction models by Poinsot and Veynante [109] explained further above, the PaSR model constitutes a representative of the second model category. The PaSR model assumption is that only a portion of a computational cell takes part in a chemical reaction, and a model expression is utilized to provide an estimate for this fraction. However, Berglund et al. do not show results obtained with pure Arrhenius chemistry, such that the influence of the PaSR model remains unclear.

Despite the fact that it seems apparently necessary to incorporate turbulence chemistry interaction, previous research did not demonstrate a dominant relevance for supersonic combustion. Förster performed RANS simulations of the supersonic flame of Cheng et al. [24, 47] both with an assumed PDF approach and with nominally laminar chemistry based on the pure Arrhenius reaction rate, see eq. 3.33. Although the results including the PDF appear to be slightly better in some aspects, a clear superiority is not obvious. Moreover, Potturi provides a comprehensive study of the influence of current turbulence chemistry interaction models in the context of supersonic combus-

tion [111, 112]. In particular, Potturi compares the influence of different versions of the PaSR model with increasing comprehensiveness and complexity with a scale similarity turbulence chemistry model and pure Arrhenius chemistry. Two different model scramjet combustors were simulated based on the just mentioned turbulence chemistry interaction models. Wall pressure results showed merely perceptible differences between the results. Potturi concludes that the influence of the investigated turbulence chemistry interaction models is minor to negligible.

Moreover, Baudoin et al. conducted LES of a subsonic flame based on five different turbulence chemistry modeling approaches [10], one of which was a flamelet model. The four remaining models based on finite-rate chemistry were the following: the PaSR model mentioned above, the eddy dissipation concept model [89], the thickened flame model [28] and a presumed PDF model. All four finite-rate chemistry approaches provided a very similar and good agreement with experimental measurements, solely the flamelet approach performed distinctly worse. Although the treated test case is subsonic, one can infer from the outcome that the effective differences between the finite-rate chemistry based turbulence chemistry interaction models are rather small, in spite of their considerably different model approaches.

In summary, it can be stated that the utilized turbulence chemistry models do not appear to have a significant influence on supersonic combustion, which is in contrast with combustion at low Mach numbers. There are two possible reasons for this: Either, the models are insufficient to reproduce the correct interaction of turbulence and combustion, or the influence is generally subordinate with respect to supersonic combustion. Noteworthy effects could be solely observed in small scale test setups, where the ignition length can be influenced by the turbulence chemistry interaction models, e.g. the supersonic flame by Cheng et al. [24]. Preliminary investigations performed within this work based on the earliest version of the PaSR model also did not show a significant influence [1]. For the stated reasons, turbulence chemistry interaction modeling by means of currently available models is neglected. However, it

[1] The applied version of the PaSR model is termed PaSR(0) by Potturi [111]. It locally dampens the species source terms $\dot{\omega}_i$, but does not require a computationally expensive second evaluation of the chemical reaction system.

should be noted that all models developed and utilized so far only considered the influence of turbulent motions on combustion. The induction of turbulence by means of combustion on a microscale level found solely very little attention in terms of modeling approaches so far. Chapter 5 presents a novel approach, which might represent a step in this direction.

4 Methods for Hybrid Reynolds-Averaged Navier Stokes and Large Eddy Simulation of Transonic and Supersonic Combustion

Since LES resolves large-scale turbulent fluctuations in contrast to RANS, it offers the potential to improve the computational prediction of fuel, air and intermediate species mixing. However, LES requires the spatial resolution of turbulent structures, whereas solely small scale turbulence is accounted for by the LES subgrid scale model. Hence, vortical structures larger than the smallest scales treated by the LES model must be accounted for by the computational mesh. Especially the near-wall regions feature small scale vortices, which account for a major portion of the turbulence production within a confined duct despite their small size. In particular, the boundary layer resolution requirements are the main reason for the enormous computational cost coupled with LES for two reasons. Firstly, the large number of required grid cells for an appropriate spatial resolution evidently increases the necessary computational effort. Secondly, the subsequently tiny size of near-wall cells drastically decreases the numerical time step due to the CFL condition, which imposes an upper limit on the ratio of time step to cell size, see eq. 3.2. The aspect of time step reduction is even more dominant than the large amount of necessary computational cells. In summary, LES increases the computational runtime of a confined duct simulation by several orders of magnitude compared to RANS. In addition to the runtime restraints, the generation of boundary layer resolving LES meshes constitutes a difficult task requiring a continual assessment of the grid resolution. Hence, if the investigation of supersonic combustion shall profit from the benefits of LES, a simplification of the LES wall treatment is required.

Before the turbulence modeling of near-wall regions is further addressed, the

role of boundary layers within wall-confined supersonic combustors shall be pointed out. Firstly, the boundary layers lead to a partial blockage of the combustor duct, which effectively corresponds to a geometry change. As a result, the velocity profiles and thus fuel residence times are influenced. Secondly, the interaction of shocks and boundary layers affects the combustor shock system, which directly influences the locations of discrete temperature changes [111]. The aforementioned effects attest the importance of boundary layers for supersonic combustors and provide enough motivation for their adequate reproduction in computational simulations.

A pragmatic approach drastically decreasing computational mesh requirements and runtimes is to utilize RANS within the boundary layers while treating all remaining regions with LES. Such a hybrid RANS/LES approach is proposed in section 4.3 of this chapter. A set of methods is presented, which serve the purpose of placing the interface between both turbulence modeling modes. The term hybridization hence refers to the placement of the interface between two separate turbulence models, one for RANS and one for LES. The goal is to provide a solution-dependent, dynamical RANS coverage of the boundary layers, which shall be discretized with preferably coarse cells. The fundamental assumption is that the underlying RANS turbulence model provides a satisfactory prediction of relevant boundary layer effects. A further major intention of the developed methods is to minimize the required user intervention in terms of both LES mesh generation and placement of the hybrid RANS/LES interface location, a desirable feature of a potential design tool.

4.1 Requirements for Hybrid RANS/LES in the Context of Supersonic Combustion

With the goal of reducing the runtime of LES simulations by utilizing RANS in the boundary layers, two requirements for the hybridization can be identified: Firstly, the variation of the boundary layer thickness must be taken into account. Thus, an adequate RANS/LES hybridization approach requires a dynamic placement of the interface between both turbulence modeling modes.

Being dynamic within this context means that the interface between RANS and LES is not fixed prior to runtime but evolves as a result of the solution in every time step [73]. Secondly, a reliable reproduction of shock boundary layer interactions must be provided. Furthermore, the boundary layers occupy a considerable portion of the channel in combustor ducts with thick boundary layers, e.g. due to a isolator section preceding the combustor. Subsequently, a large portion of the flow field would be subject to the RANS model, if the complete boundary layer was treated with RANS. However, it is desirable to keep the RANS zones as small as possible in order to enable the development of coherent turbulent structures in the LES mode. Thus, the hybridization method must provide an adequate compromise.

4.2 Existing Approaches for Hybrid RANS/LES

A competing approach to the dynamic, solution-dependent placement of the interface location between RANS and LES is the determination of fixed and constant RANS zone thicknesses prior to the simulation following the zonal DES approach proposed by Deck et al. [33]. The advantages of such an approach are the straightforward implementation on the one hand and the unambiguous location of the interface between RANS and LES on the other hand. However, zonal DES deprives the hybridization of any dynamic behavior with respect to the evolution of the local solution. As a consequence, the RANS zone is either too thick unnecessarily preventing the development of turbulent fluctuations in the LES mode, or too small leading to an unrealistic boundary layer behavior, if coarse near-wall meshes are applied.

First attempts to create hybrid RANS/LES models with a dynamic adaptation of the RANS/LES interface location suffered from grid-induced flow separation, see for example the detached eddy simulation (DES) model by Spalart et al. [126]. In particular, the principle of DES-type models is the replacement of the turbulent length scale within a RANS model by the local grid size if LES is activated [125, 126]. The selection of the turbulence modeling mode is based either on the distance to the nearest wall or the evaluation of local flow or mesh properties, or both. The cause for the aforementioned failure

mode is a spatially premature transition from RANS to LES effectively reducing the turbulent eddy viscosity in boundary layer regions potentially resulting in unphysical separation phenomena. Further developments and improvements based on the DES model followed [125], whereas the focus remained on the formulation of a preferably universally valid method applicable to various problems. The requirements of specific configurations like supersonic combustor ducts were not at the center of attention.

Larsson et al. investigate the HyShot II scramjet combustor on the basis of LES utilizing a wall model for the 10 % to 20 % lowermost portions of the boundary layers [78], such that the LES mesh resolution requirements are decisively reduced. Yet, this approach still requires the resolution of the remaining boundary layer portions. As a result, the mesh utilized by Larsson et al. [1] is refined by a factor of three in these sections compared to the combustor center and contains four times the number of cells that are utilized for the hybrid RANS/LES of the ITLR combustor presented in chapter 8.5, despite the fact that the simulations contain solely one fourth of the HyShot II combustor width. Furthermore, the investigated operational points of the HyShot II combustor feature decisively smaller boundary layer thicknesses than it is the case for the ITLR combustion cases. An approach requiring even less mesh resolution in the boundary layers than the wall-modeled LES approach is thus desirable for the investigation of the ITLR combustor by means of LES.

Further investigations of hybrid RANS/LES of supersonic combustion are provided by Potturi and Edwards [38,111,112] and Edwards et al. [36,37], in which they investigate test cases relevant for supersonic combustion. The RANS/LES hybridization utilized in their studies is based on a set of methods that build upon a blending function between RANS and LES. This blending function is designed to switch from RANS to LES at the outer portion of the logarithmic boundary layer zone [56]. Hence, the outer wake regions of the boundary layers require a mesh with high spatial resolution adequate for the application of LES. Furthermore, the experiments simulated by Potturi and Edwards feature relatively thin boundary layers [111] similar to the HyShot II combustor investigated by Larsson et al. [78], which is in contrast to the ITLR combustor

[1] Larsson et al. utilize three meshes with increasing resolution. The medium mesh features 43 million cells.

discussed in chapter 8 of this thesis.

4.3 Novel Hybridization Approach

A hybridization method is presented in the following, which contrasts with previous work. In particular, the method is intended to cover preferably the greater part of the boundary layer thickness with RANS in order to minimize the computational cost originating in the boundary layer mesh requirements of LES. Furthermore, the proposed method constitutes a generic approach, which is not tied to a specific turbulence model.

The hybridization scheme is comprised of two components: hybridization method components A and B. For simplicity, both components are referred to as methods A and B in the following. The entire hybridization method is called method C and constitutes the sum of methods A and B. The placement of the hybrid interface in method A rests upon the comparison of RANS and LES model predictions, whereas RANS is utilized as a measure and threshold for the selection of the turbulence mode. Method B contrasts with method A, since it places the hybrid interface independently of the particular model predictions. Instead, the interface determined by method B follows the sonic line indicating regions with extensive shock boundary layer interactions. The latter is especially intended to operate in the combustion region of dual-mode scramjet engines in the transition regime between ramjet and scramjet combustion, see section 8.4.

The set of hybridization methods described below finally results in three turbulence indicator fields r_A, r_B and r_C allocating an indicator value to every cell of the computational domain. The indicator fields are designed to be one in the RANS region and zero in the LES region. Therefore, the indicator fields can be utilized to merge the RANS and LES turbulence fields very conveniently, following eq. 4.1. The placeholder variable Ω can be any variable specific to turbulence modeling, e.g. the turbulent kinetic energy. Hence, the resulting field Ω is the superposition of the respective RANS and LES fields multiplied with the turbulence mode indicator field r. The ultimate purpose

of the method embodied by the turbulence mode indicator r is to deliver the hybrid RANS/LES eddy viscosity and define regions, where the scale similarity LES model discussed in section 3.4 shall be applied. The last section of this chapter briefly explains how the proposed hybridization method influences the governing equations.

$$\Omega_{hybrid} = r\Omega_{RANS} + (1-r)\Omega_{LES} \qquad r = \begin{cases} 0 & = \text{LES} \\ 1 & = \text{RANS} \end{cases} \tag{4.1}$$

As mentioned further above, the proposed hybridization method is not bound to specific turbulence models neither for RANS nor for LES. Therefore, arbitrary combinations of different turbulence models for both modeling modes are imaginable, which constitutes an important asset of the approach. However, hybridization method component A introduced in the following rests upon the availability of the turbulent viscosity. Hence, the chosen models should either be of the turbulent eddy viscosity type or be able to provide this quantity. The last section of this chapter 4.7 provides an overview of the equations within the CFD solver described in chapter 3 that are directly influenced by the hybridization scheme.

4.4 Hybridization Method Component A

Here, a RANS/LES hybridization method for supersonic flows is introduced, that combines a zonal approach with a dynamic, solution-based procedure. The method is termed hybridization method component A, or briefly worded method A. An important novelty of the approach is the combination of the benefits of a zonal approach with a dynamic procedure that places RANS where it is deemed necessary. Secondly, the novel dynamic approach builds upon the direct comparison of RANS and LES model predictions in terms of the respective turbulent viscosities $\mu_{t,LES}$ and $\mu_{t,RANS}$. The zonal part delivers the bounds for the RANS zone, whereas the dynamic part places the actual interface location in-between. Finally, this results in a binary decision whether to utilize RANS or LES at a given location. A convenient way to represent this

is the signum operator, see eq. 4.2. Note that it is defined to be one, if the argument is zero, here.

$$\text{sign(arg)} = \begin{cases} -1 & \text{if arg} < 0 \\ 1 & \text{if arg} \geq 0 \end{cases} \tag{4.2}$$

4.4.1 Minimum RANS Zone Thickness

In order to prevent LES in the cells closest to the walls and subsequent grid-induced separation, a minimum RANS zone thickness $C_{A,z,min}$ is introduced following the fundamental idea of a zonal approach [33]. The constant is specified before and fixed during the simulation. The corresponding turbulence mode indicator field $r_{A,z,min}$ results from the comparison of the distance threshold $C_{A,z,min}$ with the wall distance of each cell, cf. eq. 4.3.

$$r_{A,z,min} = \frac{1}{2} + \frac{1}{2}\text{sign}\left(\frac{\min(C_{A,z,min}, y)}{y} - 1\right) \tag{4.3}$$

4.4.2 Maximum RANS Zone Thickness

In the interest of restricting the extent of the RANS zone and in order to prevent RANS outside of the near wall regions, a maximum RANS zone indicator $r_{A,z,max}$ is introduced. It results from a comparison of the wall distance with a constant threshold $C_{A,z,max}$ for each computational cell, just as $C_{A,z,min}$. If the wall distance exceeds this threshold, LES is enforced by setting $r_{A,z,max}$ to zero. Hence, the two threshold constants $C_{A,z,min}$ and $C_{A,z,max}$ define a bounding box for the dynamic interface placement introduced in the following. The minimum and maximum thresholds are problem-specific and need to be specified by the user. Besides, separate bounding boxes might be defined for different regions of the computational domain.

$$r_{A,z,max} = \frac{1}{2} + \frac{1}{2}\text{sign}\left(\frac{\min(C_{A,z,max}, y)}{y} - 1\right) \tag{4.4}$$

4.4.3 Solution-Based Dynamic Interface

The key element of the proposed hybridization method component A is the novel dynamic interfacing represented by the turbulence mode indicator $r_{A,d}$, see eq. 4.5. It contains the solution-based portion of the indicator field r_A and places the actual interface between RANS and LES in-between the bounds prescribed by the zonal wall distance thresholds $C_{A,z,min}$ and $C_{A,z,max}$. The decision whether RANS or LES is applied is based on the comparison of RANS and LES turbulent eddy viscosities $\mu_{t,LES}$ and $\mu_{t,RANS}$, see eq. 4.5. As explained earlier, the assumption is that the RANS model provides a reasonable prediction for the magnitude of the local turbulent viscosity within the boundary layer. Hence, it is utilized as a scale for the LES model prediction, verifying its trustworthiness.

The quotient of both eddy viscosities is scaled with the inverse of the RANS and LES length scales f_w given in eq. 4.6 in order to account for the different reference length scales in the computation of each respective viscosity. Due to this scaling step, which makes the two viscosities directly comparable, a reasonable value for the constant $C_{A,d}$ in eq. 4.5 amounts to one. Despite the universality of the hybridization method, the RANS length scale for the SST model is inserted, since the SST model is exclusively applied for the RANS mode within this work.

$$r_{A,d} = \frac{1}{2} + \frac{1}{2}\text{sign}\left(\frac{\min(C_{A,d}, \frac{\mu_{t,LES}}{\mu_{t,RANS}} f_w)}{\frac{\mu_{t,LES}}{\mu_{t,RANS}} f_w} - 1\right) \tag{4.5}$$

$$f_w = \frac{l_{RANS}}{l_{LES}} = \frac{\frac{\sqrt{k}}{\beta^* \omega}}{\Delta_{LES}} \tag{4.6}$$

The purpose of this approach is to obtain a robust hybrid RANS/LES method preventing premature activation of LES resulting in erroneous boundary layer profiles and separation. The choice to utilize the RANS turbulent viscosity as a measure for the boundary layer thickness and shape constitutes a solution-oriented approach that circumvents some deficiencies of DES-like

approaches (premature separation), see section 4.2 and furthermore requires less model calibration than for example the hybrid RANS/LES approach proposed by Gieseking et al. [56].

4.4.4 Turbulence Sensor

For the sake of consistency, a turbulence sensor $r_{A,t}$ is established that serves the purpose of activating RANS only in regions, where turbulence modeling plays a relevant role. Deactivating RANS in regions with weak turbulence contributes to the idea of maximizing the space for the development of intrinsic turbulent fluctuations in the context of LES. The indicator is based on the comparison of the turbulent kinetic energy modeled with RANS k_R and the local kinetic energy e_k. If the quotient of both field variables exceeds a threshold parameter $C_{A,t}$ specified prior to simulation, the indicator becomes one and enables the application of RANS.

$$r_{A,t} = \frac{1}{2} + \frac{1}{2}\text{sign}\left(\frac{k_R}{e_k} - C_{A,t}\right) \tag{4.7}$$

4.4.5 Resulting Turbulence Indicator Field for Method A

The final turbulence mode indicator r_A for hybridization method component A is a superposition of the minimum RANS zone indicator $r_{A,z,min}$ and the product of the maximum RANS zone indicator $r_{A,z,max}$, the turbulence sensor $r_{A,t}$ and the solution-based dynamic indicator $r_{A,d}$, cf. eq. 4.8. Hence, the minimum zonal indicator is always active, while the dynamic indicator is deactivated beyond the maximum RANS zone or in regions with an insignificant influence of turbulence.

$$r_A = \frac{1}{2} + \frac{1}{2}\text{sign}\left(r_{A,z,min} + r_{A,z,max} r_{A,t} r_{A,d}\right) \tag{4.8}$$

4.5 Hybridization Method Component B

Hybridization method component A described above places the interface between RANS and LES purely based on the comparison of both model predictions. As a result, the effects of boundary layer growth and shock boundary layer interaction are taken into account by the RANS turbulence model, as demonstrated in the following chapters 6 and 8. Yet, in cases involving boundary layers with extensive dimensions, the portion of the flow treated with RANS can dominate the LES regions, such that only a small area remains for the LES part to develop resolved, coherent turbulence. Hence, it is desirable to limit the RANS zone to a reasonable minimum. However, especially shock wave boundary layer interactions should still be treated with RANS if a spatial resolution with LES grids is to be avoided. Extensive boundary layer dimensions induced by shock wave boundary layer interactions especially occur in the transition regime between ramjet and scramjet operation of a dual-mode combustion scramjet engine, see section 8.4. In order to satisfy the requirements stated above, an additional hybridization criterion is introduced that aims at the treatment of the aforementioned shock boundary layer interaction regions. This novel hybridization scheme termed hybridization method component B takes advantage of the fact that boundary layers are separated into a subsonic and supersonic portion divided by the sonic line, see section 2.4.1.

4.5.1 Sonic Line Dependent Dynamic RANS/LES Interfacing

The sonic line separates the outer supersonic flow from the subsonic near-wall region within a supersonic boundary layer [3]. Generally, the sonic portion can reach considerable dimensions within a thick boundary layer. Regions with additionally increased boundary layer thickness, e.g. due to shock boundary layer interaction, also exhibit an enlarged subsonic region resulting in a local bump in the sonic line, see section 2.4.1. Exactly the latter feature of the sonic line can be utilized to extend the RANS/LES hybridization approach in order to identify the flow segments that require RANS modeling if compu-

tationally expensive LES meshes shall be avoided in these regions.

A novel approach is proposed customized to the conditions in supersonic combustor ducts. For this purpose, an additional turbulence mode indicator $r_{B,d}$ is introduced, which is computed based on a comparison of the local Mach number with a Mach number threshold constant $C_{B,tr}$, see eq. 4.9. Setting $C_{B,tr}$ to a value of one results in a RANS treatment of the whole subsonic area below the sonic line. Choosing a smaller value for the constant results in a thinner RANS zone, which will nevertheless follow the development of the sonic line. Hence, this parameter allows to adjust the extent of the dynamic interface according to the chosen grid resolution.

$$r_{B,d} = \frac{1}{2} + \frac{1}{2}\text{sign}\left(C_{B,tr} - Ma\right) \tag{4.9}$$

4.5.2 Maximum RANS Zone Thickness

With a similar justification as previously in section 4.4.2, a maximum RANS zone thickness is defined also for method B. The purpose is to prevent a switch to RANS in subsonic regions in the core of the flow. The corresponding turbulence mode indicator $r_{B,z,max}$ is given in eq. 4.10. Although one might merge $r_{B,z,max}$ with the maximum RANS zone thickness indicator $r_{A,z,max}$ defined for method A, it appears useful to treat the two hybridization method components A and B independently, see section 8.5.

$$r_{B,z,max} = \frac{1}{2} + \frac{1}{2}\text{sign}\left(\frac{\min(C_{B,z,max}, y)}{y} - 1\right) \tag{4.10}$$

4.5.3 Resulting Turbulence Indicator Field for Method B

The resulting transonic turbulence indicator field r_B for hybridization method component B defining whether a given cell is treated with RANS or LES is given in eq. 4.11. In accordance with all previous indicators, a value of one represents RANS and a value of zero LES.

$$r_B = r_{B,d} r_{B,z,max} \tag{4.11}$$

4.6 Method C: Consolidation of Hybridization Method Components A and B

The two hybridization method components A and B are supposed to be utilized in conjunction with each other: Method A can be generally applied, especially in regions that are dominated by boundary layer growth, in order to get a proper inflow boundary layer profile and shock system for the combustor section. Such regions are for example the isolator section of a scramjet duct or generally the combustor inlet. Furthermore, the comparably thin boundary layers of engines operating in the pure scramjet regime are favorable for method A. Method B can be applied to the combustion region if the boundary layers reach a considerable fraction of the channel cross-section, thus reducing the extent of the RANS zone to a minimum in order to increase LES coverage of the combustion process. In particular, this is the case in the ramjet/scramjet transition regime, see section 8.4. In order to obtain the comprehensive hybridization method C, the turbulence mode indicators r_A for method A and r_B for method B are added providing the integrated turbulence mode indicator r_C, see. eq. 4.12[2].

$$r_C = \frac{1}{2} + \frac{1}{2}\text{sign}\left(r_A + r_B - \epsilon\right) \tag{4.12}$$

Moreover, it can be reasonable to limit the RANS zone to a fixed thickness in certain parts of the simulated domain, e.g. the near-wall regions of injector elements in order to facilitate the resolution of turbulent fuel jets, see for example chapter 6. This corresponds to a locally pure zonal hybridization approach. For this purpose, a further turbulence mode indicator r_{pz} is introduced, see eq. 4.13. This indicator sets the RANS zone thickness to a fixed

[2]The variable ϵ represents an arbitrary, very small value that is supposed to ensure that r_C becomes zero, if r_A and r_B are zero, see eq. 4.2.

value C_{pz} at portions of the computational domain pre-selected prior to the simulation.

$$r_{pz} = \frac{1}{2} + \frac{1}{2}\text{sign}\left(\frac{\min(C_{pz}, y)}{y} - 1\right) \tag{4.13}$$

4.7 Impact on the Governing Equations

The fundamental governing equations for compressible, reacting fluid flow are given in chapter 2 followed by the discussion of their modeling in the context of the developed fluid dynamics solver for supersonic combustion in chapter 3. In particular, both chapters focus on the mathematical description of turbulence within the governing equations and the associated formulation of appropriate closure terms with respect to RANS and LES. This chapter provides an approach for the hybridization of both RANS and LES turbulence closure approaches, such that RANS is utilized for the largest part of the near-wall regions. In this last section of chapter 4, the proposed hybridization method shall be related to the governing equations presented in chapters 2 and 3.

The governing equations requiring turbulence modeling are the momentum, species and energy transport equations. The mass transport equation does not require a turbulence closure due to the utilization of the Favre averaging/filtering approach, see section 2.2. Hence, there are three equations with two sets of possible turbulence closures, one for RANS given in section 3.3 and one for LES given in section 3.4. A summary of the respective closure terms is provided in table 4.1.

The outcome of the hybridization approach discussed in this chapter is a turbulence mode indicator field r_C comprised of the two parts r_A and r_B for the hybridization method components A and B. The indicator fields are designed to be zero in the LES mode and one in the RANS mode within a given computational cell, see eq. 4.1. Hence, the integral turbulence mode indicator r_C can be utilized to select the turbulence closure mode by a straightforward summation of the RANS and LES closure approaches multiplied with r_C, see eq. 4.1.

Table 4.1: Governing equation turbulence closure terms for RANS and LES

Transport equation	**RANS**	**LES**
Momentum	$T_{R,U}$ (eq. 3.6)	$T_{L,U}$ (eq. 3.21)
Species	$T_{R,Y}$ (eq. 3.8)	$T_{L,Y}$ (eq. 3.22)
Energy	$T^{I}_{R,E}$ (eq. 3.10), $T^{II}_{R,E}$+$T^{VIIa}_{R,E}$ (eq. 3.11), $T^{III}_{R,E}$ (eq. 3.12)	$T^{I}_{L,E}$ (eq. 3.24), $T^{II}_{L,E}$+$T^{IV}_{L,E}$ (eq. 3.25), $T^{III}_{L,E}$ (eq. 3.27)

As a result, the turbulence closures for the momentum, species and energy transport equations given by eqs. 2.32, 2.33, 2.43, 2.55, 2.56 and 2.60 can be formulated as stated in the following eqs. 4.14, 4.15 and 4.16. Within this context, T_U, T_Y and T_E denote the generic right-hand sides of the corresponding transport equations. The RANS closure terms are active within a given computational cell, if r_C is one. In the opposite case, the LES closure terms are active.

$$T_U = r_C T_{R,U} + (1 - r_C) T_{L,U} \tag{4.14}$$

$$T_Y = r_C T_{R,Y} + (1 - r_C) T_{L,Y} \tag{4.15}$$

$$\begin{aligned} T_E = &- r_C \frac{\partial}{\partial x_j} \left(T^{I}_{R,E} + T^{II}_{R,E} + T^{III}_{R,E} + T^{VIIa}_{R,E} \right) \\ &- (1 - r_C) \frac{\partial}{\partial x_j} \left(T^{I}_{L,E} + T^{II}_{L,E} + T^{III}_{L,E} + T^{IV}_{L,E} \right) \end{aligned} \tag{4.16}$$

Although the computable left-hand sides of the governing equations for RANS and LES have the same structure, cf. e.g. the momentum transport equations eqs. 2.32 and 2.55, the equations are subject to different operators. While the tilde and overline symbols denote ensemble averaging in the RANS case, the tilde and tophat operators denote a spatial filtering operation of the same fields in LES. However, RANS is treated solely in its unsteady mode here

(URANS), such that RANS and LES are based on the same (small) time step defined by the CFL condition, see section 3.1.2. Thus, the effective difference between RANS and LES is essentially reduced to the selection of the turbulence closure terms by means of eqs. 4.14, 4.15 and 4.16.

5 Modeling the Impact of Combustion on Turbulence

Current state-of-the-art turbulence chemistry interaction models focus on the impact of turbulence on the reacting species source terms originating in the chemical reaction equations, cf. eq. 2.5. Through different chains of reasoning various researchers developed models that modify those source terms in accordance with the assumed influence of non-resolved turbulence on the combustion process on a microscopic level; see section 3.5.2 for a discussion. Usually, it is assumed that the combustion process is limited by microscopic species mixing, when the chemical time scales become sufficiently small. However, modeling the opposite direction, namely the complementary influence of combustion on turbulence has not drawn a lot of attention, yet. Ballal investigates the effects of combustion induced turbulence based on experiments conducted with subsonic combustors and identifies the turbulence inducing effect of combustion [4]. Furthermore, DNS of supersonic diffusion flames conducted by Luo [86, 87] indicate a notable influence of combustion induced turbulence in compressible reacting flows, as discussed in the following.

In order to provide the missing counterpart to existing turbulence-chemistry interaction models, a model for combustion induced turbulence is proposed and presented in this chapter. The induction of turbulence through combustion is assumed to occur on a microscopic level according to the underlying assumptions made as a foundation for the commonly available models for turbulence chemistry interaction. In the context of LES this means that the effect is present on the unresolved subgrid scales.

The model is neither limited to solely RANS nor LES. Yet, the model requires the availability of the turbulent kinetic energy transport equation as a part of

the respective turbulence models. Since RANS generally models all turbulent structures, the novel model influences the modeling of the entire turbulent spectrum if applied to a RANS model. In the case of LES, the novel model delivers the effect only on the subgrid level. Hence, with decreasing cell size, the influence of the model vanishes.

5.1 Supersonic Combustion DNS by Luo

Various researchers investigated the effect of combustion on turbulence [4, 18, 20, 129, 130, 147]. In particular, the work of Luo and Bray [87] and Luo [86] focuses on this phenomenon in the context of supersonic combustion based on three-dimensional DNS simulations of supersonic diffusion flames. For this reason, the findings by Luo are especially relevant for the assessment of combustion induced turbulence in the context of scramjet combustors. Hence, the relevant outcome of the work of Luo [86] shall be provided at this point as a foundation for the model formulation for combustion induced turbulence given in the subsequent section 5.2.

The DNS conducted by Luo rest upon a three-dimensional Navier-Stokes solver employing a one-step chemical reaction scheme for the combustion of a generic fuel. The simulated setup consists of a fuel stream and an adjacent, parallel oxidizer stream flowing in the opposite direction. Both streams have a Mach number of 1.2 each, thus leading to the formation of a supersonic mixing layer in-between both streams. The result is a turbulent supersonic diffusion flame forming after ignition has occurred within the mixing layer. One non-reacting case and three reacting cases with increasing heat release are investigated.

In particular, Luo provides the temporal evolution of the components of the Reynolds stress and turbulent kinetic energy budget obtained by spatial integration over the mixing layer height. The comprehensive, generic turbulent kinetic energy transport equation for compressible flow in the form utilized by Luo is given in eq. 5.1 [86]. The equation is obtained from the comprehensive Reynolds stress transport equation [144]. Moreover, the naming conven-

tion for each right-hand side term utilized by Luo is provided. The first term P_{kk} constitutes the production of turbulent kinetic energy. The second term T_{kk} is the so-called triple correlation, since three velocity fluctuations are involved. Next, Ψ_{kk} is the pressure-velocity correlation and Φ_{kk} is the pressure dilatation. The pressure dilatation Φ_{kk} is the crucial component of the kinetic energy transport equation with respect to combustion induced turbulence as shown in the following. The last two terms are the viscous diffusion D_{kk} and the viscous dissipation ϵ_{kk}.

$$\begin{aligned}\frac{\partial(\overline{\rho}k)}{\partial t}+\frac{\partial(\overline{\rho}\widetilde{U_j}k)}{\partial x_j} = &\overbrace{-\overline{\rho U_i{}'' U_j{}''}\frac{\partial \widetilde{U_i}}{\partial x_j}}^{P_{kk}}\overbrace{-\frac{\partial}{\partial x_j}\left(\frac{1}{2}\overline{\rho U_i{}'' U_i{}'' U_j{}''}\right)}^{T_{kk}} \\ &\underbrace{-\frac{\partial}{\partial x_i}\left(\overline{pU_i{}''}\right)}_{\Psi_{kk}}\overbrace{+p\frac{\partial U_i{}''}{\partial x_i}}^{\Phi_{kk}}\overbrace{+\frac{\partial}{\partial x_j}\left(\overline{U_i{}''\tau_{ij}}\right)}^{D_{kk}}\overbrace{-\overline{\frac{\partial U_i{}''}{\partial x_j}\tau_{ij}}}^{\epsilon_{kk}}\end{aligned} \tag{5.1}$$

As mentioned further above, Luo integrates equation 5.1 over the mixing layer height in-between the fuel and oxidizer streams in order to obtain the integral turbulent kinetic energy budget. Due to this integration, the triple correlation T_{kk}, the pressure velocity correlation Ψ_{kk} and the viscous diffusion D_{kk} vanish, since they solely redistribute turbulent kinetic energy. Solely the production term P_{kk}, viscous dissipation ϵ_{kk} and pressure dilatation Φ_{kk} can destroy or generate turbulent kinetic energy [86]. Subsequently, Luo analyzes the temporal evolution of P_{kk}, ϵ_{kk} and Φ_{kk} for each of the four simulated cases. Two relevant findings result from this analysis: firstly, the pressure dilatation Φ_{kk} considerably increases with increasing heat release, while the influence of the remaining two terms remains approximately constant. Secondly, the pressure dilatation Φ_{kk} effectively acts as a source term for the turbulent kinetic energy and increases with heat release. Hence, it can be stated that combustion can induce turbulence through pressure dilatation. Based on this finding, the pressure dilatation term Φ_{kk} serves as the template for the novel model for combustion induced turbulence introduced in the following section 5.2.

5.2 Formulation of a Novel Model for Combustion Induced Turbulence

The foundation for the novel model for combustion induced turbulence is the insight that combustion can increase the turbulent kinetic energy through the pressure dilatation term as discussed in the previous section 5.1 describing the work of Luo [86]. In order to reproduce this process, the novel model directly approaches the modeled generation of turbulence by means of the turbulent kinetic energy transport equation. Subsequently, this results in an increase of turbulent viscosity in terms of the eddy viscosity concept, see eqs. 3.16 and 3.29 and thus increased turbulent mixing on the scales modeled by the respective turbulence model. Finally, the altered distribution of reactants and enthalpy influences the chemical reaction source terms, see eq. 3.31.

The generic transport equation for turbulent kinetic energy in the context of Favre averaging or filtering given in eq. 5.2 constitutes a template for practically all turbulence models employing the turbulent kinetic energy, see Wilcox [144]. This model equation can be part of a RANS as well as of a LES turbulence model, cf. eqs. 3.13 and 3.28. The diffusion term on the right hand side incorporates molecular and turbulent diffusion. In addition, the production P_{kk} and dissipation ϵ_{kk} of turbulent kinetic energy appear, similar to the formulation in eq. 5.1. The particular formulations of the terms on the right hand side depend on the utilized turbulence model. Yet, while eq. 5.1 given in the previous section 5.1 constitutes a comprehensive formulation of the turbulent kinetic energy transport equation derived from the Reynolds stress transport equation, the formulation given in 5.2 is the result of generic simplifications and model assumptions [144].

$$\frac{\partial(\overline{\rho}k)}{\partial t} + \frac{\partial(\overline{\rho}\widetilde{U_j}k)}{\partial x_j} = \frac{\partial}{\partial x_j}\left(d_k \frac{\partial k}{\partial x_j}\right) + P_{kk} - \epsilon_{kk} \tag{5.2}$$

Hence, the influence of combustion within state-of-the-art turbulence models is limited to the implicit modification of the density and other flow properties that may indirectly affect the modeling of turbulence, see e.g. eqs. 3.13 and

3.28. The proposed model for combustion induced turbulence adds a production source term C_{kk} to the generic model equation for the turbulent kinetic energy eq. 5.2 with the intention to remedy this deficiency, such that eq. 5.2 becomes eq. 5.3. This model source term represents the pressure dilatation Φ_{kk} identified as a crucial source of combustion generated turbulence by Luo, see the previous section 5.1. Essentially, the novel model does not add a new source term, in fact it rather reintroduces an existing term that the generic equation 5.2 is deprived of. The novelty of the model rests upon the formulation of C_{kk} in terms of the combustion process, as explained in the following.

$$\frac{\partial(\overline{\rho}k)}{\partial t} + \frac{\partial(\overline{\rho}\widetilde{U_j}k)}{\partial x_j} = \frac{\partial}{\partial x_j}\left(d_k \frac{\partial k}{\partial x_j}\right) + P_{kk} - \epsilon_{kk} + C_{kk} \tag{5.3}$$

The essential component of the source term C_{kk} is the product of computable pressure and the divergence of assumed combustion induced velocity fluctuations, see eq. 5.4. Basically, this formulation corresponds to a component of the pressure dilatation Φ_{kk} investigated by Luo and given in eq. 5.1. This product represents the expansion work conducted by turbulent fluctuations that are caused by combustion. However, the combustion induced velocity fluctuations are apriori unknown and need to be modeled and expressed in terms of computable quantities. This essential step constitutes the novel link between the fluid mechanical source term within the turbulent kinetic energy transport equation and the combustion process.

$$C_{kk} = C_{tc}\overline{p}\frac{\partial u'_{j,c}}{\partial x_j} f_c f_k \tag{5.4}$$

The proposed model for combustion induced turbulence rests upon the following, novel assumption: In order to provide a closure for the velocity fluctuations $u'_{j,c}$, an analogy to the Kolmogorov velocity microscale is drawn, see eq. 5.5. The motivation for this formulation is the assumption that the excitation of turbulence due to combustion occurs on a microscopic level as stated initially. Since the Kolmogorov microscale constitutes the smallest possible scale of turbulence, it is reasonable to refer to this length scale. Apart from this

analogy, viscosity is the measure, which defines the propensity of the fluid to develop shear forces and hence turbulence. It is assumed that the frequency of combustion induced turbulent fluctuations is equivalent to the local time scale of chemical reactions. For this purpose, the formulation for the velocity fluctuations in eq. 5.5 employs a characteristic mean chemical time scale t_c.

$$u'_{j,c} = \sqrt{\frac{\nu}{t_c}} \tag{5.5}$$

A definition of the chemical time scale t_c is necessary in order to compute the combustion induced turbulent velocity fluctuations in eq. 5.5. The time scales of chemical reactions can be defined in terms of the eigenvalues of the Jacobian of the chemical source terms [44, 65], see eq. 3.31, evaluated at the particular temperature and species composition[1]. However, each reaction rate is a function of the local species composition and temperature. Hence, it is obvious that the chemical time scale must be evaluated separately for each computational cell. Furthermore, there exists no single chemical time scale, since combustion is a combination of a multitude of chemical reactions with individual reaction rates. Thus, the remaining question is how to define an appropriate mean chemical time scale given that every involved chemical reaction features a different reaction rate.

One possible option is to utilize the slowest chemical reaction to define the chemical time scale [65]. Yet, it is unlikely that the slowest chemical reactions will dominate the transient volumetric expansion on a microscopic level, which is identified to induce turbulence, see the previous section 5.1. A more appropriate method in terms of the concept of combustion induced turbulence is to define the chemical time scale such that it is dominated by the faster reactions. For this reason, the time scale is chosen to be an average of all forward reaction rates evaluated individually for every computational cell according to eq. 5.6 [44, 57]. The denominator in eq. 5.6 denotes the sum of all species forward reaction rates over all species and reactions. The numerator expresses the sum of all species concentrations. Effectively, this can be interpreted as (the inverse of) a mean Jacobian of the forward reaction chem-

[1] Essentially, the Jacobian is the derivate of the reaction rates with respect to the species concentrations [44].

ical source terms evaluated at the local temperature and species composition within each computational cell. A fast reaction features a large reaction rate and leads to a large denominator, thus reducing the mean chemical time scale t_c. On the other hand, the reaction rate of a slow reaction will not contribute significantly to the denominator. Slow reactions instead reduce the denominator through the weighting factor N_r representing the number of reactions. Hence, the formulation in eq. 5.6 ensures that the fast reactions dominate the chemical time scale, yet the formulation takes into account that the faster reactions solely represent a portion of the combustion process.

$$t_c = \frac{\sum_{i=1}^{N_{sp}} c_i}{\frac{\sum_{j=1}^{N_r} \sum_{i=1}^{N_{sp}} \left(\nu''_{i,j} k_j^f \prod_{l=1}^{N_{sp}} c_l^{\nu'_{l,j}} \right)}{N_r}} \tag{5.6}$$

The model source term C_{kk} incorporates further components of secondary importance that shall be briefly explained in the following. The model constant C_{tc} is introduced in order to scale the source term, although no obvious reason exists to apply another value for C_{tc} than one. However, it provides the possibility to investigate the sensitivity of the solution with respect to a scaling of the source term C_{kk}, as done in chapter 7. Furthermore, C_{kk} contains two limiter functions f_c and f_k. The function f_c effectively deactivates the source term in regions, where the chemical time scale becomes larger than a specifiable maximum chemical time scale, see eq. 5.7. Actually, the source term is effectively deactivated, if the magnitude of the chemical time scale considerably exceeds the viscosity, cf. eq. 5.5. However, f_c provides the ability to control this clipping.

Furthermore, the generation of turbulent fluctuations by chemical time scales smaller than the Kolmogorov time scale is physically not possible. Eddies of this size would dissipate instantly, according to the turbulence theory of Kolmogorov. The function f_k deactivates the combustion induced source term in such a particular case in order to take this physical constraint into account, see eq. 5.8. It is not very likely that the chemical time scale will fall below the Kolmogorov time scale for the investigated cases. Nevertheless, this term em-

phasizes the motivation of the model within the concept of turbulence being tied to a minimum length scale.

$$f_c = \tanh(\frac{t_{c,max}}{t_c}) \tag{5.7}$$

$$f_k = (0.5 + 0.5\text{sign}(t_c - \tau_\eta)) \tag{5.8}$$

In order to investigate the effect of the novel model on practical combustion cases, the model is applied to the simulation of the supersonic diffusion flame in chapter 7 by means of RANS and to the hybrid RANS/LES simulation of the ITLR scramjet combustor in chapter 8.

6 Non-Reacting Jet in Supersonic Crossflow

A necessary prerequisite for the proper reproduction of combustion phenomena occurring in supersonic combustors is the capability of a numerical method to account for shock boundary layer interactions and the mixing of fuel and air. In order to validate and assess the functionality of the implemented solver with respect to these phenomena, a non-reacting supersonic injection experiment is investigated, which is conducted at the TUM Institute for Flight Propulsion [91]. In particular, the experiment allows for a study of the prediction of fuel injection coupled with a shock boundary layer interaction problem within a wall-confined duct representing a combustor section. Two simulations are performed, one based on RANS and one based on hybrid RANS/LES.

As stated in chapter 4, method B is intended to reduce the extent of the RANS zone to a reasonable minimum in cases with extensive boundary layer thickness, especially in the transition between ramjet and scramjet operation, see section 8. The jet in crossflow configuration investigated here neither features combustion induced pressure rise nor an extensive duct length, such that the boundary layers remain comparably thin. Hence, part B of the hybridization method is obsolete in this case and the hybrid simulation employs solely hybridization method component A presented in section 4.4.

6.1 Experimental Setup

Essentially, the experimental setup consists of a Laval nozzle and a strut injector as shown in figure 6.1. The injector strut is exposed to the Mach 1.9

crossflow provided by the Laval nozzle. Moreover, the injector can be moved along the axis of flow direction. Glass windows constitute the side walls and enable optical access for Schlieren photography. Carbon dioxide is injected perpendicularly through seven circular injection ports at the upper side of the injector. Each of the seven injection ports features a diameter of 0.4 mm. Due to the large injection pressure of 15 bar, the carbon dioxide jet reaches sonic conditions at the injection port outlets.

The top half of the injector features the same geometry and injection hole pattern as the upper half of the central strut injector utilized in the TUM scramjet combustor described by Fuhrmann et al. [48, 49]. The vertical distance between the injector leading edge and the upper wall amounts to 12.5 mm. However, the experimental conditions, summarized in table 6.1, differ from the actual combustor. The total temperature corresponds to the ambient temperature of 300 K, the jet fluid is carbon dioxide instead of hydrogen and the Mach number of 1.9 is slightly lower than the combustor Mach number of 2.1. Nevertheless, the prevalent flow phenomena concerning the shock system and jet injection are qualitatively the same.

Wall pressure measurements are obtained by displacing the strut along the axis of flow direction and measuring the pressure at a single pressure tap. Hence, the displacement of the strut is considered to be equivalent to a continuous wall pressure scan along the upper wall enabling a higher spatial resolution than the distance between two adjacent pressure taps would allow. Since the strut is displaced by a maximum distance of solely 32 mm, it is assumed that the change in boundary layer thickness is negligible. Additionally, Schlieren images are available supporting a comparison of computational and experimental flow fields. This comparison is a central part of this chapter, since it provides valuable information about the capability of the implemented numerical methods to predict the shape and locations of shock waves generated within the duct.

The generic situation of a perpendicular jet in a supersonic crossflow is discussed in chapter 2.4.2. In addition to this generic case, the present situation features the reflection of the shock induced by the injector ramp at the upper channel wall opposing the injector. As a consequence of this interaction,

Table 6.1: Fluid and injection properties

	Crossflow	**Jet**
Fluid	air	carbon dioxide
Total temperature	300 K	300 K
Total pressure	6.8 bar	15 bar
Mach number	1.906	1
Num. of injection holes	-	7
Diameter of injection holes	-	0.4 mm
Momentum ratio J	-	2.1

the boundary layer separates and a separation bubble forms at the upper duct wall, see section 2.4.1.2. This separation bubble locally increases the boundary layer thickness and acts as a ramp for the supersonic flow further upstream. As a result, a reflected shock wave forms and finally impinges on the injector wall.

In summary, the jet in supersonic crossflow experiment discussed here exhibits three major phenomena relevant for supersonic combustion: Firstly, shock boundary layer interaction caused by the presence of a central injector strut, secondly, penetration and mixing of the injected fluid with the crossflow, thirdly, the interaction of the injected fluid with reflected shocks.

6.2 Numerical Setup

The model parameters utilized in the subsequently presented simulations are summarized in table 6.2. The same turbulent Prandtl and Schmidt numbers are applied to the RANS and LES turbulence models. Different Schmidt numbers are applied for each of the three species involved in order to account for varying species diffusivities according to table 6.2. Table 6.3 provides the applied parameter settings for hybridization method A utilized for the hybrid RANS/LES simulation. The maximum RANS zone thickness $C_{A,z,max}$ is set to a value of 3.5 mm, such that the dynamic part of hybridization method A can potentially cover the whole boundary layer at the duct wall opposing the injector. In contrast to that, the injector wall boundary layer is treated with a pure

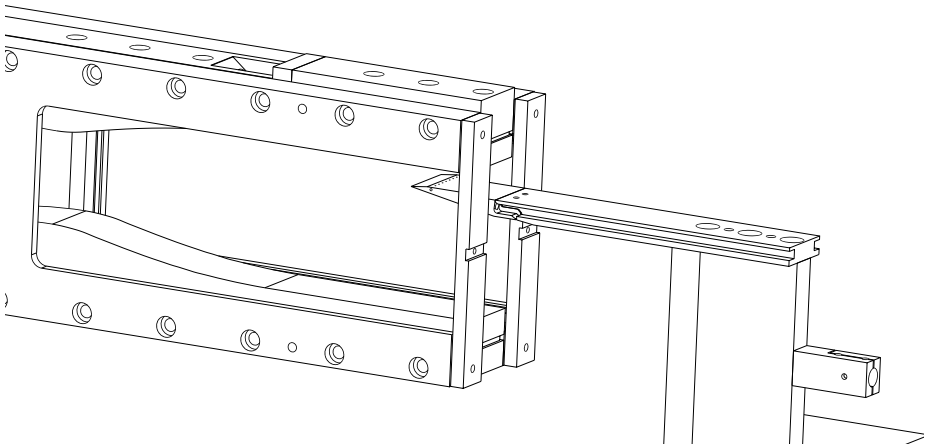

(a) Injection experiment setup

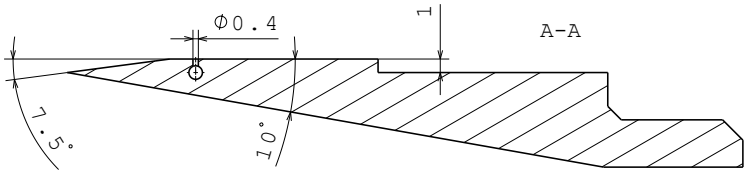

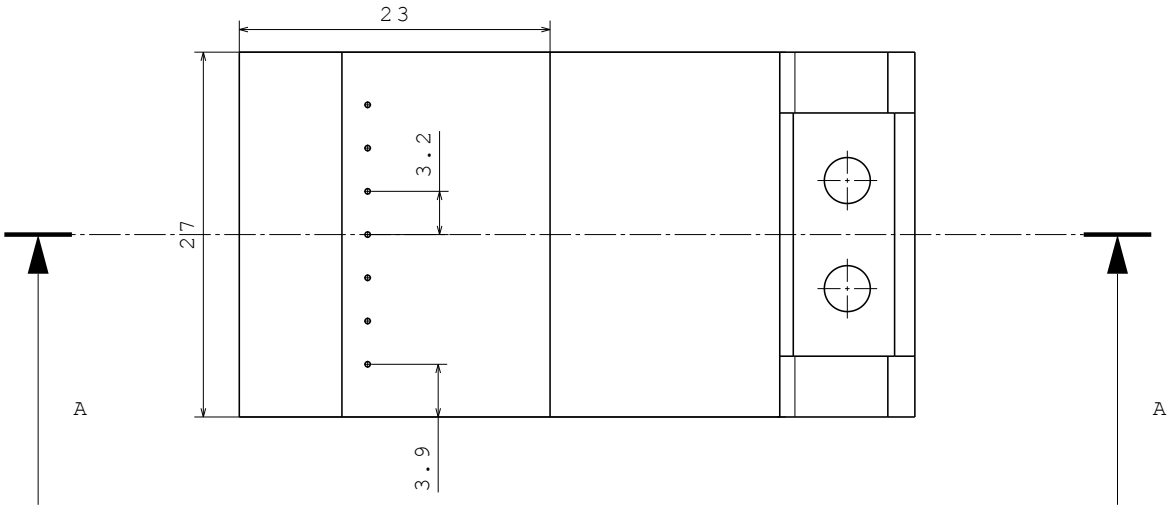

(b) Injector strut dimensions

Figure 6.1: Top: supersonic injection experiment setup; bottom: wedge injector strut; dimensions in millimeters, section of measurements: 32 mm, reference position: tip of injector wedge

Table 6.2: Simulation parameters

Pr	0.7
Sc_{CO_2}	0.98
Sc_{O_2}	0.76
Sc_{N_2}	0.75
$Pr_{t,RANS}$	0.85
$Pr_{t,LES}$	0.85
$Sc_{t,RANS}$	0.6
$Sc_{t,LES}$	0.6

Table 6.3: Hybridization method parameter settings

$C_{A,z,min}$	0.5 mm
$C_{A,z,max}$	3.5 mm
$C_{A,t}$	0.1 %
$C_{A,d}$	1.0
C_{pz}	0.35 mm

zonal hybridization approach limiting the RANS zone to a relatively thin layer. Two reasons justify this approach: Firstly, the injector wall boundary layer features a small thickness due to the short distance from the tip of the injector. Secondly, the RANS zone shall be kept at a minimum in the injection region in order to assess the capabilities of the LES mode to resolve the jet and crossflow mixing involving the intrinsic development of coherent turbulent structures. The constant RANS zone thickness C_{pz}, see section 4.6, utilized for the injector boundary layer is set to a value of 0.35 mm, see table 6.3.

6.2.1 Boundary Conditions

The crossflow inlet fields for all transported variables and properties are mapped from the outlet of a preceding simulation by Heidenfelder and Paßler [64] conducted for the Laval nozzle utilized for the experiment.

Each injection port is modeled by means of a convergent nozzle with a preceding reservoir. The throat of the nozzle corresponds to the injection port hole in the injector strut. Thus, sonic conditions are generated at the correct total pressure, corresponding to the actual injector. The static temperature and pressure are set to the experimental values of 293 K and 15 bar, whereas a von Neumann zero gradient condition is utilized for the velocity at the reservoir inlet.

Usually, LES demands the application of turbulent fluctuations at the inlet boundaries. However, this is omitted here due to several reasons: Firstly, the

most crucial part of the inflow concerning turbulence are the boundary layers. Yet, in the context of the hybrid RANS/LES methods developed within this work, the boundary layers are treated with RANS, which neither requires nor generates turbulent fluctuations. Secondly, no measurements are available defining the state of the inflow turbulence or the boundary layers. This means that even if a synthetic turbulence method was applied, there would be no possibility to assess the correctness of the applied fluctuations. Neglecting the inflow turbulence further allows for the analysis of turbulent structures developed intrinsically within the system being the purpose of the investigation.

Since no boundary layer separation at the exit was observed in the experiment, significant upstream effects originating at the outflow are not expected. Thus, a von Neumann boundary condition is applied to the outflow setting the gradient of all transported fields to zero.

Measurements concerning the wall temperatures are not available. However, since the inflow features a static temperature of solely 166 K, it is expected that a moderate heat flux will develop from the ambient atmosphere towards the flow through the wall. In order to account for this, the channel walls are set to an estimated temperature of 200 K. The same wall temperature is applied to the injector wall, which is expected to be slightly cooled by the surrounding crossflow. The velocity is subject to a no slip boundary condition at the walls. A wall function is applied to the turbulent viscosity [96]. Zero gradient boundary conditions are applied to the pressure and species mass fraction fields.

6.2.2 Computational Grids

The RANS mesh contains 6 million cells and makes use of the symmetry condition along axis A-A, cf. figure 6.1, thus covering half of the channel width. Wall functions are applied with a maximum y^+ of 48.

The hybrid RANS/LES mesh contains 16 million cells and covers the same length as the RANS mesh, but only one injection port. Therefore, the mesh has a width of 3.2 mm, cf. figure 6.1 being the distance between two injection

ports. Cyclic boundary conditions are imposed at the side walls, such that the effects of neighbor injections are taken into account. In a similar fashion as in the RANS case, the inner boundary layer is treated with a wall function approach with a maximum y^+ value of 36. The majority of computational cells is placed in the wake region of the injection port extending behind the injector strut trailing edge in the interest of an adequate resolution of the mixing of jet fluid and air. The average cell size in streamwise direction amounts to 0.375 mm, 0.4 mm in crosswise direction and 0.3 mm in the direction orthogonal to the injector wall within this region.

6.3 Comparison of RANS and Hybrid RANS/LES Results

6.3.1 Wall Pressure Distribution

The applied wall function approach reduces the computational costs of a wall-confined simulation. However, this also decreases the predictive capabilities concerning the exact size of shock induced boundary layer separation regions, since the wall-normal velocity gradient is not resolved. Its effects are solely taken into account by the algebraic wall model. Yet, Makowka et al. demonstrate that the difference between a boundary layer resolving approach and the application of wall functions is negligible in this case [91]. Figure 6.2 shows the comparison of experimental and computational wall pressures obtained with the pure RANS and hybrid method. The pressure is normalized with the total inlet pressure. Despite the deficiencies of a wall function for the description of the turbulence within the lowermost boundary layer regions, the general shape agrees well for the pure RANS as well as for the hybrid simulation, which both apply wall functions. Concerning the situation within a full combustor, the phenomenon observed here constitutes indeed an important element, yet solely one fraction of the investigated problem. In this respect, the dimension of the region influenced by the shock induced pressure rise within the separation bubble does not agree exactly with the experimental results, but still gives a satisfactory reproduction of the pressure trend.

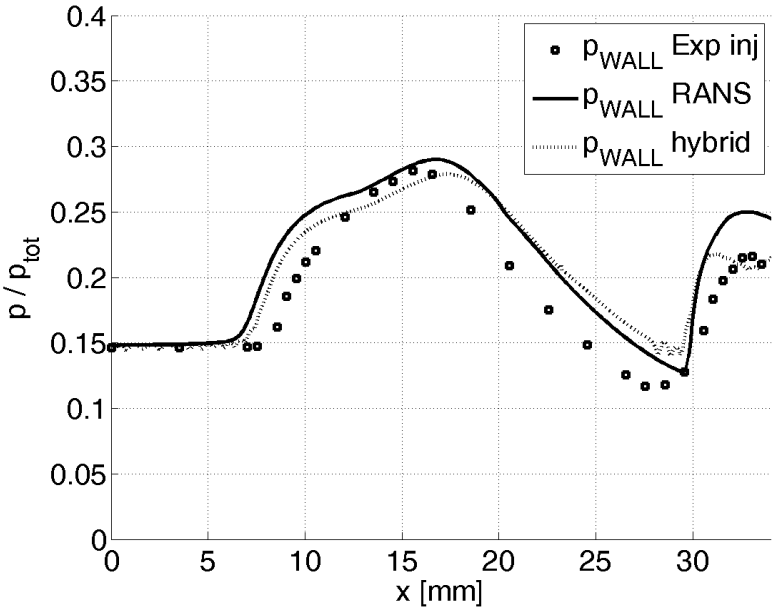

Figure 6.2: Comparison of RANS and hybrid RANS/LES wall pressures with experimentally measured wall pressure; wall pressures normalized with total inlet pressure cf. table 6.1

6.3.2 Flow Field and Shock System

Figure 6.3 demonstrates the underlying principle of hybridization method A. The method increases the size of the RANS region (colored in dark gray) in the shock boundary layer interaction region. In accordance with the illustration in figure 2.1, the shock induced boundary layer separation leads to an increase of the boundary layer thickness downstream of the interaction region, which is reflected by the thicker RANS zone compared to the inflow conditions. Exactly this feature is the purpose of the novel method: The changing boundary layer thickness is identified and accounted for by applying RANS in the respective areas.

The application of RANS in this region has several desirable consequences and effects: Firstly, the mesh does not require to have LES resolution, especially in the area involving the dominant shock boundary layer interaction. Secondly, the extent of the RANS layer is only as large as necessary in order to provide a reliable boundary layer prediction while maintaining a coarse near-

Table 6.4: Evaluation plane downstream locations measured from injection port center, see figure 6.3

Plane	S1	S2	S3	S4	S5	S6	S7	S8	S9	S10	S11
Distance [mm]	0	2	4	6	8	10	12	14	16	18	20

wall mesh at the same time. Moreover, the RANS zone thickness is considerably smaller before and and behind the separation bubble region. This leaves a maximum amount of space for the LES mode. Finally, the location of the hybrid RANS/LES interface is chosen dynamically by the hybridization model based on the current, local solution without requiring any user input. As stated in section 6.2, the injector wall boundary layer is treated with a constant RANS zone thickness in order to enable a maximum amount of LES in the jet mixing region. Hence, the RANS zone at the injector wall perceptible in figure 6.3 extends only slightly into the flow volume.

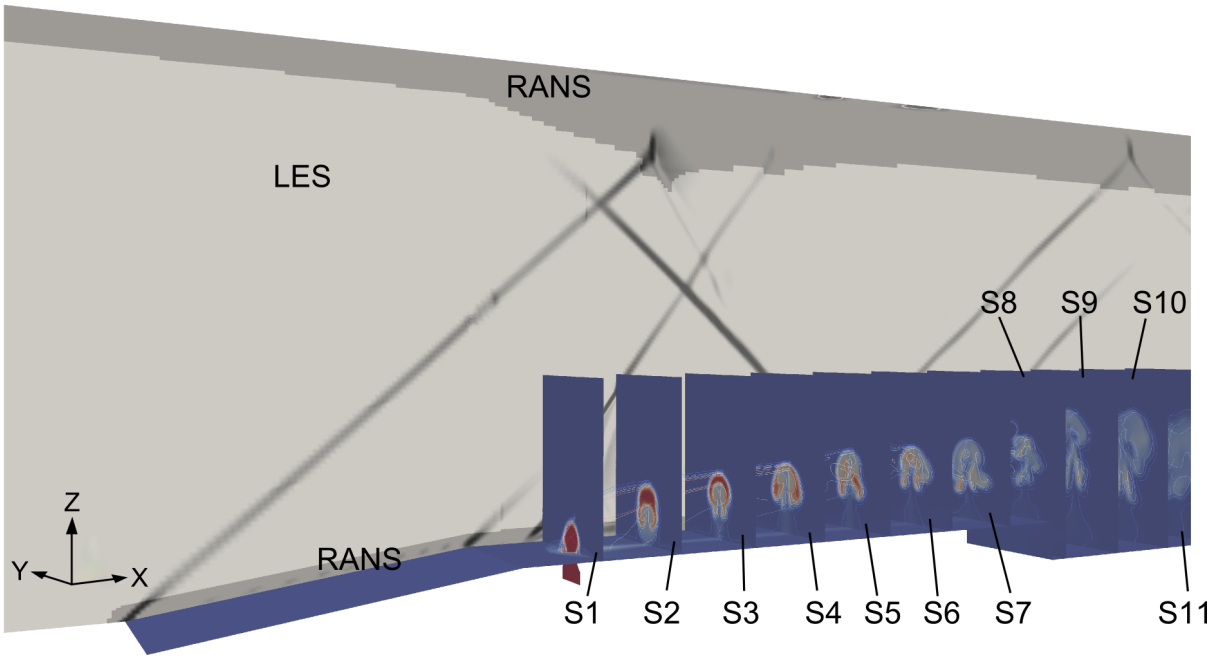

Figure 6.3: CO_2 mass fractions from hybrid RANS/LES simulation at several evaluation planes downstream of the point of injection; zero position corresponds to injection hole center; see table 6.4 for evaluation plane positions

A comparison of experimental and computational Schlieren images for the pure RANS and hybrid case is given in figure 6.4 indicating a very good general agreement of the computational results concerning the prediction of the structure of the shock system. In particular, the location, where the reflected leading edge shock impinges on the injector, matches the experimental location well in both simulations. The shock reflected at the upper duct wall is defined by the interaction of the incoming injector leading edge shock wave and the upper wall boundary layer. Hence, figure 6.4 provides evidence that both simulations reproduce this complex interaction with sufficient accuracy, despite the simplifications conducted through the wall function approach. In consequence, both RANS and hybrid RANS/LES are capable of capturing the locations of shock induced temperature and pressure increase correctly. This constitutes an important asset for the subsequent simulation of ignition and combustion in a realistic scramjet combustor.

Additionally, the shock induced separation region leads to a partial obstruction of the duct, which may act as an aerodynamic nozzle for the remaining flow outside of the boundary layer. Both simulations provide a good reproduction of this separation region size, approximately indicated by the position, where the leading edge shock and the reflected shock intersect.

Another relevant phenomenon is the bow shock induced by the injection of jet fluid, cf. figure 2.4, which induces an additional pressure rise increasing the size of the boundary layer separation region at the upper wall. Both the pure RANS and the hybrid simulation successfully predict the location, where the bow shock impinges on the duct at almost exactly the same position as in the experiment.

Moreover, the requirement for the hybrid RANS/LES is that it does not perform worse than the pure RANS with respect to the agreement with experimental validation data. On the other hand, the hybrid RANS/LES capabilities in terms of the reproduction of boundary layer effects are limited by the RANS turbulence model deficiencies. Nevertheless, the hybrid simulation features a finer mesh also in the separation bubble region, which has a positive effect on the results. For this reason, the location of reflected shock impingement matches the experiment slightly better than the pure RANS, cf. figure 6.4. In

summary, the proposed hybrid RANS/LES based on method A succeeds in predicting the crucial gas dynamic phenomena present in the given supersonic duct, being the prerequisite for further investigations.

6.3.3 Jet and Crossflow Mixing

After all, the potentially higher predictive capabilities of LES constitute the main motivation for pursuing a hybrid RANS/LES approach. With the purpose of assessing the benefits of hybrid RANS/LES in comparison to pure RANS with respect to fuel mixing, the CO_2 distributions at several cross-section planes downstream of the injection port shall be analyzed. Figure 6.3 illustrates the locations of the evaluation planes having a distance of 2 mm between each other. The downstream x-locations refer to the injection port center as the zero position.

Figures 6.6 and 6.7 show a comparison of RANS and hybrid mean CO_2 fields for the evaluation planes illustrated in figure 6.3. The first eight image pairs show y-z-planes above the injector wall, whereas the latter four image pairs refer to evaluation planes located downstream of the injector trailing edge. Two major differences between the two simulations are evident: Firstly, the simulation employing the hybrid RANS/LES approach predicts a higher penetration depth of the jet amounting to 2.5 mm, whereas the RANS predicts a smaller depth of only 2.15 mm above the injector wall. Here, the penetration depth is defined as the 1%-CO_2 iso-contour. Secondly, the counter-rotating vortex pair, cf. figure 2.4, is clearly visible in the hybrid simulation recognizable by the CO_2 agglomerations sideways of the symmetry plane. In contrast to that, the counter-rotating vortex structure is vaguely perceptible in the RANS simulation. The high turbulent diffusivity originating in the RANS model spreads the CO_2 over a large region and solely indicates the approximate extent of the distribution of jet fluid. Yet, the CO_2 field based on the RANS simulation is deprived of any discernible structure.

Figure 6.8 shows instantaneous hybrid RANS/LES CO_2 fields for the same evaluation planes as in figures 6.3, 6.6 and 6.7. Again, the vortical structure of the counter-rotating vortex pair is prominent. In addition to that, the turbulent

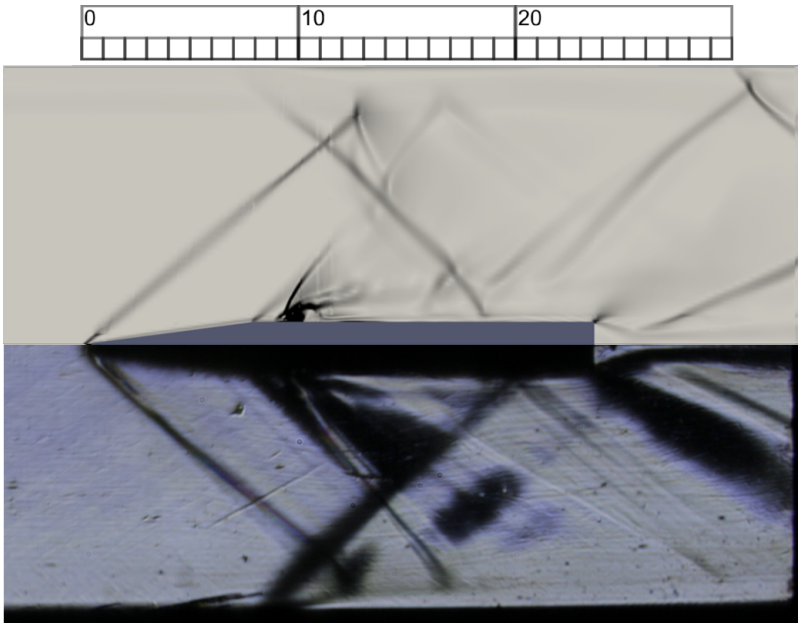

(a) RANS

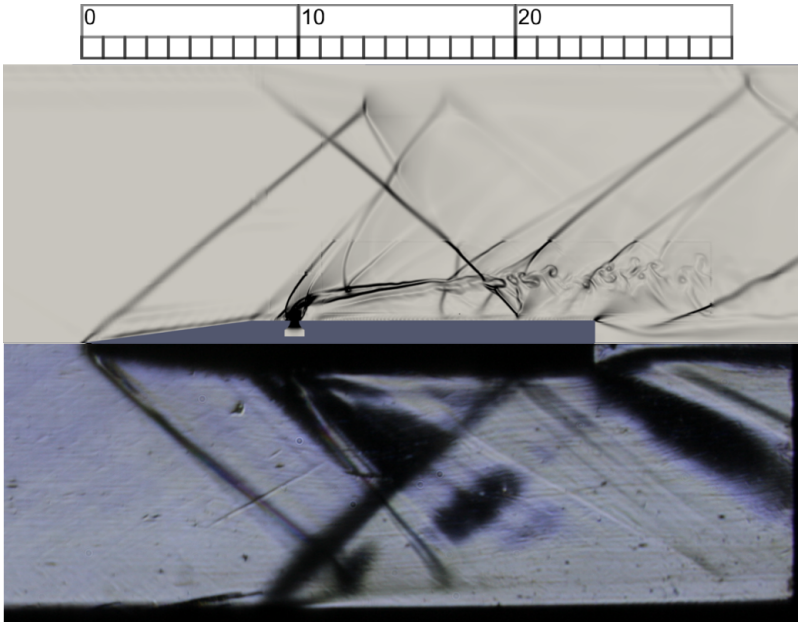

(b) Hybrid RANS/LES

Figure 6.4: Computational Schlieren images (top half of images) versus experimental Schlieren images (bottom half of images); top: pure RANS; bottom: hybrid RANS/LES; zero position corresponds to tip of injector strut, length scale in millimeters

distribution of CO_2 becomes evident starting at x = 10 mm downstream of the injection location. The injected CO_2 is subject to turbulent transport in lateral directions outside the large scale vortical structure of the counter-rotating vortex pair. As stated previously, no synthetic turbulence is imposed neither at the domain inlets nor at the RANS/LES interface. Hence, the turbulent motions resulting in the chaotic CO_2 distribution perceptible in figure 6.8 are an intrinsic consequence of the jet in crossflow configuration.

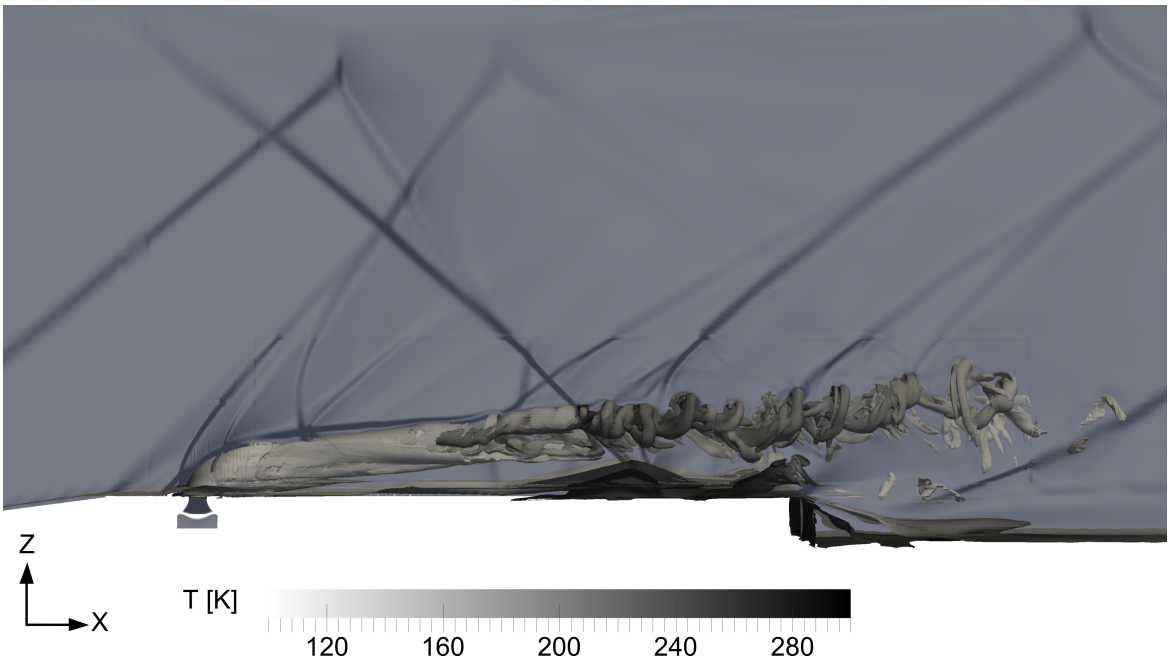

Figure 6.5: Computational Schlieren image corresponding to figure 6.4b overlaid with Q-criterion 1e11-iso-contour colored by temperature

The location where the irregular, turbulent structures become prominent corresponds quite accurately to the position, where the reflected leading edge shock impinges on the injector wall, cf. figures 6.4, implying a connection. Especially the three-dimensional Q-criterion iso-contours [21] plotted in figure 6.5 illustrate the sudden appearance of coherent turbulent structures at this location. The shock passes through the CO_2 jet and leads to baroclinic vorticity generation being the result of a misalignment between the local density and pressure gradients. The pressure gradient is obviously imposed by the impinging shock, which is also visible through the sharp temperature rise on the right hand side of figure 6.5. The density gradient is given by the presence of

the CO_2 jet. The result is the transient distortion of the previously well-defined counter-rotating vortex structure. Nevertheless, the mean field still features the vortex pair, see figures 6.6 and 6.7. Thus, the vorticity induced by the impinging shock can be regarded as a transient phenomenon that promotes the mixing of jet fluid and air, yet it does not prevent the propagation of the dominating vortex. In addition to the reflected leading edge shock, the bow shocks induced by neighbor injections also impinge on the jet and add further vorticity by imposing additional pressure gradients, as can be inferred from figure 6.5.

6.3.4 Summary

In summary, the hybrid method satisfies the requirement to correctly predict the position where the reflected leading edge shock impinges on the central injector. The correctness of this prediction even exceeds the RANS result, which is attributed to the generally higher mesh resolution. Yet, the computational investigation of the ITLR combustor in chapter 8 shows that the deficiencies of the RANS approach remain if the finer hybrid RANS/LES mesh is applied in that case.

An important aspect is that the hybrid RANS/LES method provides the benefit of resolving the vortical structures dominating the jet in supersonic crossflow configuration, in particular the counter-rotating vortex pair and the superimposed vorticity induced by baroclinic effects. This stands in strong contrast with the RANS simulation, which is not capable of resolving turbulent transport phenomena of this kind. Moreover, differences exist in terms of the jet penetration depths predicted by RANS and the hybrid approach, since the hybrid simulation predicts a slightly larger penetration of the carbon dioxide jet. The improved capabilities of LES to resolve scalar transport mixing as compared to RANS gives reason to expect that the penetration depth predicted by the hybrid RANS/LES is more correct.

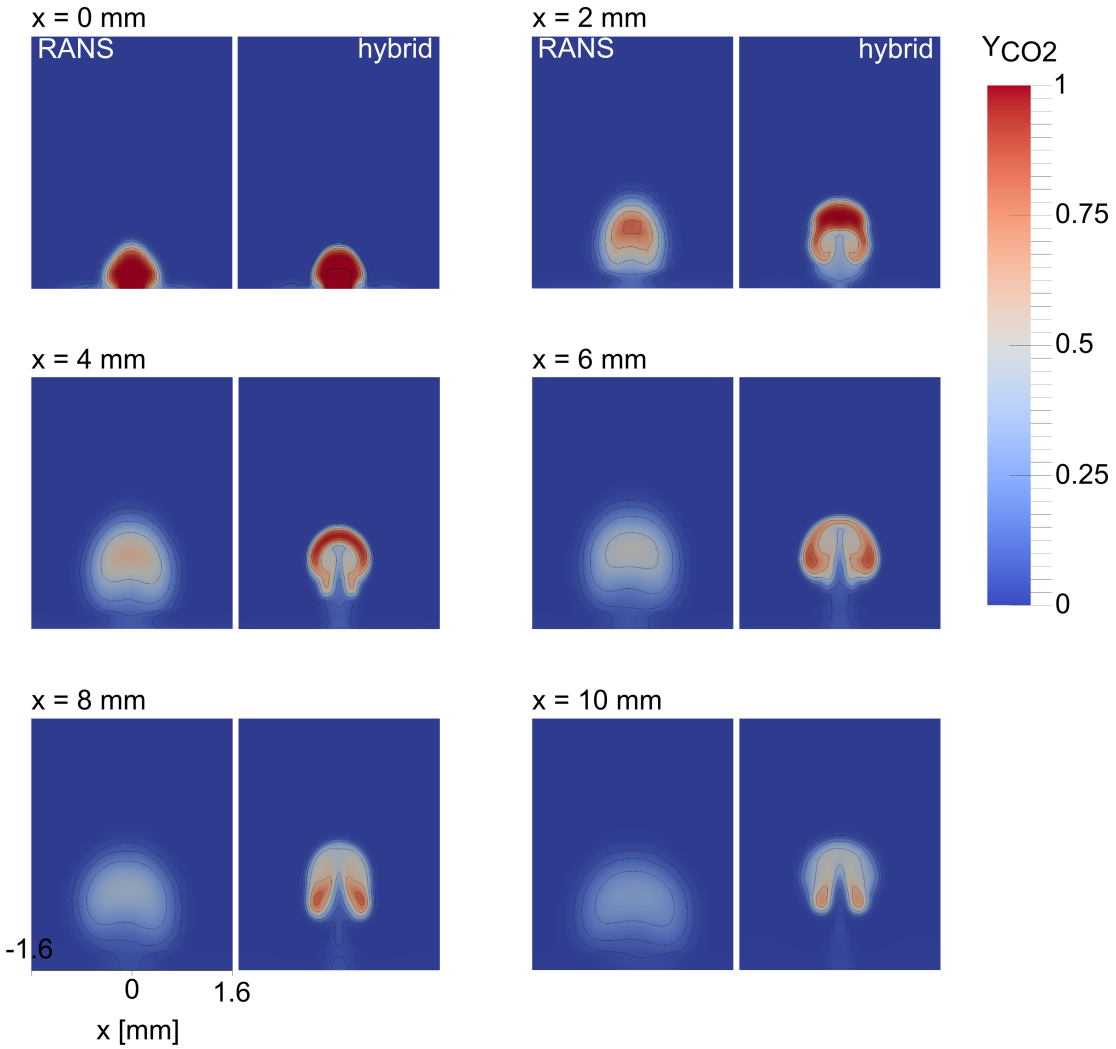

Figure 6.6: Comparison of RANS and hybrid RANS/LES CO_2 contours for several y-z-planes at downstream locations shown in figure 6.3

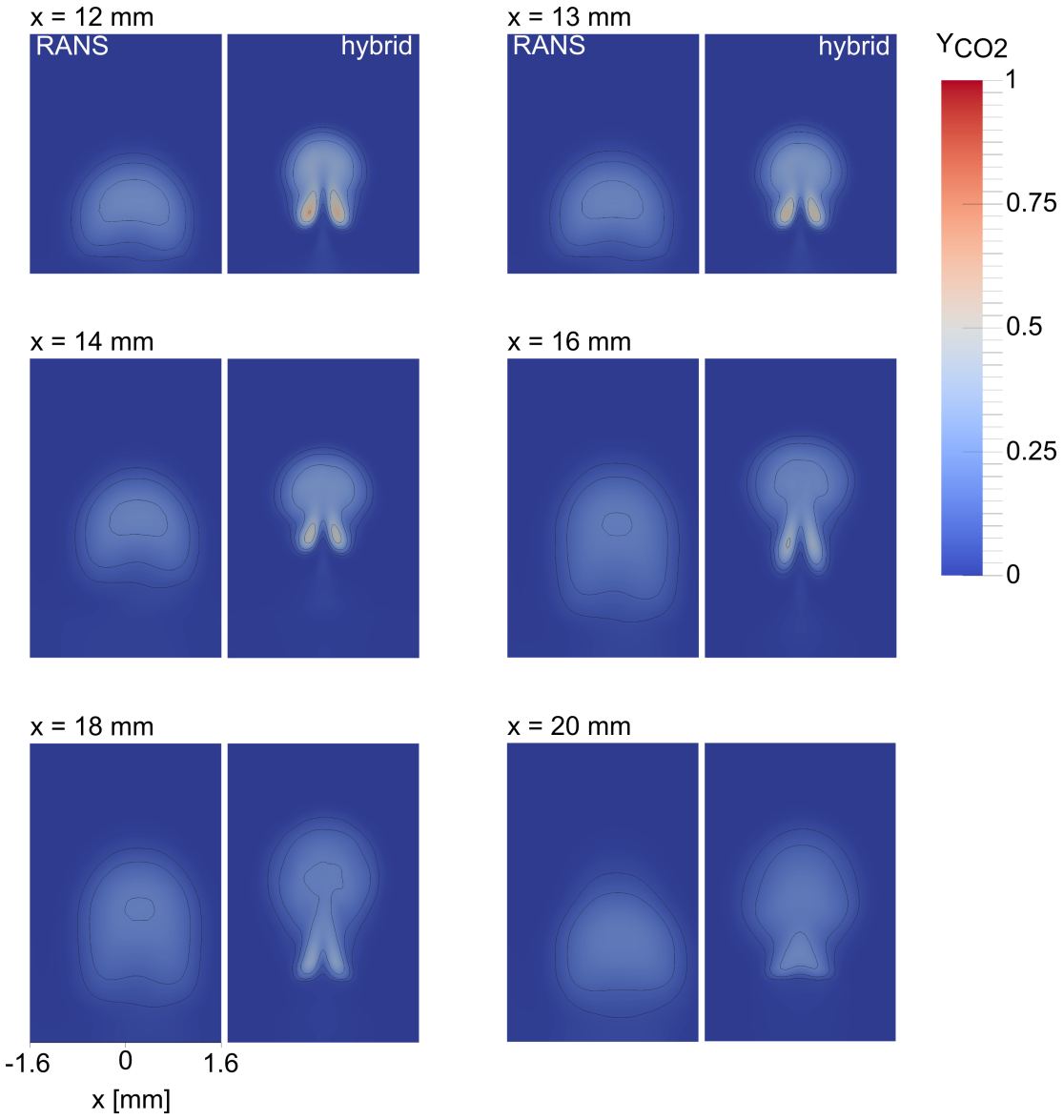

Figure 6.7: Comparison of RANS and hybrid RANS/LES CO_2 contours for several y-z-planes at downstream locations shown in figure 6.3

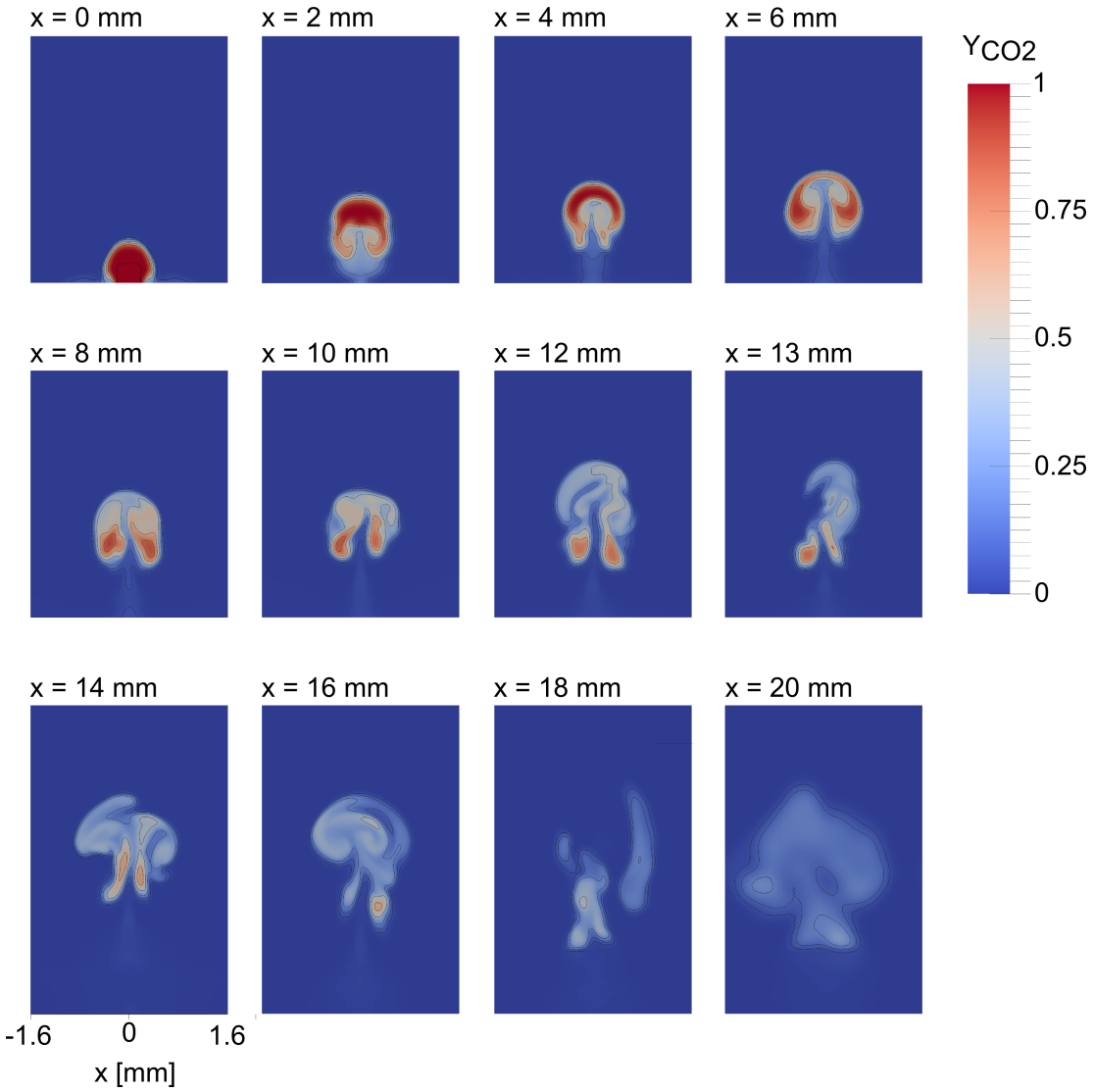

Figure 6.8: Instantaneous hybrid RANS/LES CO_2 contours for several y-z-planes at downstream locations shown in figure 6.3

7 Supersonic Diffusion Flame

Well-documented fundamental supersonic combustion experiments with publicly accessible data are rare. Cheng et al. conducted an often-cited experiment in 1994 [24], in which they investigate a generic supersonic diffusion flame. The experimental setup consists of an annular precombustion chamber enhanced with a hydrogen injector in the center of the chamber exit, cf. figure 7.1. The precombustor can be thought of as a hydrogen fueled rocket engine with lean combustion and therefore only partial oxygen consumption. The vitiated air exiting the precombustor exhibits a significant temperature level induced by the precombustion and ignites the hydrogen injected at the outlet. Finally, this results in the actual supersonic diffusion flame further downstream being the matter of investigation here. The experiment by Cheng et al. is especially valuable due to the availability of temperature and species concentration profiles measured by means of Raman spectroscopy. Nevertheless, there exist issues concerning the simulation of the Cheng flame related to uncertainties with respect to the inflow boundary conditions that will be discussed in the following.

This chapter provides a validation of the implemented solver discussed in chapter 3 with respect to the simulation of supersonic combustion by means of RANS. Subsequently, light shall be shed on the following aspects: Firstly, it is demonstrated that the differences between the application of a first order accuracy time integration and a fourth order Runge-Kutta scheme are negligible in the given context. Secondly, the effect of the model for combustion induced turbulence derived in chapter 5 is analyzed. The latter aspect is supported by a comparison with a variation of the turbulent Prandtl and Schmidt numbers. Although both approaches are based on different motivations, the common effect is an increase in turbulent diffusivity. The local effect of the developed model for combustion induced turbulence contrasts with the global increase

of turbulent diffusivity based on the turbulent Schmidt and Prandtl number variation.

7.1 Experimental Setup

A section view of the radially symmetrical precombustor geometry is shown in figure 7.1. The experimental measurements are available at the illustrated locations denoted in the relative distance x/D measured from the hydrogen injector outlet. The inner diameter D of the hydrogen injector utilized as the reference length amounts to 2.36 mm. The precombustor nozzle features an inner diameter of 17.78 mm and a half-angle of 4.3° resulting in a divergent vitiated air free stream, cf. 7.1. The wall between the hydrogen injector duct and the vitiated air outflow has a thickness of 0.725 mm at the exit. The hydrogen injector protrudes beyond the precombustor exit and provides hydrogen at sonic conditions at a static temperature of 545 K. The nominal fuel mass flow rate amounts to 0.000362 kg/s. The conditions of the vitiated air exiting the precombustor nozzle as denoted by Cheng et al. are given in table 7.1.

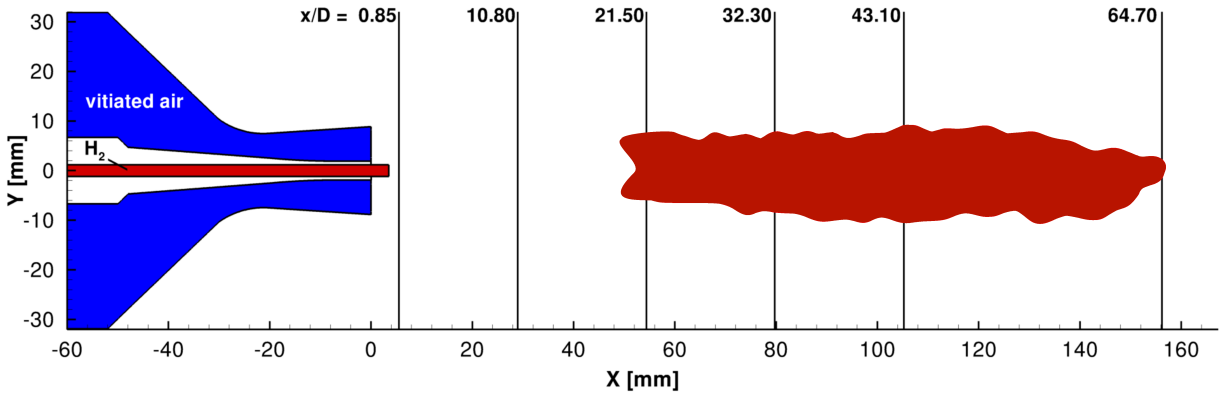

Figure 7.1: Setup of the supersonic diffusion flame experiment by Cheng et al. [24] with approximate flame location

The density and velocity gradients between the inner hydrogen jet and the annular vitiated air jet induce a mixing layer, which results in a lateral distribution and temperature rise of the hydrogen. Sufficient conditions for ignition are provided by the vitiated air static temperature of 1250 K being a

Table 7.1: Cheng precombustor vitiated air conditions

	Experiment [24]	Simulation	Simulation Gerlinger et al. [54]
Vitiated air mass flow rate	0.09633 kg/	0.0955 kg/s	0.0944 kg/
Total pressure	7.78 bar	7.66 bar	7.66 bar
Total temperature	1750 K	1920 K	1920 K
Exit static pressure	1.07 bar	1.167 bar	1.15 bar
Exit static temperature	1250 K	1244 K	1280 K
Exit Mach number	2.0	1.9	1.9

result of the preceding precombustion. Finally, flame stabilization occurs approximately at x/D = 25, which marks the beginning of the combustion region. Furthermore, the vitiated air stream contains considerable amounts of water being the product of the preceding precombustion. Table 7.2 lists the vitiated air chemical species mass fractions according to the publication of Cheng.

Although the experimental setup is radially symmetrical, cf. figure 7.1, the measured species concentration and temperature profiles exhibit a deviation from this symmetry. The reasons for this partial asymmetries are unknown but might arise from a deformation of the precombustor nozzle or non-uniform precombustion.

7.2 Precombustor Simulation

While the determination of the fuel injection conditions gives no cause for concern, the situation is different for the conditions of the vitiated air exiting the precombustor. Without any doubt experimental work is subject to uncertainties. As long as the resulting lack of clarity does not determine the system behavior, the nominal experimental settings can be utilized for further investigations, e.g. by means of numerical simulations. However, the supersonic diffusion flame experiment discussed here features several uncertainties, which require consideration for a reasonable simulation setup. The nominal vitiated air conditions denoted by Cheng et al. [24] assume chemical equilibrium. Yet, Gerlinger et al. [54] have shown that the negligence of inflow radicals in simu-

Table 7.2: Species mass fractions at the precombustor inflow

Y_{O_2}	Y_{N_2}	Y_{H_2O}
0.245	0.58	0.175

lation leads to a considerably later ignition than in the experiment, if reasonable numerical models and settings are applied. Furthermore, perfect chemical equilibrium at the precombustor outflow appears questionable given the relatively short precombustor length. Hence, a preceding precombustor simulation is conducted in order to provide a correct inflow field for the actual supersonic diffusion flame simulation. The nominal experimental vitiated air conditions and the conditions derived from the precombustor simulation are summarized in table 7.1 together with the precombustor conditions determined by Gerlinger et al. [54].

The inlet stagnation temperature and pressure for the precombustor simulation are matched to the setup of Gerlinger et al. [54], since their numerical study provides the most comprehensive investigation of the Cheng supersonic flame precombustor flow to date. The species distribution at the precombustor inlet is set to the nominal experimental values given in the paper by Cheng et al. [24], see table 7.2. The precombustor geometry is also extracted from the original publication. Figure 7.2 illustrates the utilized two-dimensional precombustor wedge mesh consisting of 60000 cells. Effectively, a zero velocity condition and the total pressure and temperature are imposed at the domain inflow corresponding to the values summarized in table 7.1. Wall functions for the turbulent viscosity are applied with average y^+ values of 30 at the domain walls. Von Neumann zero gradient boundary conditions are imposed at the domain outlet. The outlet corresponds to the inflow plane of the actual supersonic diffusion flame simulation. Hence, the result of the precombustor simulation is mapped onto the vitiated air inlet of the subsequent supersonic flame simulation.

Chemical kinetics are modeled with the 21-step hydrogen reaction mechanism by O'Conaire et al. [104] in order to obtain reliable intermediate species distributions at the precombustor nozzle exit. As a result of the chemical reac-

tions within the precombustor simulation, an average OH mole fraction of approximately 0.0007 is obtained at the precombustor exit, which is of the same order of magnitude as the findings of Gerlinger et al. [54].

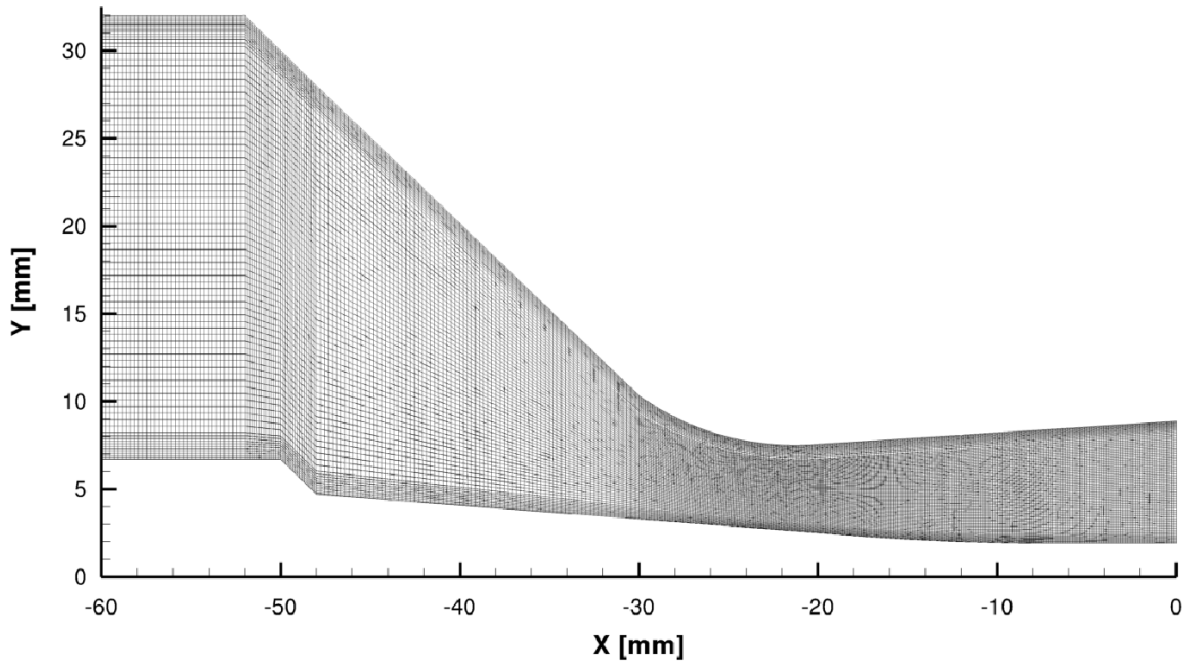

Figure 7.2: Computational mesh for the precombustor simulation

7.3 Numerical Setup

As stated earlier, the experimentally measured species concentration and temperature profiles lack the expected symmetry to some extent, although the precombustor is designed to be radially symmetrical. Since no trustworthy or quantifiable information about the reasons for this asymmetry in the flame structure are available, the lack of symmetry is neglected within the simulation. Hence, the topology of the simulated geometry can be reduced to a two-dimensional wedge through the utilization of the nominal radial symmetry saving computational costs. A full three-dimensional RANS simulation is not expected to provide any additional information in this case. This is in contrast to a LES, which would require a three-dimensional treatment in order to

resolve turbulent structures.

Corresponding to the simulations conducted for the precombustor flow, the simulations presented in this section are based on the comprehensive mechanism by O'Conaire et al. [104].

7.3.1 Computational Grid

The utilized mesh has a two-dimensional wedge topology in order to exploit the nominal radial symmetry of the experimental setup. It contains 56000 hexahedral cells and features a wedge angle of 4°. The vitiated air inlet corresponds to the outlet of the precombustor simulation discussed above and is discretized with 24 cells. The smaller hydrogen inlet slightly protrudes beyond the vitiated air inlet and features five grid points. Figure 7.3 illustrates the mesh section close to the precombustor outlet. The mesh resolution remains constant in x-direction. A boundary layer resolving mesh is not required at the protruding hydrogen injector due to the application of wall functions.

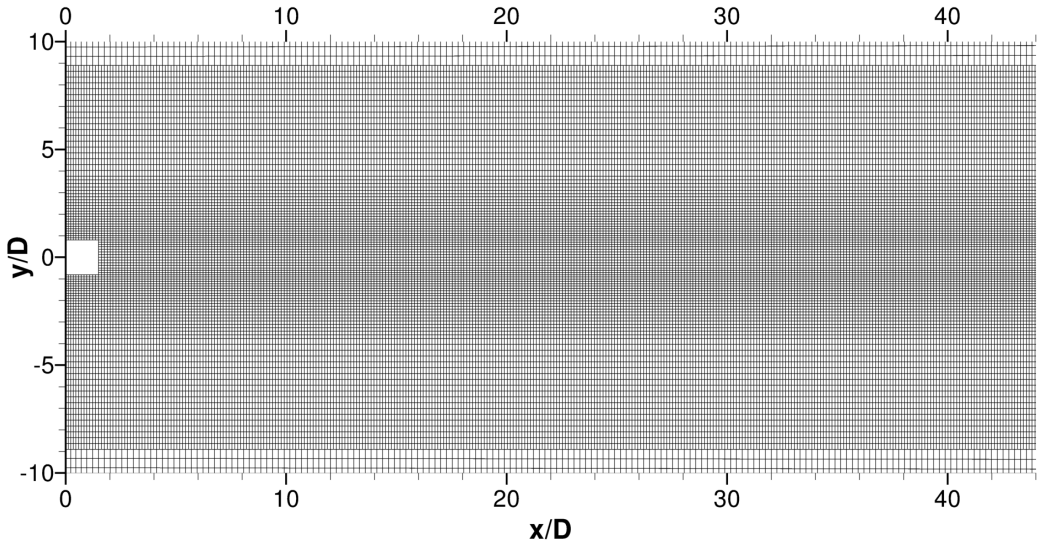

Figure 7.3: Computational mesh for the main simulation

7.3.2 Boundary Conditions

The vitiated air inflow boundary conditions are crucial for a proper simulation setup, as discussed previously. Hence, the precombustor simulation outflow is mapped onto the vitiated air inflow boundary. Due to this step, the inlet features the required inflow radicals originating in the precombustion process as well as a realistic velocity profile that influences the shear layer development further downstream.

Zero gradient boundary conditions are applied to all fields at the domain outflow opposing the inlet as well as at the side of the domain. The boundary neighboring the vitiated air inflow is treated equally with zero gradient boundary conditions, except for the velocity. A moderate air inflow of 20 m/s is imposed at this boundary in order to represent the suction effect of the high speed air jet to some extent. Yet, the influence of this setting is expected to be small. Wall functions are applied at the hydrogen injector wall protruding beyond the precombustor nozzle exit.

7.4 Unsteady Reynolds-Averaged Navier Stokes Simulation

A set of RANS simulations with varying setups is investigated in order to provide a validation of the implemented methods discussed in chapter 3 and chapter 5. As for all other simulations in this thesis, the time step of the simulations is dictated by the CFL condition, see section 3.1.2, thus yielding a small time step in the order of 5e-9 s in the cases presented here. Hence, the simulations basically represent URANS simulations. For this reason, the simulation results presented in the following are the outcome of temporal averaging over approximately 0.5 ms.

The following aspects are examined: Firstly, the RANS simulation based on the reference settings is evaluated. This simulation serves as the basis for the following simulations. Secondly, a comparison is drawn between the results obtained with a fourth order Runge-Kutta time integration scheme and the first order explicit Euler reference results. Thirdly, the effect of decreasing the

Table 7.3: List of RANS simulations

Test case	Pr_t	Sc_t	C_{tc}	Time integration
Ref	1.0	1.0	0	Euler
RK	1.0	1.0	0	RK4
SP	0.7	0.7	0	Euler
CT1	1.0	1.0	1.0	Euler
CT2	1.0	1.0	0.75	Euler
CT3	0.7	0.7	0.75	Euler

turbulent Prandtl and Schmidt numbers is investigated effectively implying a general increase of turbulent diffusivity in the whole domain. Finally, the influence of the combustion induced turbulence model introduced in chapter 5 is evaluated and compared to the global modification of the turbulent diffusivity through the turbulent Prandtl and Schmidt numbers. A summary of the simulated setups is given in table 7.3.

Figures 7.4 and 7.5 provide the computed temperature and H_2O mole fraction profiles for the reference simulation and the Runge-Kutta RK case together with the experimentally measured data. Figure 7.6 illustrates the corresponding two-dimensional mean temperature fields obtained with both simulations. Moreover, figures 7.8, 7.9, A.6 and A.7 provide the H_2O, OH, H_2 mole fraction and temperature profiles for the remaining setups listed in table 7.3. Finally, figures 7.7 through 7.13 illustrate the mean temperature fields for the reference setup in their upper halves. The corresponding mean temperature fields for the modified setups listed in table 7.3 are shown in the lower halves. The corresponding H_2O and OH mass fraction plots are given in appendix A. The downstream locations of the profile evaluation planes are given in figure 7.1.

7.4.1 Reference Case

The simulation denoted with the abbreviation Ref serves as the reference for the remaining setups discussed in this chapter. The turbulent Prandtl and Schmidt numbers are set to values of 1.0 each. Furthermore, the interaction

of turbulence and chemistry is neglected. Time integration is based on the first order explicit Euler scheme.

Figure 7.4 shows the temperature and H_2O mole fraction data for the first three measurement locations x/D = 0.85, x/D = 10.80 and x/D = 21.50 downstream of the precombustor exit. Combustion has not started at x/D = 0.85 and x/D = 10.80, yet. Hence, the comparison of the computational and experimental results at these locations indicates that the inflow conditions computed with the precombustor simulation match the experimental setting reasonably well.

The corresponding comparison for the three subsequent evaluation planes at x/D = 32.30, x/D = 43.10 and x/D = 64.70 is given in figure 7.5. As mentioned initially, the flame anchors approximately at x/D = 25 in the experiment. Hence, the two locations x/D = 21.50 and x/D = 32.30 mark the approximate beginning and end of the ignition region. Especially in those two slices, the unexplained asymmetry in the experimental results becomes obvious that was mentioned initially: Firstly, the two temperature and H_2O peaks left and right of the symmetry axis at x/D = 21.50 clearly exhibit different values. Secondly, the separate side peaks in both profiles merge into one at x/D = 32.30, however, the peak values feature a clear offset from the center line. In contrast to that, the computational profiles for the reference case still exhibit two distinct temperature and H_2O peaks at the x/D = 32.30 location. Although this is in contrast to the experiment, it is in accordance with other RANS investigations performed for the Cheng flame, which show the same qualitative behavior [47, 54]. Either, relevant information about the experimental boundary conditions are missing that might influence the flame development, or the applied models exhibit deficiencies that cause this structural deviation.

Furthermore, the reference simulation still predicts two distinct peaks in the temperature and H_2O profiles at x/D = 43.10, although they appear smaller than in the previous slices. This indicates that the main combustion region has not completely reached the centerline of the flow, yet. Here, the experimental data exhibit a smaller offset from ideal symmetry. Finally, at the last position x/D = 64.70, also the reference simulation predicts the profile maxima at the centerline. The computational prediction of the temperature distribution matches the experimental data well, which exhibit an almost ideally

symmetry at this last location.

7.4.2 Time Integration Scheme Influence

In order to assess potential differences between the explicit Euler time integration scheme and a higher order explicit time integration procedure, the reference setup is computed with the classical fourth order Runge-Kutta scheme, see table 7.3. The corresponding simulation is denoted by RK in the following figures. The presented results are temporal averages of URANS simulations that are unsteady in nature due to the small necessary time steps enforced by the CFL condition, see the previous section 7.4. The goal at this point is to demonstrate that the integrated numerical error introduced by the first order Euler time integration has an insignificant effect compared to the higher-order Runge-Kutta scheme, at least in the context of the investigated cases and the utilized small time step.

Essentially, Runge-Kutta schemes consist of a series of first order Euler subintegration steps, the results of which is weighted and added up to the final time step result. The choice of the weighting factors determines the order and thus numerical accuracy of the scheme. Generally, a higher order time integration scheme leads to a smaller numerical error and should therefore be superior to a lower order scheme, which constitutes the motivation for the application of such a method. The classical Runge-Kutta scheme applied here consists of four explicit Euler substeps and is of fourth order [32, 40].

In principle, the time step of one full Runge-Kutta step should be four times larger than a pure explicit Euler time step without losing numerical stability, since the utilized Runge-Kutta scheme is comprised of four explicit Euler steps. In reality, the effective numerical stability of the Runge-Kutta time integration of the governing equations utilized here allows only for a smaller time step increase. In the RK simulation, a CFL number of 0.4 is utilized in contrast to 0.3 for the explicit Euler simulations implying a time step increase by a factor of less than two. Paired with the computational overhead for storing and evaluating the intermediate time steps, the application of the fourth order Runge-Kutta scheme results in computational runtimes that are approx-

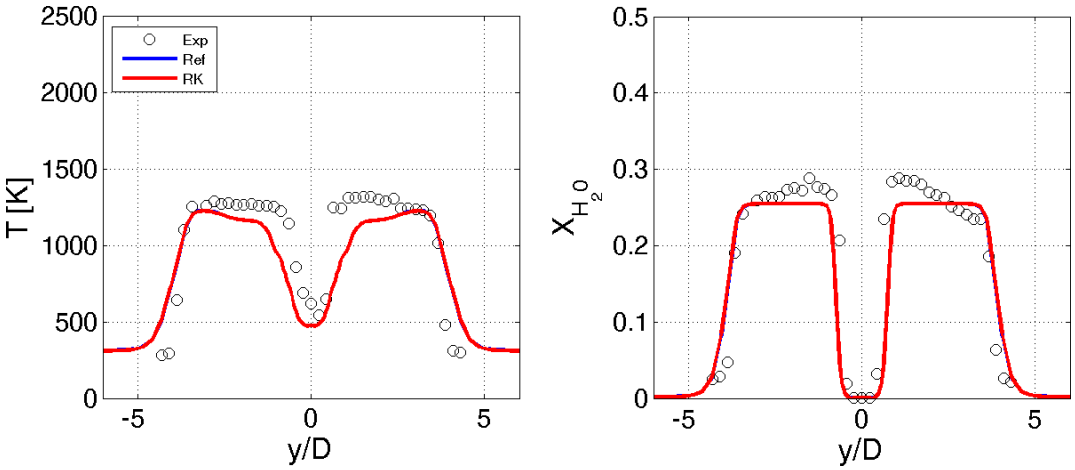

(a) x/D = 0.85

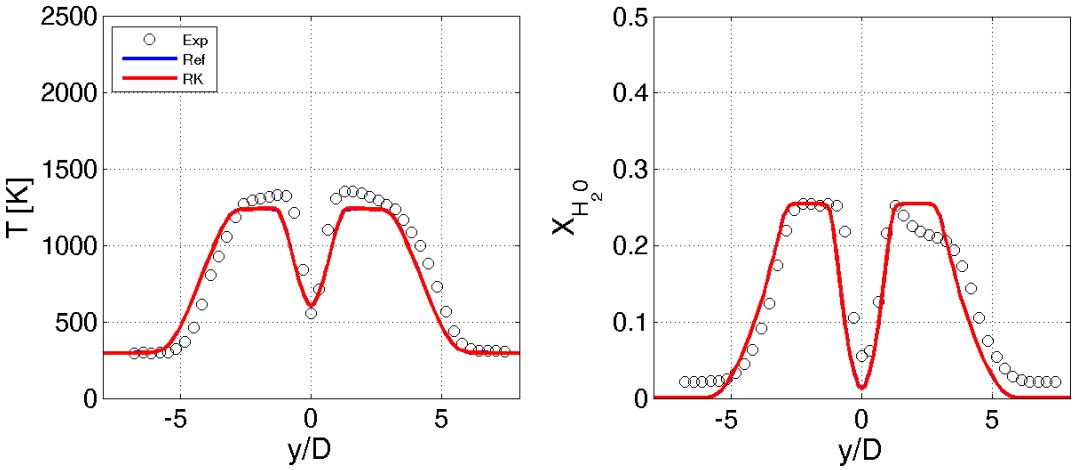

(b) x/D = 10.80

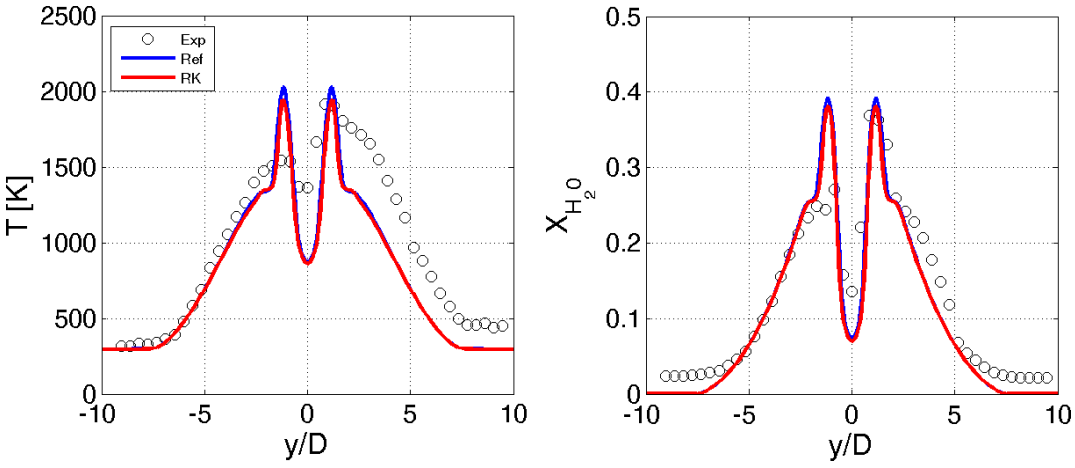

(c) x/D = 21.50

Figure 7.4: Mean temperature and H_2O mole fractions profiles for the Ref and RK simulations

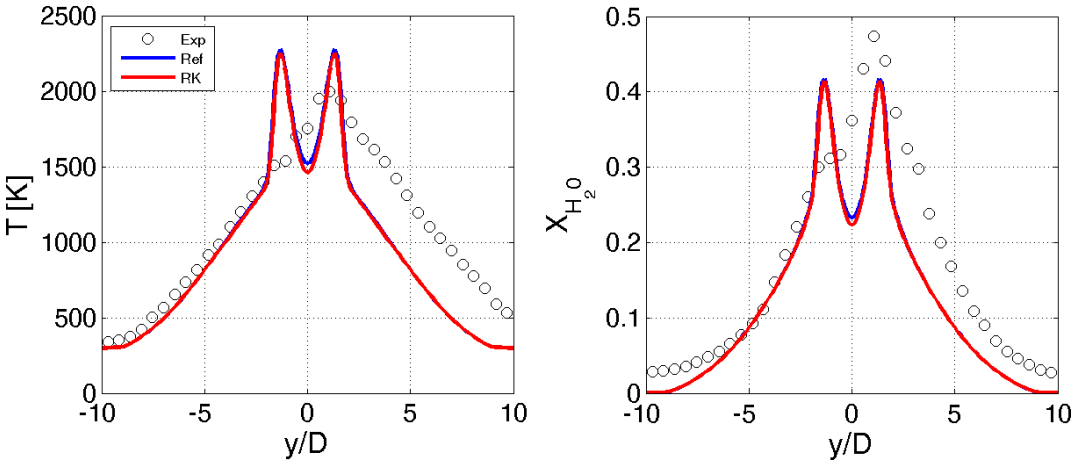

(a) x/D = 32.30

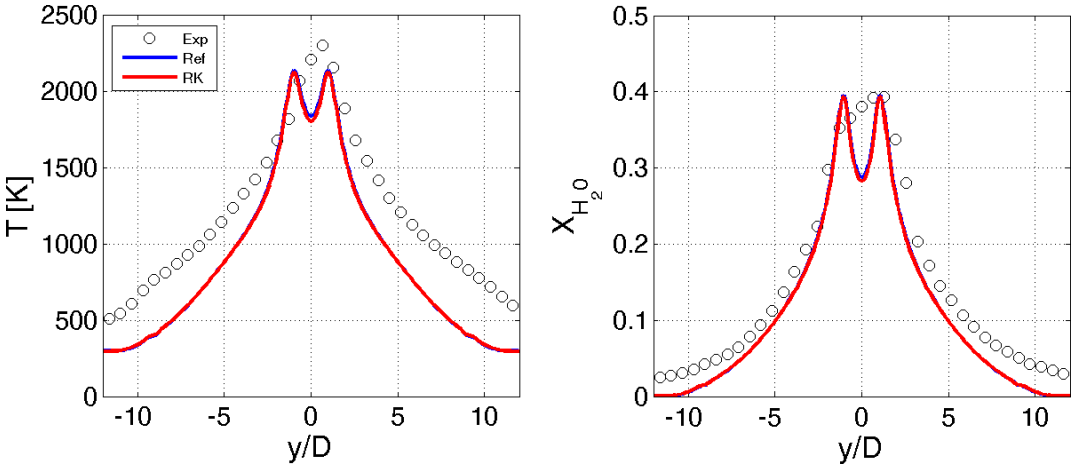

(b) x/D = 43.10

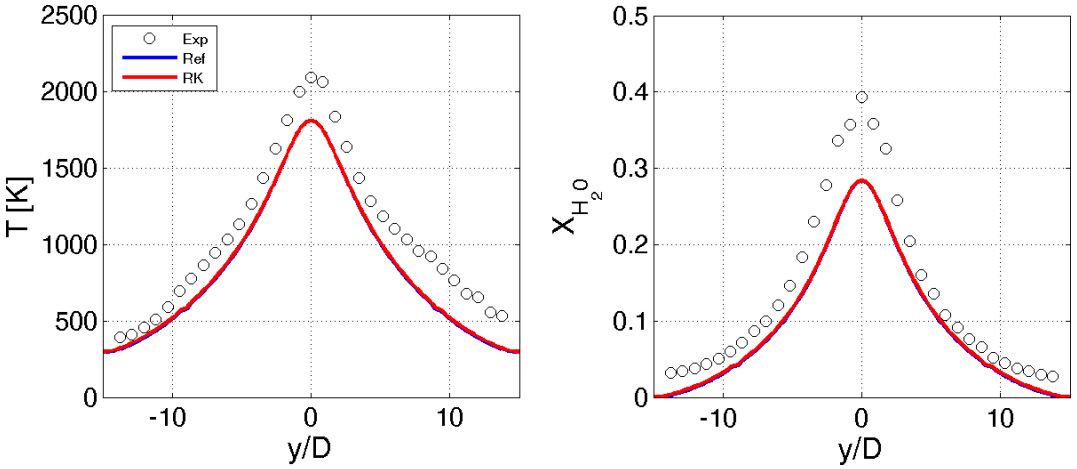

(c) x/D = 64.70

Figure 7.5: Mean temperature and H_2O mole fractions profiles for the Ref and RK simulations

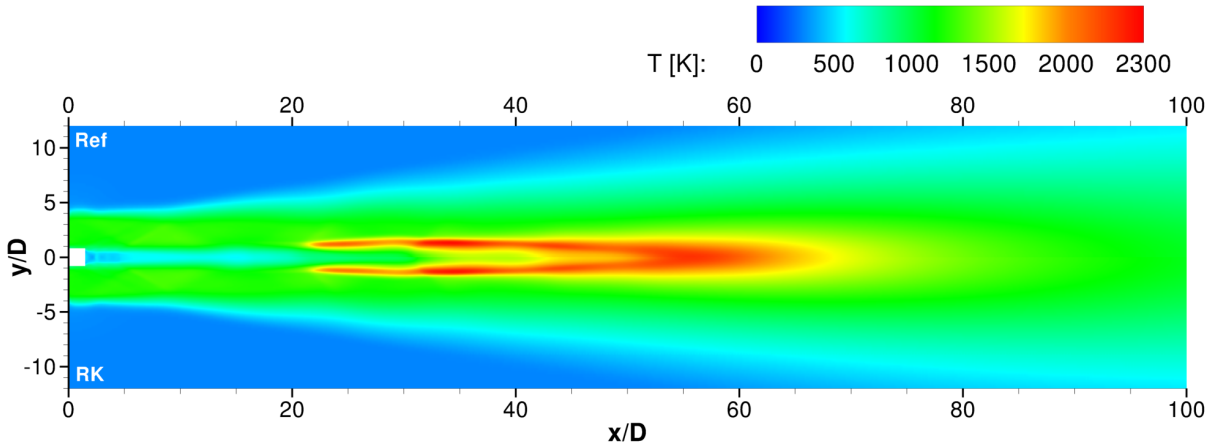

Figure 7.6: Mean temperature fields for the reference simulation Ref (top) and the RK simulation with Runge-Kutta 4^{th} order time integration (bottom)

imately three to four times larger than for the pure explicit Euler approach. Therefore, it is desirable to apply the computationally less accurate yet inexpensive Euler scheme, if the results do not deviate from the nominally better Runge-Kutta results.

The comparison of time-averaged temperature fields for the pure Euler and Runge-Kutta simulations is shown in figure 7.6. Indeed, no significant differences can be recognized between the two time integration approaches. Also the temperature and H_2O profiles in figures 7.4 and 7.5 show merely irrelevant discrepancies between the reference simulation and the Runge-Kutta case. The profiles are mostly indistinguishable, see also figure A.1 in the appendix. Solely minor deviations exist for the data at the symmetry axis for the locations x/D = 32.30 and x/D = 43.10. Altogether, the change of the time integration scheme has a far smaller effect than for example a variation of the turbulent Prandtl and Schmidt numbers, cf. figure 7.7. For this reason, the numerical diffusivity introduced by the larger numerical error of the first order Euler scheme compared to the Runge-Kutta procedure appears to be negligible.

On the basis of this comparison, the explicit Euler time integration scheme is applied to all remaining simulations in this thesis instead of the Runge-Kutta

approach. Certainly, the application of a higher-order scheme seems generally preferable and might lead to a refinement of the computational results in some cases. However, one motivation of this thesis is to provide models that allow for reasonable computational runtimes of full supersonic combustor simulations. Hence, tradeoffs need to be made and the one at hand appears to be a reasonable one.

7.4.3 Influence of Turbulent Schmidt and Prandtl Numbers

A RANS turbulence model needs to account for the whole spectrum of turbulent structures. This requirement is obviously seldom met with perfection. Furthermore, the turbulent diffusivity predicted with the SST eddy viscosity model utilized here is intended to reproduce the unclosed turbulent correlations in the momentum transport equations. The application to the closure of turbulent terms in the remaining transport equations is not self-evident. The justification for the application also within the transport equations for the chemical species and energy is owed to the logical assumption that the corresponding turbulent transport happens as a result of the momentum transport. However, in order to account for possible variations in the turbulent transport as compared to the turbulent transport of momentum, the turbulent Schmidt and Prandtl numbers were introduced in the transport equations for the chemical species and energy, see eqs. 3.24 and 3.25. A reduction of the turbulent Schmidt and Prandtl numbers effectively increases the modeled turbulent diffusivity within the respective transport equations. However, potential local variations of turbulent transport are not accounted for, since this increase acts globally and homogeneously on the entirety of transported fields. Still, the global setting of turbulent Schmidt and Prandtl numbers remains a valid approach in computational fluid dynamics. Here, the SP case applies turbulent Schmidt and Prandtl numbers both set to 0.7 in contrast to 1.0 utilized for the reference setup. The goal is to demonstrate the effect of this parameter choice, firstly, in comparison to the reference simulation and secondly, as a basis for the assessment of the subsequently presented results obtained with the model for combustion induced turbulence.

Figure 7.7 illustrates the time-averaged mean temperature fields for both the reference and the SP case. The corresponding H_2O and OH mass fraction fields are provided in figure A.2 in the appendix. Ignition starts slightly earlier for the SP setup and the flame is considerably shorter. Nevertheless, the shape of the flame remains unchanged. In contrast to the experiment, the SP simulation predicts minima in the temperature and H_2O profiles at x/D = 32.30 and x/D = 43.10 given in figure 7.9 similarly to the reference setup. These minima are less distinct in the SP case due to the increased diffusivity, but still fail to meet the experiment at these locations though. Moreover, the SP result clearly underestimate the temperature and water profiles at the last evaluation plane at x/D = 64.70 indicating that the shorter flame length does not match the experiment well.

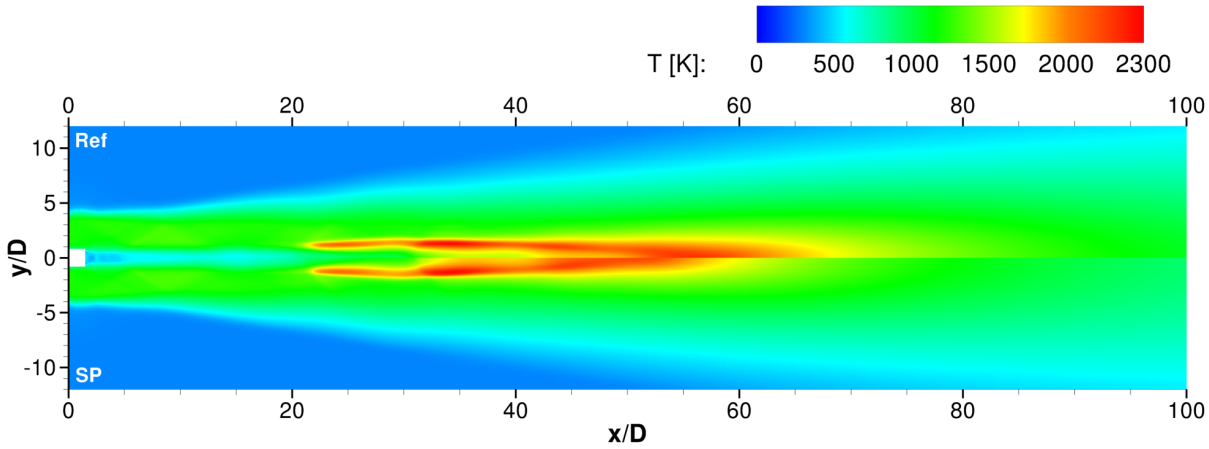

Figure 7.7: Mean temperature fields for the reference simulation Ref (top) and the SP simulation with decreased Pr_t and Sc_t (bottom)

In summary, the global increase of turbulent diffusivity based on the turbulent Schmidt and Prandtl numbers yields a minor improvement at the x/D = 32.30 and x/D = 43.10 locations and a deterioration at the last evaluation plane compared to the reference case. Obviously, different settings of the turbulent scaling parameters Pr_t and Sc_t can be investigated. However, the statement made here is that the global scaling of the turbulent eddy viscosity can indeed improve results at certain locations, but might negatively affect the outcome at other locations. The turbulent viscosity provided by the turbulence model exhibits deficiencies that require a local correction. Scaling this deficiency in

terms of Pr_t and Sc_t in the context of species and energy and transport does not remedy this issue.

7.4.4 Combustion Induced Turbulence Model Influence

The purpose of the model for combustion induced turbulence introduced in chapter 5 is to provide an approximation for the generation of turbulence by means of combustion. Hence, the combustion induced source term was deliberately placed in the transport equation for the turbulent kinetic energy influencing the local evolution of turbulence. Since the eddy viscosity is computed on the basis of the kinetic energy in term of the SST closure, the model acts on all fields, thus also on the transport of momentum. Furthermore, the inclusion of the model for combustion induced turbulence changes the eddy viscosity on a local basis. This especially contrasts with the scaling of the eddy viscosity within the species and energy transport equations by means of Pr_t and Sc_t.

In order to evaluate the effects of the novel model, it is applied to the reference simulation setup Ref with varying settings, see table 7.3. The CT1 simulation applies the model to the original Ref setup with the model parameter C_{tc} set to 1.0, whereas the CT2 case utilizes a reduced C_{tc} value of 0.75 to assess the sensitivity with respect to the scaling of the model source term. Finally, the CT3 simulation also applies the reduced C_{tc} value of 0.75 and utilizes the decreased turbulent Prandtl and Schmidt numbers as previously applied in the SP case. All other parameters and boundary conditions remain unchanged with respect to the reference case Ref.

The effect of the proposed model on the distribution of the turbulent kinetic energy becomes obvious from figure 7.10. Compared to the reference simulation shown in the top image, the CT1 simulation utilizing the new model exhibits a clear increase of turbulent kinetic energy in the combustion region located close to the symmetry axis from x/D = 20 onwards. The effects of this increase in modeled turbulence is discussed in the following.

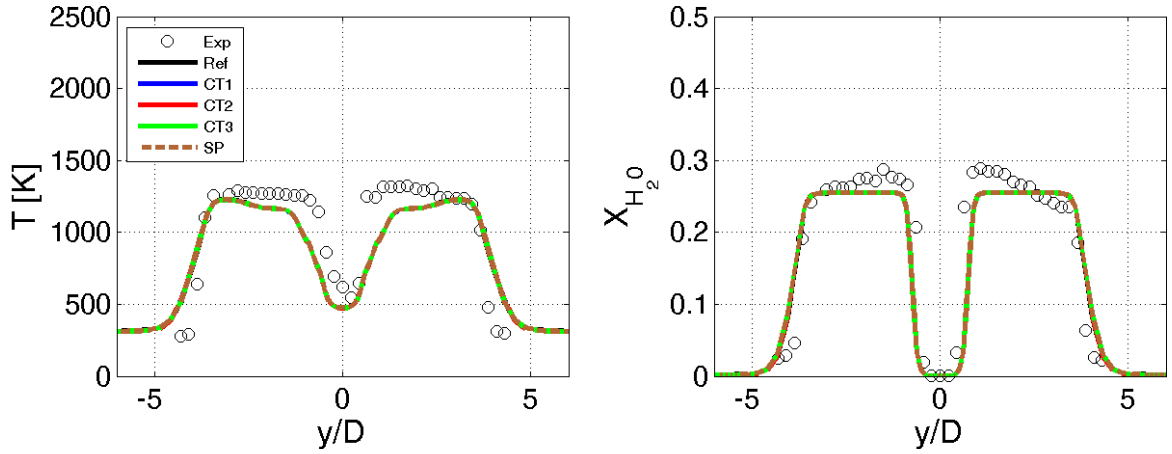

(a) x/D = 0.85

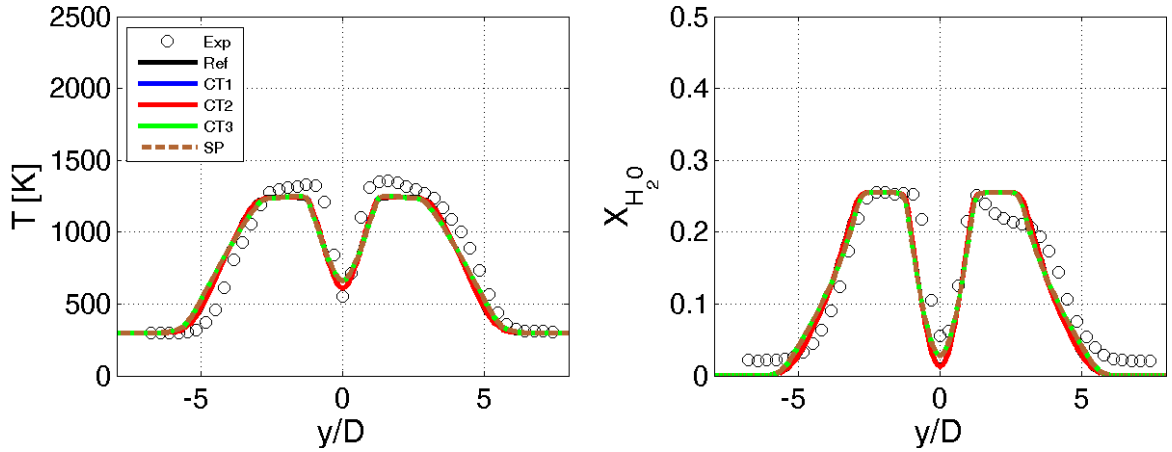

(b) x/D = 10.80

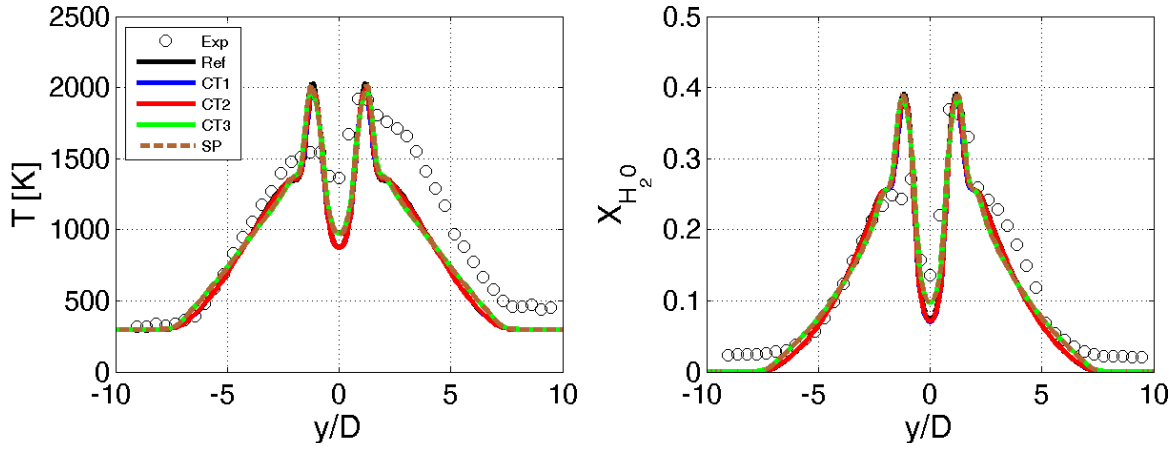

(c) x/D = 21.50

Figure 7.8: Mean temperature and H_2O mole fractions

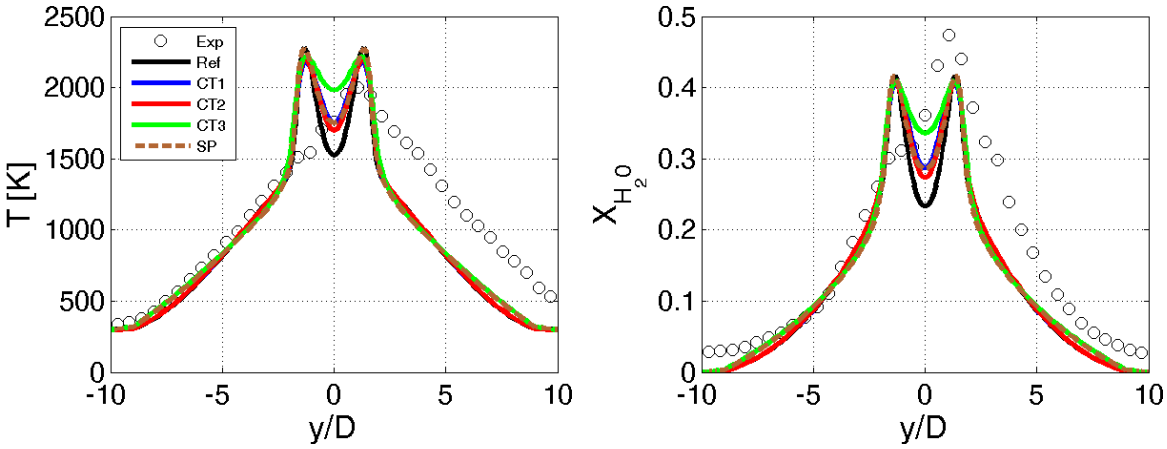

(a) x/D = 32.30

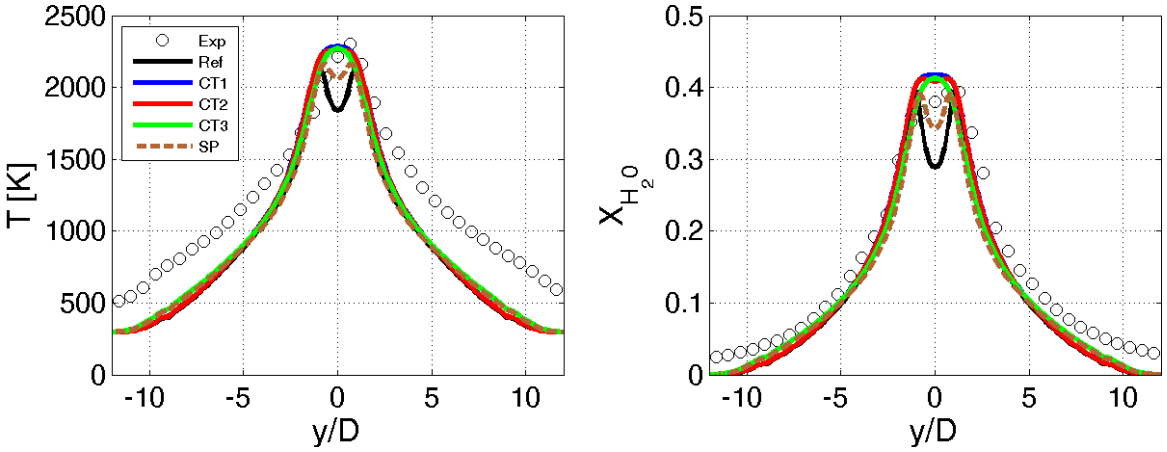

(b) x/D = 43.10

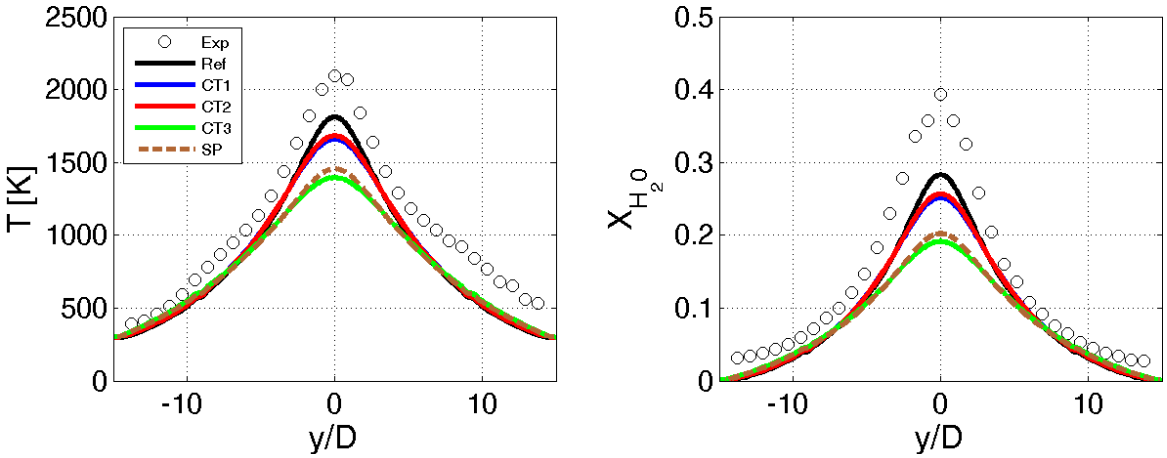

(c) x/D = 64.70

Figure 7.9: Mean temperature and H_2O mole fractions

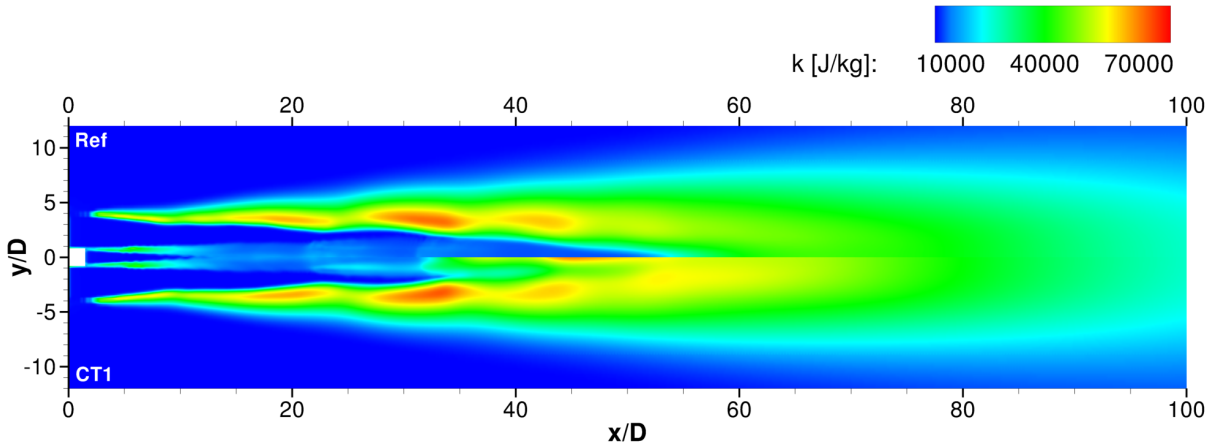

Figure 7.10: Mean modeled turbulent kinetic energy fields for the reference simulation Ref (top) and the CT1 simulation with combustion induced turbulence (bottom)

The lower half of figure 7.11 shows the mean temperature field of the CT1 simulation, the corresponding field for the reference case is given in the top part. The corresponding time-averaged mean OH and H_2O fields are provided in figure A.3 in the appendix. Evidently, the model for combustion induced turbulence changes the appearance of the flame. The increased turbulent viscosity in the combustion region leads to an earlier distribution of reactants towards the center line and thus an earlier ignition and formation of the combustion region. As a result, the flame appears shorter and wider than in the reference case. Furthermore, large values of OH mass fractions are not limited to a relatively thin zone in the initial mixing region as is the case for the reference setup, see A.3.

Regarding the comparison of computational results with the experimental findings, the first two downstream evaluation planes shown in figures 7.8 and A.6 do not show any significant difference between the CT1 simulation including combustion induced turbulence and the reference setup. This is as expected, since combustion does not occur at these locations, yet, hence the proposed model is inactive. The situation is similar at the beginning of the combustion region at x/D = 21.50. Here, the difference between the CT1 and Ref profiles is still barely perceptible. At x/D = 32.30 though, the CT1 simulation leads to a visible increase of temperature and water at the center line in-

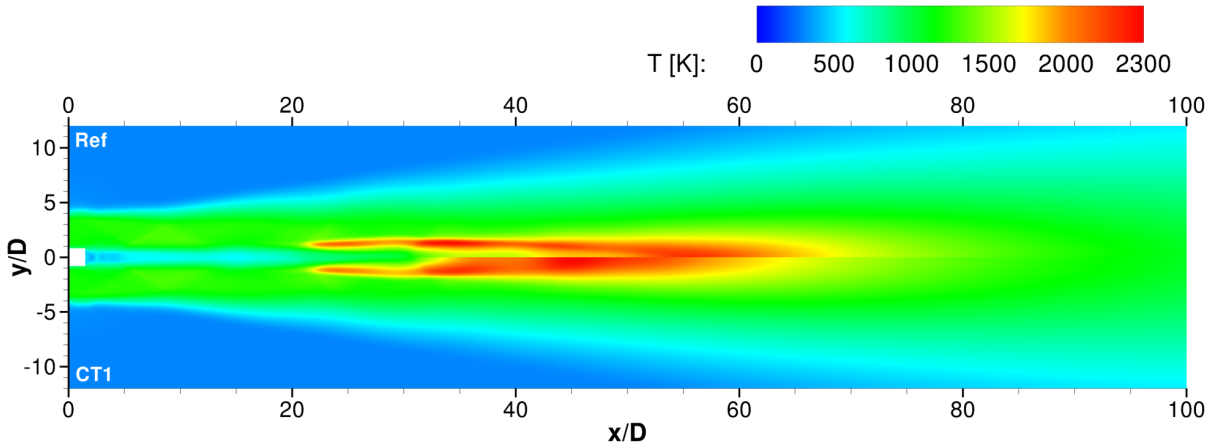

Figure 7.11: Mean temperature fields for the reference simulation Ref (top) and the CT1 simulation with combustion induced turbulence (bottom)

dicating that the beginning combustion induces turbulence, which increases the transport of heat and reactants.

The positive effect of the novel model becomes evident at the x/D = 43.10 location, cf. figures 7.9. As discussed previously and shown in figure 7.11, the model leads to an earlier ignition and distribution of species, which effectively expands the flame towards the centerline. Whereas the reference simulation still predicts two distinct temperature peaks and fails to meet the experimental flame structure to some extent, the CT1 case succeeds in predicting temperature and H_2O maxima at the center. The experimental temperature, H_2O and H_2 mole fraction profiles are matched reasonably well.

The last evaluated position at x/D = 64.70 reveals an interesting behavior. While the simulation including the model for combustion induced turbulence performed better at the preceding location, the reference setup performs slightly better here. The temperature, H_2O and OH profiles for the reference setup are matched well, while the CT1 case leads to an underestimation of the reference results. Nonetheless, this slight deterioration of the results at this last location is considerably less pronounced than for the SP case, which clearly underestimates the experimental data at x/D = 64.70. Further conclusions can be drawn from a comparison with the simulated fields in fig-

ure 7.7 that were obtained with the SP setup featuring decreased turbulent and Prandtl numbers, cf. table 7.3. The reduction of both parameters from 1.0 to 0.7 effectively increases the turbulent diffusivity in the transport equations for the internal energy and species transport, see eqs. 3.24 and 3.25. This results in a general and homogeneous increase of eddy viscosity and thus modeled turbulent transport within the species and energy transport equations for the entire simulated domain independently of the local solution. On the other hand, the model for combustion induced turbulence only increases the turbulent diffusivity in regions, where significant combustion is present in order to account for the local lack of modeled turbulence. Regions outside of the combustion zone are unaffected. In particular, the CT1 simulation delivers a better agreement with the measured data for the x/D = 43.10 plane than both the SP and the reference cases indicating a more intense combustion up to this point. At the same time, the CT1 results lie closer to the better Ref results than the profiles obtained with the SP simulation for the last data set at x/D = 64.70.

The CT2 setup utilizes a reduced source term for combustion induced turbulence by setting the C_{tc} constant to 0.75. Hence, the effects described for the CT1 case based on a C_{tc} constant value of 1.0 are marginally less pronounced here, resulting in a slightly longer flame and later ignition, cf. figures 7.11 and 7.12. Nonetheless, the change of the flame structure induced by the model is still evident. Ultimately, the differences between the CT1 and CT2 cases concerning the flow fields are rather marginal. Likewise, the temperature and species mole fraction profiles at the measurement planes do not differ significantly between the two cases, cf. figures 7.8 through A.7. The CT2 setup produces slightly lower OH and higher H_2 profiles at the symmetry axis implying a lightly underestimated turbulent mixing and combustion in comparison to the CT1 case. This behavior is as expected, since the reduction of the source term for combustion induced turbulence leads to a smaller turbulent viscosity. At this point it is noteworthy to recall the results for the turbulent Schmidt and Prandtl number variation: While this variation led to a significant change in the flame length, a similar change of the model constant C_{tc} does not alter the results considerably. Ultimately, the comparison of the CT1 and CT2 simulations implies that the model for combustion induced turbulence exhibits

a robustness with respect to the scaling of the model source term, which is a desirable feature.

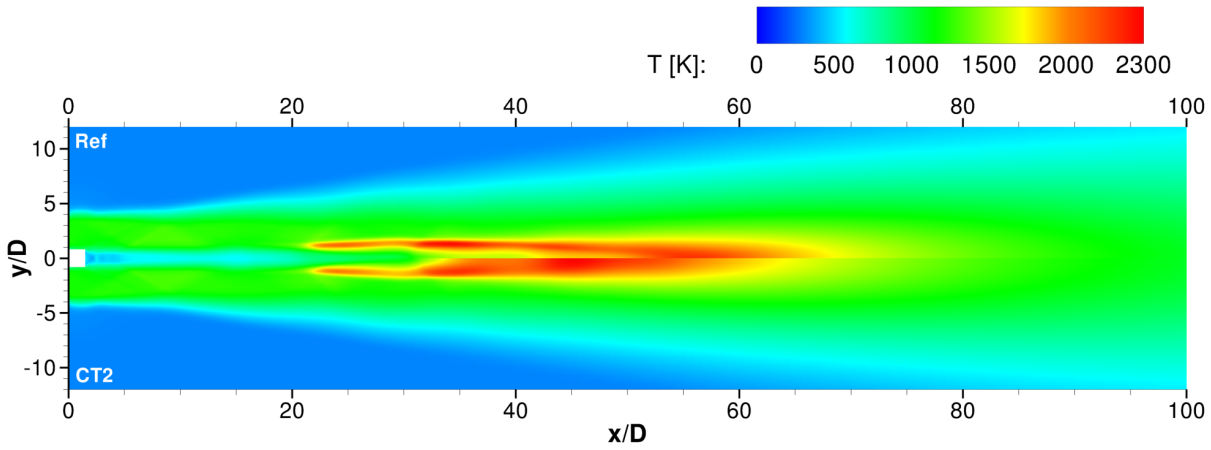

Figure 7.12: Mean temperature fields for the reference simulation Ref (top) and the CT2 simulation with combustion induced turbulence (bottom)

Finally, the CT3 simulation combines the model for combustion induced turbulence and the increased turbulent diffusivity through the decreased turbulent Prandtl and Schmidt numbers utilized in the SP case. Hence, this setup is expected to generate the most turbulent diffusion and thus fastest reactant mixing among all setups listed in table 7.3. Therefore, it is also expected that the CT3 case predicts the shortest flame. Indeed, a comparison of the resulting fields for CT3 given in figure 7.13 with the remaining cases provides proof for this assumption. The region with high temperatures of 2000 K and above ends already at approximately x/D = 55 due to the early and intense combustion. On the contrary, the corresponding main reaction regions ends downstream of x/D = 60 in the CT1, CT2 and SP cases. Likewise, the temperature and species profiles indicate the earliest combustion and fuel consumption for the CT3 setup. Yet, the uncertainty concerning the measured temperature and water profiles represented by the asymmetry of the experimental data at x/D = 21.50 and x/D = 32.30 does not allow conclusions about which prediction is more correct within the ignition region though. Moreover, the prediction of the temperature and reaction products are clearly underestimated at x/D = 64.70. A relevant finding is that the model for combustion induced tur-

bulence still reproduces the good results obtained with the CT1 and CT2 setups at the x/D = 43.10 location, but the globally increased diffusivity through decreased Pr_t and Sc_t deteriorates the results at the last evaluation plane x/D = 64.70 almost exactly as in the SP case.

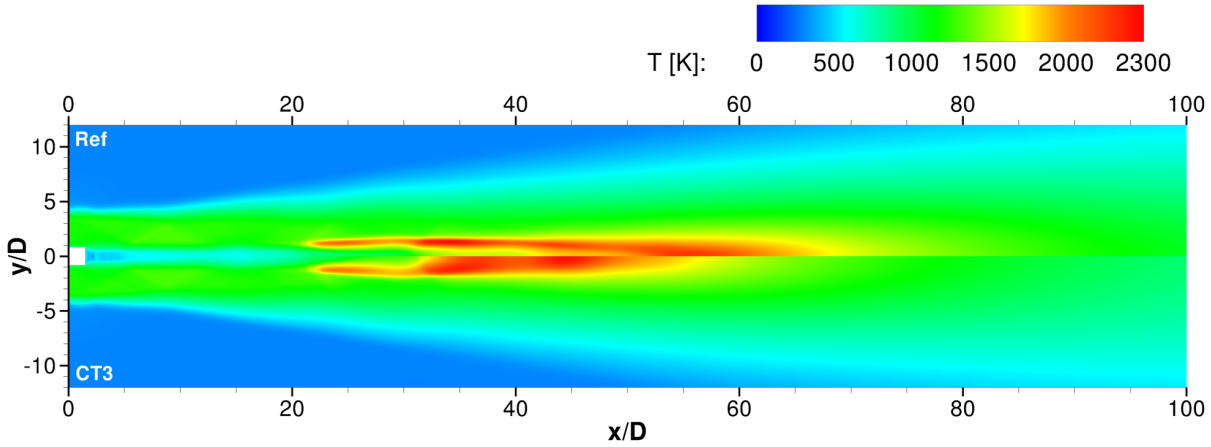

Figure 7.13: Mean temperature fields for the reference simulation Ref (top) and the CT3 simulation with combustion induced turbulence (bottom)

7.4.5 Summary

This chapter provides a validation of the developed flow solver in its RANS mode based on the supersonic diffusion flame by Cheng et al. [24]. The results are in accordance with previous numerical investigations of the flame [47,54]. Furthermore, additional RANS simulations are conducted in order to investigate the effect of the novel model for combustion induced turbulence described in chapter 5. The result is that the novel model provides increased turbulent diffusion in the combustion region and leads to an improved distribution of reactants towards the center line. The latter is in better agreement with the experiment within the main combustion region, although the differences are not large. On the other hand, the global increase of turbulent diffusion through decreased turbulent Prandtl and Schmidt numbers does not alter the flame structure and solely shortens the flame, thus deteriorating the results in comparison to the reference case. Hence, the selective increase of turbulent

diffusivity within the combustion region based on the insight that combustion induces turbulence, as investigated by Luo [86, 87], can indeed provide a benefit.

8 ITLR Scramjet Combustor

8.1 Experimental Setup

The Institute of Aerospace Thermodynamics (ITLR) at the University of Stuttgart conducts experiments with a supersonic hydrogen combustor [5, 139, 140] shown in figure 8.1. The combustion chamber operates at inlet Mach numbers ranging from 1.7 to 2.5. Generally, the combustor inlet Mach number is smaller than the flight Mach number due to the preceding compression in the engine intake, which is not part of the experimental setup. The combustor inlet corresponds to the throat of the preceding Laval nozzle utilized to generate the supersonic velocity. A system of three electrical pre-heaters increases the air inflow total temperature to 1300 K. A screw compressor delivers the total pressure of 6.0 bar at the inlet. The total pressure and temperature approximately correspond to a flight Mach number of five at an altitude of 30 km taking into account the international standard atmosphere (ISA). The test rig allows continuous operation with testing times of several minutes.

Furthermore, the combustor features a staged injection system with a lobed central strut injector and two wall injection elements further downstream, see figure 8.2. The central injector generates large-scale streamwise vortices that strongly enhance the mixing of hydrogen and air. The wall injectors consist of ramps generating additional vortices. Hydrogen is injected at sonic conditions through slots at the injector trailing edges. In the case of the central injectors, the slots are parallel to the main flow direction, whereas the wall injector slots feature an injection angle of 12° relative to the main flow axis. The combustor features a symmetry about the x-z-plane in the middle of the chamber. Further symmetries do not exist due to the lobed central injector geometry, see figure 8.2.

The central injector leading edge and the trailing edge are located 421 mm and 507 mm downstream of the Laval nozzle throat respectively, cf. table 8.1. Thus, the distance between the inlet and the central injector leading edge amounts to approximately one third of the entire chamber length, see figure 8.1. The technological relevance of such a configuration is given in systems including a constant-height isolator preceding the combustion chamber [123] serving the purpose of isolating the combustion region from the engine intake. The distance between the Laval nozzle and the combustion region leads to a considerable increase in boundary layer thickness, cf. eq. 2.62. In addition, the relatively low density induced by the simulated altitude yields a comparably small Reynolds number at the inlet, see eq. 2.61, further promoting the boundary layer thickness. In consequence, the boundary layer blocks a considerable portion of the combustor channel cross-section. Ultimately, the boundary layer thickness is further increased through shock boundary layer interactions downstream of the central injector, e.g. promoting the formation of shock trains, see section 2.4.1. The origin of the coordinate system utilized within this work is located at the sidewall in the center of the Laval nozzle throat, cf. figures 8.1 and 8.3.

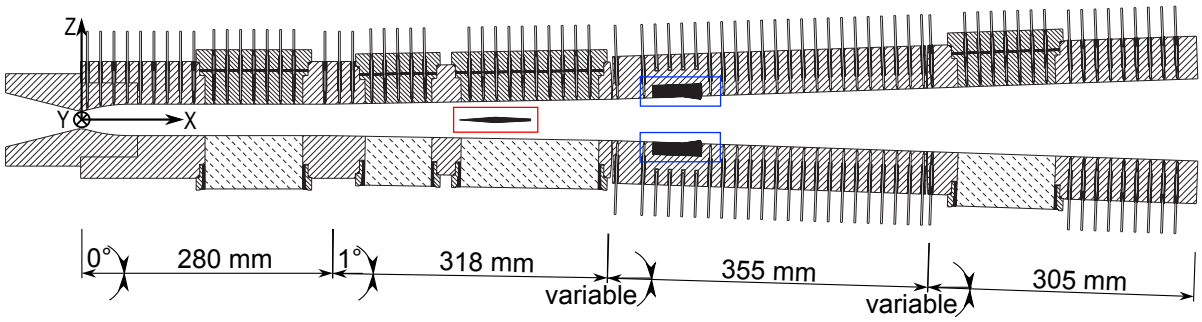

Figure 8.1: ITLR supersonic model combustion chamber at University of Stuttgart with attached Laval nozzle, vortex generating central strut injector (red) and two wall injectors (blue)

Moreover, the combustor flow expands against ambient laboratory pressure. As a result, a boundary layer separation region forms in the rear combustor section close to the chamber exit. Due to the relatively low chamber pressure at the outflow, the separation region length amounts to approximately one fourth of the chamber length, at least in the case without fuel injection and

Table 8.1: ITLR supersonic combustion chamber data

Inlet Mach number	2.5	-
Inlet total temperature	1300	K
Inlet total pressure	6.0	bar
Length	1258	mm
Constant channel width	40	mm
Constant isolator height	35.4	mm
Channel outlet height	92.56	mm
Central inj. length	86	mm
Central inj. width	40	mm
Central inj. leading edge position	421	mm
Wall inj. leading edge position	677.4	mm
Wall inj. trailing edge position	696.4	mm

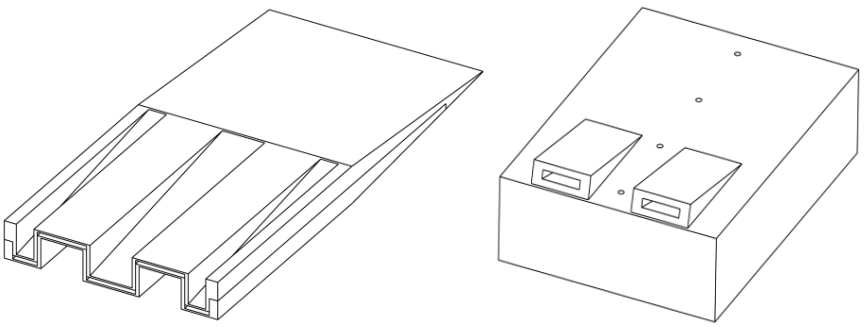

Figure 8.2: Left: central strut injector; right: one wall injector element comprised of two ramps

subsequent combustion.

Experimental data consist of wall pressure measurements along the upper and lower wall centerlines. The measurement locations are indicated by the pressure taps in figure 8.1. Particular wall segments can be exchanged by segments containing pressure taps. Pressure data for the full combustor length are only available at the upper wall though. The lower wall measurements feature less pressure probes close to the inflow and outflow.

8.2 Numerical Setup

8.2.1 Investigated Operational Points

Only the highest Mach number of 2.5 is considered within this investigation, since it constitutes the most relevant combustor inlet velocity for supersonic combustion out of the available experimental configurations. The lower Mach numbers are rather located within the ramjet portion of the dual mode scramjet operational range [121] and are thus neglected. The classification of the modes of operation of the ITLR combustor in terms of scramjet propulsion systems is discussed further below in section 8.4.

The fuel equivalence ratios of the respective investigated operational points are summarized in table 8.2. All cases feature the same total temperature, total pressure and inlet Mach number given in table 8.1. Case NR is a non-reacting case without fuel injection. Case S is a single-injection case with hydrogen injection solely through the central injector strut. Following the work and naming convention of Banica et al. [5], the ITLR combustor features three combustion modes at single-staged injection: Firstly, a strong combustion mode involving local thermal choking occurring at fuel equivalence ratios ϕ larger than 0.26. Secondly, a weak combustion mode at equivalence ratios lower than 0.17. Thirdly, an intermediate range for ϕ ranging from 0.18 to 0.25, which is characterized through strong oscillations between weak and strong combustion modes though. Hence, case S represents the strong combustion mode, the result of which is a mainly subsonic combustion region behind the central injector strut. The weak combustion mode results in combustion occurring solely in the shock train at the chamber exit, which is formed due to the ambient laboratory pressure. Thus, the latter mode is not considered here, since it does not have technological relevance. The two-staged injection test cases T1 and T2 both feature central and wall injection, whereas T2 exhibits the larger equivalence ratios. In contrast to the single-staged injection mode, stable supersonic/transonic combustion is established at equivalence ratios of 0.2 and below, if wall injection is enabled.

Table 8.2: Investigated operational points

Test case	ϕ_1	ϕ_2
NR	0	0
S	0.30	0
T1	0.15	0.15
T2	0.20	0.20
IT2	0.20	0.20

Here, it shall be noted that describing an operational point as stable solely means that the flame remains anchored behind the fuel injectors and thus remains within the combustor. It does not imply that the combustion process is steady in every aspect. The contrary is to be expected due to the large-scale vortex induced by the central injector. Yet, the only available quantitative experimental results being the wall pressure measurements provide solely temporal long-term averages and hence do not allow for a temporal resolution of the involved unsteady sub-processes. Indeed, the measured mean wall pressure profiles feature only very little variation indicating a stable mean field. However, high-speed chemiluminescence images of the ITLR combustor indicate considerable fluctuations in the location of the combustion zone. Thus, a stable operational point in the context of the ITLR combustor can be best described as an intrinsically unsteady process, yet resulting in a reasonable pseudo-steady time average. Transient phenomena, which remain more or less unexplored in the experiment, can have crucial consequences for the mean field and the operation of the combustor as shown in section 8.5.2 on the hybrid RANS/LES simulation of the T2 operational point.

All four test cases are treated with RANS, in order to validate the general capability of the developed solver to simulate a complete supersonic combustor at different operating conditions. Hybrid RANS/LES simulations are performed solely for the NR and T2 cases, since case T2 features the largest technological relevance and constitutes the most frequently investigated test case for the ITLR combustor [139]. In addition, the ignition sequence for the two-staged injection case T2 is simulated by means of RANS in case IT2.

8.2.2 Numerical Settings

Both RANS and hybrid RANS/LES simulations apply eddy viscosity type turbulence models as discussed in sections 3.3 and 3.4. Within this context, varying turbulent diffusivities within the energy and species transport equations are considered through turbulent Prandtl and Schmidt numbers Pr_t and Sc_t different from one. The turbulent Prandtl number for the RANS mode is set to 0.85 and the turbulent Schmidt number is set to 0.6 in all RANS and hybrid RANS/LES simulations based on previous experience made at ITLR. A turbulent Prandtl number of 0.7 is utilized in the LES mode of the hybrid simulations, see e.g. Berglund et al. [12]. Yet, a relevant result of the investigation of the supersonic diffusion flame by Cheng et al. in chapter 7 is that a variation of the turbulent Prandtl and Schmidt numbers influences the results to some extent, but does not change the structure of the flame.

Although there exist more specialized reaction schemes for supersonic combustion problems, the technically detailed reaction scheme by O'Conaire et al. [104] is applied, following all preceding simulations in this work. The O'Conaire mechanism constitutes a widely-validated and hence reliable scheme, which motivates its application despite the comparably large number of treated reactions. Solely the ignition sequence simulation in case IT2 deviates therefrom and applies the 12-step reduced hydrogen reaction scheme by Boivin et al. [16] for reasons of computational efficiency.

The simulations presented in this chapter are evolved and averaged for at least two chamber flow-through-times. The flow-through time is defined as the time span the fluid needs to cross the distance between the tip of the central injector and the chamber exit at the nozzle outflow freestream velocity at Mach 2.5. This distance amounts to 0.825 m, whereas the mean velocity is 1200 m/s yielding a flow-through-time of 0.675 ms. Hybrid RANS/LES simulations are initialized from RANS simulations and evolved for several flow-through-times before averaging is conducted.

8.2.3 Boundary Conditions

As mentioned initially, the supersonic flow exiting the combustor experiences the ambient pressure provided by the laboratory environment. This leads to flow separation at the end of the combustor, since the flow is overexpanded. Nevertheless, in order to simplify the numerical stabilization of the computations, a zero-gradient pressure boundary condition is imposed at the outflow for all combustion simulations. Although the separation bubble caused by the overexpansion has a considerable extent, it does not influence the combustion region upstream, because the flow is mainly supersonic prior to separation. In addition, the pressure rise due to combustion delays and reduces the extent of the separation region. A further argument in favor of neglecting the backpressure is to verify, whether the S, T1 and T2 flames remain stable without backpressure. For the stated reasons, it seems legitimate to perform the aforementioned simplification with respect to the pressure outflow boundary condition. As a consequence, experimental and numerical wall pressures do not match close to the outflow. Independently, the non-reacting simulations are carried out with the correct ambient backpressure, yet at the cost of increased runtime and unstable simulation runs. The purpose is to obtain qualitative information about the exiting separation bubble and shock train. The latter is a prerequisite for the simulation of the ignition process in case IT2.

Furthermore, the combustion chamber walls are water cooled, such that the walls effectively draw thermal energy from the flow. Hence, the isothermal temperature boundary conditions applied by Vellaramkalayil are adapted [139, 140]. The temperature is set to a fixed value of 400 K at the sidewall and the upper and lower channel walls. The central injector is cooled by the subsequently injected hydrogen, yet, it experiences high heat loads due to the combustion region immediately downstream. For this reason, the central injector wall temperature is set to 600 K.

The application of LES actually requires the generation of coherent turbulent fluctuations at the domain inflow in order to predict a correct boundary layer behavior and initiate turbulent motions in the fluid downstream. However, no inflow turbulence is imposed in the hybrid RANS/LES simulations for the following reasons: Firstly, the major portion of turbulent motions is generated intrinsically within the combustor, mainly due to the lobed central strut injector, which induces large scale streamwise vortices. Secondly, the developed hybrid RANS/LES approach is designed to treat the boundary layer with RANS, such that turbulent fluctuations are not required at the inlet boundaries. The boundary layer, however, accounts for most of the turbulence at the inlet. This constitutes a convenient side effect of the hybridization methods introduced in chapter 4. Moreover, no measurements are available concerning the turbulence entering the Laval nozzle. Hence, it would be difficult to obtain the exact turbulent inflow state for a fully resolved LES. For the same reasons, no artificial turbulence is imposed at the hydrogen injection slots.

8.2.4 Computational Grids

Both computational grids for RANS and hybrid RANS/LES are based on the same topology, yet feature different levels of refinement. The meshes cover the upper and lower half of the combustor and take advantage of the x-z symmetry plane at the centerline, therefore reducing the mesh size by 50 %, see figure 8.3. Near-wall regions exhibit similar resolutions for both meshes due to the fact that the hybrid simulations employ RANS wall-functions in the boundary layers, cf. figures 8.4 and 8.5. It should be noted that the RANS/LES hybridization methods presented in chapter 4 do not require the application of wall functions. However, the obvious consequence of a wall function approach is a substantial runtime reduction compared to the full resolution of wall-normal boundary layer gradients. On the one hand, this runtime reduction is due to the smaller number of computational cells in the boundary layer. On the other hand, larger near-wall cells lead to a considerably larger time step, see eq. 3.2 defining the CFL condition. Here, the latter aspect of time step increase constitutes the main reason for the reduction in computational time originating in the application of wall functions.

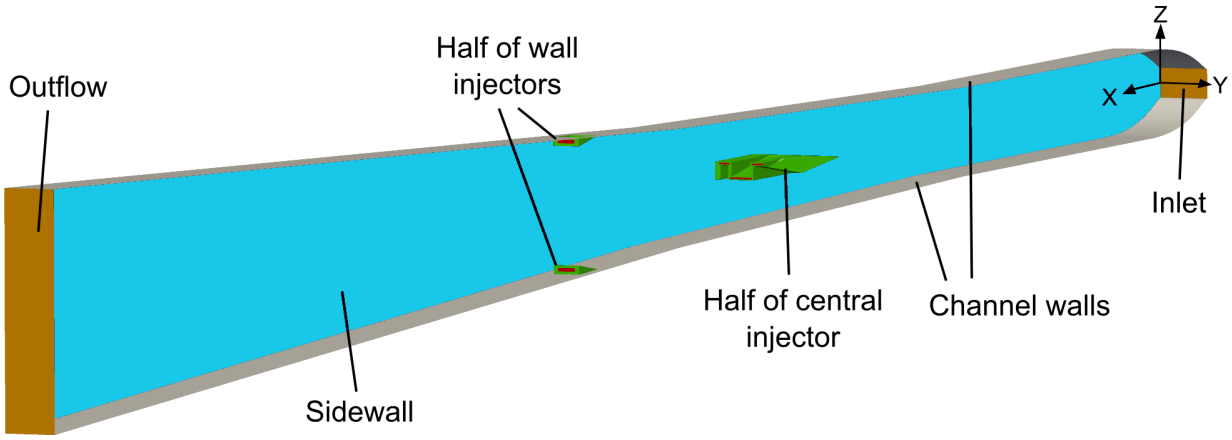

Figure 8.3: Computational domain

8.2.4.1 RANS

RANS simulations are conducted on a computational mesh containing 6.4 million cells at a time step of 1.3e-8 s. As discussed above, wall functions for the turbulent eddy viscosity are applied allowing for relatively coarse cells in the boundary layers resulting in an average y+ value of 40 at the upper and lower chamber walls. Mesh refinement is focused on the flame stabilization and main combustion region between the central injector trailing edge, see figure 8.4, and the wall injector elements, see figure 8.5. The mesh is based on the grid topology and grid sensitivity study conducted for the ITLR combustor by Banica et al. [5]. The RANS mesh utilized here features approximately 50 % more cells than the finest mesh investigated in their study in order to ensure a sufficient resolution of the combustion region and the combustor shock system as a foundation for the comparison with hybrid RANS/LES results. Furthermore, Banica et al. conclude that the influence of the y+ value on the wall pressure results related to the wall function approach is minor. The average y+ value of 40 utilized here is on the smaller end of the range, which Banica et al. deem appropriate. In addition to the grid study by Banica et al., the T2 flame RANS is also conducted on the finer hybrid RANS/LES mesh introduced in the following in order to demonstrate the mesh-independence of the RANS results utilizing the developed flow solver, see section 8.3.5.

8.2.4.2 Hybrid RANS/LES

The computational mesh for the hybrid RANS/LES simulations inherits the topology of the RANS mesh, see figure 8.3. Yet, the hybrid mesh features higher grid densities between the central injector trailing edge, see figure 8.4, behind the wall injectors, see figure 8.5 and towards the exit in order to capture turbulent vortical structures with the LES mode. As a result, the total cell count is increased to 11.2 million cells, which results in an increase by a factor of 1.75 in comparison to the RANS mesh. The cell sizes in the core region downstream of the central injector indicated by the cone emerging from the central injector trailing edge in figure 8.4 feature the following resolutions: between 0.175 mm and 0.3347 mm in x-direction, 0.158 mm in y-direction and between 0.0579 mm and 0.415 mm in z-direction. Moreover, the entire combustor cross-section features cell sizes between 0.2 mm and 0.392 mm in x-direction up to 73 mm downstream of the wall injector trailing edges. The mesh further downstream features growing cell sizes in x-direction of 0.44 mm up to 1.056 mm at the chamber exit.

The simulations are conducted with a time step of 1.08e-8 s, which is 17 % smaller than the RANS time step due to the reduced minimum cell size. Wall functions are applied in order to compute the turbulent eddy viscosity for the RANS mode of the hybrid turbulence model as described further above for the RANS mesh.

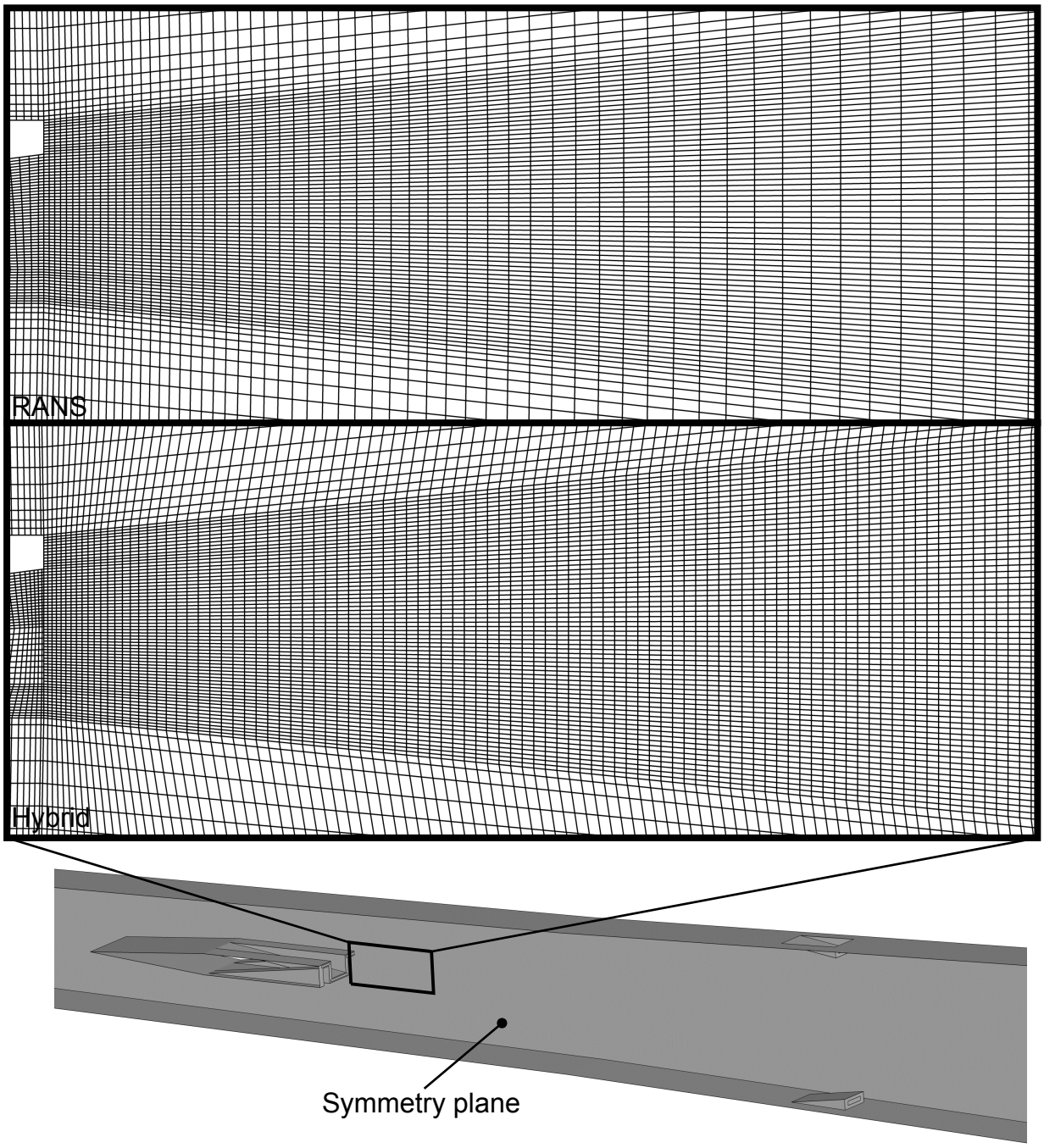

Figure 8.4: ITLR mesh segments behind the central injector at the symmetry axis, RANS (top) and hybrid RANS/LES mesh (bottom)

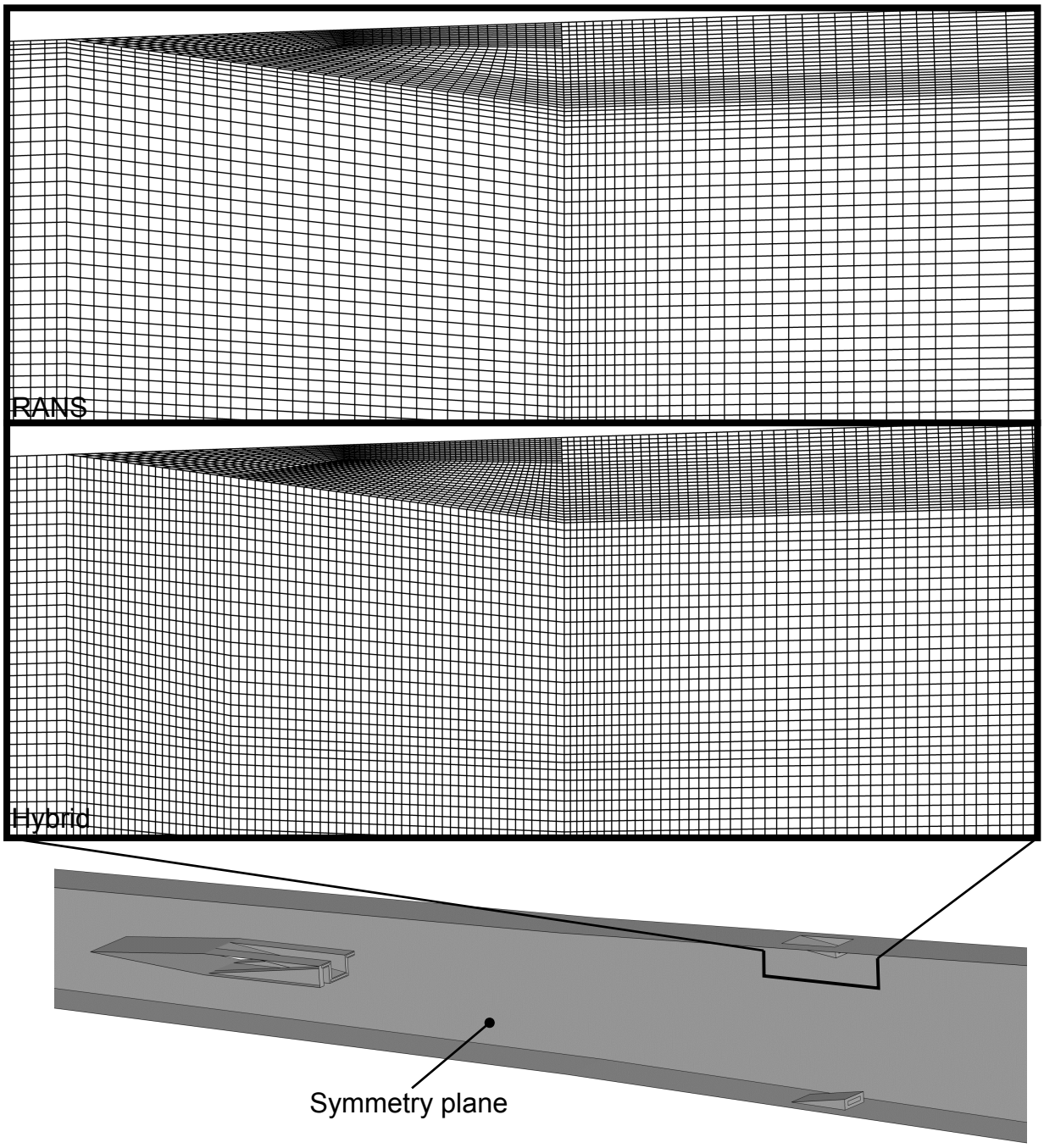

Figure 8.5: ITLR mesh segments at the upper wall injector at the symmetry axis, RANS (top) and hybrid RANS/LES mesh (bottom)

8.3 Unsteady Reynolds-Averaged Navier Stokes Simulation Results

8.3.1 Non-reacting Case NR

Figures 8.7a and 8.7b depict the comparison of experimental and computational wall pressures for both the upper and lower walls for the non-reacting case NR. The point of origin corresponds to the Laval nozzle throat, see figure 8.1. In contrast to the subsequently discussed combustion cases, the NR simulation employs a pressure far field boundary condition at the outlet setting the ambient pressure to 1 bar in order to account for the laboratory atmosphere. Generally, a very good agreement between experimental and numerical results is obtained until approximately x=800 mm.

The shock wave generated by the central injector leading edge induces separation bubbles at the upper and lower chamber walls represented by the distinct pressure rise downstream of x=440 mm extending until x=500 mm in both wall pressure plots. The pressure peaks further downstream until x=650 mm originate in the reflected leading edge shock, see also the computational Schlieren image in figure 8.6. Moreover, the backsides of the wall injectors represent convex corners, cf. figures 8.2 and 8.3. Hence, the pressure drop around x=700 mm is the result of expansion fans forming behind the wall injector elements at the upper as well as at the lower wall.

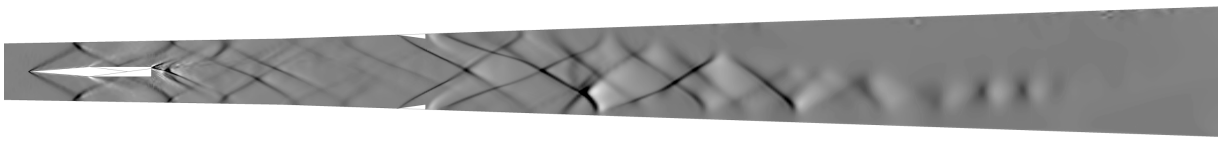

Figure 8.6: Case NR RANS instantaneous Schlieren image at symmetry plane

Computational and experimental data diverge between x=800 mm and x=1000 mm, due to the fact, that the utilized RANS turbulence model predicts a too early backpressure induced separation followed by a continuous wall pressure rise. The continuous increase of wall pressure downstream of the separation location is due to the two-dimensional structure of the separation region

consisting of upper and lower wall separation bubbles and an enclosed shock train, as described further below. The premature boundary layer separation is a general propensity of the k-ω model part of the underlying SST turbulence model with respect to the modeling of boundary layer separation [99, 134]. In contrast to that, the separation location observed in the experiment amounts to x=900 mm. Yet, both predictions of the separation location are in accordance with the Summerfield criterion for backpressure induced boundary layer separation developed for thrust nozzles [45]. The criterion states that separation occurs at the location, where the static pressure reaches approximately 25% to 40% of the backpressure (here: 0.25 to 0.4 bar), which is the case for both experiment and simulation. In general, a scramjet engine would encounter decisively smaller backpressures in a realistic operational scenario without the formation of a separation region at the outflow. For this reason, the mismatch between experiment and simulation is not of crucial technological relevance. Nevertheless, the backpressure induced shock system exiting the chamber is relevant for the ignition sequence of the model combustor discussed later, thus it is incorporated here.

Figure 8.8 illustrates the magnitude of the mean velocity field at the combustor symmetry plane and several selected downstream locations. The first four cross-sections upstream of the central injector show the boundary layer growth along the isolator section of the combustor. As a result, the boundary layer consumes approximately one fourth of the channel height at the central injector. The subsequent three slices show the dominant vortex generated by the lobed central injector. The velocity field close to the exit reveals an asymmetry with respect to the upper and lower chamber half, since the separation bubble at the upper wall is considerably larger than its lower wall counterpart. This agrees with previous computational investigations of the ITLR combustor [139, 140]. Furthermore, the Schlieren image in figure 8.6 clearly shows the development of a shock train exiting the chamber being a result of the constriction of the channel due to the separation bubbles. Subsonic regions can be recognized by consistently gray areas due to the lack of shock or expansion fan induced pressure gradients. Moreover, the shock train follows the asymmetrical bending of the separation bubbles. The larger subsonic region within the separation zone at the upper wall promotes ignition and the upstream

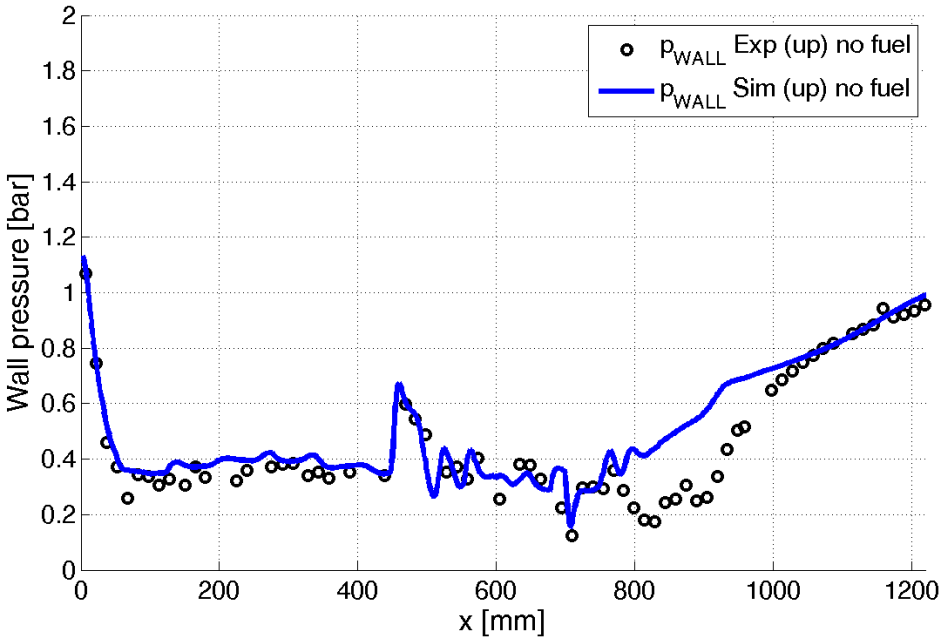

(a) Upper wall

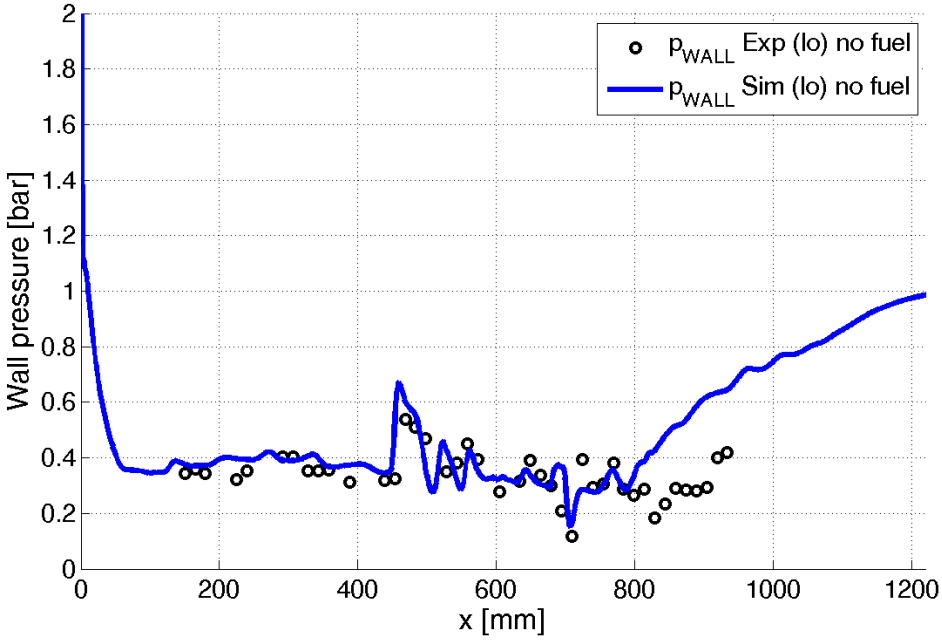

(b) Lower wall

Figure 8.7: Non-reacting case NR experimental and RANS simulation mean wall pressures without fuel injection

propagation of the flame during the ignition sequence, as shown in the following.

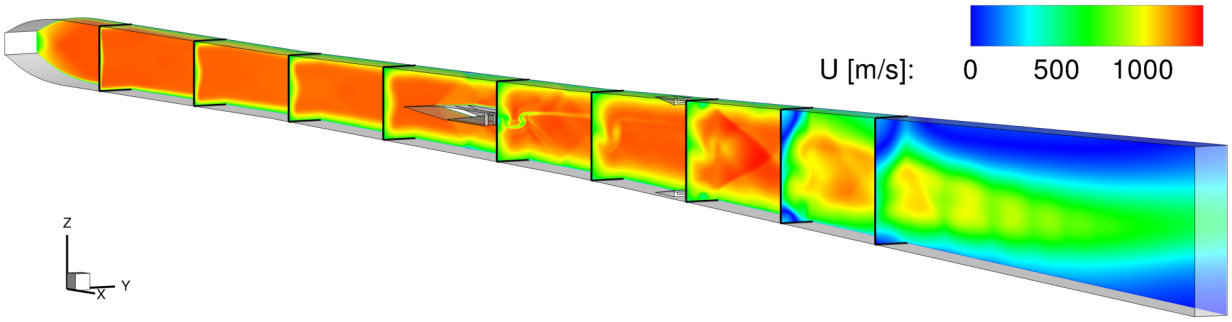

Figure 8.8: Non-reacting case NR RANS velocity magnitude at symmetry plane and several cross-sections

The NR simulation demonstrates the capability of the developed solver to reproduce the non-reacting combustor flow field in accordance with experimental results. This constitutes a necessary prerequisite for the combustion simulations presented and discussed in the following.

8.3.2 Single-staged Fuel Injection Case S

The fuel equivalence ratio for the single-staged injection case S corresponds to 0.3 and represents a high-equivalence ratio strong combustion mode of the ITLR combustor, see section 8.2.1. The comparison of experimental and computational wall pressures for this case is provided by figures 8.12a and 8.12b for the upper and lower walls respectively. Generally, experimental and computational results match well and exhibit the same trend. In contrast to the non-reacting case NR, a distinct pressure peak due to the interaction of the leading edge shock with the upper and lower chamber walls is not perceptible anymore, since the intense combustion leads to a strong pressure rise between x=380 mm and x=700 mm. Both experiment and simulation are in agreement with respect to the location of the onset of pressure rise around x=380 mm. Hence, the combustion induced pressure rise impacts the flow

upstream of the central injector leading edge located at x=421 mm. Thus, the subsonic portions of the flow at this high equivalence ratio are large enough to allow information to travel upstream finally affecting the flow before it reaches the injector and flame region. The mean Mach number distribution on the combustor mid plane in figure 8.9b shows that an extensive subsonic region emerges from the sidewall and extends up to the symmetry plane close to the wall injectors. Within this context, the Schlieren image in figure 8.11 barely features density gradients downstream of the central injector providing further evidence for the subsonic/transonic nature of the combustor flow in case S. Nevertheless, major portions of the flow remain supersonic at the symmetry plane, see figure 8.9a. Although neither the case S simulation nor the results obtained by Banica et al. [5] obtained for the ITLR chamber indicate thermal choking of the entire combustor at the equivalence ratio of 0.3, the large combustion induced pressure rise constricts the purely supersonic part of the flow in the vicinity of the central injector more than it is the case for the T1 and T2 flames discussed further below, see sections 8.3.5 and 8.3.5.

Moreover, the boundary layer separation initiated by the ambient laboratory pressure is postponed as compared to the non-reacting case NR, resulting in a separation further downstream around x=1100 mm. As mentioned initially, the simulation does not include the atmospheric backpressure for reasons of computational stability. The latter is the cause for the pressure mismatch after x=1100 mm. Notwithstanding the above, the shock system indicated by the experimental pressure peaks downstream of the wall injector location at x=700 mm is matched exceptionally well by the simulation. On the other hand, the simulation underpredicts the maximum mean pressure. While the experiment provides a maximum pressure peak of 1.55 bar, the RANS simulation provides a peak value of 1.35 bar. Nevertheless, the 1-σ standard deviation confidence intervals[1] for the computational wall pressure in figures 8.12a and 8.12b show that the experimental peak pressure is in the range of simulated transient pressure fluctuations. Moreover, the wall pressure standard deviation intervals imply the largest fluctuations in pressure and thus combustion close to the location of maximum pressure indicating considerable oscillations in the

[1] The 1-σ standard deviation confidence intervals for the computational wall pressures are computed on the basis of the same unsteady pressure data utilized for the computation of the mean wall pressure.

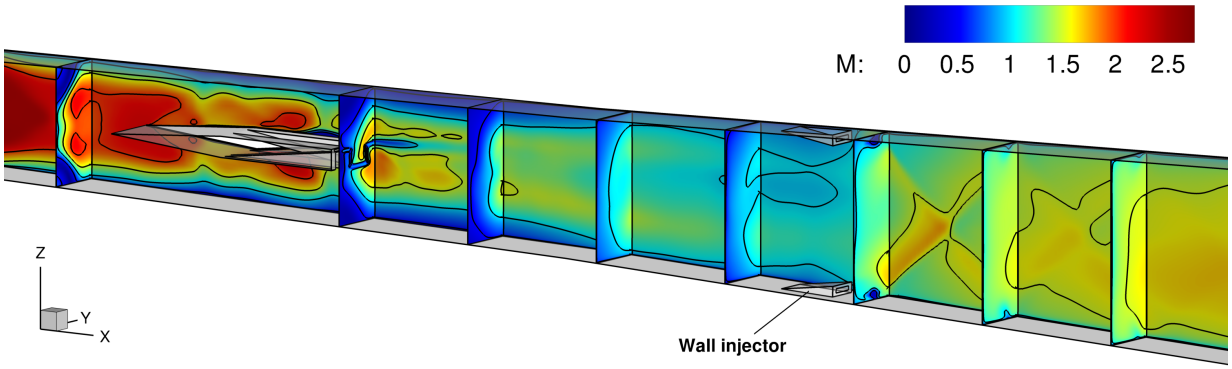

(a) Combustor symmetry plane and several y-z planes in main combustor section

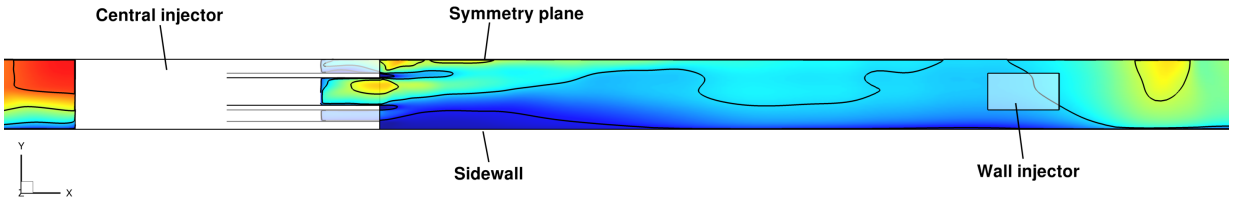

(b) Top view on the combustor x-y mid plane

Figure 8.9: Case S RANS mean Mach number distributions on two-dimensional cut planes, black lines indicate Mach-isocontours at 0.5-intervals

combustion process there.

Figure 8.10 illustrates regions with mean temperatures above 1400 K, thus showing the extent of the combustion region. The combustion zone occupies the major portion of the chamber height between the central and wall injectors, see figure 8.10. Furthermore, the two illustrations reveal that ignition and flame stabilization occur close to the wall immediately behind the central injector. This is plausible for the following two reasons: Firstly, the velocity in the boundary layer is relatively small leading to larger fuel residence times in comparison to the core of the chamber. Secondly, the smaller velocity in turn leads to a higher static temperature by means of fundamental gas dynamic theory expressed by the isentropic relations [2]. Thus, both ignition delay and fuel residence time are favorable for ignition close to the walls. Subsequently, the combustion zone expands in lateral direction further downstream until

the combustor symmetry plane is reached approximately at the half distance between central injector trailing edge and the wall injectors. Furthermore, the distortion of the combustion zone perceptible in the 2D temperature slices in figure 8.10a is the result of the large-scale vortex induced by the central injector.

The wall injector elements deflect both the flow and the heat release region towards the chamber center, see figure 8.10. The lack of lateral expansion of the combustion zone behind the wall injectors is the consequence of the re-acceleration to supersonic velocities evidenced by the oblique shock system, see the Schlieren image in figure 8.11. Since no fuel is injected through the wall injection slots, the near-wall regions downstream of the wall injectors do not feature combustion induced heat release.

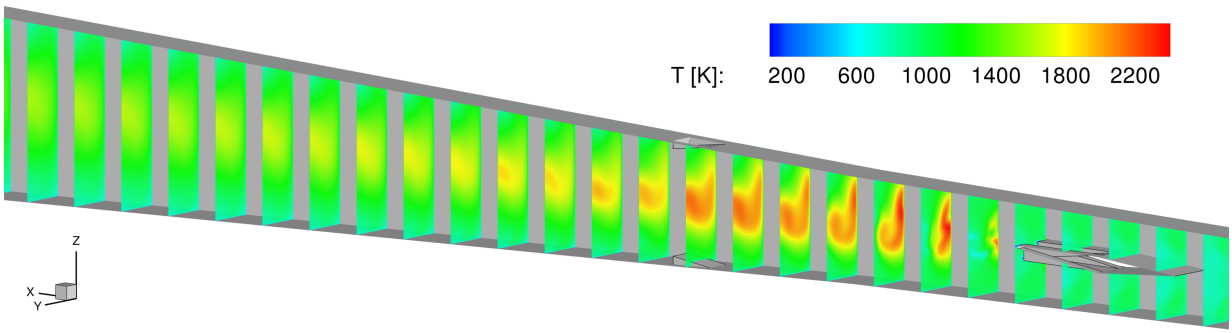

(a) Mean temperature field at selected y-z-planes

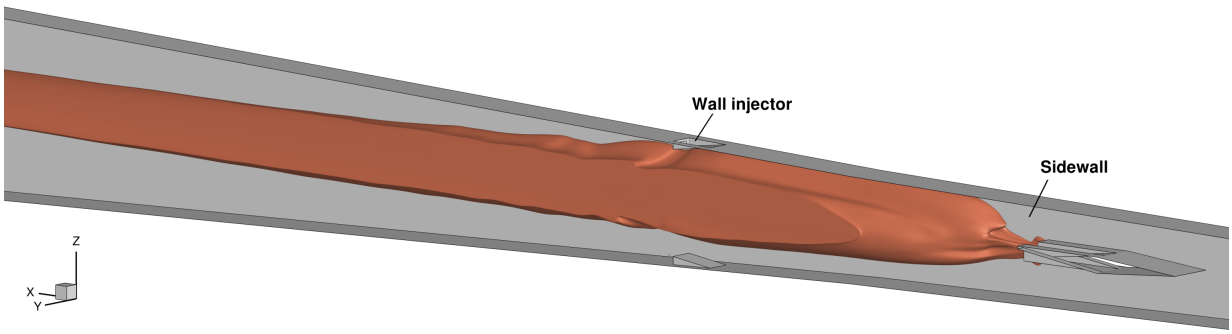

(b) Mean temperature isocontours at 1400 K

Figure 8.10: Case S RANS simulation mean temperatures in main combustion region

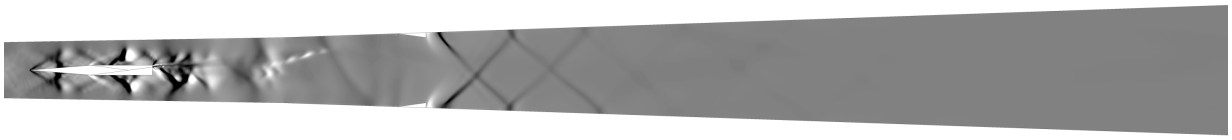

Figure 8.11: Case S RANS instantaneous Schlieren image at symmetry plane

Neither the experiment nor the simulation for case S exhibit considerable differences between the upper and lower wall data. In particular, the instantaneous Schlieren image in figure 8.11 does not exhibit any relevant asymmetry behind the wall injector elements anymore, which is in contrast to case NR. Ultimately, this homogenization is linked to the vast extent of the combustion region between the central and wall injectors featuring comparably low Mach numbers and subsonic zones, illustrated in figure 8.9. The connection between the Mach number, extent of the subsonic zone and the increased homogenization of the flow is the following: On the one hand, the complex three-dimensional flow field inside the combustor can be regarded as a set of numerous mixing layers caused by local, lateral velocity gradients. On the other hand, supersonic shear layers feature generally a smaller growth rate concerning the width of the layer compared to their subsonic counterparts, see Papamoschou and Roshko [105, 124] and Lewis and Hastings [83]. In a more general sense, the mixing layer growth rate decreases with increasing Mach number [141]. For this reason, it can be expected that the mixing layers within the portion of the flow featuring lower Mach numbers will lead to a locally improved interchange between adjacent flow regions. A contrast to this is provided by the two-staged injection modes T1 and T2 discussed in the following sections 8.3.3 and 8.3.5, which feature higher Mach numbers in the core of the flow. Especially the wall pressure data for the T1 flame indicate a considerably larger asymmetry than it is the case for the S flame.

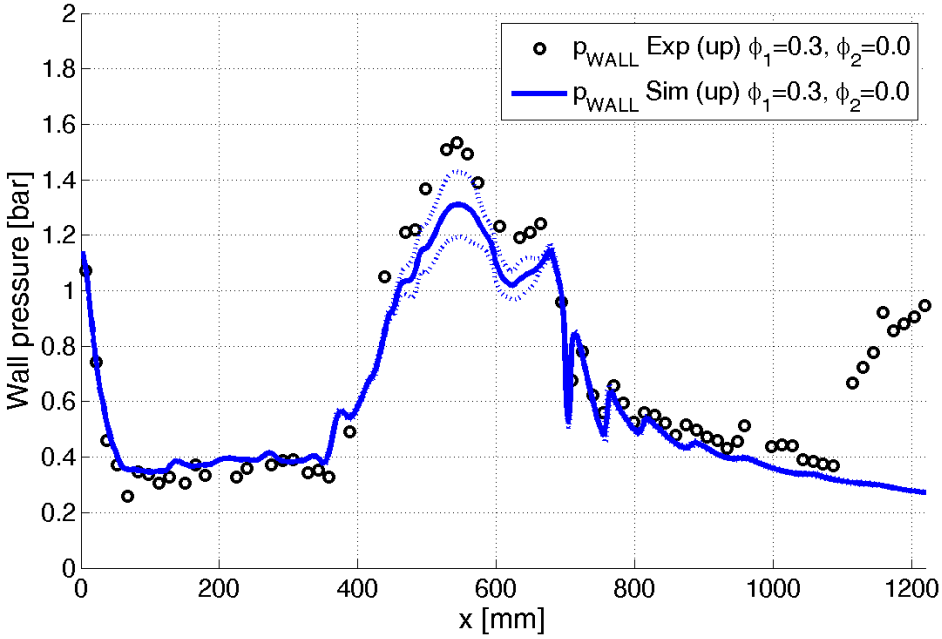

(a) Upper wall

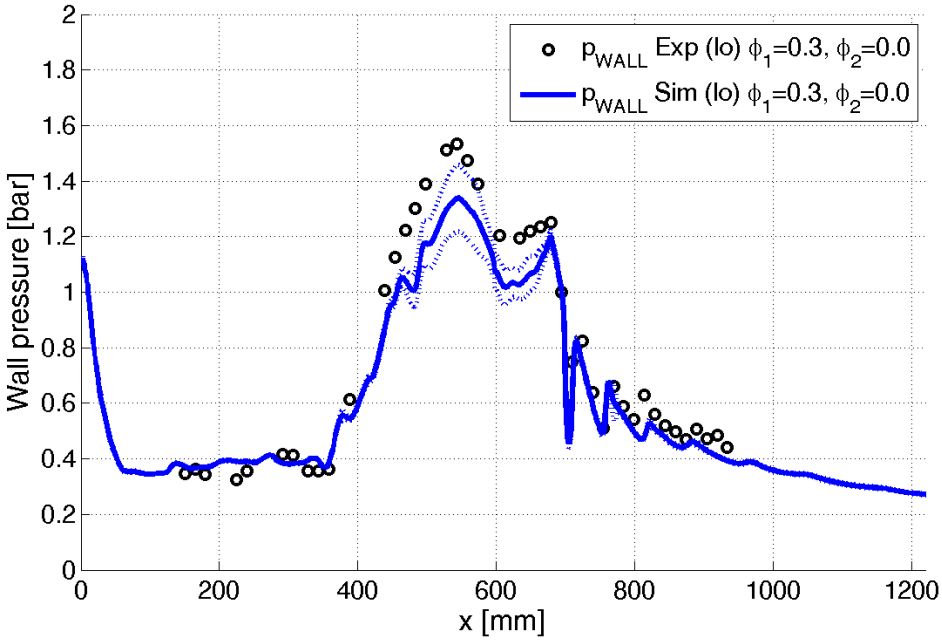

(b) Lower wall

Figure 8.12: Case S experimental and RANS simulation mean wall pressures with central strut fuel injection at equivalence ratio $\phi_1 = 0.3$; dotted lines indicate $1-\sigma$ confidence interval

8.3.3 Two-staged Fuel Injection Case T1

Figures 8.14a and 8.14b show experimental and computational upper and lower wall pressures for the two-staged injection case T1. The fuel equivalence ratios ϕ_1 and ϕ_2 of both 0.15 represent a rather lean two-staged operational point of the ITLR combustor, see section 8.2.1. In contrast to the single-staged, high-equivalence ratio case S, see figures 8.12a and 8.12b, the separation bubble generated by the leading edge shock about x=450 mm is clearly distinguishable from the subsequent combustion induced pressure rise. Hence, it can be stated that the combustion process does not influence the flow upstream of the injector significantly. The pressure reaches a peak value of 1.2 bar around x=700 mm in the experiment for both the upper and lower wall. The computational results follow the trend well, yet predict a slightly smaller mean peak pressure of approximately 1.1 bar. Both experimental and computational pressures feature a sharp decline behind the wall injector elements downstream of x=700 mm. Especially the simulated lower wall pressure exhibits a noticeable pressure drop at this location. Moreover, the alternating lower wall pressure data between x=550 mm and x=700 mm indicate the presence of a shock system with a close succession of shock waves. The latter is confirmed by the instantaneous computational Schlieren image illustrated in figure 8.13, which clearly shows a shock system between the central and wall injectors. This implies that the core flow is mainly supersonic in this region, although local and transient subsonic regions still exist. This is in contrast to case S, see figures 8.9 and 8.11.

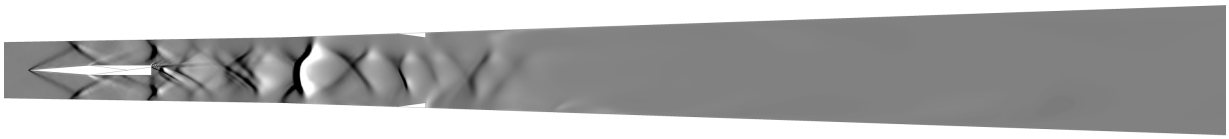

Figure 8.13: Case T1 RANS instantaneous Schlieren image at symmetry plane

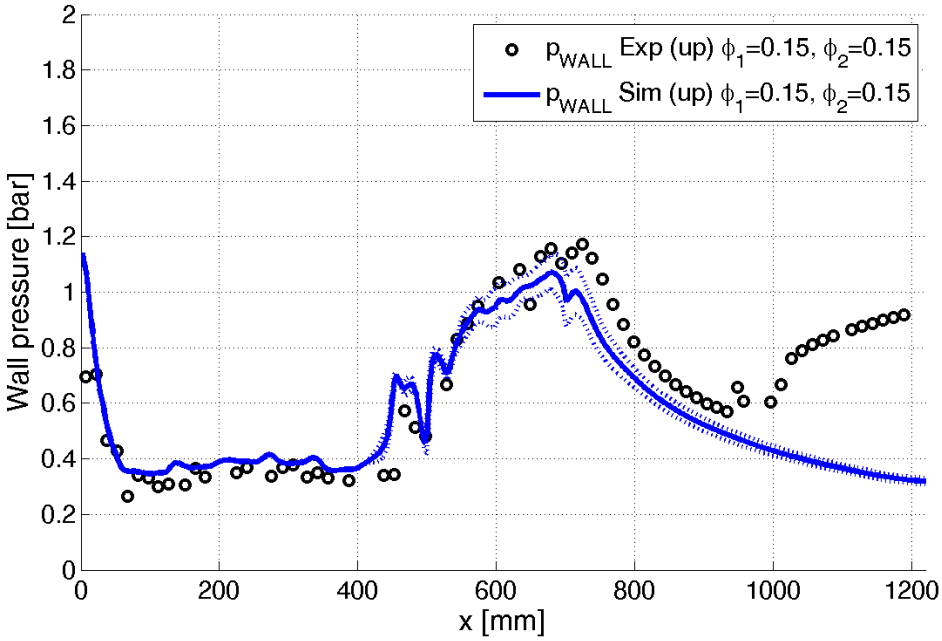

(a) Upper wall

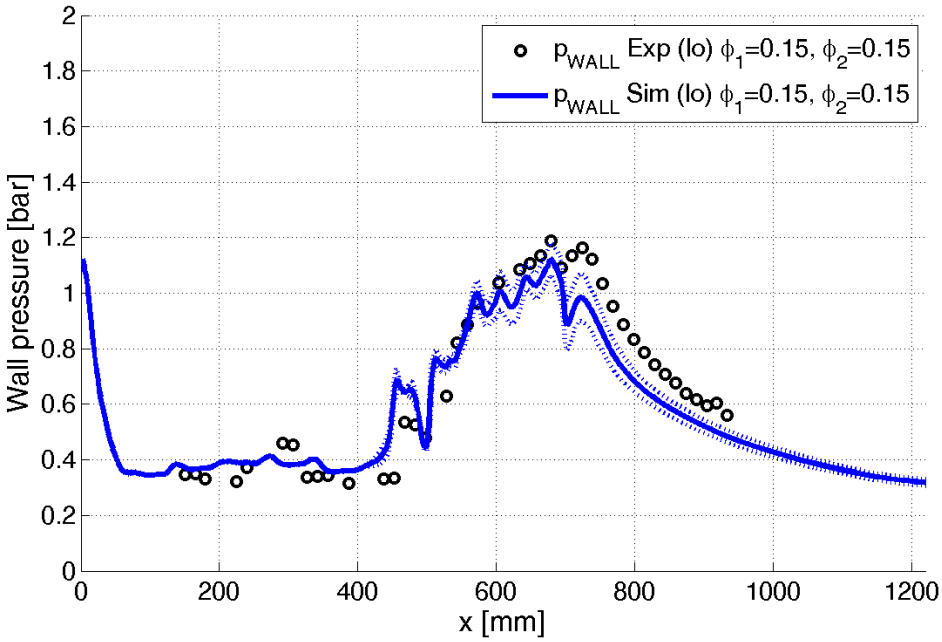

(b) Lower wall

Figure 8.14: Case T1 experimental and RANS simulation mean wall pressures with central strut and wall fuel injection at equivalence ratios $\phi_1 = 0.15$ and $\phi_2 = 0.15$; dotted lines indicate $1-\sigma$ confidence interval

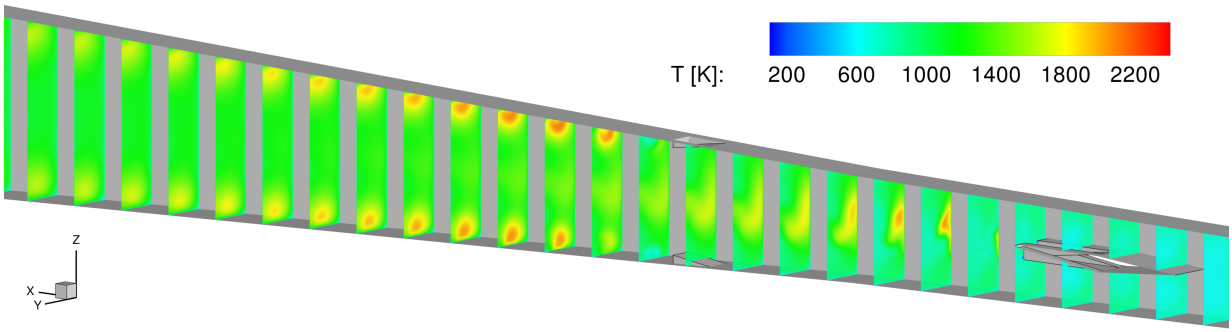

(a) Mean temperature field at selected y-z-planes

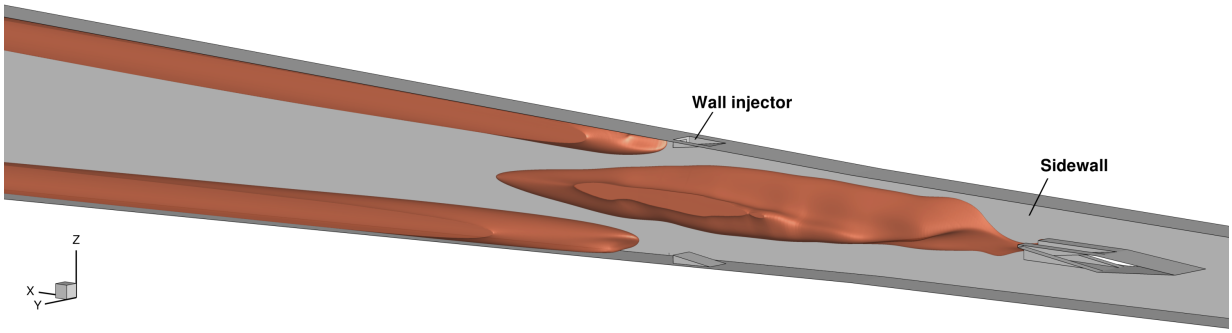

(b) Mean temperature isocontours at 1400 K

Figure 8.15: Case T1 RANS simulation mean temperatures in main combustion region

Figure 8.15b provides a three-dimensional view of the T1 flame indicated by mean temperature isocontours at 1400 K. Regions with higher temperatures are enclosed within this isocontour. Additionally, the corresponding figure 8.15a shows two-dimensional temperature fields on selected y-z-planes. In contrast to the single-staged injection case S, two separate combustion zones form behind the wall injectors due to the staged injection. These remain detached from the combustion region in the core of the flow. Ignition and flame stabilization occur immediately behind the central injector close to the wall alike case S. The reasons are similar, see the previous section on case S for an explanation. However, the combustion region requires a considerably larger downstream distance to reach the combustor symmetry axis. The temperatures in the main combustion region between the central and wall injectors

are generally lower than in case S, which features a higher equivalence ratio.

In further contrast to case S, see figure 8.10, the lateral expansion of the combustion zone in y-direction does not occur continuously. Instead, the growth of the combustion zone in lateral direction takes place in distinct steps between the central injector and wall injectors, see figure 8.16. The reason is the interplay of shock waves and combustion zones dominating the T1 flame. This interplay shall be explained on the basis of figure 8.17: Figures 8.17a and 8.17b show the instantaneous computational Schlieren images and temperature fields at the combustor symmetry plane and the x-y plane in the combustor center. Figure 8.17c illustrates the corresponding lateral y-component of the instantaneous velocity field in the x-y combustor center plane. The y-component of the velocity field is a result of the large streamwise vortices generated by the central injector. The distribution of the lateral velocity reveals that initial flame expansion towards the center line is due to the vortex structure induced by the injector, although it is obviously promoted by the combustion induced pressure rise and subsequent expansion. In consequence, the expanding combustion zone deflects the still non-reacting portion of the flow, since it serves as an aerodynamic ramp promoting the development of further shocks, see figure 8.17a. Primarily, the dominant combustion zone emerging at the wall closely behind the central injector is visible. Yet, additional combustion pockets appear close to the symmetry plane further downstream. Evidently, these pockets form immediately downstream of shock waves, which are perceptible in the Schlieren image in figure 8.17a. Hence, the shock induced temperature rise leads to auto-ignition and flame stabilization of these combustion pockets, see figure 8.18. As a result of this entire process described above, a mutually dependent, unsteady system of shocks and combustion zones develops and finally results in the mean field shown in figure 8.15.

In summary, mode T1 features a substantially different combustion zone structure than the rather subsonic case S. Nevertheless, ignition occurs in the small subsonic layer immediately behind the central injector in both cases for the reasons given in section 8.3.2. The large portions of the combustion zone in case S featuring Mach numbers close or below one promote the lateral ex-

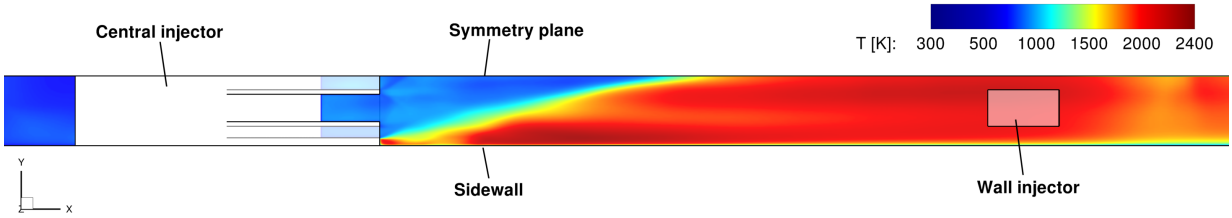

(a) Case S

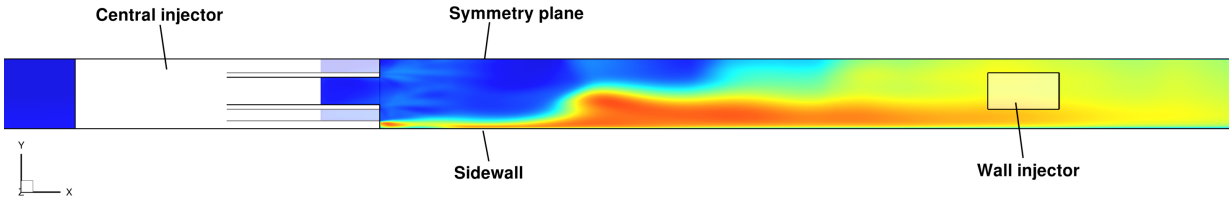

(b) Case T1

Figure 8.16: Mean temperature fields for case S and T1 RANS simulations on the combustor x-y mid plane

change of information and thus homogenization of the flame region due to the increased mixing layer growth rate at lower Mach numbers [83, 105, 124], see also section 8.3.2. In contrast to that, larger portions of the core flow remain supersonic in case T1, such that the combustion process is mainly a mutually dependent interplay of shock waves and immediately following pockets of combustion, which constitutes the "supersonic nature" of the T1 flame. The essence of this interplay is illustrated in figure 8.20 and is based on the simplified assumption that the flow can be separated in neighboring streamtubes with different velocities, which form a compressible compound flow [14, 59]. The justification for this segmentation of the flow field into adjacent streamtubes builds upon the aforementioned reduced mixing layer growth rate in high Mach number flows [105, 124], see section 8.3.2. Although there certainly is interchange and mixing between adjacent streamtubes, the tendency towards reduced mixing layer development allows for the aforementioned segmentation of the flow field at least in a qualitative sense [83]. Exchange between neighboring streamtubes due to turbulent or diffusive transport processes is thus reduced compared to a slow subsonic flow field. Instead, adjacent streamtubes influence each other through local changes in shape and extent. A change in lateral dimension of one streamtube, e.g. caused by a local

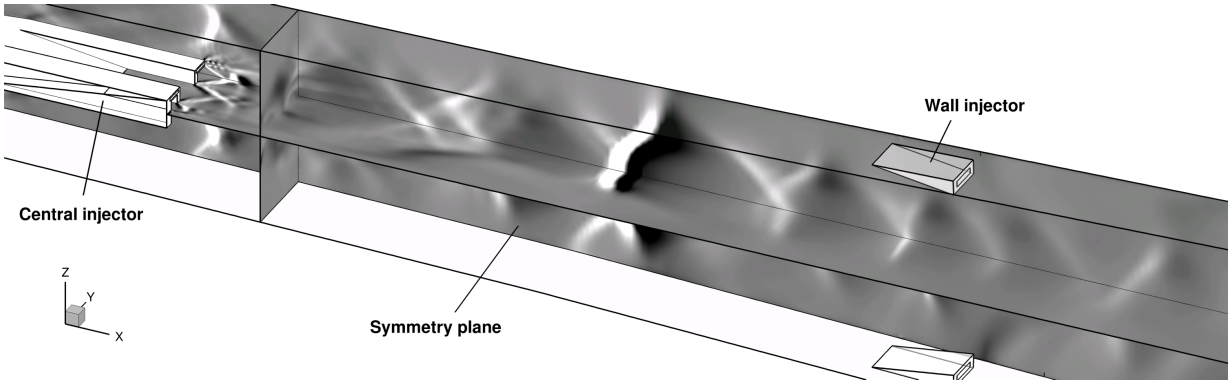

(a) Schlieren images

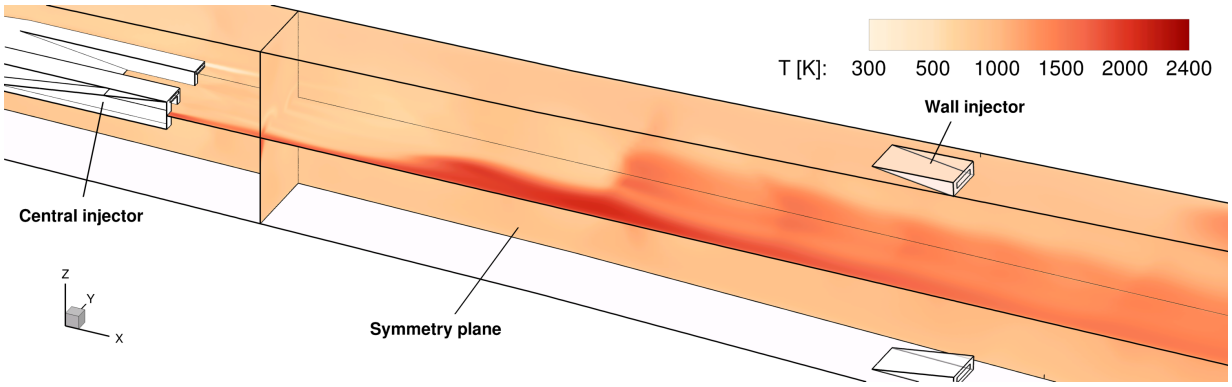

(b) Temperature

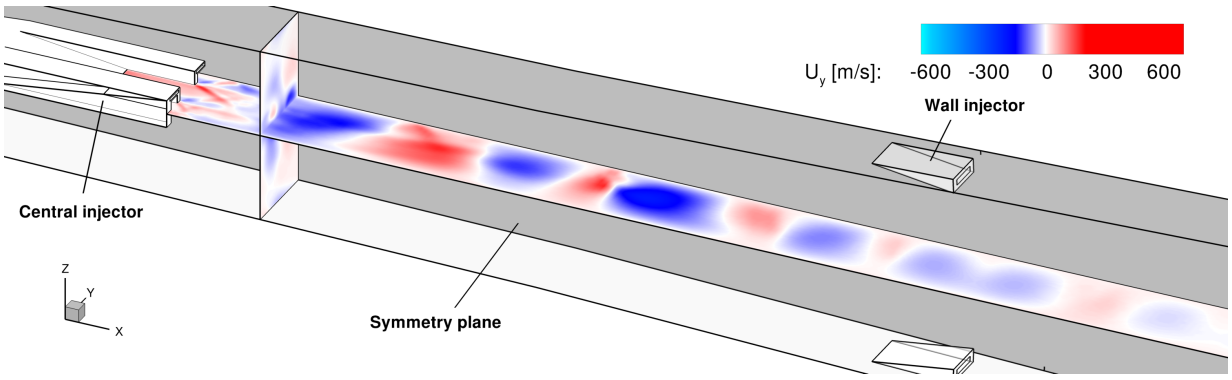

(c) Y-component of velocity

Figure 8.17: Case T1 RANS instantaneous fields at combustor symmetry plane, x-y mid plane and one selected y-z-plane

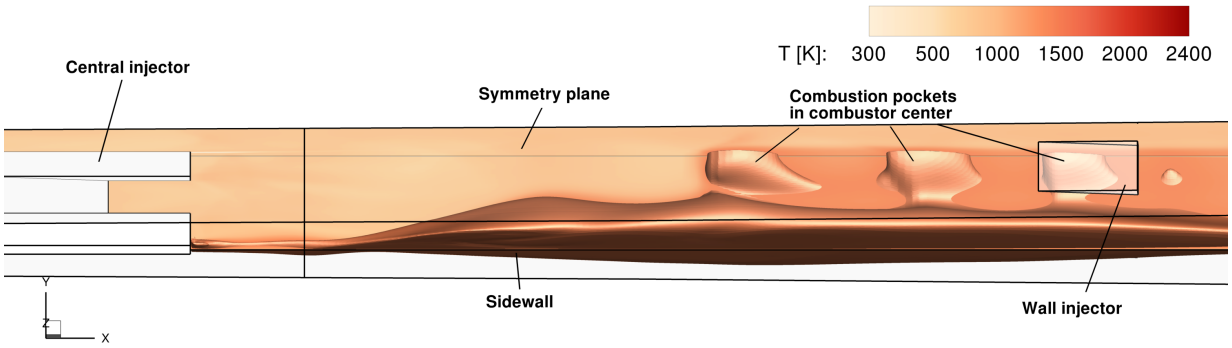

Figure 8.18: Case T1 RANS instantaneous 2D temperature fields at x-y combustor mid plane and symmetry plane and 3D temperature isocontour at 1400 K

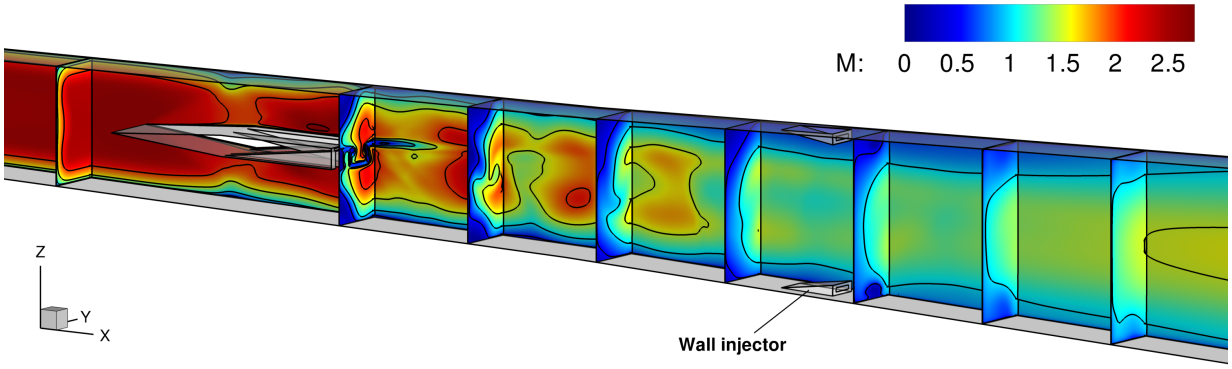

(a) Combustor symmetry plane and several y-z planes in main combustor section

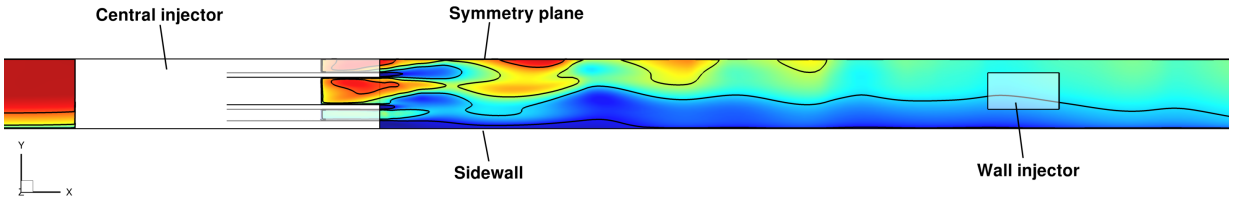

(b) Top view on the combustor x-y mid plane

Figure 8.19: Case T1 RANS mean Mach number distributions on two-dimensional cut planes, black lines indicate Mach-isocontours at 0.5-intervals

combustion induced pressure rise, acts as an aerodynamic ramp or nozzle for neighboring streamtubes, thus changing the flow conditions there, as shown in the schematic image in figure 8.20. In consequence, shocks S1, S2 and S3 emerge that can lead to the ignition of adjacent streamtubes. The T1 flame also features this ignition mechanism, see figures 8.17a and 8.18. The situation illustrated in figure 8.20 represents solely one exemplary state. Ignition in streamtube 1 could also occur immediately behind shock S1, or streamtube 2 might also be supersonic but feature a different Mach number than streamtube 1. The flow might also feature more than two regions with different inflow conditions leading to additional streamtubes.

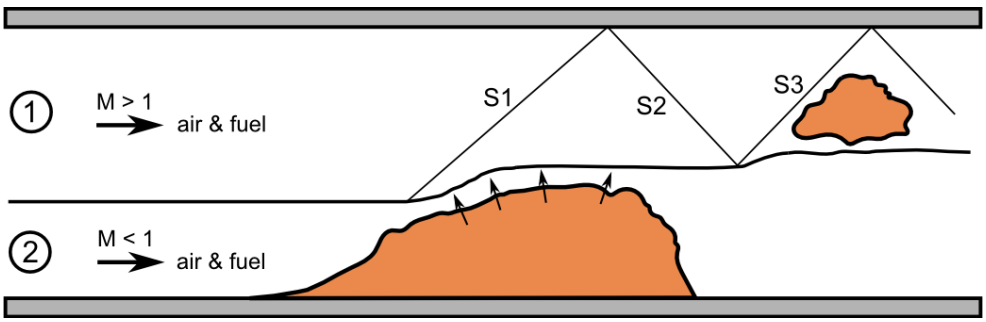

Figure 8.20: Schematic interplay of two adjacent streamtubes, whereas streamtube 1 is supersonic, streamtube 2 is subsonic; initial ignition occurs close to wall in subsonic streamtube 1; combustion induced expansion of streamtube 1 leads to shock S1 and subsequent shocks S2 and S3; orange areas mark zones with significant combustion

Within this context, the aforementioned "supersonic nature" of the T1 flame does not imply that the flow is supersonic in every aspect. The boundary layers still exhibit vast subsonic layers and the Schlieren image in figure 8.17a proves that local subsonic regions exist also at the symmetry axis, e.g. in the form of a Mach disk with subsequent re-acceleration to supersonic velocities. The large extent of the boundary layers present in the ITLR combustor additionally promotes the formation of subsonic combustion zones. However, the structure of the combustion zone is dominated by the gas dynamic processes described above that are attributed to supersonic combustion.

8.3.4 Two-staged Ignition Sequence IT2 for Case T2

The purpose of the ignition sequence simulation IT2 is twofold: Firstly, the ability of the developed flow solver to predict unsteady processes changing the mean flow field shall be demonstrated by means of URANS. Secondly, the ignition process and in particular its time scale shall be investigated. As opposed to the S, T1 and T2 RANS simulations discussed in sections 8.3.2, 8.3.3 and 8.3.5, case IT2 is based on a slightly coarser mesh incorporating solely 4.1 million cells. The coarsening of the mesh towards the outflow increases the numerical stability of the computations. Moreover, the reduced 12-step hydrogen reaction scheme by Boivin et al. [16] developed for supersonic combustion is employed for reasons of computational efficiency. The simulation is initiated from the non-reacting case NR including the laboratory backpressure. The latter results in the formation of separation regions and a shock train close to the chamber exit, cf figure 8.6. Furthermore, hydrogen is injected at the central and wall injection elements at fuel equivalence ratios ϕ_1 and ϕ_2 of both 0.2 corresponding to the two-staged injection case T2.

The instantaneous temperature fields of the simulated combustor ignition process shown in figure 8.22 reveal the formation and upstream propagation of a combustion zone at the outflow. The low velocities within the extensive subsonic boundary layer separation region close to chamber exit paired with the shock train result in an increase of static temperature. Hence, the still unburned hydrogen injected further upstream experiences conditions promoting ignition. This initial combustion zone emerges at the upper wall, since the boundary layer separation region is larger than at the lower wall, see figure 8.6. Once initial ignition has occurred, the combustion induced pressure rise leads to an upstream expansion of the heat release region. As a result, the Mach number falls below one downstream of the flame front. The expanding combustion region reaches the wall injectors at 0.6 ms and ignites the hydrogen there. The remaining portion of the heat release zone expands further upstream and reaches the central injector at approximately 1.2 ms, which is in accordance with experimental observations of this process [90].

Figure 8.21 illustrates the instantaneous wall pressures at the time steps cor-

responding to figure 8.22. The temporal evolution of the flame front features a sharp pressure rise separating the supersonic flow upstream from the region with hot burnt gases downstream. In particular, the wall pressure upstream of the flame front remains unaffected, which is a consequence of the supersonic flow velocity. The entire process from initial ignition at the outflow until the quasi-steady wall pressure corresponding to case T2 is obtained takes approximately 3 ms [90].

The essential result of the IT2 simulation is that the developed solver is able to predict unsteady effects changing the mean field within a full combustor by means of RANS.

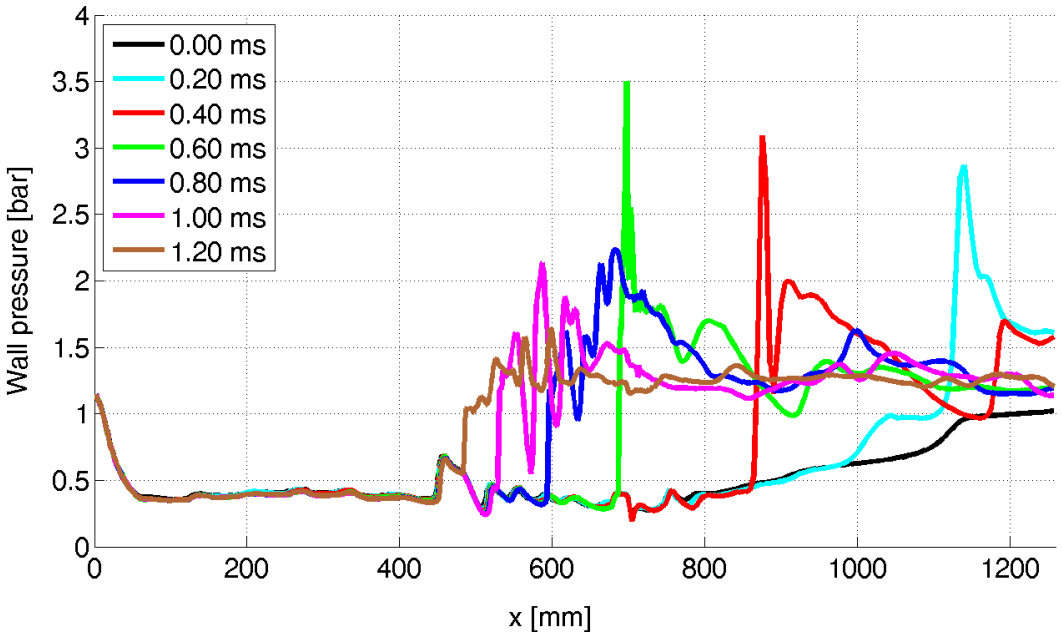

Figure 8.21: Instantaneous wall pressure snapshots of the combustor ignition sequence RANS simulation for case T2, instants of time correspond to images in figure 8.22

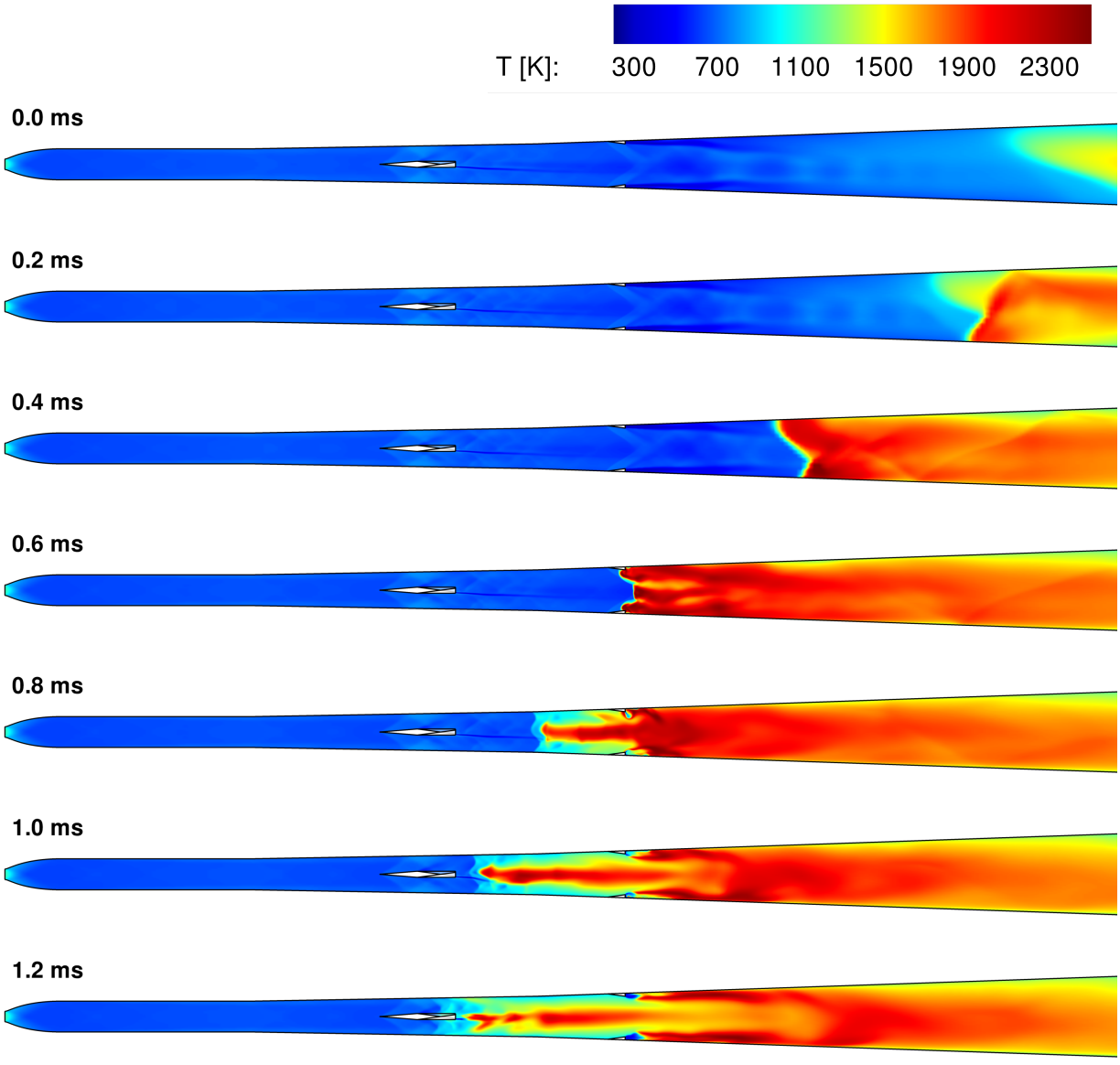

Figure 8.22: Combustor ignition sequence for case T2 simulated with RANS, temperature cuts at one fourth of channel width

8.3.5 Two-staged Fuel Injection Case T2

Figures 8.23a and 8.23b provide the experimentally and computationally obtained wall pressures for the two-staged fuel injection case T2. Both fuel equivalence ratios for the central and wall injector stages ϕ_1 and ϕ_2 amount to 0.2. This operational point constitutes the most commonly investigated combustion test case at ITLR. The pressure level between the central injector trailing edge at x=500 mm and the wall injectors at x=700 mm is increased compared to case T1, cf. figures 8.14a and 8.14b. Nevertheless, a distinct pressure peak in the experimental data originating in the shock induced by the central injector leading edge is perceptible, which is in contrast to case S, cf. figures 8.12a and 8.12b.

The simulation follows the experimental pressure trend well, yet, the leading edge shock pressure rise and combustion induced pressure rise further downstream are indistinguishable. Generally, the simulation slightly overpredicts the combustion induced pressure rise between x=500 mm and x=600 mm. The experimental wall pressure drops continuously downstream of x=700 mm until the beginning of the backpressure-induced separation region at x=950 mm. The computational results exhibit a continuing pressure decrease further downstream, since atmospheric backpressure is neglected.

The 1-σ standard deviation confidence intervals of the computational wall pressure plotted in figures 8.23a and 8.23b reveal strong pressure fluctuations in the region behind the wall injectors around x=700 mm, while the pressure remains stable at all other locations. The T1 flame discussed previously also exhibits a prominent wall pressure variance in the vicinity of the wall injectors, yet this effect is more pronounced here. This fluctuations can be explained by the flow conditions at the wall injectors: The large combustion zone downstream of the central injector induces perturbations in the flow field, in addition to the already existing unsteadiness originating in the large vortex generated by the central injector. Hence, the shock induced by the wall injector ramps as well as the expansion fans at the wall injector ramp trailing edges experience transient fluctuations in velocity, temperature and all remaining flow properties. Therefore, the hydrogen injected into the wake of the wall injectors

is subject to a likewise varying succession of compressions and expansions of transient intensities. Hence, also local ignition delay and fuel residence times are subject to oscillations. Finally, this results in the spatially and temporally unsteady combustion in this region and explains the large uncertainty embodied by the 1-σ standard deviation confidence interval for the computational pressure. Yet, this pressure disturbance does not propagate further upstream in the RANS simulation, as indicated by the small pressure 1-σ confidence intervals upstream of x=700 mm in figure 8.23. This aspect is in contrast to the hybrid RANS/LES simulation of the T2 operational point presented in section 8.5.2. In summary, it can be stated that unsteady, fluctuating combustion should be generally anticipated, if a vortex-generating injector is paired with a staged injection further downstream.

Additionally, the T2 flame RANS simulation is conducted on the finer hybrid RANS/LES mesh described in section 8.2.4. The resulting differences in the simulated wall pressures based on the two meshes are only marginal, see figure 8.23. Hence, two conclusions can be drawn: It can be stated that the RANS mesh provides sufficient spatial resolution. Secondly, the differences between the RANS and hybrid RANS/LES simulations presented in section 8.5 are not due to the different meshes but due to the different turbulence modeling approaches.

The mean Mach number distribution in the main combustion region between the central and wall injectors shown in figure 8.24 represents an intermediate state between cases S and T1. Clearly, a broad subsonic region exists emerging at the near-wall flame stabilization location immediately behind the central injector. Nevertheless, distinct supersonic pockets exist close to the chamber symmetry axis. The Schlieren image in figure 8.25 also demonstrates that the flow remains partly supersonic in the core. The steep shock angles indicate a low Mach number though, which decreases with every shock. Turner and Smart term this mode of combustor operation separated combustion mode and classify it as a transient state between ramjet and scramjet operation [137]. In this particular case, a shock train with distinct Mach disks forms with subsonic velocities and immediate re-acceleration to supersonic speeds before the next Mach disk is approached. This latter aspect is in partial con-

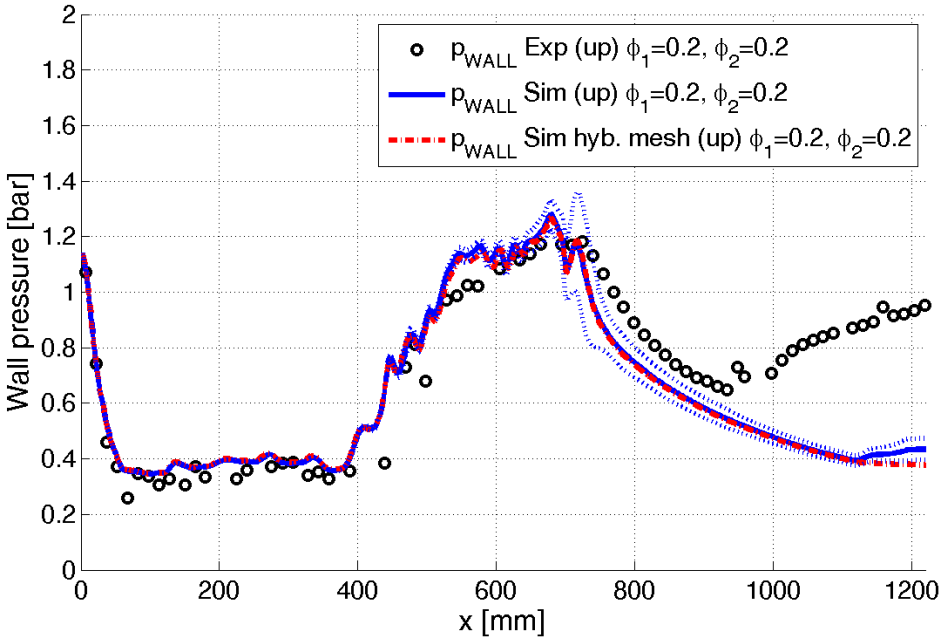

(a) Upper wall

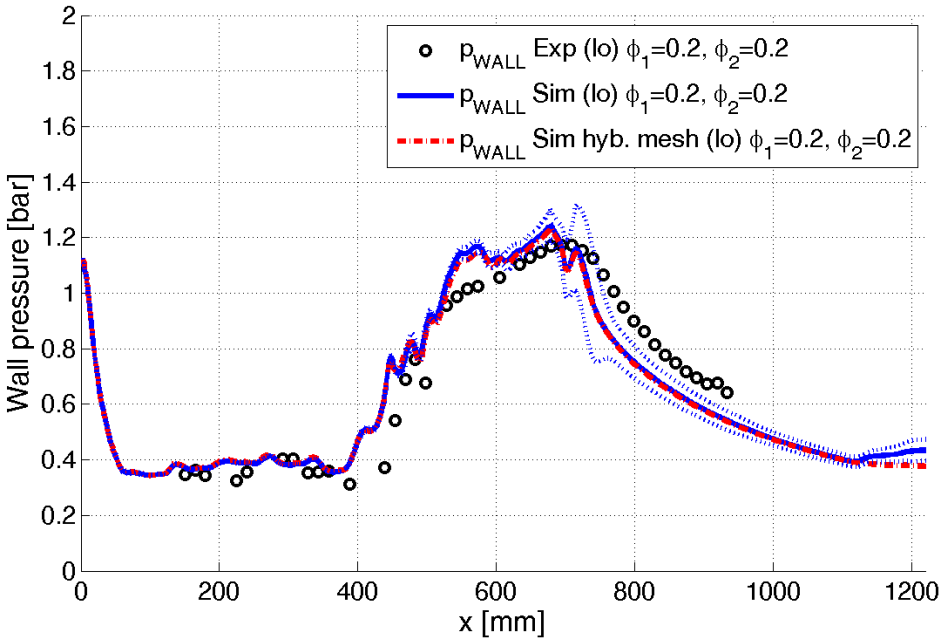

(b) Lower wall

Figure 8.23: Case T2 experimental and RANS simulation mean wall pressures (RANS and hybrid mesh) with central strut and wall fuel injection at equivalence ratios $\phi_1 = 0.20$ and $\phi_2 = 0.20$, dotted blue lines indicate $1-\sigma$ confidence interval

trast to the hybrid RANS/LES simulation of the T2 flame discussed in the following section 8.5.2.

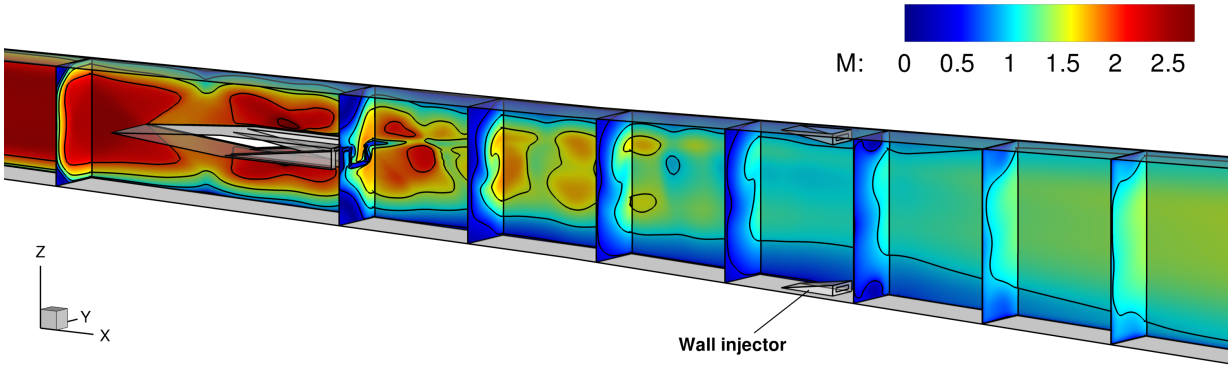

(a) Combustor symmetry plane and several y-z planes in main combustor section

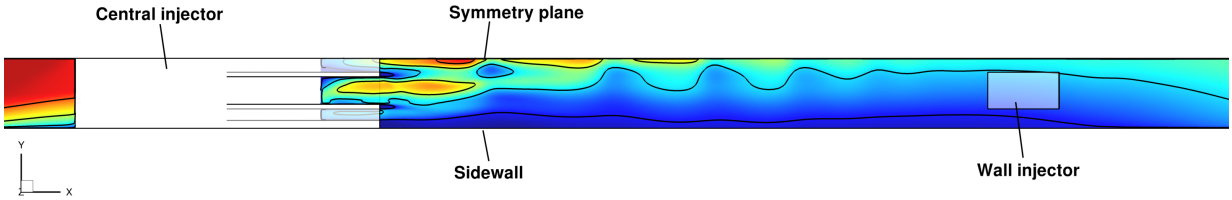

(b) Top view on the combustor x-y mid plane

Figure 8.24: Case T2 RANS mean Mach number distributions on two-dimensional cut planes, black lines indicate Mach-isocontours at 0.5-intervals

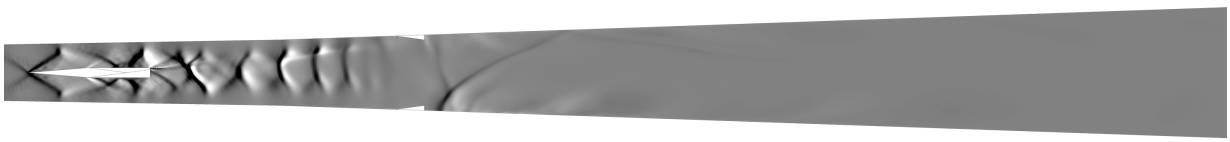

Figure 8.25: Case T2 RANS instantaneous Schlieren image at symmetry plane

The mean temperature fields illustrated in figure 8.26 show the extent of the combustion region. Alike case T1, two distinct combustion regions develop aft of the wall injectors due to the staged wall injection. The heat release region reaches the symmetry plane earlier than in case T1. In spite of the aforementioned shock train and lower Mach numbers, the flame structure provided by

the T2 RANS simulation exhibits similar characteristics as the T1 flame that were attributed to supersonic combustion, see section 8.3.3. As discussed in the previous section on case T1, the flame structure of the T1 flame is the result of a gas dynamically controlled interplay and mutual feedback between combustion generated volume expansion and thereby induced shock structures. Nevertheless, the T2 operational point features considerable subsonic flow regions especially in the vicinity of the wall injectors, see figure 8.24. Essentially, this corresponds to a transition between ramjet and scramjet operation as mentioned previously. A discussion and classification of the investigated operational points of the ITLR combustor follows in the subsequent section 8.4.

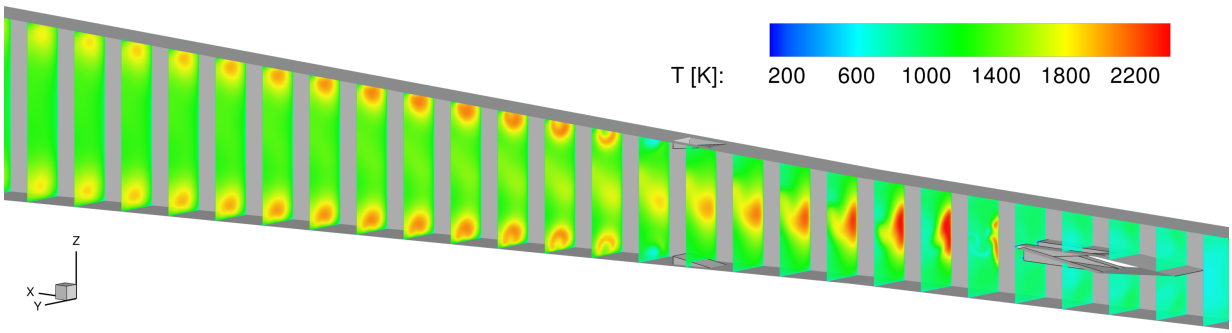

(a) Mean temperature field at selected y-z-planes

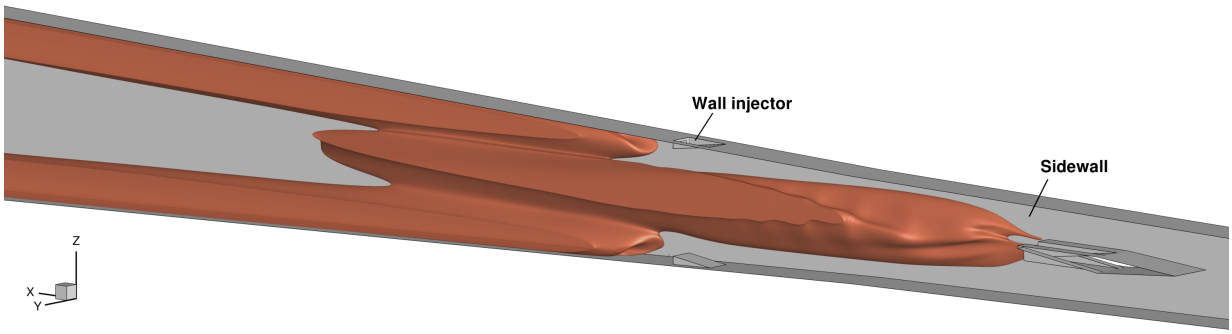

(b) Mean temperature isocontours at 1400 K

Figure 8.26: Case T2 RANS simulation mean temperatures in main combustion region

8.4 Classification of Combustor Operation

Here, the investigated operational points of the ITLR combustor shall be related to common classifications of scramjet/ramjet operational regimes. The attempt to categorize the mode of operation provides the link between the physical interpretation of the operational points discussed further above and the conditions in an engine system. Furthermore, it provides the motivation for the application of the hybrid RANS/LES methods introduced in chapter 8.5.

An important aspect within this context is the dual-mode combustion concept. A scramjet engine is referred to as a dual-mode combustor, if it can operate both in ramjet or in scramjet mode [97]. The deceleration to subsonic velocities does not occur due to a geometrical throat like in a conventional ramjet but due to combustion induced thermal choking within a shock train effectively serving as a thermal throat. The dual-mode capability is especially desirable for the relevant flight Mach number regime from Mach four to eight [137], since ramjet operation can be more efficient at lower Mach numbers, whereas scramjet operation is favorable at the top end of this range [133]. The existence of pure ramjet and scramjet operation modes within one combustor obviously includes the transition between the two regimes.

No unique classification exists for the intermediate states between purely supersonic and subsonic combustion modes of an engine. Yentsch and Gaitonde [145] define the pure scramjet mode by the absence of strong shocks upstream of the combustion zone. The ramjet mode on the other hand features a strong shock or shock system upstream of the combustion region and significant influence of the combustion zone on the wall pressure distribution further upstream, see figure 2.3. According to the definition utilized by Yentsch and Gaitonde, the operational points of the ITLR chamber T1 and T2 are of scramjet type, see figure 8.24, since the core flow remains supersonic. Yet, case S already features significant deceleration to Mach numbers closely above one upstream of the central injector trailing edge, see figure 8.9. Moreover, all cases feature a combustion-induced wall pressure rise upstream of the location of fuel injection located at the central injector trailing edge. Fotia et al. effectively

separate ramjet and scramjet modes by their respective wall pressure profiles such that solely the cases without significant combustion induced wall pressure rise upstream of the injection location are defined to be of scramjet type [41–43]. According to this perspective, the investigated ITLR cases are not pure scramjet operational points, since all wall pressure profiles for cases S, T1 and T2 feature increased wall pressures upstream of the central injector trailing edge (approximately at x=500 mm), see figures 8.12, 8.14 and 8.23, compared to the non-reacting case given in figure 8.7.

A more appropriate description of the combustion mode matching the intermediate state in-between ramjet and scramjet mode given in the ITLR combustor is provided by Turner and Smart [137]. They provide the definition of a transitional mode, which they term separated combustion mode, see also Curran et al. [31]. The combustion induced pressure rise does not lead to thermal choking as in ramjet mode, yet. Hence, this mode does not generate a normal shock train, cf. figure 2.3 and subsonic combustion. However, the combustion induced pressure rise is large enough to generate extensive boundary layer separation. The boundary layer separation in turn leads to the generation of a dominant oblique shock system, see figure 8.27, which does not feature strong shocks though. Yet, this mode features extensive subsonic near-wall regions within the combustor, which confine the supersonic core flow [31, 41]. Especially the investigated T1 and T2 operational modes of the ITLR combustor match this definition of the ramjet/scramjet transitional state, see figures 8.19 and 8.24.

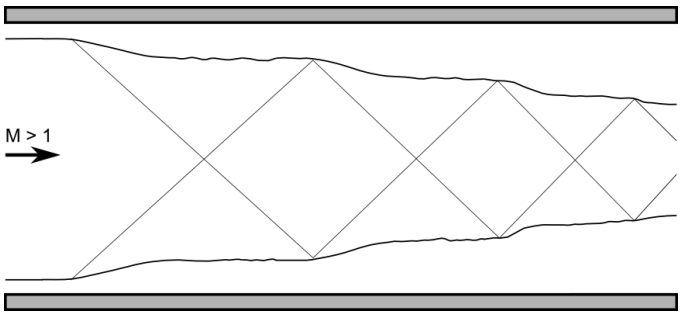

Figure 8.27: Oblique shock system and extensive boundary layer separation in ramjet/scramjet transitional separated combustion mode [137]

In consequence, the operational points investigated by means of URANS in

section 8.3 above are of a transitional type between ramjet and scramjet operation in the context of a dual-mode combustion engine. This provides both the challenge and the motivation for the hybrid RANS/LES investigation of the ITLR combustor in the subsequent section 8.5, since the two following components must be taken into account by the hybrid RANS/LES method: Firstly, the extensive boundary layer growth due to the combustion induced pressure rise and secondly, the resulting oblique shock train and its feedback on the combustion process. Now, the purpose of the two parts of the RANS/LES hybridization scheme becomes more vivid: While method A accounts for the "conventional" boundary layer growth e.g. due to the duct length, method B is intended to dominate in regions with extensive boundary layer growth due to combustion induced pressure rise identified by the large extent of the subsonic portion of the boundary layers. Hence, method B enables RANS in the subsonic near-wall regions, if extensive boundary layer separation is present, which Turner and Smart identify as a characteristic feature of the transitional separated combustion mode between ramjet and scramjet combustion.

At this point it is worth to recall, why only method A was utilized for the hybrid RANS/LES simulation of the supersonic injection experiment described in chapter 6: Due to the lack of any combustion induced pressure rise or an extensive duct length, the investigated duct wall boundary layer is comparably thin and lacks any excessive boundary layer separation. Therefore, method B designed for the ramjet/scramjet transition regime is obsolete in this case. Furthermore, Chemnitz [23] performed hybrid RANS/LES simulations of the supersonic combustor at the Institute of Flight Propulsion at TUM [48, 49] utilizing the flow solver introduced in chapter 3 and the hybrid RANS/LES method A described in section 4.4 of this thesis. The TUM combustor flow field is mainly supersonic with a thin subsonic combustion region behind the central injector. Hence, the flow regime of the combustor at the TUM Institute of Flight Propulsion is not of the same transitional type as the ITLR combustor discussed here but rather of supersonic type with a small and short subsonic core flow [23]. For this reason, no extensive subsonic boundary layer regions form at the duct walls rendering method B again obsolete in this case.

8.5 Hybrid Reynolds-Averaged Navier Stokes and Large Eddy Simulation

The following hybrid RANS/LES investigations of the non-reacting case NR and the T2 flame apply the full hybridization method C being comprised of the hybridization method components A and B introduced in chapter 4. Method B accounts for the extensive boundary layer thickness within the combustor shock system being a characteristic feature of the separated combustion mode discussed in the previous section 8.4. Method A rests upon a comparison of RANS and LES turbulence model predictions, which are scaled beforehand in order to allow for a direct comparison. LES is activated in a given computational cell, if its scaled subgrid turbulent viscosity exceeds the RANS counterpart. The result is a hybridization, which can account for the boundary layer growth along the downstream direction and the interaction of shock waves and boundary layers as demonstrated in chapter 6. In contrast to the purely model-prediction based selection of the local turbulence mode in hybridization method component A, method B places the RANS/LES interface following the sonic line within the boundary layer. The purpose of method B is to ensure that RANS is activated in regions with extensive shock induced boundary layer separation indicated by deflections of the sonic line, while the remaining outer portions of the boundary layer are treated with LES. Hence, hybridization method component B allows to reduce the portion of the combustor channel treated with RANS to a minimum leaving more space for the LES mode. Nevertheless, method B ensures that the subsonic near-wall regions defining the separated combustion mode [137] are treated with RANS, see the previous section 8.4.

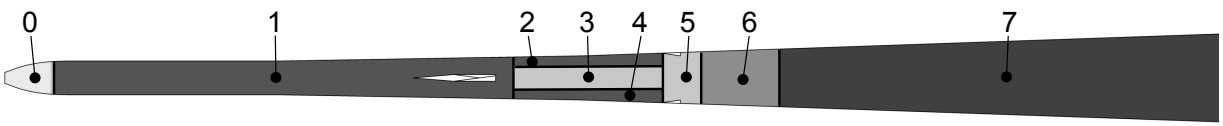

Figure 8.28: Separate maximum RANS zone thickness regions

The common hybridization method parameter settings valid for the hybrid

RANS/LES simulations presented below are given in table 8.3. With the purpose of adjusting and confining the influence of the two hybridization method components, the computational domain is split into several regions with local settings for the maximum RANS zone thicknesses $C_{A,z,max}$ for method A and $C_{B,z,max}$ for method B, see chapter 4. The boundaries of the respective regions are illustrated in figure 8.28 are specified in table 8.5. The transition between adjacent regions is smoothed by a linear blending of RANS zone thickness, yet, no significant effects related to this setting could be observed.

The settings for $C_{A,z,max}$ and $C_{B,z,max}$ individually utilized for each region are listed in table 8.4. These settings are valid for both the non-reacting and the T2 simulation. The result is a compromise between a large extent of the LES region but yet sufficient RANS boundary layer coverage. Region 2, 3 and 4 downstream of the central injector feature a common value of 2.5 mm for the maximum RANS zone thickness $C_{A,z,max}$, such that hybridization method A can solely set the wall-closest portion of the boundary layer to RANS. In contrast, the maximum RANS zone thickness $C_{B,z,max}$ for method B is set to 9 mm in order to enable RANS modeling of shock boundary layer interactions in regions 2, 3 and 4. The purpose is to maximize the extent of the chamber cross section available for the development of coherent turbulent structures by means of LES in the main combustion region between the central injector trailing edge and the wall injectors. Next, region 5 covering the immediate vicinity of the wall injectors features a generally truncated RANS zone for the purpose of enabling LES in the fuel injection and mixing region close to wall injection slots. In order to account for the subsequent boundary layer growth, regions 6 and 7 further downstream feature larger thresholds.

Adjusting the maximum RANS zone thicknesses within specific regions does not contradict with the objective of the hybrid RANS/LES approach defined in chapter 4, which was to provide a dynamic, self-adjusting interfacing scheme. It merely constitutes a reasonable possibility to limit the extent of the RANS zone according to the specific requirements of the simulated setup, resulting in the settings discussed above and given in table 8.4 in this case. In fact, the multitude of combustion simulations, conducted as a basis for the final T2 flame simulation presented in this chapter, exhibited merely a minor sensitiv-

Table 8.3: Hybridization method parameter settings

$C_{A,z,min}$	1.4 mm
$C_{A,t}$	0.1 %
$C_{A,d}$	1.0
$C_{B,z,min}$	1.4 mm
$C_{B,tr}$	1.0
C_{pz}	2.5 mm

Table 8.4: RANS zone thicknesses for individual regions shown in figure 8.28

Region	$C_{A,z,max}$	$C_{B,z,max}$
0	2.0 mm	1.0 mm
1	9.0 mm	9.0 mm
2	2.5 mm	9.0 mm
3	2.5 mm	3.0 mm
4	2.5 mm	9.0 mm
5	2.0 mm	3.0 mm
6	6.0 mm	6.0 mm
7	6.0 mm	10.0 mm

Table 8.5: Definition of regions shown in figure 8.28

Region	X_{min} [mm]	X_{max} [mm]	Y_{min} [mm]	Y_{max} [mm]	Z_{min} [mm]	Z_{max} [mm]
0	0	500	0	20	-46.28	46.28
1	500	525	0	20	-46.28	46.28
2	525	680	0	20	12	46.28
3	525	680	0	20	-12	12
4	525	680	0	20	-46.28	-12
5	680	720	0	20	-46.28	46.28
6	720	800	0	20	-46.28	46.28
7	800	1258	0	20	-46.28	46.28

ity of the mean wall pressure with respect to a variation of the maximum RANS zone threshold settings. The maximum RANS zone thickness setup defined by tables 8.4 and 8.5 thus represents a reasonable setting that is supposed to promote the operation of the hybridization scheme components introduced in chapter 4, yet other parameter sets would lead to comparable results concerning the mean wall pressure.

In a similar way to the injection experiment simulation presented in chapter 6, the central injector boundary layer is treated with a pure zonal RANS zone featuring a constant thickness C_{pz} of 2.5 mm. This exception is made for the following reason: The central injector boundary layer is short and thus considerably thinner than the boundary layers of the combustor channel. Hence,

it appears preferable to reduce the RANS zone thickness to a minimum at this location in order to maximize the space available for the development of coherent turbulent structures within the LES mode.

8.5.1 Non-reacting Case NR

Figure 8.29 illustrates the regions occupied by the RANS mode in the non-reacting case NR determined by the developed hybridization method. The methods place the interface between RANS and LES such that it follows the boundary layer growth, which is especially visible in the isolator section, cf. also figure 8.30. Hybridization method component B is practically inactive due to the lack of combustion induced boundary layer separation/growth. Hence, the extent of the RANS zone is determined by hybridization method component A and the maximum RANS zone thresholds given in table 8.4. Due to the small threshold for the maximum RANS zone thickness of method part A adjusted for the subsequent combustion simulation, the main combustor section in-between the central injector trailing edge and the wall injectors features solely a thin RANS zone. Yet, the case NR results are practically insensitive to the RANS zone thickness in this section provided that the vicinity of the central injector remains treated with RANS. The latter is important to provide a reliable treatment of the central injector leading edge shock impinging on the upper and lower chamber walls and the thick boundary layer profile entering the main combustor section.

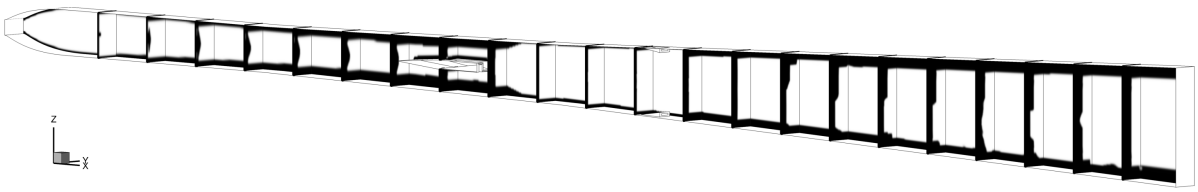

Figure 8.29: Case NR hybrid RANS/LES simulation RANS regions (instantaneous $r_C > 0$) indicated by black areas

Figure 8.32 provides the comparison of hybrid RANS/LES and experimental wall pressures for the non-reacting case NR. Computational and experimental results agree well. Additionally, the wall pressures are almost identical with the results obtained with the pure RANS simulation, cf. figure 8.7 indicating that both simulations predict a similar shock system and extent of the shock boundary layer interaction regions. Furthermore, also the instantaneous Schlieren image in figure 8.31 and the mean velocity field illustrated in figure 8.30a are practically identical with the RANS result concerning the main features like shock positions and the extent and shape of the boundary layer separation region close to the outflow. Both the mean velocity field in figure 8.30a and the instantaneous field in figure 8.30b feature the dominant injector vortex also visible in the RANS results.

In summary, these observations prove that the developed hybrid RANS/LES approach fulfills the requirement stated in chapter 4 to provide results, which are at least equal or better than obtained with a pure RANS with respect to the available experimental wall pressure measurements. In addition to the good agreement with experimental and RANS results, the hybrid simulation resolves turbulent structures indicated by local distortions in the Schlieren image in figure 8.31 and the instantaneous velocity field illustrated in figure 8.30b. However, it should be noted that the flow in the non-reacting case is mainly dominated by gas dynamic phenomena, which are influenced and confined by shock boundary layer interactions. Indeed, turbulence plays a rather subordinate role for the flow field and shock system outside of the boundary layers here. This changes with fuel injection and subsequent combustion, since turbulent mixing of reactants and hot reaction products becomes a determining effect. The spatial and temporal resolution of the larger scales of this process is a crucial benefit of LES as shown in the subsequent section 8.5.2.

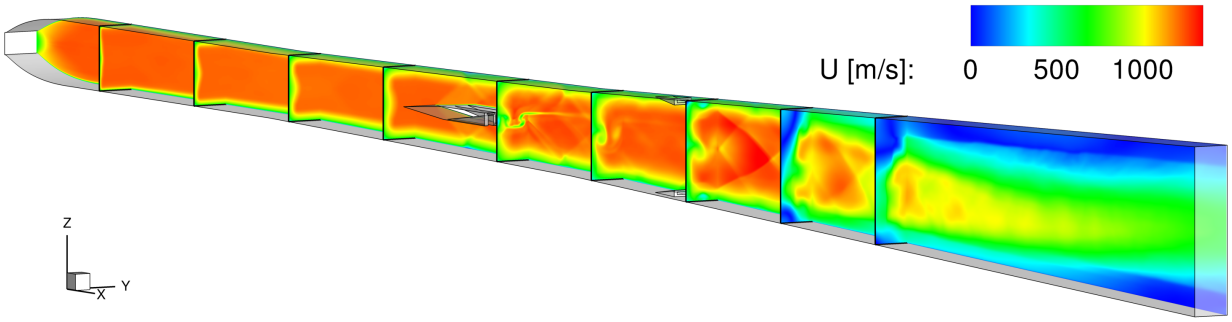

(a) Mean

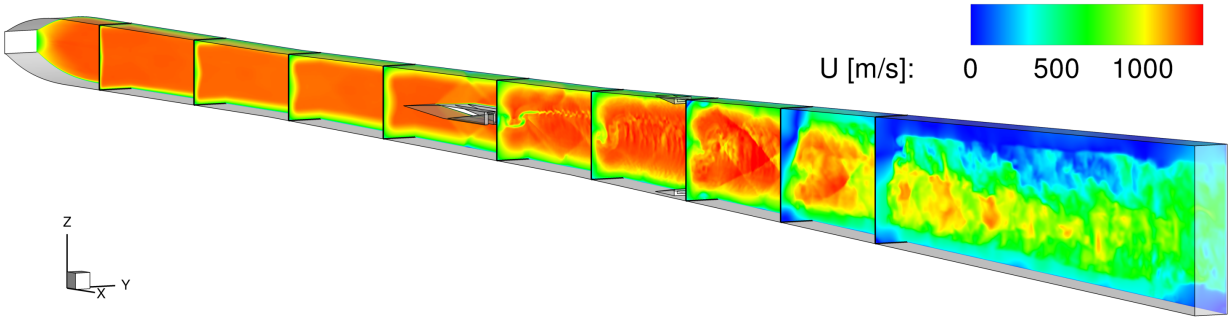

(b) Instantaneous

Figure 8.30: Non-reacting case NR hybrid RANS/LES mean and instantaneous velocity magnitude at symmetry plane and several cross-sections

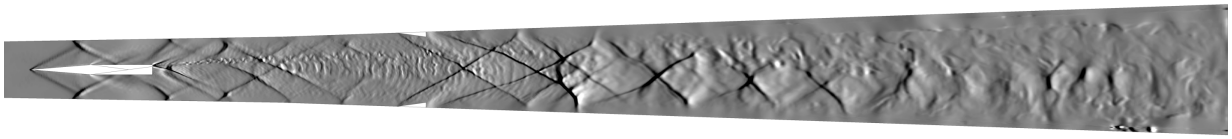

Figure 8.31: Case NR hybrid RANS/LES instantaneous Schlieren image at symmetry plane

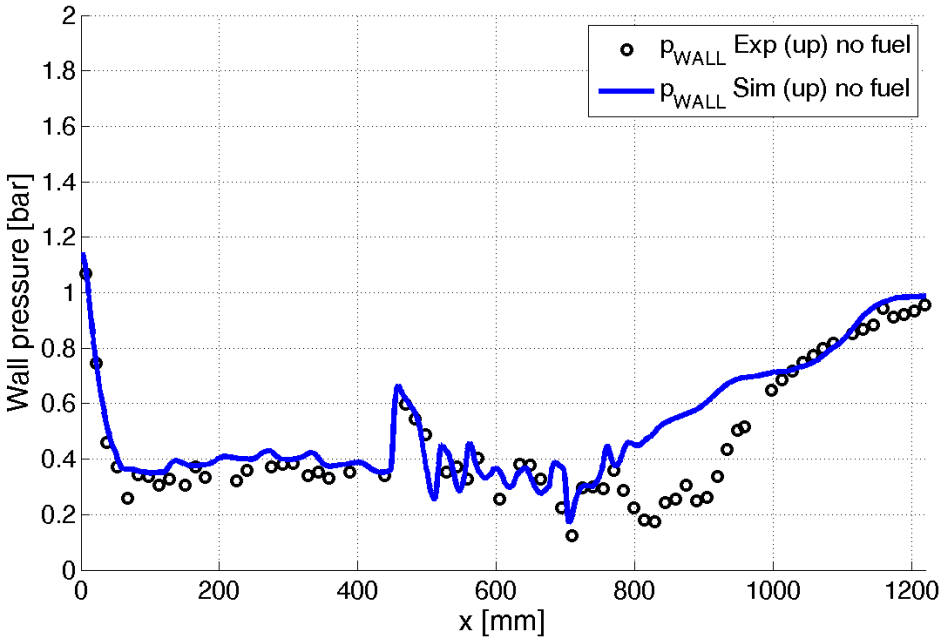

(a) Upper wall

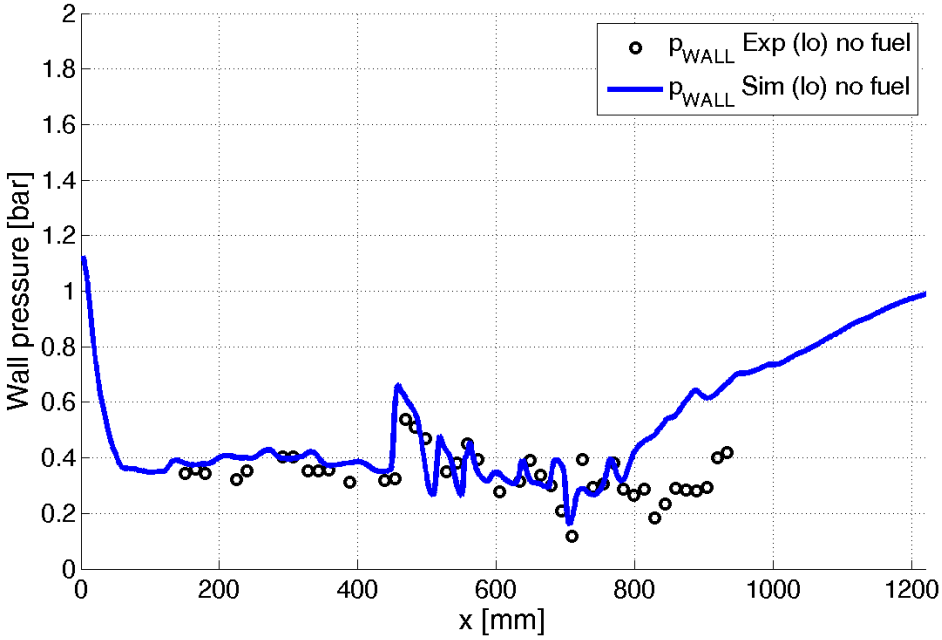

(b) Lower wall

Figure 8.32: Non-reacting case NR experimental and hybrid RANS/LES simulation mean wall pressures without fuel injection.

8.5.2 Two-staged Fuel Injection Case T2

8.5.2.1 Flow Field Analysis and Comparison to RANS

Before the computational flow fields are analyzed and compared with the experiment, the operation of the utilized hybridization method shall be discussed being comprised of two components A and B, see chapter 4. Figure 8.33 shows instantaneous fields of the turbulence mode indicators r_C, r_B and their respective difference at the combustor symmetry plane. The integral indicator r_C is the sum of the two turbulence mode indicator components for methods A and B. Thus, the difference of r_C and r_B shown in figure 8.33c presents the portion of the integral turbulence mode indicator r_C that is solely contributed by the solution based hybridization method A. Figure 8.33a shows an increasing and smooth RANS zone growth in the isolator section up to the central injector trailing edge. This is in accordance with the boundary layer growth already observed in the non-reacting case NR. Figure 8.33c shows that this desired behavior is a result of method A, which could already demonstrate its ability to account for boundary layer growth in the simulation of the injection experiment presented in chapter 6.

Furthermore, the region between the central and wall injectors features a thick boundary layer with dominant shock-induced boundary layer separation being a characteristic feature of the separated combustion mode, see section 8.4. The RANS zone in-between the central injector and the wall injection elements follows the strongly distorted boundary layer. Figures 8.33b and 8.33c prove that hybridization method component B dominates the definition of the RANS zone in this section being the intention of the chosen settings for $C_{A,z,max}$ and $C_{B,z,max}$. The enlarged section in figure 8.33a sheds light on the effect of method B: The figure shows the instantaneous integral turbulence mode indicator r_C, the Schlieren image corresponding to this location and the Mach 1 iso-contour. Method B evidently follows the sonic line and leads to an increase of RANS zone thickness at locations of shock impingement. The Mach line constitutes a good measure for the boundary layer contour in the transonic channel section downstream of the central injector. Yet, the subsonic layer occupies only a small portion of the near-wall region further up-

stream and downstream, since the combustion induced increase of boundary layer thickness characteristic for the separated combustion mode is limited to the main combustion region in-between the injectors. Figure 8.33c shows that these remaining regions are dominated by hybridization method component A. In addition, the RANS zone is truncated at the wall injection elements in order to enable LES modeling of the mixing and combustion of the wall-injected hydrogen.

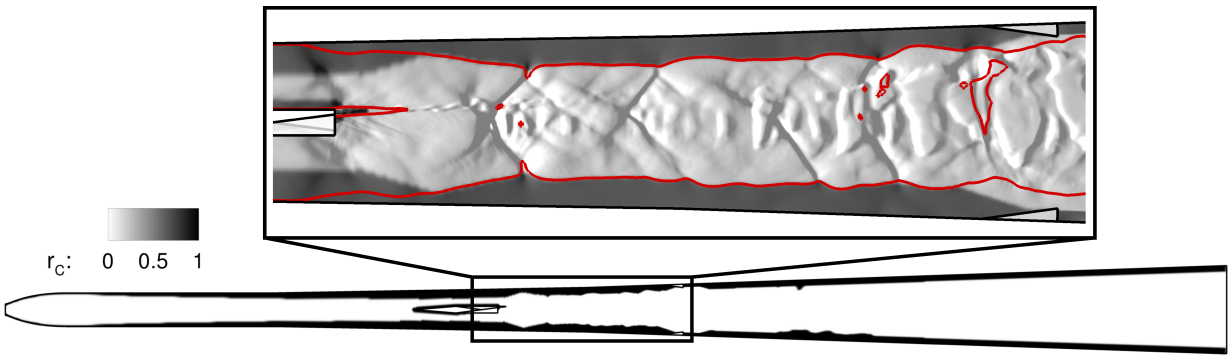

(a) r_C

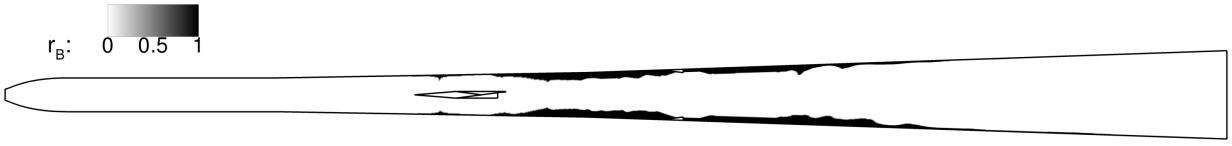

(b) r_B

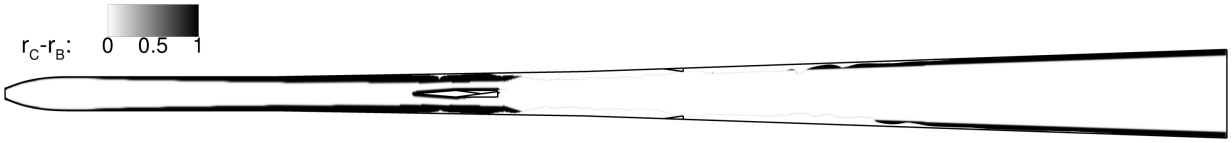

(c) r_C - r_B with border of r_C

Figure 8.33: Instantaneous turbulence mode indicator fields r_C, r_B and the separate contribution of r_A at the symmetry plane, red line indicates Mach 1 iso-contour

Finally, the three-dimensional distribution of the RANS zone based on the integral turbulence mode indicator r_C is illustrated in figure 8.34 for one selected time step. In particular, the main combustion zone between the central injector trailing edge and the wall injectors exhibits noticeable variations in RANS zone thickness in lateral direction besides the variations along the x-axis discussed above. In addition, the spatially inhomogeneous turbulence mode in-

dicator field is subject to transient variations in time, since both hybridization method components A and B react to changes in the flow field, e.g. the locations of shock boundary layer interactions. Since no backpressure is taken into account in the simulation, the boundary layer far downstream of the wall injectors plays a subordinate role, thus the RANS zone is truncated there in favor of the LES mode, see figure 8.33c.

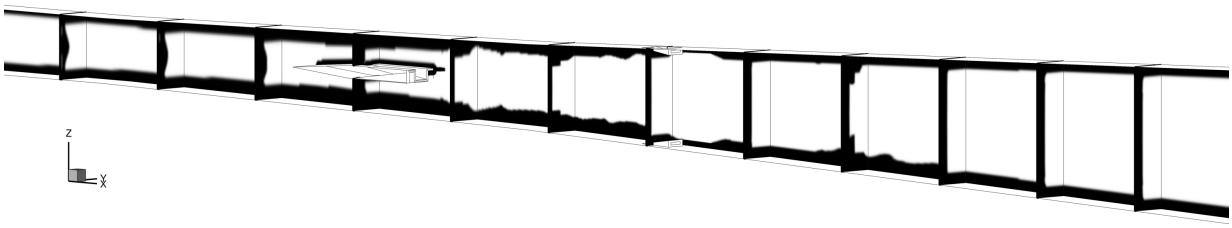

Figure 8.34: Case T2 hybrid RANS/LES simulation RANS regions (instantaneous $r_C > 0$) indicated by black areas

The comparison of computational and experimental wall pressures is given in figure 8.35. In general, both experiment and simulation agree well and exhibit the same trend. The pressure mismatch downstream of x=950 mm is due to the simplified pressure outflow boundary condition. A noteworthy result is that the computational pressure almost exactly matches the experiment up to x=600 mm. This is in contrast to the T2 RANS simulation, which overpredicted the pressure at this location, cf. figure 8.23. According to this, the hybrid simulation provides a more realistic prediction of the combustion induced pressure rise and hence the combustion process at least up to this location. Additionally, the hybrid simulation clearly features a distinction between the pressure rise induced by combustion and the pressure rise due to the central injector leading edge shock, which is a further contrast to the RANS case, cf. figure 8.23. The T2 RANS simulation was also carried out on the finer hybrid RANS/LES mesh, see again figure 8.23, yet, the results show that the RANS simulation does not perform better on the finer mesh.

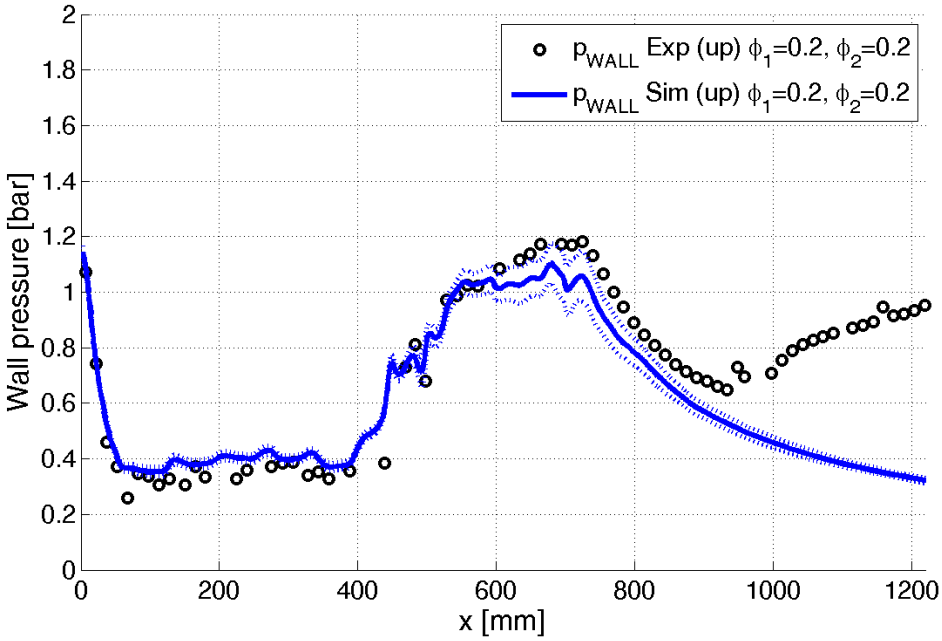

(a) Upper wall

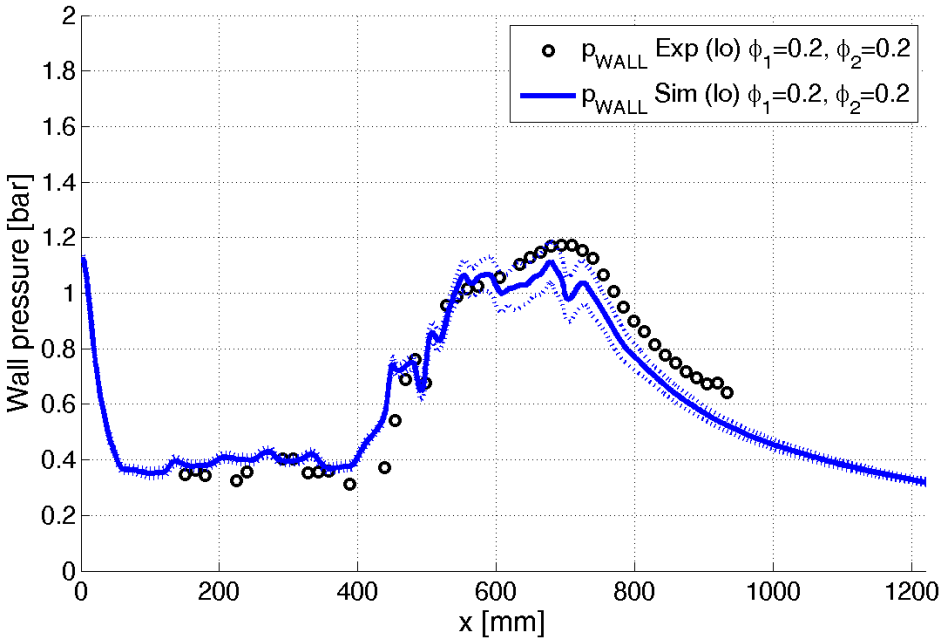

(b) Lower wall

Figure 8.35: Case T2 experimental and hybrid RANS/LES simulation mean wall pressures with central strut and wall fuel injection at equivalence ratios $\phi_1 = 0.2$ and $\phi_2 = 0.2$, dotted lines indicate $1-\sigma$ confidence interval

Moreover, the hybrid RANS/LES pressure rise close to the wall injection elements is slightly underpredicted, although the 1-σ confidence intervals for the computational wall pressure indicate that the experimental measurements are within the range of the hybrid simulation. In contrast to the T2 RANS simulation, the pressure fluctuations are not limited to the vicinity of the wall injectors but appear in the major portion of the combustion region between x=500 mm and x=800 mm. The relevance of this important observation is discussed in section 8.5.2.2. Results for the upper and lower walls are slightly asymmetrical both in the simulation and in the experiment. The latter was also observed in the T2 RANS simulation, see section 8.3.5.

Figure 8.38b shows the structure of the combustion zone indicated by mean temperature isocontours at 1400 K, whereas figure 8.38a shows the corresponding mean temperature distributions at several y-z-planes. The general shape of the flame is similar to the two-staged injection cases simulated with RANS. A main combustion region forms between the central and wall injectors, whereas initial flame stabilization occurs at the sidewall immediately downstream of the central injector. Furthermore, the heat release region downstream of the central injector trailing edge reaches the combustor symmetry plane slightly later than in the RANS case. As a consequence, the local Mach numbers remain tendentially rather supersonic in the center of the chamber, see figure 8.37. For this reason, the shock system downstream of the central injector features oblique shocks with relatively flat angles compared to the T2 RANS, see the Schlieren image in figure 8.36.

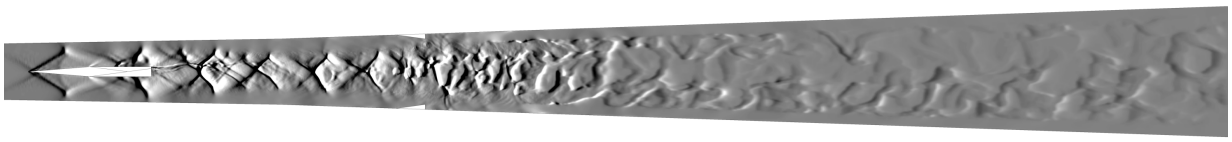

Figure 8.36: Case T2 hybrid RANS/LES instantaneous Schlieren image at symmetry plane

Wall injection generates two additional lateral zones of combustion that occupy the near-wall regions. The mean ignition location of those two side flames resides slightly further downstream than in the RANS case, cf. figure

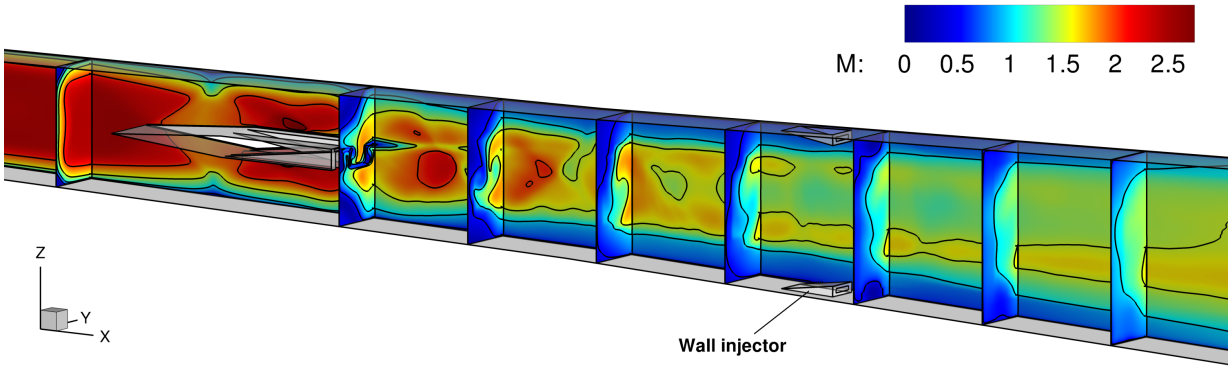

(a) Combustor symmetry plane and several y-z planes in main combustor section

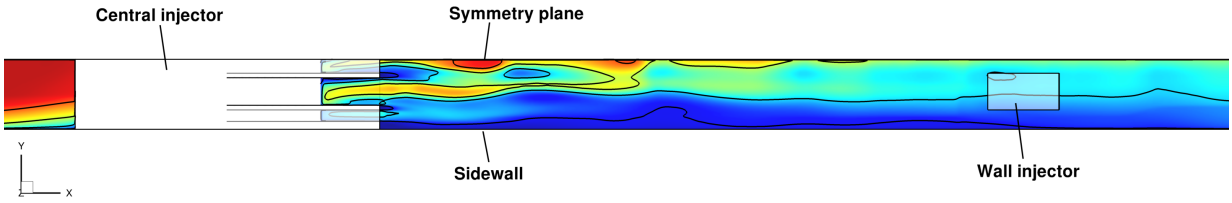

(b) Top view on the combustor x-y mid plane

Figure 8.37: Case T2 hybrid RANS/LES mean Mach number distributions on two-dimensional cut planes, black lines indicate Mach-isocontours at 0.5-intervals

8.26, which results in the slightly decreased pressure rise at this location. Nevertheless, the instantaneous three-dimensional temperature field with temperatures above 1400 K exemplarily illustrated in figure 8.39 indicates an intense turbulent combustion, which anchors behind the wall injectors.

8.5.2.2 Formation and Propagation of Unsteady Pressure Waves

The operational points of the ITLR combustor are intrinsically unsteady processes, yet resulting in pseudo-steady mean fields, like the mean temperature field for the T2 flame shown in figure 8.38, see the explanation in section 8.2.1. A relevant source of unsteadiness is the dominating large-scale vortex induced by the central injector, see e.g. the Schlieren image for the non-reacting hybrid RANS/LES case in figure 8.31. An exemplary sequence of four

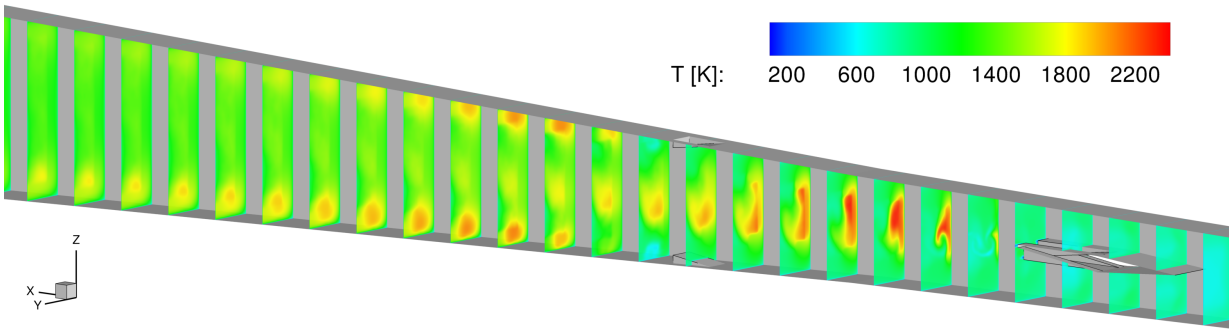

(a) Mean temperature field at selected y-z-planes

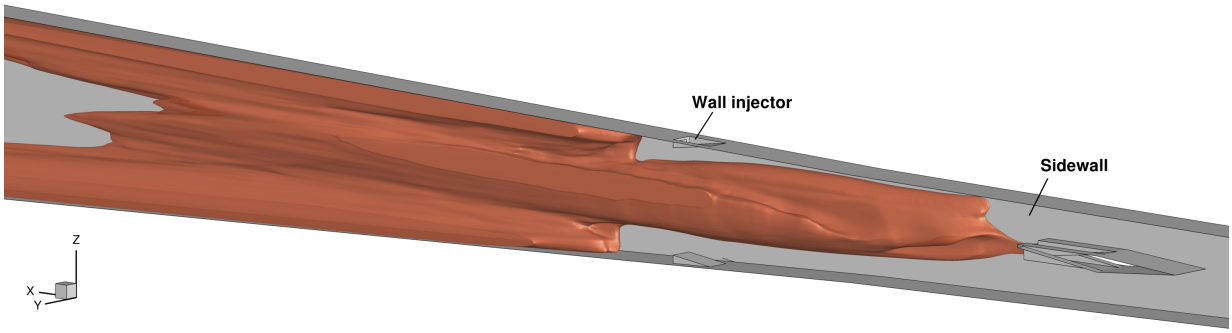

(b) Mean temperature isocontours at 1400 K

Figure 8.38: Case T2 hybrid RANS/LES simulation mean temperatures in main combustion region

instantaneous illustrations of the combustion zone obtained with the hybrid RANS/LES simulation is given in figure 8.39. In particular, the figure shows the three-dimensional temperature iso-contours at 1400 K, which serve as a qualitative threshold for the combustion zone enclosing regions with higher temperatures. The time span between the first and the third image amounts to 0.64 ms, which approximately corresponds to one chamber flow-through-time, see section 8.2.2. The images show a large-scale turbulent wrinkling of the flame. However, the most notable information provided by the image sequence is that the location of fuel ignition behind the wall injectors varies considerably with time. The first image at 0 ms shows that both lateral combustion zones anchor very closely behind the wall injectors. The second image at 0.236 ms, however, shows that the ignition location for the wall injector fuel

is shifted considerably downstream, especially for the lower wall in this case. Subsequently, the ignition location moves upstream resulting in a flame anchoring closely behind the wall injectors again as illustrated in the third image at 0.640 ms. This phenomenon is recurring, as indicated by the last image of the sequence at 0.908 ms, which again shows a downstream shift of the wall injector ignition location.

Moreover, the 1-σ standard deviation confidence intervals of the computational wall pressure in figure 8.35 suggest considerable transient pressure fluctuations between the central injector trailing edge and the region behind the wall injectors. Both phenomena, the non-constant location of fuel ignition illustrated in figure 8.39 and the aforementioned pressure fluctuations, are interconnected. In fact, the pressure fluctuations are the result of a coherent pressure wave caused by the oscillating wall injector ignition, as can be inferred from figure 8.40: The depicted waterfall diagrams for the upper and lower combustor walls illustrate the temporal evolution of the simulated, instantaneous wall pressures at the chamber symmetry plane. The underlying pressure data are the result of five chamber flow-through times. The diagrams reveal that the pressure disturbances originating behind the wall injectors at x=700 mm move upstream until they reach the central injector. Once a pressure wave reaches the central injector trailing edge, it basically ceases to exist and a further pressure wave emerges at the wall injectors. The pressure disturbances propagate at a speed of approximately 350 m/s against the main flow direction as can be inferred from the roughly linear slope of the pressure maxima over time.

Also the RANS simulation for case T2 predicted considerable wall pressure oscillations close to the wall injectors. The origin of these fluctuations was attributed to the combustion induced unsteady flow field upstream of the wall injectors leading to intermittently changing flow conditions behind the wall injectors, which in turn influences the location of ignition, see section 8.3.5. However, the large turbulent viscosity originating in the RANS turbulence model leads to an intense diffusive equalization of all flow properties. This effectively dampens local, transient phenomena including the pressure oscillations generated by the varying fuel ignition location at the wall injec-

tors. Compared with this, the hybrid RANS/LES not only allows the development of coherent turbulent structures, it generally enables the resolution of transient effects that remain hidden if RANS methods are utilized, which are massively diffusive.

This does not imply that unsteady RANS is generally incapable of predicting unsteady effects, the URANS investigation concerning the IT2 ignition case proves the opposite. Yet, the IT2 ignition sequence comes along with a change of the entire mean combustor flow field, which can be reproduced with unsteady RANS. The pressure disturbance discussed here, however, constitutes a transient phenomenon occurring in addition to the more or less steady mean flow, which unsteady RANS is not able to reproduce. The ability to resolve such intermittent effects remains a characteristic benefit of LES and provides a motivation for the application of this turbulence modeling approach.

Here, the following mechanism is postulated for the formation of pressure waves propagating upstream in the partly supersonic ITLR combustor flow: Combustion obviously increases the static temperature within the heat release regions. As a direct consequence, the speed of sound increases reducing the local Mach number, assuming that the velocity remains roughly constant. The rising speed of sound at an approximately constant velocity promotes the propagation of information in lateral directions. Due to transient, excessive heat release, e.g. because of re-ignition of the hydrogen immediately behind the wall injectors, spatially limited thermal choking may occur resulting in a local subsonic zone. O'Byrne et al. [103] describe regions with local thermal choking as obstacles for the flow effectively blocking a portion of the channel having the ability to induce an upstream-propagating shock wave within a scramjet combustor duct. Laurence et al. also observe upstream propagating pressure waves in a dual-mode scramjet combustor, which they also attribute to local thermal choking [79, 80]. From these findings it can be concluded that once local thermal choking has occurred, a combustion induced pressure wave may form possessing the ability to propagate against the mean flow direction. Here, this phenomenon is discovered within the T2 mode of the ITLR combustor by means of hybrid RANS/LES.

However, as soon as the disturbance reaches the central injector, the speed

of sound suddenly decreases, since no combustion induced temperature rise exists upstream of the injector trailing edge. Hence, the propensity of the flow to transmit information is abruptly limited. In consequence, the non-reacting flow upstream of the central injector trailing edge serves as a barrier for the pressure wave, which ceases to exist.

Theoretically, the pressure wave might lead to excessive boundary layer separation either at the combustor or central injector walls, which in turn could deflect the flow such that indeed a shock system with further upstream influence would develop. The image sequence in figure 8.39 indeed shows that the upstream part of the flame jumps forward towards the central injector at 0 ms and 0.640 ms. In fact, the single-staged injection mode S investigated by means of RANS in section 8.3.2 actually features low supersonic/transonic velocities in the vicinity of the central injector, see the Schlieren image in figure 8.11. Hence, the flow in case S features the propensity to transmit pressure waves further upstream than for case T2, here. However, no upstream propagating pressure waves are induced due to the lack of wall injection in case S.

The investigations on combustion induced inlet unstart of the HyShot II scramjet combustor conducted by Laurence et al. revealed similar upstream propagating pressure disturbances [79,80]. The authors identify two processes that can lead to such an upstream propagation: thermal choking on the one hand and boundary layer separation on the other hand. Local thermal choking results in the generation of pressure waves that adapt the upstream flow to the changed conditions. In contrast to that, the pressure gradient induced by combustion can lead to boundary layer separation with subsequent formation of a shock system that might propagate further upstream. Further, Laurence et al. hold the opinion that the initiator for the unsteady inlet unstart process is local thermal choking, as stated further above. Although the phenomenon observed in the hybrid RANS/LES of the T2 case is qualitatively similar to the process investigated by Laurence et al., a decisive difference exists: While combustion induced inlet unstart represents a massive transformation of the mean flow field, alike the ignition sequence IT2, the process identified within the T2 combustion mode rather constitutes an intermittent fluctua-

tion of the otherwise steady mean flow field. The phenomenon observed here does not lead to thermal choking and inlet unstart of the whole combustor, since the pressure disturbance stops downstream of the central injector.

In summary, it can be stated that the unsteady flow field induced by the vortex-generating central injector combined with the staged wall injection induces oscillations with respect to the location of wall injector ignition. These oscillations in turn generate pressure disturbances that travel upstream. The given explanation for the upstream propagation of combustion induced pressure waves is in accordance with the opinion of Laurence et al., since it is assumed that local thermal choking initiates the unsteady process. Theoretically, the adverse pressure gradient induced by the pressure wave might lead to local boundary layer separation either at the combustor or central injector walls. This might lead to the damage or destruction of the combustor for two reasons: Firstly, excessive boundary layer separation might block the channel and lead to an engine unstart. Secondly, a boundary layer separation at the central injector would result in increased static temperatures and possibly fuel ignition within the separation regions. The consequence would be a thermal overload of the injector and failure of the entire engine.

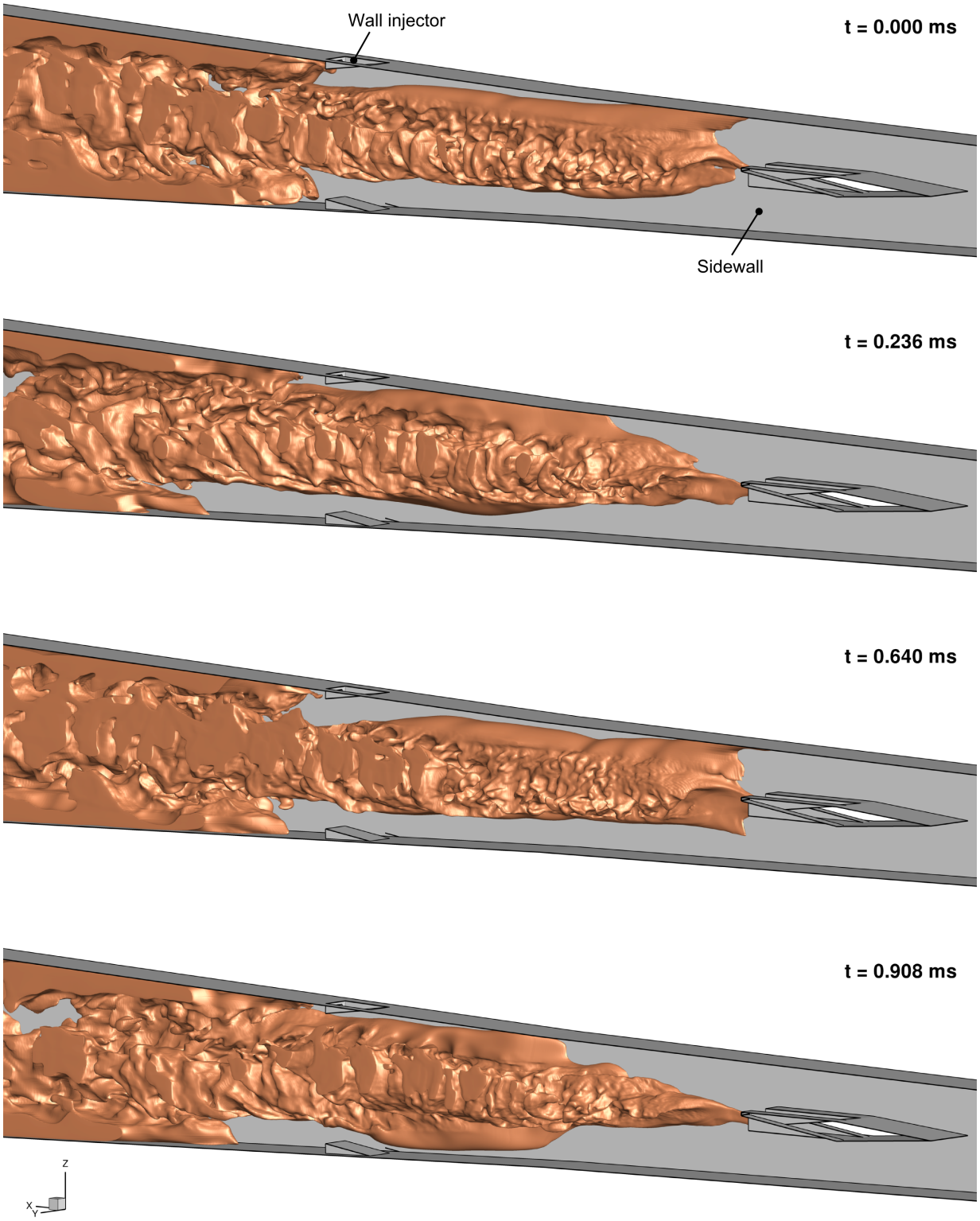

Figure 8.39: Case T2 hybrid RANS/LES simulation iso-contours of instantaneous temperature at 1400 K indicating combustion zone

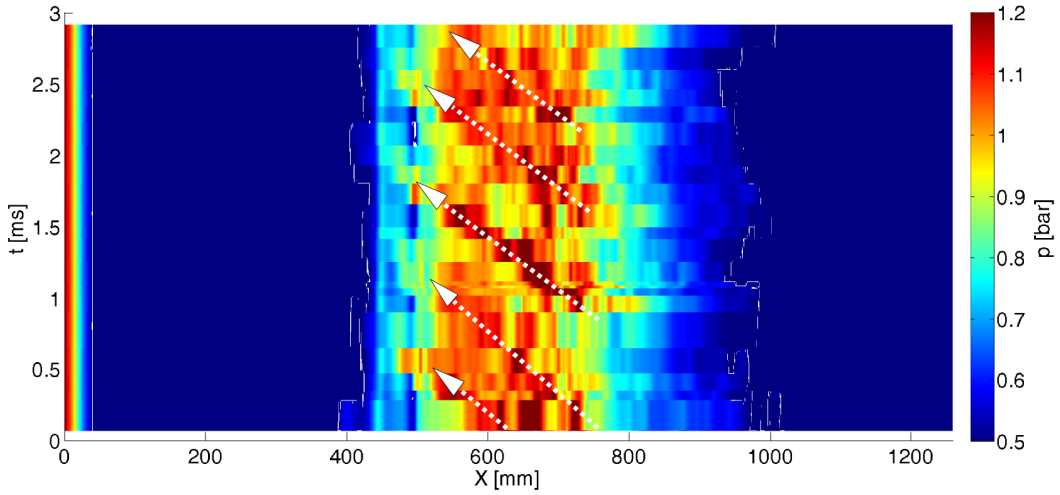

(a) Upper wall

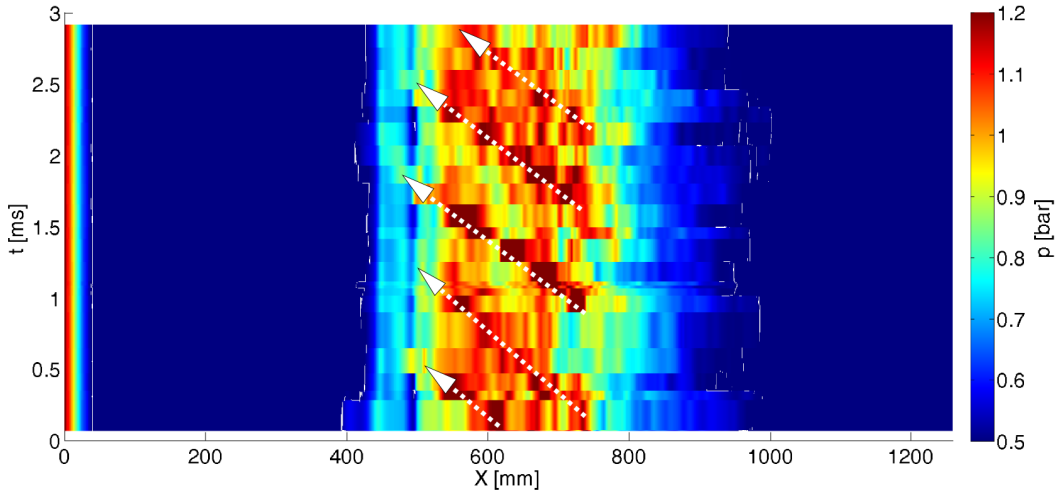

(b) Lower wall

Figure 8.40: Case T2 hybrid RANS/LES simulation waterfall diagram for upper and lower wall pressures at symmetry line over time, colormap truncated to values between 0.5 bar and 1.2 bar; arrows indicate upstream propagating pressure waves

8.5.2.3 Combustion Induced Turbulence

Finally, the influence of the novel model for combustion induced turbulence introduced in chapter 5 shall be addressed. The outcome of the discussion about the necessity for turbulence chemistry interaction modeling in section 3.5.2 was that state-of-the-art turbulence chemistry interaction models do not appear to have significant influence on the simulation of supersonic combustion in full combustor ducts. Yet, currently available models solely take into account one direction of this interaction being the influence of turbulence on combustion. However, the novel model presented in chapter 5 acts in the reverse direction, since it describes the generation of turbulence by means of combustion on a microscale level. It is postulated, that this model thus represents a missing counterpart to the available model approaches.

A further hybrid RANS/LES simulation of case T2 is conducted, which features the same setup as the previously analyzed hybrid RANS/LES T2 simulation. The only difference is the application of the novel model, which introduces an additional production source term in the transport equation for the turbulent kinetic energy, see eq. 5.3. This source term is based on the assumption that combustion induces micro-scale turbulent fluctuations, which remain unresolved by the computational mesh. The model is active both in the RANS zones as well as in the LES regions acting within the turbulent kinetic energy transport equation of each respective turbulence model.

Figure 8.41 provides the comparison of wall pressures obtained for the two hybrid RANS/LES simulations. Although the simulation employing the model for combustion induced turbulence exhibits a slightly increased wall pressure level in the center of the main combustion region around x=600 mm, the difference between the two cases is evidently marginal. The conclusion is twofold: On the one hand, the novel model for combustion induced turbulence complements existing turbulence chemistry interaction models by establishing an approach for the missing influence of combustion on turbulence. On the other hand, the influence of this novel model for the simulation of entire supersonic combustors appears to be of the same comparably small importance as for the existing turbulence chemistry interaction models.

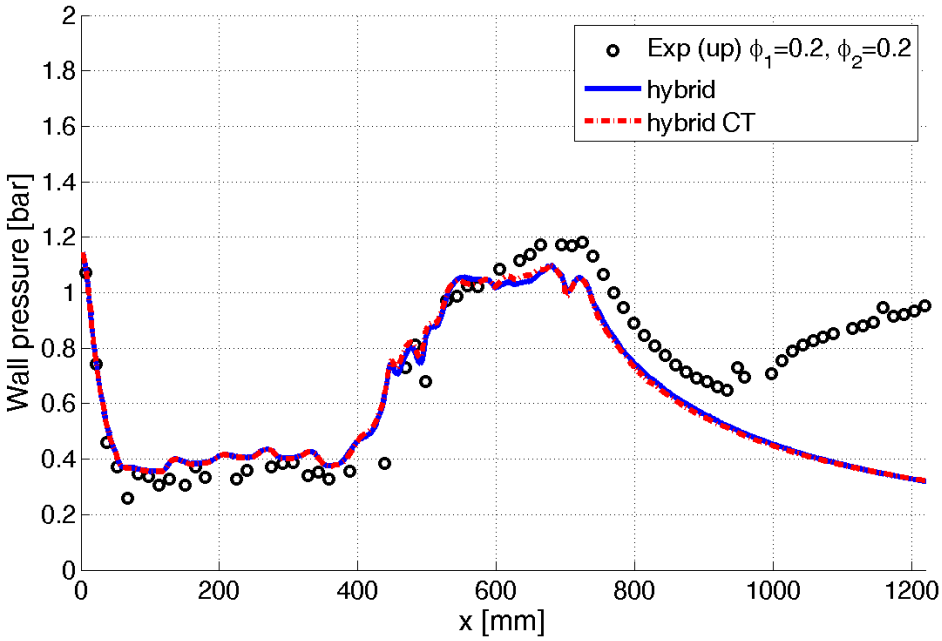

(a) Upper wall

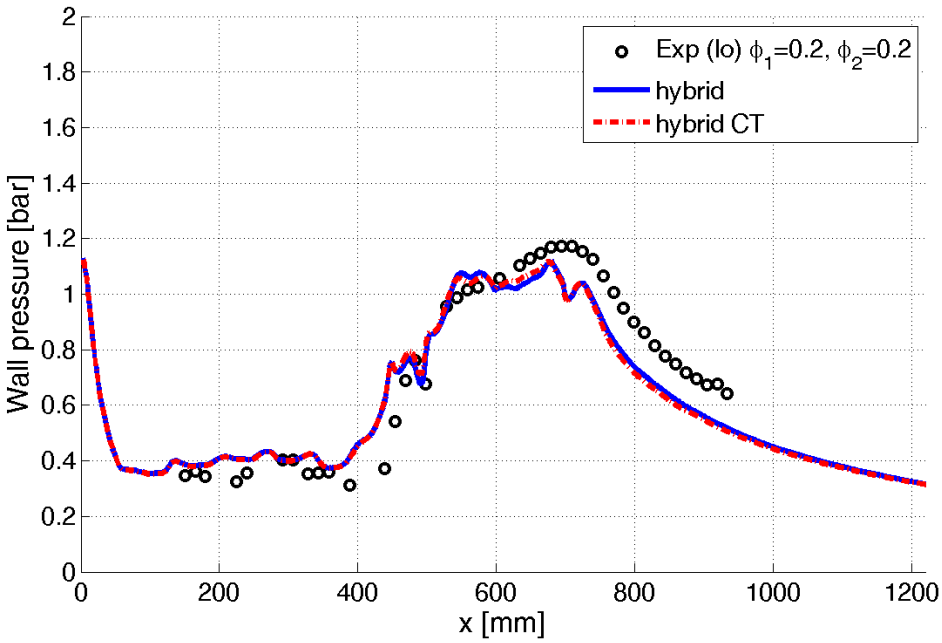

(b) Lower wall

Figure 8.41: Case T2 hybrid RANS/LES with (CT) and without application of the model for combustion induced turbulence

9 Conclusions

A computational fluid dynamics solver has been developed for the simulation of supersonic combustion on the basis of OpenFOAM. The solver rests upon a compressible, density-based formulation and is explicit in time. Combustion is treated by means of finite-rate chemistry in order to account for the spatial diversity of species compositions and temperatures encountered in supersonic combustion. The solver is capable of employing both RANS and LES.

The capability of the solver to account for several facets influencing the simulation of supersonic combustor ducts has been investigated. These aspects include: The interaction of shock waves and boundary layers, the perpendicular injection of a jet into a supersonic crossflow and finally the combustion process itself. Combustion has been investigated by means of RANS and the hybrid RANS/LES method developed within this work. The developed and implemented solver and methods have proven to provide results that are in good agreement with available experimental validation data concerning both purely gas dynamical as well as combustion-related phenomena.

Two model approaches have been developed and implemented based on the novel solver: Firstly, a method for the hybridization of RANS and LES turbulence modeling outlined in chapter 4. Secondly, a model for combustion induced turbulence has been proposed in chapter 5.

9.1 Conclusions About LES and Hybrid RANS/LES

A method for the hybridization of RANS and LES has been developed tailored for the simulation of supersonic combustor ducts. The method is composed of two components that are supposed to work in conjunction with each other.

The purpose of the hybridization of RANS and LES is to provide the benefits of LES for the simulation of supersonic combustion, while maintaining reasonable runtimes due to the application of RANS in near-wall regions. The functionality of the developed hybridization methods has been successfully demonstrated based on the simulation of a non-reacting, wall-confined supersonic injection experiment in chapter 6 and the simulation of a reacting supersonic combustor in chapter 8.

In general, there are two major aspects regarding the potential benefits of LES with respect to supersonic combustion: On the one hand, the mean fields provided by LES may be a better prediction of reality, since the energy-bearing vortices are resolved instead of being modeled in terms of deficient RANS models. On the other hand, LES is capable of resolving transient effects, that might be neither observable in experiments, nor predictable by unsteady RANS.

The simulations of the ITLR combustor have proven that unsteady RANS is capable of predicting different modes of operation in good agreement with experimental validation data, even for the complex flow field dominated by highly three-dimensional vortices and extensive shock boundary layer interactions. Additionally, the characteristics of supersonic combustion, being the mutual dependency of shock systems and combustion zones, could be identified. Thus, RANS appears to be sufficient for the simulation of supersonic combustor ducts from the point of view of a technology developer.

A benefit of hybrid RANS/LES is the spatial and temporal resolution of turbulent mixing providing a potentially better prediction of this process compared to RANS. However, the major benefit provided by the hybrid RANS/LES method, at least in the case of the ITLR combustor, is the aforementioned resolution of transient effects that remain hidden in unsteady RANS. The hybrid RANS/LES of the high-equivalence ratio two-staged injection mode of the ITLR combustor revealed the recurring generation of combustion induced pressure waves, that propagate upstream until they reach the central injector, where they cease to exist. The origin of these pressure disturbances is attributed to local thermal choking induced aft of the wall injectors.

In terms of future applications, RANS and hybrid RANS/LES could be utilized in conjunction with each other. RANS would suffice to predict the pressure distribution and mean flow structure, while particular load points could be investigated by means of hybrid RANS/LES in search for relevant transient effects that might influence the combustor.

9.2 Instabilities in Supersonic Combustors

The pressure disturbances discovered in the hybrid RANS/LES of the ITLR combustor have the potential to damage or destroy the engine. The adverse pressure gradient induced by the upstream-propagating pressure wave can lead to boundary layer separation and the generation of subsequent shock waves. The resulting obstruction of the channel would deteriorate the performance of the system. Yet, the consequences would be even more severe, if hydrogen injected at the central injector trailing edge got into the separation induced recirculation zones at the central injector ramps. In this case, subsonic combustion would occur upstream of the intended injection location and destroy the injector. Finally, this would lead to the failure of the engine.

In summary, even though the investigated combustor operates at high transonic velocities, combustion instabilities induced in the rear combustor section can influence the flow and combustion further upstream. The combination of a vortex-generating central injector with a staged injection further downstream promotes a highly fluctuating flow field, being the cause for the combustion instabilities. The transonic flow in combustors operating within the transitional separated combustion mode, see section 8.4, where extensive subsonic and supersonic zones coexist, provides the prerequisite for the upstream-propagation of these instabilities.

A further necessary step is the experimental investigation of these transient combustion oscillations. Existing experimental high-speed chemiluminescence images of the ITLR combustor provide evidence for transient fluctuations of the flame. Yet, even higher temporal resolutions are necessary in order to resolve these effects. Finally, the relevance for the operational stability of the

ITLR combustor should be assessed and transfered to scramjet combustors in general.

9.3 Combustion Induced Turbulence

A novel model for combustion induced turbulence has been introduced in chapter 5 contrasting with currently available turbulence chemistry interaction models that solely take into account the influence of turbulence on combustion. The model complements existing models by establishing an approach for the missing influence of combustion on turbulence. The developed approach rests upon the assumption that the frequency of small-scale vortices generated by combustion is linked to a mean chemical time scale. The fluctuating velocity field resulting from the combustion induced turbulence is computed from the local viscosity and this time scale. Finally, a source term is added to the transport equation of turbulent kinetic energy, regardless of whether a RANS or LES model is applied. This source term is computed based on the pressure expansion work that the combustion induced velocity fluctuations induce. In consequence, the new model increases the turbulent viscosity in regions where significant combustion occurs, thus enhances the distribution of intermediate species in terms of an eddy viscosity turbulence closure approach.

The results obtained in the context of the simulation of the supersonic hydrogen diffusion flame in chapter 7 are encouraging. Yet, the influence of this model is marginal for the simulation of the ITLR combustor by means of hybrid RANS/LES, see section 8.5.2.3. Altogether, the micro-scale effect of combustion on turbulence appears to have a similarly small significance for the simulation of full supersonic combustor ducts as is the case for existing turbulence chemistry interaction models, see section 3.5.2.

References

[1] OpenFOAM: User Guide, Version 2.1.1.

[2] J. D. Anderson. *Modern Compressible Flow*. McGraw-Hill, 3rd edition, 2004.

[3] H. Babinsky and J. K. Harvey. *Shock Wave-Boundary-Layer Interactions*. Cambridge University Press, 2011.

[4] D.R. Ballal. Combustion-Generated Turbulence in Practical Combustors. *Journal of Propulsion and Power*, 4:385–390, 1988.

[5] M. C. Banica, T. Scheuermann, J. Chun, B. Weigand, and J. von Wolfersdorf. Numerical Study of Supersonic Combustion Processes with Central Strut Injection. *Journal of Propulsion and Power*, 26:869–874, 2010.

[6] J. Bardina, J. H. Ferziger, and W. C. Reynolds. Improved Subgrid Scale Models for Large Eddy Simulation. In *13th Fluid and Plasma Dynamics Conference, Snowmass, CO, USA*, 1980.

[7] J. Bardina, J. H. Ferziger, and W. C. Reynolds. Improved Turbulence Models Based on Large Eddy Simulation of Homogeneous, Incompressible,Turbulent Flows. Technical Report Report TF-19, Thermosciences Division, Dept. Mechanical Engineering, Stanford University, 1983.

[8] G. K. Batchelor. *An Introduction to Fluid Dynamics*. Cambridge University Press, 2000.

[9] G. A. Batley, A. C. McIntosh, and J. Brindley. The Baroclinic Effect in Combustion. *Mathematical and Computer Modelling*, 24:165–176, 1996.

[10] E. Baudoin, R. Yu, Bai, K. J. Nogenmyr, X. S. Bai, and C. Fureby. Comparison of LES Models Applied to a Bluff Body Stabilized Flame. In *47th AIAA Aerospace Sciences Meeting including The New Horizons Forum and Aerospace Exposition, Orlando, FL, USA*, 2009.

[11] R. E. Bensow and C. Fureby. On the Justification and Extension of Mixed Models in LES. *Journal of Turbulence*, 8(54):1–17, 2008.

[12] M. Berglund, E. Fedina, C. Fureby, and J. Tegner. Finite Rate Chemistry Large-Eddy Simulation of Self-Ignition in a Supersonic Combustion Ramjet. *AIAA Journal*, 48:540–550, 2010.

[13] M. Berglund and C. Fureby. LES of Supersonic Combustion in a Scramjet Engine Model. *Proceedings of the Combustion Institute*, 31:2497–2504, 2007.

[14] A. Bernstein, W. H. Heiser, and C. Hevenor. Compound-Compressible Nozzle Flow. *ASME Journal of Applied Mechanics*, 34:548–554, 1967.

[15] S.F. Billig, P.J. Waltrup, and R.D. Stockbridge. Integral-Rocket Dual-Combustion Ramjets: A New Propulsion Concept. *Journal of Spacecraft and Rockets*, Vol.17:416–424, 1980.

[16] P. Boivin, C. Jimenez, A.L. Sanchez, and F.A. Williams. An Explicit Reduced Mechanism for H2-Air Combustion. *Proceedings of the Combustion Institute*, 33(1):517 – 523, 2011.

[17] R. Borghi. On the Structure and Morphology of Turbulent Premixed Flames. In C. Casci, editor, *Recent Advances in the Aerospace Sciences*, pages 117–138. Plenum, 1985.

[18] R. Borghi and D. Escudie. Assessment of a Theoretical Model of Turbulent Combustion by Comparison with a Simple Experiment. *Combustion and Flame*, 56:149–164, 1984.

[19] M. Bouchez, A. S. Roudakov, V. I. Kopchenov, V. L. Semenov, and D. Scherrer. French-Russian Analysis of Kholod Dual-Mode Ramjet Flight Experiments. In *AIAA/CIRA 13th International Space Planes and Hypersonics Systems and Technologies, Capua, Italy*, 2005.

[20] K. N. C. Bray, P. A. Libby, G. Masuya, and J. B. Moss. Turbulence Production in Premixed Turbulent Flames. *Combustion Science and Technology*, 25:127–140, 1981.

[21] P. Chakraborty, S. Balachandar, and R. J. Adrian. On the Relationships between Local Vortex Identification Schemes. *Journal of Fluid Mechanics*, 535:189–214, 2005.

[22] M. Chase, C. Davies, J. Downey, D. Frurip, R. McDonald, and A. Syverud. JANAF Thermochemical Tables. *Journal of Physical and Chemical Reference Data*, 14:Appendix 1, 1985.

[23] A. Chemnitz. Hybride RANS/LES-Simulation der Strömung und Verbrennung in einer Überschallbrennkammer. Master's thesis, Technische Universität München, 2015.

[24] T. S. Cheng, J. A. Wehrmeyer, R. W. Pitz, Jr. O. Jarrett, and G. B. Northam. Raman Measurement of Mixing and Finite-Rate Chemistry in a Supersonic Hydrogen-Air Diffusion Flame. *Combustion and Flame*, 99:157–173, 1994.

[25] H. Choi and P. Moin. Effects of the Computational Time Step on Numerical Solutions of Turbulent Flow. *Journal of Computational Physics*, 113:1–4, 1994.

[26] T. J. Chung. *Computational Fluid Dynamics*. Cambridge University Press, 2002.

[27] P. A. T. Cocks. *Large Eddy Simulation of Supersonic Combustion with Application to Scramjet Engines*. PhD thesis, University of Cambridge, 2011.

[28] O. Colin, F. Ducros, D. Veynante, and T. Poinsot. A Thickened Flame Model for Large Eddy Simulations of Turbulent Premixed Combustion. *Physics of Fluids*, 12:1843–1863, 2000.

[29] N. A. Cumpsty. *Jet Propulsion*. Cambridge University Press, 1997.

[30] E. T. Curran. Scramjet Engines: The First Forty Years. *Journal of Propulsion and Power*, 17:1138–1148, 2001.

[31] E. T. Curran, W. H. Heiser, and D. T. Pratt. Fluid Phenomena in Scramjet Combustion Systems. *Annual Review of Fluid Mechanics*, 28:323–360, 1996.

[32] W. Dahmen and A. Reusken. *Numerik für Ingenieure und Naturwissenschaftler*. Springer, 2nd edition, 2008.

[33] S. Deck, P.-E. Weiss, M. Pamiès, and E. Garnier. Zonal Detached Eddy Simulation of a Spatially Developing Flat Plate Turbulent Boundary Layer. *Computers & Fluids*, 48:1–15, 2011.

[34] N. C. Dröske, K. Makowka, P. Nizenkov, J. J. Vellaramkalayil, J. von Wolfersdorf, and T. Sattelmayer. Validation of a Novel OpenFOAM Solver using a Supersonic, Non-reacting Channel Flow. In *19th AIAA International Space Planes and Hypersonic Systems and Technologies Conference, Atlanta, GA, USA*, 2014.

[35] S. Eberhardt and S. Hickel. Large-Eddy Simulation of a Central Strut Injector with Perpendicular Injection for Scramjet Applications. In *5th European Conference for Aeronautics and Space Sciences (EUCASS), Munich, Germany*, 2013.

[36] J. R. Edwards, J. A. Boles, and R. A. Baurle. Large-Eddy/Reynolds-averaged Navier–Stokes Simulation of a Supersonic Reacting Wall Jet. *Combustion and Flame*, 159:1127–1138, 2012.

[37] J. R. Edwards, J.-I. Choi, and J. A. Boles. Large-Eddy/Reynolds-averaged Navier–Stokes Simulation of a Mach 5 Compression-Corner Interaction. *AIAA Journal*, Vol. 46, No. 4:977–991, 2008.

[38] J. R. Edwards, A. Potturi, and J. A. Fulton. Large Eddy/Reynolds-Averaged Navier-Stokes Simulations of Scramjet Combustor Flow Fields. In *48th AIAA/ASME/SAE/ASEE Joint Propulsion Conference & Exhibit, Atlanta, GA, USA*, 2012.

[39] F. Ettner. *Effiziente numerische Simulation des Deflagrations-Detonations-Übergangs*. PhD thesis, Technische Universität München, 2013.

[40] J.H. Ferziger and M. Peric. *Computational Methods for Fluid Dynamics*. Springer, 2nd edition, 1999.

[41] M. L. Fotia. Mechanics of Combustion Mode Transition in a Direct-Connect Ramjet-Scramjet Experiment. *Journal of Propulsion and Power*, 31:69–78, 2015.

[42] M. L. Fotia and J. F. Driscoll. Isolator–Combustor Interactions in a Direct-Connect Ramjet-Scramjet Experiment. *Journal of Propulsion and Power*, 28:83–95, 2012.

[43] M. L. Fotia and J. F. Driscoll. Ram-Scram Transition and Flame/Shock-Train Interactions in a Model Scramjet Experiment. *Journal of Propulsion and Power*, 29:261–273, 2013.

[44] R. O. Fox. *Computational Models for Turbulent Reacting Flows*. Cambridge University Press, 2003.

[45] M. Frey. *Behandlung von Strömungsproblemen in Raketendüsen bei Überexpansion*. PhD thesis, Universität Stuttgart, 2001.

[46] J. Fröhlich. *Large Eddy Simulation turbulenter Strömungen*. Teubner Verlag, 2006.

[47] H. K. Förster. *Einfluss der Turbulenz-Chemie Interaktion auf das Zündverhalten schwach stabilisierter Überschallflammen*. PhD thesis, Technische Universität München, 2009.

[48] S. Fuhrmann. *Gestufte Injektion und Verbrennung in einer Scramjet-Brennkammer*. PhD thesis, Technische Universität München, 2012.

[49] S. Fuhrmann, A. Hupfer, and H.-P. Kau. Investigations on Multi-Stage Supersonic Combustion in a Model Combustor. In *17th International Space Planes and Hypersonic Systems and Technologies Conference, San Francisco, CA, USA*, 2011.

[50] C. Fureby, M. Chapuis, E. Fedina, and S. Karl. CFD Analysis of the HyShot II Scramjet Combustor. *Proceedings of the Combustion Institute*, 33:2399–2405, 2011.

[51] W. Gabler. *Gemischbildung, Flammenstabilisierung und Verbrennung in einer gestuften Überschallbrennkammer*. PhD thesis, Technische Universität München, 1996.

[52] E. Garnier, Adams. N, and P. Sagaut. *Large Eddy Simulation for Compressible Flows*. Springer, 2009.

[53] P. Gerlinger. *Numerische Verbrennungssimulation: Effiziente numerische Simulation turbulenter Verbrennung*. Springer, 2005.

[54] P. Gerlinger, K. Nold, and M. Aigner. Influence of Reaction Mechanisms, Grid Spacing, and Inflow Conditions on the Numerical Simulation of Lifted Supersonic Flames. *International Journal for Numerical Methods in Fluids*, 62:1357–1380, 2010.

[55] A. Ghosh. *The Role of Density Gradient in Liquid Rocket Engine Combustion Instability*. PhD thesis, University of Maryland, 2008.

[56] D. A. Gieseking, J.-l. Choi, J. R. Edwards, and H. A. Hassan. Compressible-Flow Simulations Using a New Large-Eddy Simulation/Reynolds-Averaged Navier-Stokes Model. *AIAA Journal*, 49:2194–2209, 2011.

[57] V. Golovitchev, N. Nordin, R. Jarnicki, and J. Chomiak. 3-D Diesel Spray Simulations Using a New Detailed Chemistry Turbulent Combustion Model. In *CEC/SAE Spring Fuels & Lubricants Meeting & Exposition, Paris, France*, 2000.

[58] C. J. Greenshields, H. G. Weller, L. Gasparini, and J. M. Reese. Implementation of semi-discrete, non-staggered central schemes in a colocated, polyhedral, finite volume framework, for high-speed viscous flows. *International Journal for Numerical Methods in Fluids*, 63:1–21, 2010.

[59] E. M. Greitzer, C. S. Tan, and M. B. Graf. *Internal Flow*. Cambridge University Press, 2004.

[60] C. Grünig. *Gemischbildung und Flammenstabilisierung bei Pylon-Einblasung in Überschallbrennkammern*. PhD thesis, Technische Universität München, 1999.

[61] M. R. Gruber, A. S. Nejad, T. H. Chen, and J. C. Dutton. Transverse Injection from Circular and Elliptic Nozzles into a Supersonic Crossflow. *Journal of Propulsion and Power*, 16:449–457, 2000.

[62] J. Gullbrand and F. K. Chow. The Effect of Numerical Errors and Turbulence Models in Large-Eddy Simulations of Channel Flow, with and without Explicit Filtering. *Journal of Fluid Mechanics*, 495:323–341, 2003.

[63] N. E. Hass, M. K. Smart, and A. Paull. Flight Data Analysis of HyShot 2. In *13th AIAA/CIRA International Space Planes and Hypersonic Systems and Technologies Conference, Capua, Italy*, 2005.

[64] J. Heidenfelder and A. Paßler. Numerische Auslegung und Konstruktion eines Überschallprüfstands. Technical report, Technische Universität München, 2011.

[65] B. J. Isaac, A. Parente, C. Galletti, J. N. Thornock, P. J. Smith, and L. Tognotti. A Novel Methodology for Chemical Time Scale Evaluation with Detailed Chemical Reaction Kinetics. *Energy Fuels*, 27:2255–2265, 2013.

[66] D. Jacob, G. Sachs, and S. Wagner, editors. *Basic Research and Technologies for Two-Stage-to-Orbit Vehicles*. Wiley-VCH, 2005.

[67] S. Jakirlic. *Reynolds-Spannungs-Modellierung komplexer turbulenter Strömungen*. PhD thesis, Universität Erlangen-Nürnberg, 1997.

[68] H. Jasak, H.G. Weller, and A.D. Gosman. High Resolution NVD Differencing Scheme for Arbitrarily Unstructured Meshes. *International Journal for Numerical Methods in Fluids*, 31:431–449, 1999.

[69] S. Karl. *Numerical Investigation of a Generic Scramjet Configuration*. PhD thesis, Technische Universität Dresden, 2011.

[70] S. Kawai and S. K. Lele. Large-Eddy Simulation of Jet Mixing in Supersonic Crossflows. *AIAA Journal*, 48:2063–2083, 2010.

[71] R. J. Kee, M. E. Coltrin, and P. Glarborg. *Chemically Reacting Flow: Theory and Practice*. John Wiley & Sons, 2003.

[72] R. Keppeler. *Entwicklung und Evaluierung von Verbrennungsmodellen für die Large Eddy Simulation der Hochdruck-Vormischverbrennung*. PhD thesis, Universität der Bundeswehr München, 2013.

[73] B. Kniesner. *Ein hybrides LES/RANS-Verfahren für konjugierte Impuls-, Wärme- und Stoffübertragung mit Relevanz zu Brennkammerkonfigurationen*. PhD thesis, Technische Universität Darmstadt, 2008.

[74] A. N. Kolmogorov. The Local Structure of Turbulence in Incompressible Viscous Fluid for Very Large Reynolds Numbers. *Proceedings of the USSR Academy of Sciences*, 30:301–305, 1941.

[75] A. N. Kolmogorov. A Refinement of Previous Hypotheses Concerning the Local Structure in Turbulence in Viscous Incompressible Fluid at High Reynolds Number. *Journal of Fluid Mechanics*, 1:82–85, 1962.

[76] A. Kurganov, S. Noelle, and G. Petrova. Semidiscrete Central-Upwind Schemes for Hyperbolic Conservation Laws and Hamilton-Jacobi Equations. *SIAM Journal on Scientific Computing*, 23:707–740, 2001.

[77] A. Kurganov and E. Tadmor. New High-Resolution Central Schemes for Nonlinear Conservation Laws and Convection-Diffusion Equations. *Journal of Computational Physics*, 160:241–282, 2000.

[78] J. Larsson, S. Laurence, I. Bermejo-Moreno, J. Bodart, S. Karl, and R. Vicquelin. Incipient Thermal Choking and Stable Shock-Train Formation in the Heat-Release Region of a Scramjet Combustor. Part II: Large Eddy Simulations. *Combustion and Flame*, 162:907–920, 2015.

[79] S. J. Laurence, S. Karl, J. Martinez Schramm, and K. Hannemann. Transient Fluid-combustion Phenomena in a Model Scramjet. *Journal of Fluid Mechanics*, 722:85–120, 2013.

[80] S. J. Laurence, D. Lieber, J. Martinez Schramm, K. Hannemann, and J. Larsson. Incipient Thermal Choking and Stable Shock-Train Formation in the Heat-Release Region of a Scramjet Combustor. Part I: Shock-Tunnel Experiments. *Combustion and Flame*, 162:921–931, 2015.

[81] C. Lechner and J. Seume. *Stationäre Gasturbinen*. Springer, 2nd edition, 2010.

[82] M. Lesieur. *Turbulence in Fluids*. Springer, 4th edition, 2008.

[83] M. J. Lewis and D. E. Hastings. Application of Compound Compressible Flow to Nonuniformities in Hypersonic Propulsion Systems. *Journal of Propulsion*, 5:626–634, 1988.

[84] S. Liu, C. Meneveau, and J. Katz. On the Properties of Similarity Subgrid-scale Models as Deduced from Measurements in a Turbulent Jet. *Journal of Fluid Mechanics*, 275:83–119, 1994.

[85] T. S. Lund. The Use of Explicit Filters in Large Eddy Simulation. *Computers and Mathematics with Applications*, 46:603–616, 2003.

[86] K. H. Luo. Combustion Effects on Turbulence in a Partially Premixed Supersonic Diffusion Flame. *Combustion and Flame*, 119:417–435, 1999.

[87] K. H. Luo and K. N. C. Bray. Combustion-Induced Pressure Effects in Supersonic Diffusion Flames. *Symposium (International) on Combustion*, 27:2165–2171, 1998.

[88] A. Lyubar. *Numerisch effiziente Modellierung von Überschallbrennkammern mit detaillierter Kinetik*. PhD thesis, Technische Universität München, 2005.

[89] B. F. Magnussen. On the Structure of Turbulence and a Generalized Eddy Dissipation Concept for Chemical Reaction in Turbulent Flow. In *19th Aerospace Science Meeting, St. Louis, MO, USA*, 1981.

[90] K. Makowka, N. C. Dröske, J. J. Vellaramkalayil, T. Sattelmayer, and J. von Wolfersdorf. Unsteady RANS Investigation of a Hydrogen-Fueled Staged Supersonic Combustor with Lobed Injectors. In *19th AIAA International Space Planes and Hypersonic Systems and Technologies Conference, Atlanta, GA, USA*, 2014.

[91] K. Makowka, M Gurtner, D. Paukner, T. Sattelmayer, and O. Haidn. Numerical and Experimental Investigation of a Central Strut Injector with

Perpendicular Injection for Scramjet Applications. In *5th European Conference for Aeronautics and Space Sciences (EUCASS), Munich, Germany*, Munich, Germany, 2013.

[92] K. Makowka, M. Gurtner, D. Paukner, T. Sattelmayer, and O. Haidn. Semi-Zonal Hybrid RANS/LES Turbulence Modeling with RANS Sensor Based Interfacing Applied to Supersonic Flows. In *19th AIAA International Space Planes and Hypersonic Systems and Technologies Conference, Atlanta, GA, USA*, 2014.

[93] L. A. Marshall, C. Bahm, G. P. Corpening, and R. Sherrill. Overview With Results and Lessons Learned of the X-43A Mach 10 Flight. In *AIAA/CIRA 13th International Space Planes and Hypersonics Systems and Technologies, Capua, Italy*, 2005.

[94] S. Menon, P.-K. Yeung, and W.-W. Kim. Effect of Subgrid Models on the Computed Interscale Energy Transfer in Isotropic Turbulence. *Computers & Fluids*, 25:165–180, 1996.

[95] F. R. Menter. Two-Equation Eddy-Viscosity Turbulence Models for Engineering Applications. *AIAA Journal*, 32:1598–1605, 1994.

[96] F. R. Menter, J. Ferreira, T. Esch, and Konno B. The SST Turbulence Model with Improved Wall Treatment for Heat Transfer Predictions in Gas Turbines. In *Proceedings of the International Gas Turbine Congress*, 2003.

[97] T. Mitani, N. Chinzei, and T. Kanda. Reaction and Mixing-Controlled Combustion in Scramjet Engines. *Journal of Propulsion and Power*, 17:308–314, 2001.

[98] T. Mitani and T. Kouchi. Flame Structures and Combustion Efficiency Computed for a Mach 6 Scramjet Engine. *Combustion and Flame*, 142:187–196, 2005.

[99] B. Morgan, K. Duraisamy, N. Nguyen, S. Kawai, and S. K. Lele. Flow Physics and RANS Modelling of Oblique Shock/Turbulent Boundary Layer Interaction. *Journal of Fluid Mechanics*, 729:231–284, 2013.

[100] Y. Moule, V. Sabelnikov, and A. Mura. Highly Resolved Numerical Simulation of Combustion in Supersonic Hydrogen–air Coflowing Jets. *Combustion and Flame*, 161:2647–2668, 2014.

[101] A. L. Murray and C. H. Lewis. Supersonic Turbulent Boundary-Layer Flows with Mass Injection Through Slots and/or Porous Walls. Technical report, National Aeronautics and Space Administration, 1975.

[102] A. Nakayama and S. N. Vengadesan. On the Influence of Numerical Schemes and Subgrid–stress Models on Large Eddy Simulation of Turbulent Flow Past a Square Cylinder. *International Journal for Numerical Methods in Fluids*, 38:227–253, 2002.

[103] S. O'Byrne, M. Doolan, S. R. Olsen, and A. F. P. Houwing. Analysis of Transient Thermal Choking Processes in a Model Scramjet Engine. *Journal of Propulsion and Power*, 16:808–814, 2000.

[104] M. O'Conaire, H. J. Curran, J. M. Simmie, W. J. Pitz, and C. K. Westbrook. A Comprehensive Modeling Study of Hydrogen Oxidation. *International Journal of Chemical Kinetics*, 36:603–622, 2004.

[105] D. Papamoschou and A. Roshko. Observations of Supersonic Free Shear Layers. *Sadhana*, 12:1–14, 1988.

[106] E. Perez. *Ariane 5 User's Manual Issue 5 Revision 1*. Arianespace, 2011.

[107] N. Peters. *Turbulent Combustion*. Cambridge University Press, 2000. ISBN 0-521-66082-3.

[108] R. H. Pletcher, J. C. Tannehill, and D. A. Anderson. *Computational Fluid Mechanics and Heat Transfer*. CRC Press, 2013.

[109] T. Poinsot and D. Veynante. *Theoretical and Numerical Combustion*. R T Edwards Inc, 2nd edition, 2005.

[110] S. B. Pope. *Turbulent Flows*. Cambridge University Press, 2000.

[111] A. S. Potturi. *Numerical Simulation of High-Speed Combustion Processes in Scramjet Configurations*. PhD thesis, North Carolina State University, 2014.

[112] A. S. Potturi and J. R. Edwards. Large-Eddy / Reynolds-Averaged Navier-Stokes Simulation of Cavity-Stabilized Ethylene Combustion. In *19th AIAA International Space Planes and Hypersonic Systems and Technologies Conference, Atlanta, GA, USA*, Atlanta, Georgia, 2014.

[113] S. A. Ragab, S.-C. Sheen, and Sreedhar M. An Investigation of Finite-Difference Methods for Large-Eddy Simulation of a Mixing Layer. In *30th Aerospace Sciences Meeting & Exhibit, Reno, NV, USA*, 1992.

[114] R. H. Rogers. The development of the boundary layer in supersonic shear flow. In *Ministry of Aviation Aeronautical Research Council Current Papers*, 1962.

[115] A. S. Roudakov, V. L. Semenov, and J. W. Hick. Recent Flight Test Results of the joint CIAM-NASA Mach 6.5 Scramjet Flight Program. Technical Report TP-1998-206548, NASA, 1998.

[116] V. Sabelnikov and C. Fureby. LES Combustion Modeling for High Re Flames Using a Multi-phase Analogy. *Combustion and Flame*, 160:83–96, 2013.

[117] P. Sagaut. *Large Eddy Simulation for Incompressible Flows*. Springer, 2nd edition, 2004.

[118] T. Sander. *Verlustarme Pilotierung von Überschallflammen durch gasdynamisch optimierte Nebenstrom–Injektoren*. PhD thesis, Technische Universität München, 2003.

[119] H. Schlichting and K. Gersten. *Grenzschichttheorie*. Springer, 10th edition, 2006.

[120] U. Schumann. Subgrid Scale Model for Finite Difference Simulations of Turbulent Flows in Plane Channels and Annuli. *Journal of Computational Physics*, 18:376–404, 1975.

[121] C. Segal. *The Scramjet Engine*. Cambridge University Press, 2009.

[122] J. Smagorinsky. General Circulation Experiments with the Primitive Equations, I. The Basic Experiment. *Monthly Weather Review*, 91:99–164, 1963.

[123] M. Smart. Scramjet Isolators. In *AVT-185 RTO AVT/VKI Lecture Series*, 2010.

[124] A. J. Smits and J.-P. Dussauge. *Turbulent Shear Layers in Supersonic Flow*. Springer, 2006.

[125] P. R. Spalart, S. Deck, M. L. Shur, K. D. Squires, M. Kh. Strelets, and A. Travin. A New Version of Detached-eddy Simulation, Resistant to Ambiguous Grid Densities. *Theoretical and Computational Fluid Dynamics*, 20:181–195, 2006.

[126] P. R. Spalart, W.-H. Jou, M. Strelets, and S. R. Allmaras. Comments on the Feasibility of LES for Wings, and on a Hybrid RANS/LES Approach. In *Proceedings of first AFOSR international conference on DNS/LES, Ruston, LA, USA*, 1997.

[127] D. B. Spalding. Mixing and Chemical Reaction in Steady Confined Turbulent Flames. *13th Symposium (International) on Combustion*, 13:649–657, 1971.

[128] J. H. Spurk. *Fluid Mechanics*. Springer, 1997.

[129] S. H. Starner and R. W. Bilger. LDA Measurements in a Turbulent Diffusion Flame with Axial Pressure Gradient. *Combustion Science and Technology*, 21:259–276, 1980.

[130] S. H. Starner and R. W. Bilger. Measurement of Scalar-Velocity Correlations in a Turbulent Diffusion Flame. *Symposium (International) on Combustion*, 18:921–930, 1981.

[131] S. Stolz and N. A. Adams. Large-Eddy Simulation of High-Reynolds-number Supersonic Boundary Layers Using the Approximate Deconvolution Model and a Rescaling and Recycling Technique. *Physics of Fluids*, 15:2398–2412, 2003.

[132] S. Stolz, N. A. Adams, and L. Kleiser. The Approximate Deconvolution Model for Large-Eddy Simulations of Compressible Flows and its Application to Shock-Turbulent-Boundary-Layer Interaction. *Physics of Fluids*, 13:2985–3001, 2001.

[133] G. A. Sullins. Demonstration of Mode Transition in a Scramjet Combustor. *Journal of Propulsion and Power*, 9:515–520, 1993.

[134] C. Tian and Y. Lu. Turbulence Models of Separated Flow in Shock Wave Thrust Vector Nozzle. *Engineering Applications of Computational Fluid Mechanics*, 7:182–192, 2013.

[135] E. Toro, M. Spruce, and W. Speares. Restoration of the Contact Surface in the HLL-Riemann Solver. *Shock Waves*, 4:25–34, 1994.

[136] E. F. Toro. *Riemann Solvers and Numerical Methods for Fluid Dynamics*. Springer, 3rd edition, 2009.

[137] J. C. Turner and M. K. Smart. Mode Change Characteristics of a Three-Dimensional Scramjet at Mach 8. *Journal of Propulsion and Power*, 29:982–990, 2013.

[138] S. R. Turns. *An Introduction to Combustion*. McGraw-Hill, 2nd edition, 2000.

[139] J. J. Vellaramkalayil. *Experimental and Numerical Investigations of Different Injection Schemes in a Supersonic Combustion Chamber*. PhD thesis, Universität Stuttgart, 2014.

[140] J. J. Vellaramkalayil, T. Scheuermann, and J. von Wolfersdorf. Analysis of a Two-Staged Supersonic Combustion Chamber using Experiments and Simulations. In *Proceedings of the 17th AIAA International Space Planes and Hypersonic Systems and Technologies Conference, San Francisco, CA, USA*, number AIAA 2011-2247, San Francisco, CA, USA, 2011.

[141] A. W. Vreman. *Direct and Large-eddy Simulation of the Compressible Turbulent Mixing Layer*. PhD thesis, University of Twente, 1995.

[142] U. Walter. *Astronautics*. Wiley-VCH, 2008.

[143] R. J. Weber and J. S. MacKay. An Analysis of Ramjet Engines using Supersonic Combustion. Technical report, NACA TN 4386, 1958.

[144] D. C. Wilcox. *Turbulence Modeling for CFD*. DCW Industries, 3rd edition, 2006.

[145] R. J. Yentsch and D. V. Gaitonde. Unsteady Three-Dimensional Mode Transition Phenomena in a Scramjet Flowpath. *Journal of Propulsion and Power*, 31:104–122, 2015.

[146] A. Yoshizawa and K. Horiuti. A Statistically-Derived Subgrid-Scale Kinetic Energy Model for the Large-Eddy Simulation of Turbulent Flows. *Journal of the Physical Society of Japan*, 54:2834–2839, 1985.

[147] S. Zhang and C. J. Rutland. Premixed Flame Effects on Turbulence and Pressure-Related Terms. *Combustion and Flame*, 102:447–461, 1994.

[148] V. P. Zhukov. Verification, Validation, and Testing of Kinetic Mechanisms of Hydrogen Combustion in Fluid-Dynamic Computations. *International Scholarly Research Network ISRN Mechanical Engineering*, 2012, 2012.

Appendix

A Supplementary URANS Results for the Supersonic Diffusion Flame Simulations

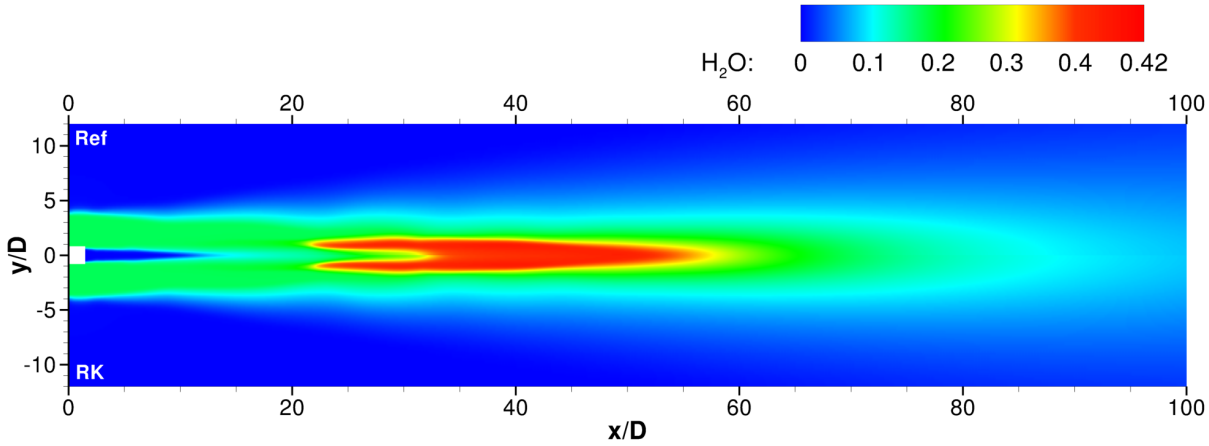

(a) H_2O

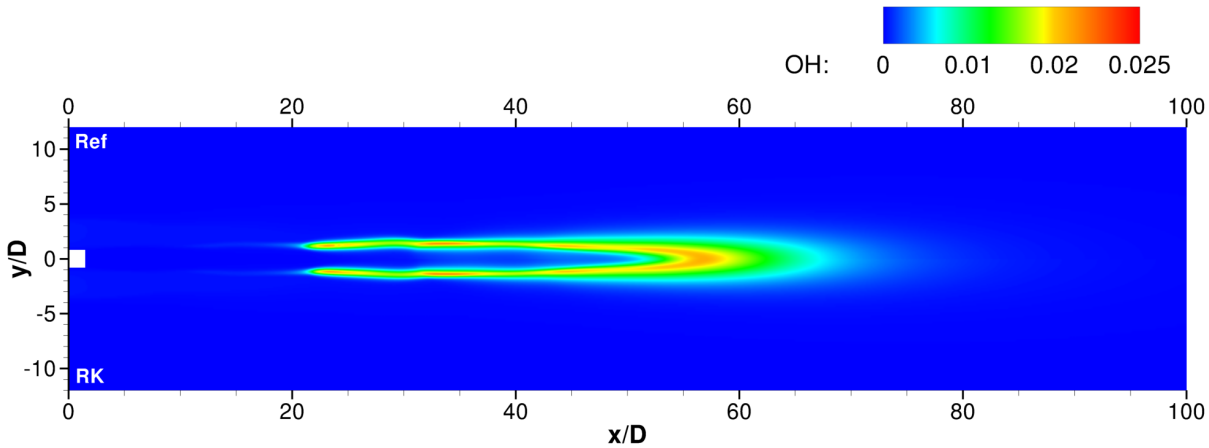

(b) OH

Figure A.1: H_2O and OH mass fraction fields for the reference simulation Ref (top) and the RK simulation with Runge-Kutta 4^{th} order time integration (bottom)

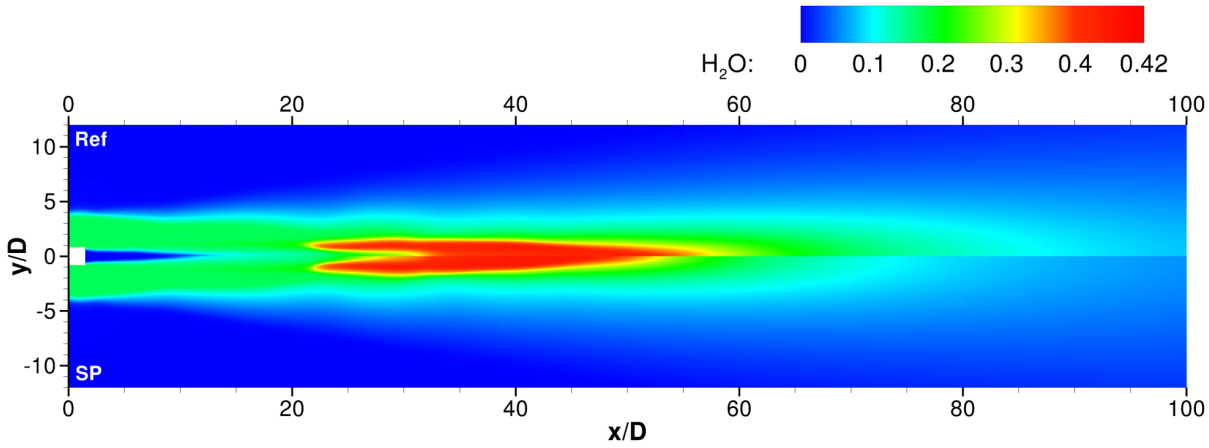

(a) H_2O

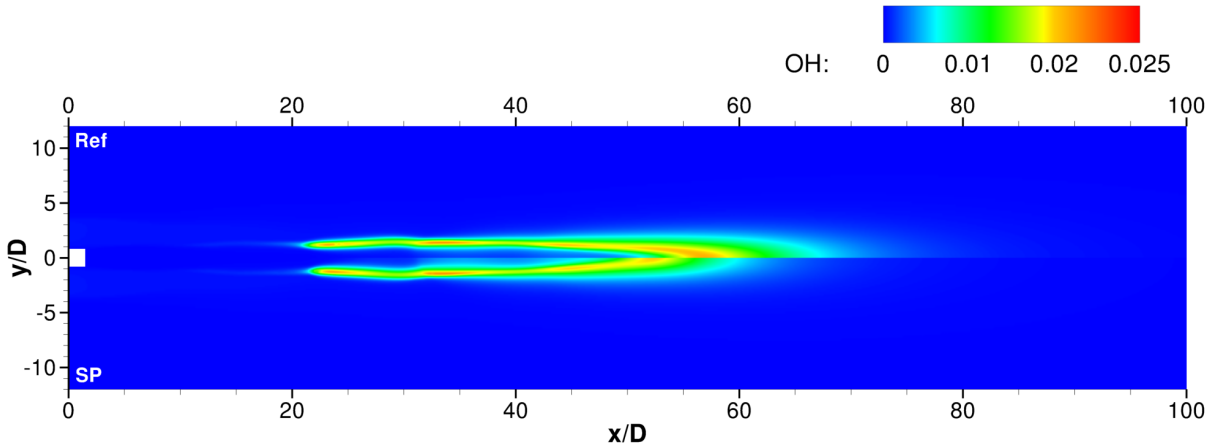

(b) OH

Figure A.2: H_2O and OH mass fraction fields for the reference simulation Ref (top) and the SP simulation with decreased Pr_t and Sc_t (bottom)

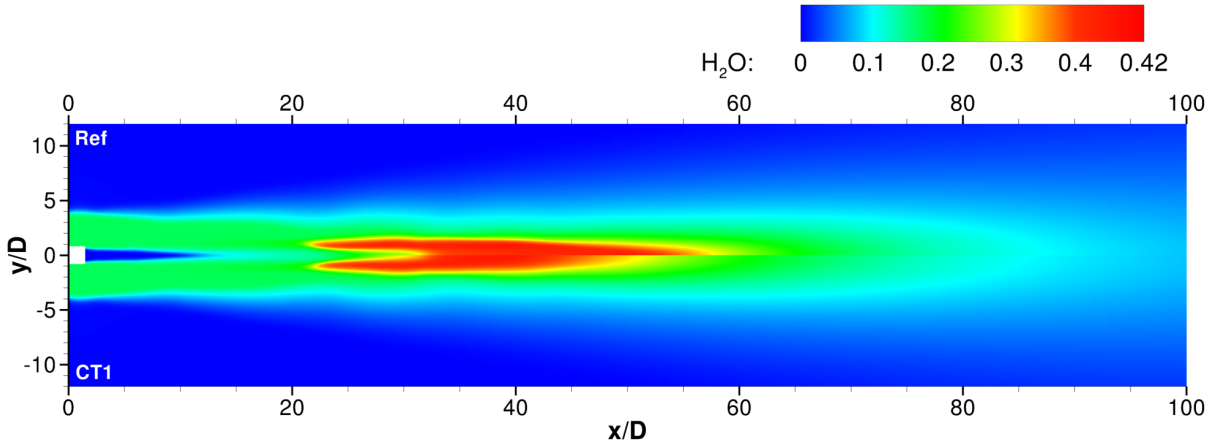

(a) H_2O

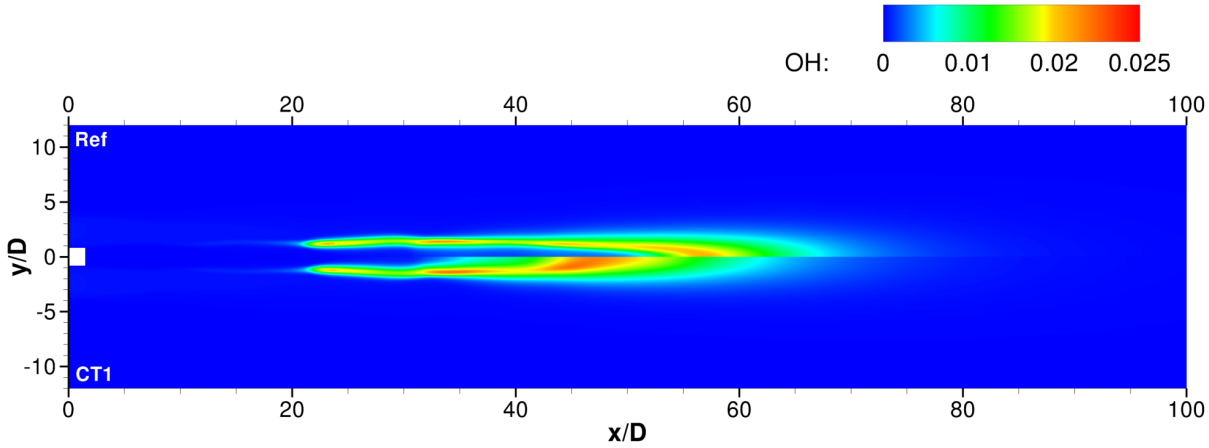

(b) OH

Figure A.3: H_2O and OH mass fraction fields for the reference simulation Ref (top) and the CT1 simulation with combustion induced turbulence (bottom)

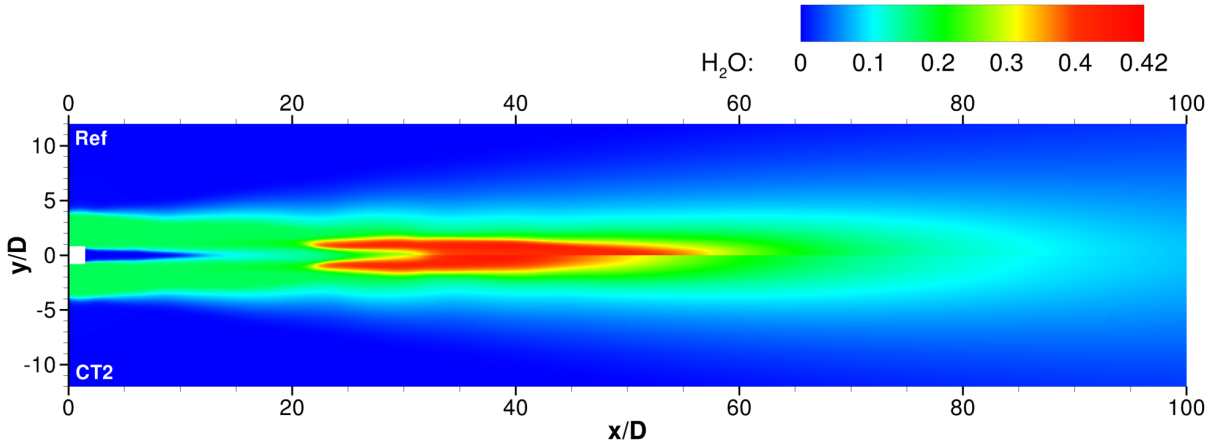

(a) H_2O

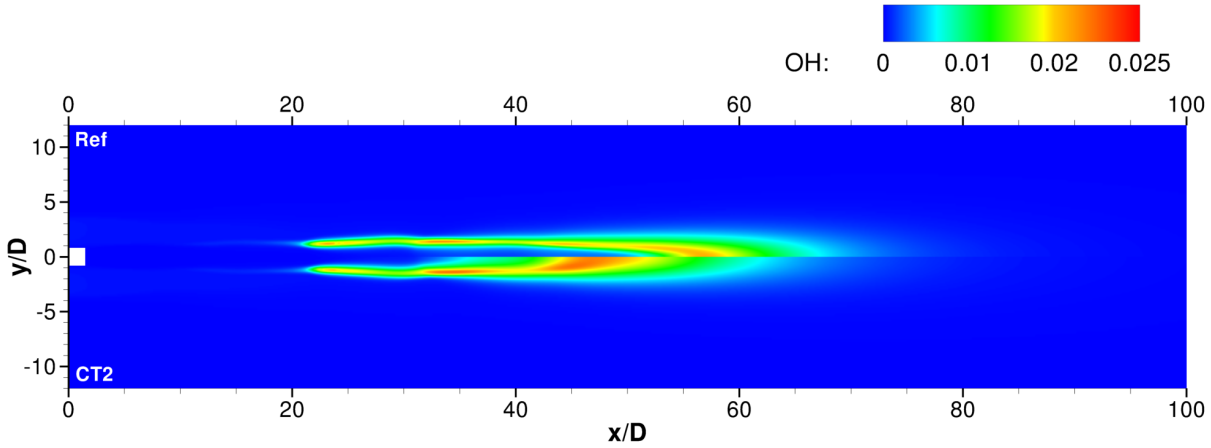

(b) OH

Figure A.4: H_2O and OH mass fraction fields for the reference simulation Ref (top) and the CT2 simulation with combustion induced turbulence (bottom)

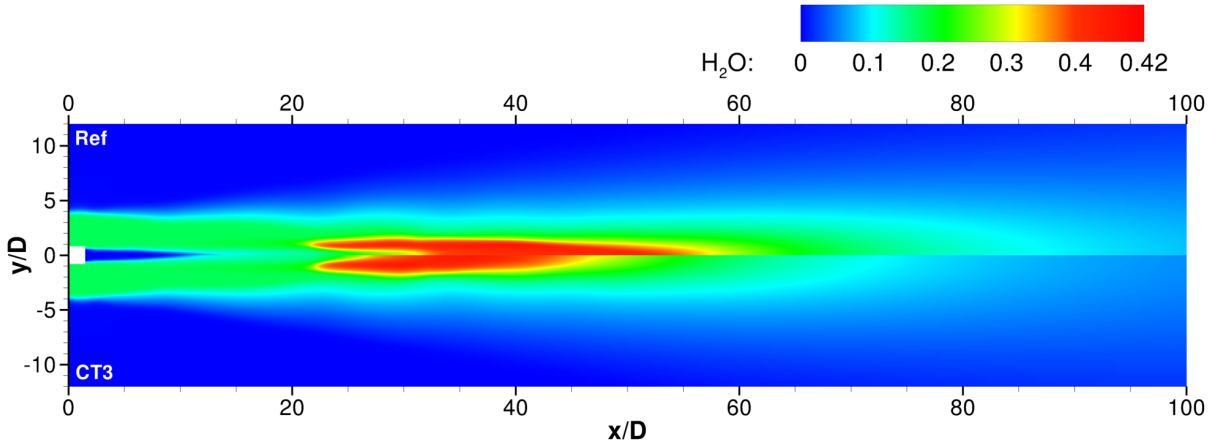

(a) H_2O

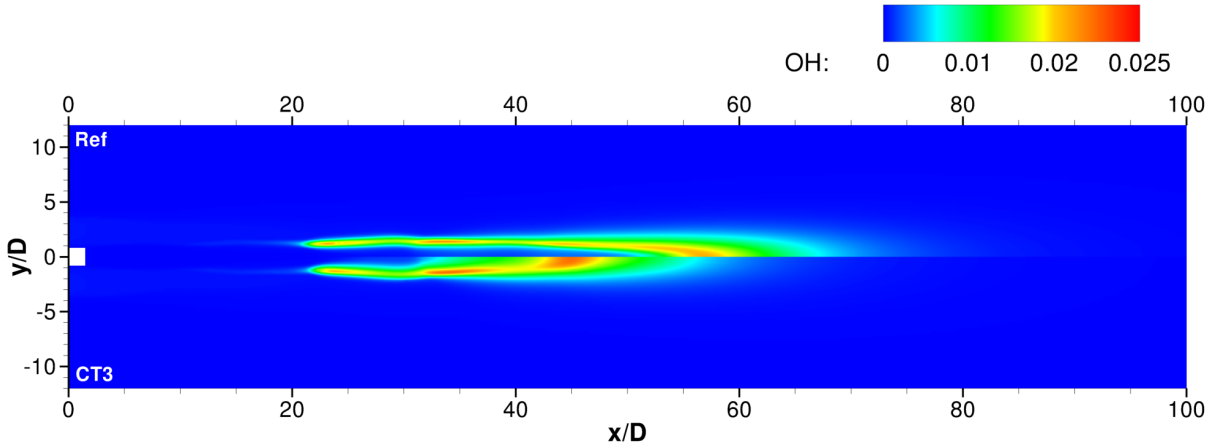

(b) OH

Figure A.5: H_2O and OH mass fraction fields for the reference simulation Ref (top) and the CT3 simulation with combustion induced turbulence (bottom)

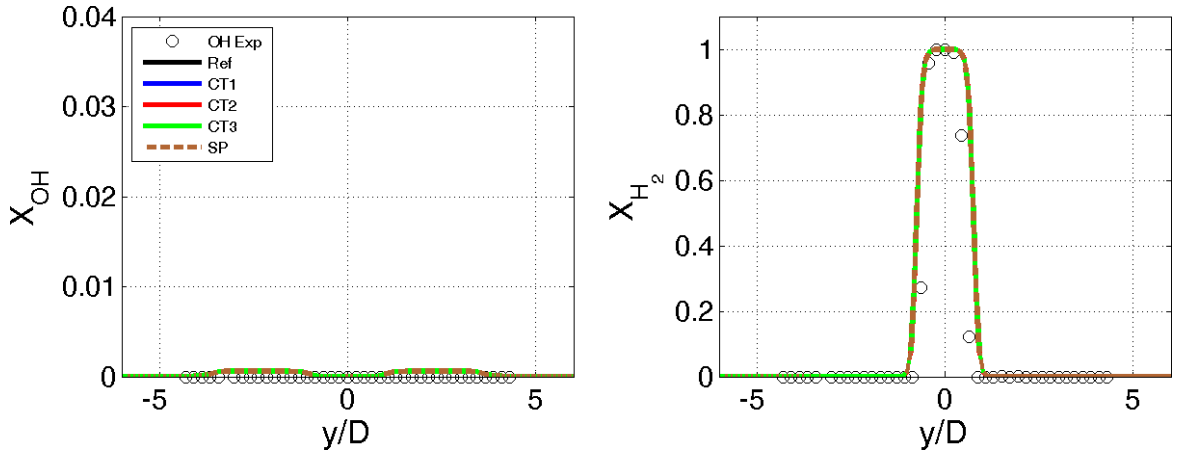

(a) x/D = 0.85

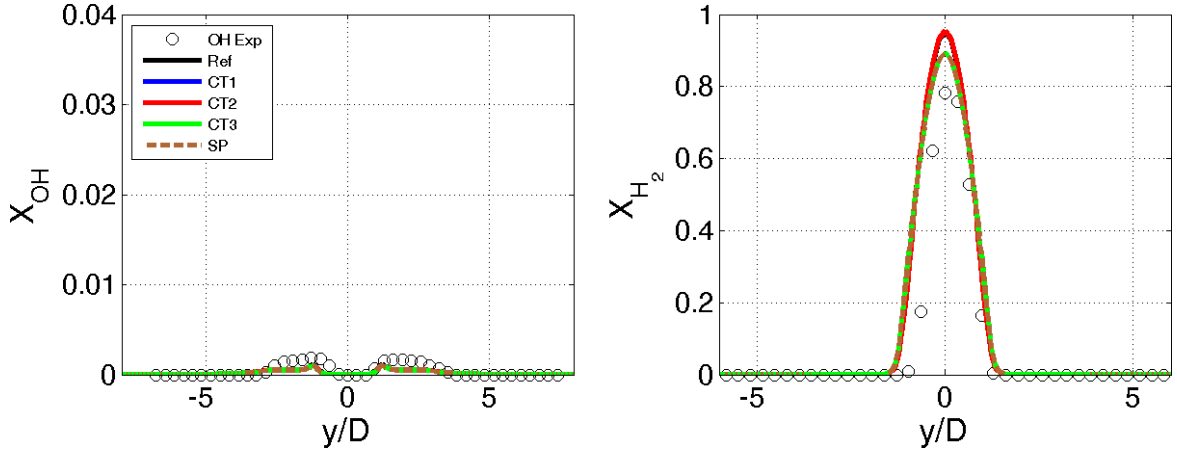

(b) x/D = 10.80

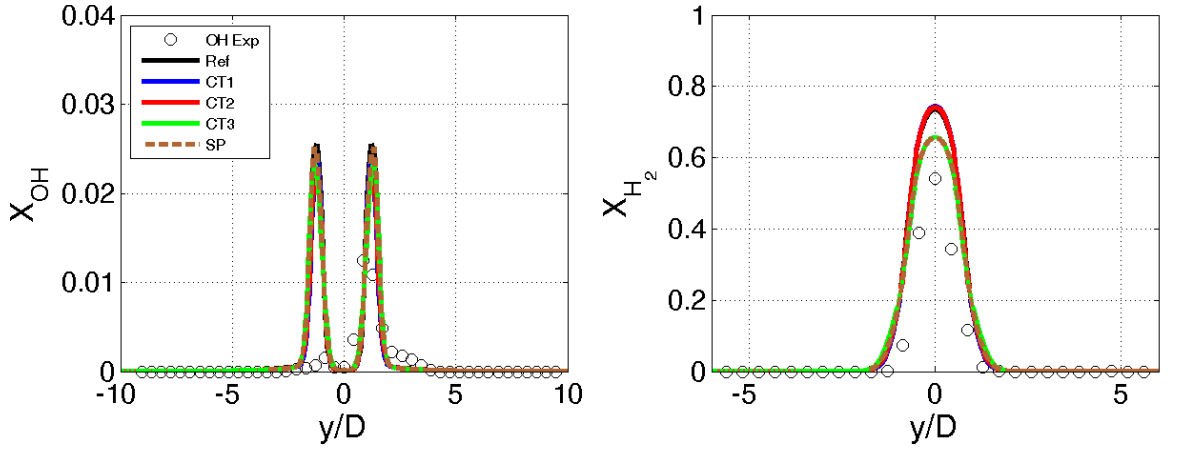

(c) x/D = 21.50

Figure A.6: Mean OH and H_2 mole fractions

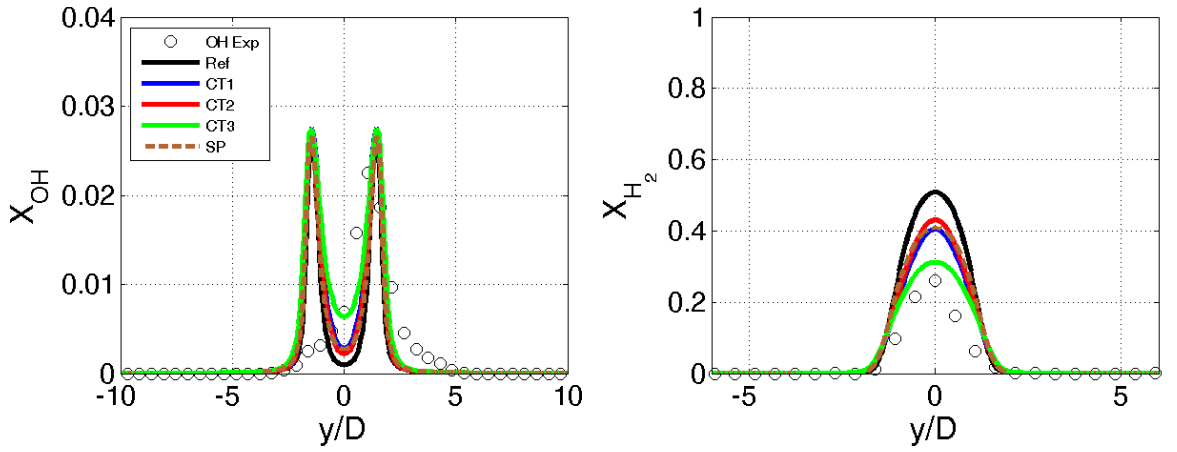

(a) x/D = 32.30

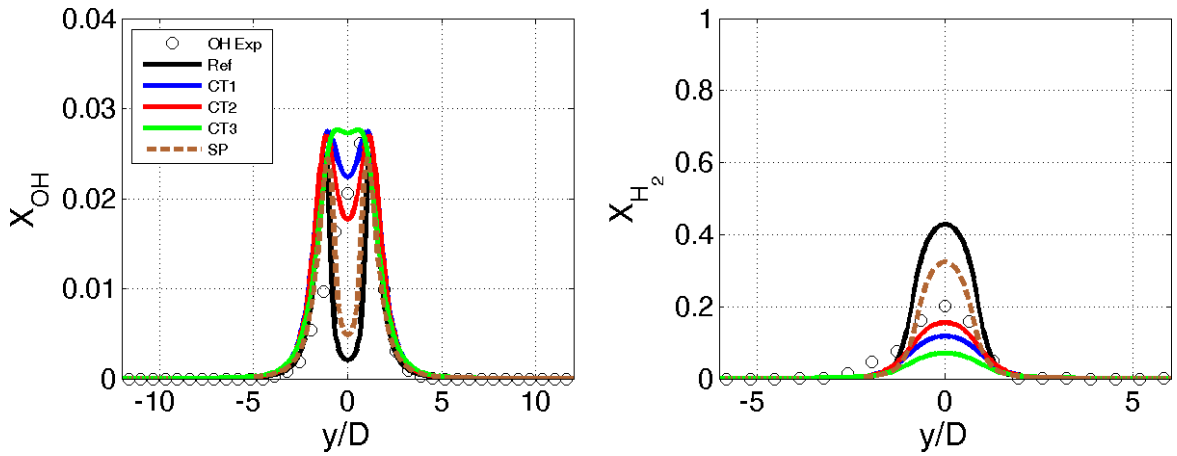

(b) x/D = 43.10

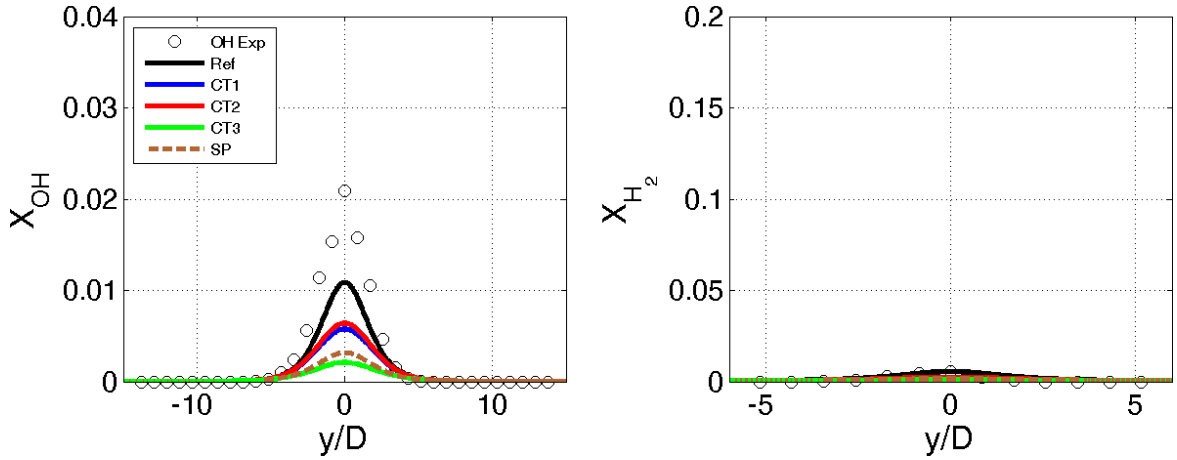

(c) x/D = 64.70

Figure A.7: Mean OH and H_2 mole fractions